In situ TEM Investigations of Catalysis Dynamics in Service Conditions

By

Boao Song

B.S., Nanjing University of Science and Technology, 2012

M.S., University of Rochester, 2014

THESIS

Submitted as partial fulfillment of the requirements

for the degree of Doctor of Philosophy in Mechanical Engineering

in the Graduate College of the

University of Illinois at Chicago, 2020

Chicago, Illinois

Defense Committee:
    Dr. Reza Shahbazian-Yassar, Chair and Advisor
    Dr. Arunkumar Subramanian
    Dr. Matthew Daly, Department of Civil, Materials, and Environmental Engineering
    Dr. Yuzi Liu, Argonne National Laboratory
    Dr. Wissam A. Saidi, University of Pittsburgh

ACKNOWLEDGEMENTS

CONTRIBUTION OF AUTHORS

This section and Chapter 3-4[1, 2], partial of Chapter 5[3] are from the published or submitted first-author articles with written permission from the journals. They are included in the Appendix.

Contribution of authors in Chapter 3

B. Song and R. Shahbazian-Yassar conceived the idea. B. Song carried out the (S)TEM and *in situ* TEM experiments. K. He, Y. Yuan, and S. Sharifi-Asl provided necessary TEM support. W. Saidi carried out the DFT calculations. B. Song and M. Cheng draw the schematic figures. Y. Yuan, W. Saidi and J. Lu provided necessary help in manuscript writing.

Contribution of authors in Chapter 4

B. Song and R. Shahbazian-Yassar conceived the idea. B. Song carried out the (S)TEM and *in situ* TEM experiments. T. Yang and W. Saidi carried out the DFT calculations. Y. Liu, Y. Yuan, S. Sharifi-Asl, and M. Cheng provided necessary (S)TEM and SEM support.

Contribution of authors in Chapter 5

B. Song and R. Shahbazian-Yassar conceived the idea. Y. Yang and M. Zachariah prepared the HEA samples. B. Song carried out the (S)TEM and *in situ* TEM experiments. M. Rabbani, T. Yang, and W. Saidi carried out the DFT calculations. Y. Liu, K. He, X. Hu, Y. Yuan, and V. Dravid provided necessary (S)TEM support.

SUMMARY

In this thesis, we studied the behavior of nanoscale materials exposed to liquid, gas, and high temperature environments. This study was enabled by the utilization of *in situ* transmission electron microscopy (TEM) for the study of nanoscale reactions. We performed our *in situ* TEM evaluation using silicon nitride (SiN)-membrane gas cells, SiN-membranes with resistive Joule heating, and SiN-membrane liquid cells. Specifically, key insights are obtained for synthesis of two-dimensional (2D) heterostructures, degradation mechanisms of 2D-supported heterogeneous catalysts under service conditions, and behavior of high-entropy alloy materials in redox gaseous environments.

Initially, the nucleation and growth processes of noble metal nanoparticles on 2D supports are investigated. Recently, noble metal nanoparticles with high surface area, suitable orientation and strong resistant to aggregation is of highly demand in design of next generation catalysts. 2D materials, a promising substrate for noble metal nanoparticles, provide a facile way to control particle size, orientation and prevent aggregation. However, little is known on how two-dimensional substrates influence the nucleation and growth process of noble nanoparticles. Dynamic characterization of such events preserving the liquid environment is key to unveil the underlying mechanisms of substrate-noble metal interactions during their nucleation and growth processes. Utilizing the advanced liquid-cell TEM technique, *in situ* observation of nucleation and growth process of gold nanoparticles on ultrathin MoS_2 nanoflake is achieved. It is found that growth of Au nanoparticle behaves significantly different on pristine MoS_2 and defective MoS_2. Electrochemical Oswald ripening governs Au growth on pristine MoS_2, while the sulfur

iv

vacancies on defective MoS_2 provide strong adsorption sites that promote particle diffusion and coalescence. The results help further understanding of synthesis conditions that can achieve desirable morphology of heterogeneous catalysts.

In the subsequent study, the degradation mechanisms of 2D material supported catalysts in service conditions are investigated. Although 2D materials supported mono- and core-shell nanoparticles offer a promising way to achieve better catalytic activity and selectivity, little is known on how 2D substrates influence the durability of the supported catalysts due to the limited characterization methods of dynamic degradation events. Utilizing the advanced *in situ* gas-cell TEM technic combined with DFT calculation, significant difference in sintering kinetics of Pt and Au@Pt core-shell on MoS_2 are observed under vacuum, N_2, H_2 and air environments. Due to the Pt-H interactions, Pt nanoparticles are less stable on MoS_2 in H_2 than in vacuum and N_2. In contrast, small size Au@Pt core-shell nanoparticles are more stable than larger ones and similar size Pt NPs in H_2 due to the alloying effect and inertia to H_2 dissociation. This finding provides key insights into how nanoparticles stability can be tuned by controlling reaction with ambient atmosphere and interactions with 2D supports. Additionally, this study addresses catalysis degradation mechanisms in environments more closely to the actual application conditions.

In another study, the oxidation and reduction behaviors of high entropy alloy (HEA) nanoparticles (NPs) in atmospheric pressure oxidizing/reducing environments are investigated. With five or more principle elements in the form of homogeneous mixed solid solutions in a single-phase, HEA NPs offer a promising way to achieve supreme mechanical properties, thermal stability and corrosion resistance. However, little is known on such NPs behave under critical conditions involving oxidizing gases due to

v

the limited characterization methods of dynamic events. Utilizing the advanced *in situ* gas-cell TEM technic combined with DFT calculation, the high-temperature oxidation and reduction of FeCoNiCuPt HEA NPs in real-time are successfully captured. Combining the *in situ* STEM-EDS and STEM-EELS analyses, the oxidation of HEA NPs are found to be governed by Kirkendall effects displaying outwards segregation of Fe, Co, Ni and Cu. The oxidation states of transition metals are further determined by EELS and HRTEM. During oxidation, localized ordering from metal oxide are observed to form in an overall disordered oxide matrix. In the reduction process, further segregation of Cu into Cu NPs is identified. The HEA NPs transform into HEA core and oxide shell structure, with individual Cu NPs at external surface of the oxide. These findings provide key insights into HEA NPs oxidation and reduction kinetics, and shed light on future design of highly stable alloys with wide applications in structural materials, energy conversion, and advanced catalysis.

It is expected that the *in situ* TEM techniques are to be developed rapidly in future, possibly with wider range of capabilities and further improved resolutions. In addition to provide fundamental understandings and insights on materials development, the studies presented in this thesis can serve as guideline and references for the ongoing efforts in microscopy techniques process improvements.

TABLE OF CONTENTS

LIST OF FIGURES

Figure 1-1. Two major *in situ* liquid phase TEM techniques: **(a)** Schematic of MEMS-based liquid cell TEM device. The capability of introducing electrochemical stimuli is demonstrated. Inset shows example of 2D materials supported nanoparticles in the liquid cell. **(b)** Schematic of graphene liquid cell setup. The liquid pocket is formed by sandwiching two graphene layers.. 2

Figure 1-2. (I) The electron beam induced reduction of Ag ions and the electron beam current influenced growth mechanisms on Ag nanocrystals. Reprinted with permission from [6]. Copyright (2012) American Chemical Society. **(II)** TEM images and simulated TEM images showing the Pt nanocrystal growth process in liquid. [13] Copyright © 2014, American Association for the Advancement of Science. **(III)** (a) Gold seed in dry state. (b-c) Dendrites growth of gold in precursor solution. (d-f) TEM images at different times recorded after c showing the growth directions. Reprinted with permission from [8]. Copyright (2013) American Chemical Society. **(IV)** Pt@Au nanoparticle shape evolution in $HAuCl_4$ flow and citric acid solution (a-c) and without the flow (d-f). Schematic shape evolution is shown in g. Reprinted with permission from [30]. Copyright (2015) American Chemical Society. **(V)** $CH_3NH_3PbI_3$ precipitation process under electron beam evaporation. Reprinted with permission from [31]. Copyright (2016) American Chemical Society. 8

Figure 1-3. (I) Schematic illustration of the electrochemical liquid cell setup to study the Si nanowire lithiation/delithiation. Reprinted with permission from [34]. Copyright (2013) American Chemical Society. **(II)** (a) Potential cycling profile of Pt-Ni alloy. (b-g) Disappearance of Ni-rich particle during cycling. (h) Intensity profile of the Ni-rich particle in b-g. (i) Dissolution rate corresponding to h.[35] Published by The Royal Society of Chemistry. **(III)** STEM images showing growth of Li_2O_2 on current collector (a) and in electrolyte (b). (c-d) Growth kinetics corresponding to a and b. [36]© 2018 Elsevier Ltd. All rights reserved. **(IV)** TEM images showing the TiO_2 NPs under UV exposure at different times, suggesting the formation of surface shell over the NPs. [38]Copyright © 2018, Springer Nature..11

Figure 1-4. (a) Schematic of environmental TEM showing the electron microscope chamber modified by differential pumping systems. (b) Schematic of MEMS-based gas cell device focusing on the specimen region from a special designed TEM holder. 14

Figure 1-5. (I) *In situ* ETEM image series of Pd NPs in Ar gas at different temperatures. The scale

LIST OF TABLES

Chapter 1   Introduction

1.1 Introduction to *in situ* liquid phase TEM

TEM, a technique ideal for obtaining high spatial resolution information of materials structures, is widely used in understanding the structure and chemistry of advanced materials. Since the working principle of TEM relies on the accelerated electron beam interactions with sample, conventional TEM requires maintaining high vacuum in the microscope chamber and specimen region. Therefore, the obtained information reflects specimen in vacuum condition. Liquid-phase TEM, a technique involving special design in specimen region that allows the sample stay in liquid without influencing the high vacuum in TEM chamber, is demonstrated earlier as in 1974 where an environmental chamber with thin film windows was designed for the microscope column.[4] This technique has further been developed in the past decades and has opened the possibility to observe samples in liquid phase as well as liquid-phase reactions with high spatial and temporal resolution. Reactions that beyond the observation capabilities of conventional TEM are now easily applicable for *in situ* liquid-phase TEM, such as nucleation and growth of materials,[5-13] electrochemical reactions between electrolyte and electrode,[14-16] corrosion process happens on solid-liquid interfaces,[17-20] and so forth. These capabilities provide direct evidences of localized phenomena that can help address relationships between materials properties and dynamic reactions during syntheses and applications. Recently, there are two major *in situ* liquid phase TEM techniques: MEMS-based liquid cell TEM and graphene liquid cell (GLC) TEM, as shown in Figure

1-1. They will be discussed separately in the following sections.
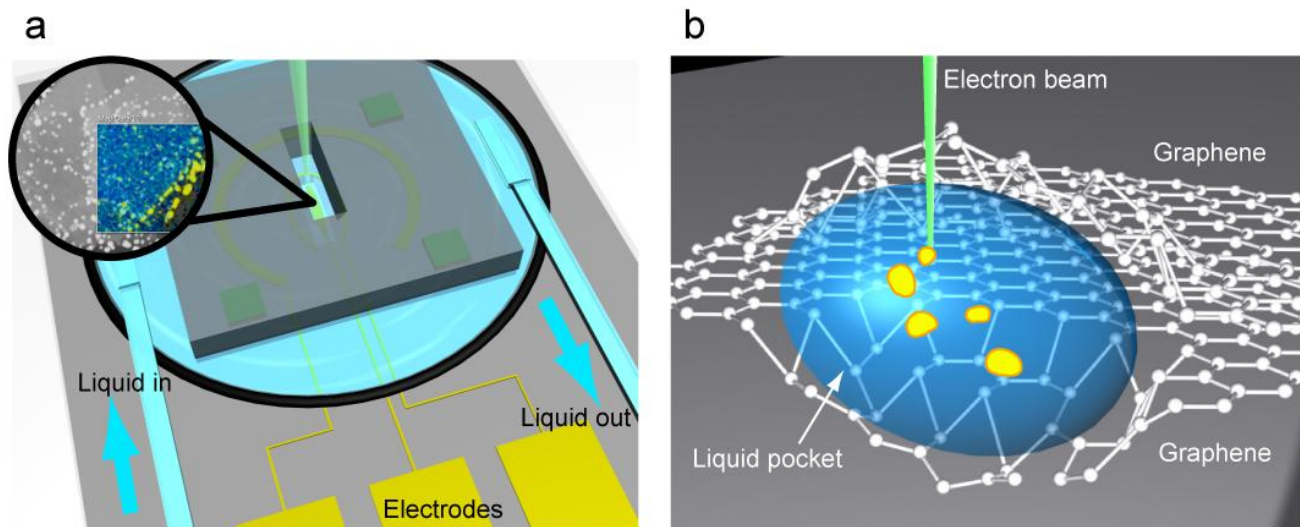
Figure 1-1. Two major *in situ* liquid phase TEM techniques: **(a)** Schematic of MEMS-based liquid cell TEM device. The capability of introducing electrochemical stimuli is demonstrated. Inset shows example of 2D materials supported nanoparticles in the liquid cell. **(b)** Schematic of graphene liquid cell setup. The liquid pocket is formed by sandwiching two graphene layers.

1.1.1 MEMS-based liquid cell TEM

Since the idea of isolating liquid between two layers to prevent influencing high vacuum in electron microscope chamber, *in situ* liquid TEM has been conducted by utilizing microchips made from silicon equipped with electron transparent silicon nitride membrane. Figure 1-1a shows the schematic of MEMS-based liquid cell TEM setup. The specimens are loaded onto the SiN membrane region carefully due to the thin (usually less than 50 nm) and fragile nature of the membrane. This step can be achieved by different methods depending on the specimen size, shape, physical and chemical properties. Currently,

2

drop-casting of sample dispersion, physical vapor deposition, and focused ion beam (FIB) are several common methods aiming to load the specimen while preserving the SiN membrane.[21] Then another microchip is used to pair with the one with specimen on that, fully sealed with gaskets, and then assembled onto TEM holder, forming a liquid cell around the specimen area. The distance between two microchips is controlled by spacers, ranging from tens of nm to more than 1 μm. The SiN membrane, commonly called the transparent window, serves as the observation window for the isolated specimen. However, due to the high vacuum in the microscope chamber, the SiN window may bulge when liquid is inside the cell, resulting in a liquid thickness gradience in different regions.[21] This effect may or may not influence the dynamic behaviors and should be carefully considered when performing *in situ* liquid TEM experiments. Electron scattering will happen when the electron beam pass through the SiN window and the liquid layer before reaching the specimen, resulting in a decrease of resolution compare to imaging in vacuum condition. By carefully tuning the liquid thickness, SiN window thickness, specimen physical and chemical properties, the spatial resolution is possible to reach atomic level.[22] The temporal resolution, which is another essential factor in observing dynamic reactions, is determined by the imaging techniques involving parameters such as camera speed in TEM, scanning dwell time and frame time in STEM. The MEMS-based liquid cell TEM technique has been developed and commercialized by several companies including (by alphabet order) DENSsolutions, Hummingbird Scientific and Protochips. These specialized *in situ* TEM holders have the capability of forming static liquid cell and dynamic flow cell, by controlling the open or isolation of liquid inlets/outlets. The dynamic flow cell setup further opens the possibility to observe reaction in its very beginning and early stage, when the reaction agent is flowed into the cell after

3

the electron microscope fully aligned and ready for imaging. There are experimental setups with more than one liquid inlet that allows flowing mixture of two solutions simultaneously or at different time into the cell, and thus being more beneficial in studying complex dynamics when there are more than two reaction agents involved.

Further, advanced designs of MEMS microchips are becoming available that external stimuli can be applied to sample region including biasing and heating. These are achieved by carefully designing the microchips with electrodes. Experiments involving electrochemical reactions and high-temperature liquid reactions are possible to be studied by these setups.[23, 24] The *in situ* MEMS-based liquid TEM is therefore becoming widely applicable for various fields related to materials synthesis, nanomaterials self-assembly, life sciences, electronic devices, energy storage materials including batteries and fuel cells, and so forth.[21]

1.1.2 Graphene liquid cell TEM

Although the MEMS-based liquid cell TEM technique are under fast development, it exist short comes including reduced spatial resolution due to electron scattering on SiN membrane, reduced signal-to-noise ratio (SNR) for analytical EDS and EELS, complexity of assembling the *in situ* holder, and requirement of using holder with specialized design in specimen region. To address these, a raising method that utilizing graphene layer to replace SiN membrane are attracting attentions. This is achievable due to the special properties of graphene that include high stability, high strength, ease of fabricating single or few layer, and more importantly, the high conductivity and low atomic number.[25] Figure 1-1b shows the

4

schematic of GLC setup. The capillary force between liquid and graphene perfectly sealed the top and bottom graphene layers. Therefore, graphene is an ideal alternation for SiN membrane and can provide better spatial resolution for HRTEM and analytical EDS/EELS.[26] The liquid cell pocket size, ranging from nanometer to micrometer diameter, is determined by the properties and fabrication process of graphene layers, and can be tuned to accommodate different specimen dimensions.[21] In addition, GLC benefits from the lack of requiring special designed specimen holder such that it is easier to be applied in wider range of microscopes.[27] Recently, studies utilizing GLC have reported focus on specimen including bacteria, cells, nanoparticles, biomaterials, polymers, and so forth.[26]

1.2 Applications of *in situ* liquid phase TEM

1.2.1 Materials synthesis and self-assembly

Understanding how materials behave during synthesis process is crucial for development of novel materials structures with ideal chemical composition. The *in situ* liquid-phase TEM is powerful tool for the observation of materials behaviors in liquid environment during synthesis. This includes crystallization, nucleation, growth, self-assembly, dissolution, polymerization, corrosion, etching, and so forth.

The nucleation and growth mechanism of materials in liquid is a field with plenty of theories but little experimental studies due to the lack of instrument providing high spatial and temporal resolution. This issue is being overcame benefiting from the development of *in situ* liquid cell TEM with nanoscale and millisecond temporal resolution. Back to 2009, the study utilizing liquid cell TEM to directly observe the colloidal Pt nanocrystals growth in liquid[28] established a general protocol for liquid-phase TEM, and

5

prove that sub-nanometer resolution imaging is achievable in the liquid. Later on, many new studies performed, pushing the frontier of liquid cell TEM for a wide range of materials including monometallic nanoparticles, bimetallic core-shell structures, nanowires, nanocubes, nanoplates, ceramics, biomaterials, metal organic frameworks (MOFs), perovskite nanoparticles, and so forth. For example, PbS nanoparticle growth from precursor was directly captured in a multi-component solution by liquid cell TEM.[10] It was shown that electron beam could serve as external stimuli to trigger the nucleation and growth process. Later, it was found that electron beam could control the nucleation and growth processes of Ag nanoparticles (Figure 1-2I), where lower beam currents (7 pA) allow reaction limited growth while higher beam currents (40 pA) yield diffusion limited growth, resulting in different nanocrystal morphology.[6] Thus, the nucleation and growth processes have been widely studies utilizing this electron beam triggered self-assembly technique. For instance, growth of Pd in aqueous Pd salt solutions containing Au seeds were captured by liquid cell TEM, resulting in formation of Au-Pd core-shell nanostructures.[29] The deposition of Pd was found to be a reduction process by electron beam generated radicals such as hydrated electrons in solution. The growth process was further shown to be limited by the diffusion of hydrated electrons. Similarly, another study focused on growth of dendritic gold nanowires from gold seed in aqueous solution showed the growth process is limited by diffusion,[8] as shown in Figure 1-2III. In addition, the growth of Pt nanoseed were observed in liquid TEM with different growth rate on different facets, resulting in the formation of Pt nanocubes (Figure 1-2II).[13] As such, different morphology of nanostructures with one or more principle elements can be grown in liquid through the careful control of electron beam conditions. This aspect has been further demonstrated by several studies, such as the

6

nucleation and growth of Au on Pt icosahedral nanoparticles[30] in Figure 1-2IV and dissolution of Pt

nanoparticles during oxidative etching in $HAuCl_4$ solution.[17]

It should be noted that the *in situ* liquid TEM technique is not limited to crystalline materials and high

atomic number elements. It has been successfully applied to biominerals, polymers and organic

macromolecular materials. $CaCO_3$ nucleation and growth processes in a biomimetic matrix solution were

captured inside liquid cell, and the formation of metastable amorphous calcium carbonate was controlled

by calcium ions binding.[12] In the example of metal-organic frameworks (MOFs), the nucleation and

growth dynamics of zeolitic imidazolate framework-8 (ZIF-8) MOFs were observed to be limited by local

depletion of monomers in solution at surface.[7] The nucleation, growth and aggregation of hybrid

$CH_3NH_3PbI_3$ perovskite nanoparticles were captured by electron beam evaporation method (Figure 1-2V),

and reveals complex dynamic behavior that does not follow classical Lifshitz-Slyozov-Wagner (LSW)

growth theory.[31] The biological sample, for example ferritin, can be encapsulated by GLC[32, 33] to

enable the observation in liquid phase with nanometer spatial resolution by tuning the electron beam

conditions.

Figure 1-2. (I) The electron beam induced reduction of Ag ions and the electron beam current influenced growth mechanisms on Ag nanocrystals. Reprinted with permission from [6]. Copyright (2012) American Chemical Society. **(II)** TEM images and simulated TEM images showing the Pt nanocrystal growth process in liquid. [13] Copyright © 2014, American Association for the Advancement of Science. **(III)** (a) Gold seed in dry state. (b-c) Dendrites growth of gold in precursor solution. (d-f) TEM images at different times recorded after c showing the growth directions. Reprinted with permission from [8]. Copyright (2013) American Chemical Society. **(IV)** Pt@Au nanoparticle shape evolution in HAuCl$_4$ flow and citric acid solution (a-c) and without the flow (d-f). Schematic shape evolution is shown in g. Reprinted with permission from [30]. Copyright (2015) American Chemical Society. **(V)** CH$_3$NH$_3$PbI$_3$ precipitation process under electron beam evaporation. Reprinted with permission from [31]. Copyright (2016) American Chemical Society.

8

Overall, *in situ* liquid-phase TEM enables the studies that provide deep understanding on nanocrystal nucleation and growth mechanism and shed light on the design of materials synthesis methodologies.

1.2.2 Energy related materials

Benefiting from the specialized design of MEMS microchip with built-on electrodes, electrochemical reactions are possible to be triggered inside the liquid cell, allowing direct observation of complex electrochemical behaviors at interfaces, and provide high spatial resolution for studies of energy related materials including batteries, fuel cells, electrocatalysis, and so forth.

A major research effort has been put into fundamental understanding of battery behaviors during charge and discharge processes. Using three electrodes configuration involving working, counter and reference electrodes on MEMS microchip, the liquid cell can be assembled with electrode materials such as $LiCoO_2$, $LiFePO_4$, Li metal, and with organic electrolytes similar to working conditions in lithium-ion batteries. The liquid cell TEM holder can be connected to potentiostats, allowing the control of electrochemical reactions in potentiostatic and galvanostatic modes. Plenty of phenomena can be observed directly including formation of solid electrolyte interface (SEI) layer at electrode-electrolyte interface, Li dendrite growth in the electrolyte, electrochemical lithiation processes on electrodes, and degradation of commercialized electrolytes. For instance, lithiation and delithiation processes of Si nanowire electrodes were captured in real time in electrolytes inside the liquid cell TEM (Figure 1-3I).[34] It was found that single nanowire displays core-shell mechanism under lithium insertion, with increased in total diameter

9

of the wire along the axial direction.

Beyond metal-ion batteries, liquid-phase TEM is also powerful in exploring other energy related materials like lithium-air system and fuel cell that involves electrochemical catalytic reactions. For example, the oxygen reduction reaction (ORR) in fuel cell cycling induced degradation of Pt-Ni alloy was monitored in real-time.[35] As shown in Figure 1-3II, the nanocatalysts' structural dynamics were captured involving migration and coalescence, dissolution and redeposition and these help to address the complex unknown process happened on catalysts during fuel cell electrochemical cycling. In another study, the charge and discharge processes of a Li-O$_2$ battery have been directly observed at nanoscale resolution (Figure 1-3III).[36] The nucleation and growth of Li$_2$O$_2$ were identified to be ion-diffusion limited reactions on both electrode-electrolyte interface and electrolyte environment. During OER catalytic reaction on Co$_3$O$_4$ nanoparticles, cyclic voltammetry and chronopotentiometry were performed in standard electrochemistry conditions by liquid cell TEM.[37] Chemical and structural evolutions during OER in various aqueous electrolytes were analyzed and surface amorphization on Co$_3$O$_4$ nanoparticles were observed. Moreover, it is interesting that HER at solid-solution interface is also possible to be explored by liquid cell TEM. A study using UV light fiber introduced into microscope analyzed the photocatalytic behavior of TiO$_2$ nanoparticles in water.[38] As shown in Figure 1-3IV, he surface hydrogenated shell formed across TiO$_2$ nanoparticles at initial H$_2$ formation stage is shown to be the reason that promotes hydrogen evolution reaction (HER).

Figure 1-3. (I) Schematic illustration of the electrochemical liquid cell setup to study the Si nanowire lithiation/delithiation. Reprinted with permission from [34]. Copyright (2013) American Chemical Society. **(II)** (a) Potential cycling profile of Pt-Ni alloy. (b-g) Disappearance of Ni-rich particle during cycling. (h) Intensity profile of the Ni-rich particle in b-g. (i) Dissolution rate corresponding to h.[35] Published by The Royal Society of Chemistry. **(III)** STEM images showing growth of Li_2O_2 on current collector (a) and in electrolyte (b). (c-d) Growth kinetics corresponding to a and b. [36]© 2018 Elsevier Ltd. All rights reserved. **(IV)** TEM images showing the TiO_2 NPs under UV exposure at different times, suggesting the formation of surface shell over the NPs. [38]Copyright © 2018, Springer Nature.

Besides MEMS-based liquid cell TEM, GLC is also well established technique for study of energy related materials. For example, liquid electrolyte was sandwiched between graphene layers and Si NPs immersed in the liquid. The electron beam was used to trigger the chemical lithiation of Si NPs and the whole process was captured with high spatial resolution. It was found the lithiation can take place preferentially at certain crystal orientations, and isotropic diffusion of Li ions can happen at inner regions of the Si NPs.

1.3 Introduction of *in situ* gas phase TEM

TEM is a power tool to study materials structure and chemical composition with down to sub-angstrom spatial resolution. Since the TEM principle relies on the interactions of accelerated electrons with specimen that resulted in various types of scattering, the conventional TEM techniques require maintaining high vacuum in the electron beam chamber and the specimen region. Specimens have to be firstly thin to a certain level for allowance of electron transmission, fixed on a support usually a holy TEM grid, and then keep in vacuum condition during TEM analyses. Recently, the developments in material science and engineering are calling for advanced TEM characterization techniques involving methods that allow study of materials under complex conditions other than vacuum. Till now, there are several *in situ* TEM techniques under fast development involving liquid-phase TEM that allow specimen to immerse in solution, and gas-phase TEM that allow specimen to expose to gases molecules. The first technique has been discussed in previous chapter. Here, *in situ* gas-phase TEM will be focused.

Study materials that exposed to ambient gas environment under TEM is a long-term research goal back to as early as 1968, few decades after the invention of TEM. A gas reaction specimen chamber with

12

high temperature capability reaching 1000 °C was constructed inside the TEM electron beam pathway, allowing the specimen exposed to gas layer at pressure of 300 Torr.[39] This was believed to be the first successful incorporation of differential pumping system into TEM to achieve the imaging of specimen in gas environment. This technique has been under fast development after the commercialization of so-called environmental TEM (ETEM) in 2008,[40] combining with the advanced field emission electron source, opens the ability to study solid-gas reactions at atomic level. The schematic of ETEM is shown in Figure 1-4a. Benefiting from this design, the gas introduced to the TEM specimen region can be variating from inert gas to O_2, H_2, CO_2, CO and so forth. The further developments utilizing special designed TEM holder with closed cell set up similar to MEMS-based liquid cell TEM are communalized by several companies, with additional capabilities including added heating and biasing on the studied specimens (Figure 1-4b).[41] The pressure at the specimen region can reach 1 atm or even more in this closed cell setup,[42] and different gas mixture can be preset and loaded into the specimen chamber with controllable speed.[43] Since the electron scattering on gas molecules is significant less than on liquid, spatial the resolution degradation because of gas is much reduced.[42] Recently reports have successfully observed single atom even using the MEMS-based gas-cell TEM technique.[44] Combined with direct detection camera that allows fast imaging speed, the gas-phase TEM is an ideal technique for very high spatial and temporal resolution studies on material dynamics in application of catalysis, corrosion, fuel cell, oxidation and reduction, and so forth.
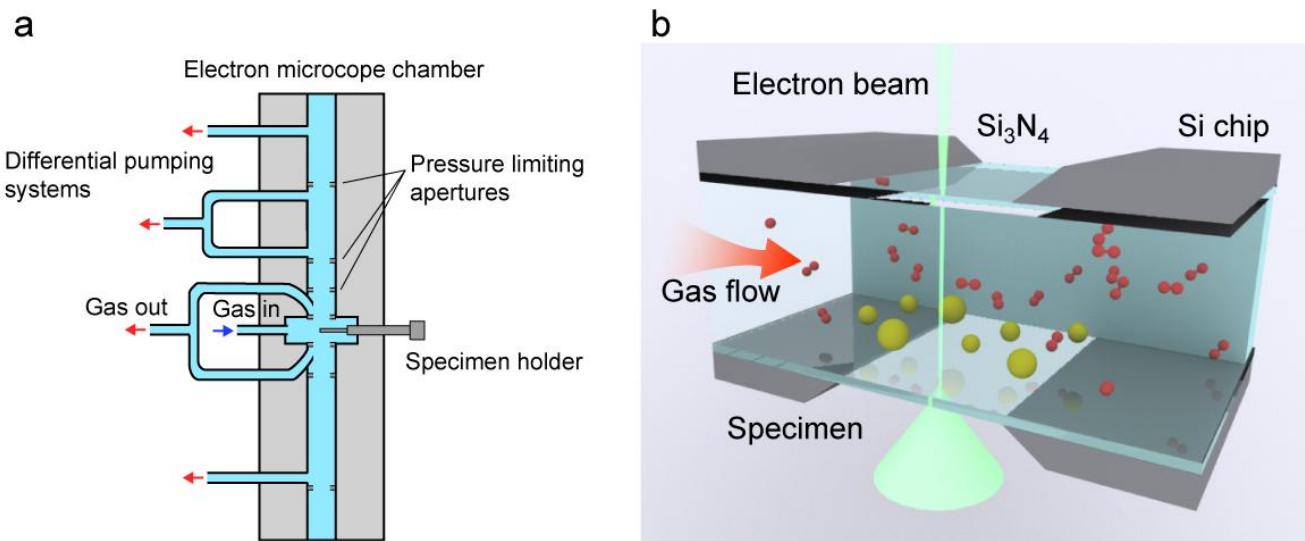
Figure 1-4. (a) Schematic of environmental TEM showing the electron microscope chamber modified by differential pumping systems. (b) Schematic of MEMS-based gas cell device focusing on the specimen region from a special designed TEM holder.

1.3.1 Environmental TEM (ETEM)

ETEM is a basic technique proposed soon after the invention of TEM, with the idea that isolate the specimen chamber to let the sample expose to external environment but maintain the high vacuum in the other regions of electron beam path. As shown in Figure 1-4a, pressure limiting apertures are installed inside the microscope chamber to separate the column into different pressure regions, and confine the gas flow between each regions. Differential pumping systems are then installed between each isolated region to provide high pressure in the specimen region but limit the pressure at a much lower level in other electron beam path regions.[45] Therefore, any gas escape from the pressure limiting apertures will be pumped out by the differential pumping systems in a circulated manner. These pumping systems are

14

further mechanically modified in order to reduce vibrations that can influence TEM imaging. In the recent developed ETEM, pressure in specimen region can reach around 13 mbar while the other region in electron beam chamber can maintain 10^{-8} mbar (10^{-6} Pa) that maintain a minimum electron scattering on the gas molecules.[40] The design of ETEM allows the use of *in situ* TEM holders such as heating, biasing, cooling with either conventional TEM grid or MEMS device as sample support, thus provide more capabilities for studying material dynamics in complex environments.[45]

1.3.2 *In situ* Gas cell TEM

Similar to MEMS-based liquid cell TEM, the liquid isolated between two microchips can be replaced by gas, allowing the specimen to be exposed in gas environment. Figure 1-4b shows the schematic of MEMS-based gas cell TEM device focusing on the specimen region. Compare to ETEM, this design is beneficial for studies that require the gas environment to be at one atmosphere,[42] and is easy to accommodate with conventional TEMs without the need to mechanically modify the electron beam column. Gases can be flowed into the cell using gas inlets, while at the same time the reaction gas products can be collected at the outlet and perform further analyses. In addition, there is capability to mix more than one type of gas before flowing into the cell, and thus opens the possibility to study materials dynamics under complex gas compositions.[43] The distance between two microchips can range from tens of nm to few microns, as the multiple electron scattering when passing through the gas layer is significantly less than liquid layer.[42] Therefore, atomic resolution HRTEM and STEM imaging can be achieved in gas cell TEM experiments. The temporal resolution is again determined by imaging techniques involving parameters such as camera

15

speed in TEM and scanning dwell time and frame time in STEM. Currently, major commercialized MEMS-based gas cell TEM techniques include companies (by alphabet order) DENSsolutions, Hummingbird Scientific and Protochips. In addition, there are microchip designs that allow adding heat or bias to the sample region to achieve real time control of local temperature ranging from RT to more than 1000 °C,[40] or performing electrochemical tests on sample exposing to gas environment. Benefiting from the MEMS devices, thermal drift during temperature rise are significantly reduced compared to furnace based heating holder, allowing easier real-time imaging and analytical tests.[42] As such, *in situ* gas TEM is becoming a powerful tool to study wide range of catalysis and structural materials and their properties including thermal, corrosion and oxidation behaviors happens on solid-gas interfaces.

1.4 Applications of *in situ* gas phase TEM

1.4.1 Catalysis

Various of solid-gas reactions triggered by catalysts serve as key process for manufacturing products, so the in depth understanding of catalysis reactions is beneficial for not only industrial applications but also daily life. The ability of flowing gases into the TEM chamber while adding external stimuli like heating and biasing makes *in situ* gas cell TEM an ideal tool for study of catalysis reactions. From monometallic and bimetallic to alloy catalysts, nanoparticle to single-atom morphology, the *in situ* gas cell TEM can be utilized to analyze the structural and compositional evolutions in conditions that reflect the catalysts actual service environments, with sub-angstrom spatial resolution and ultra-fast temporal resolutions. This information extended the knowledge of catalysts' as-synthesized properties to the catalysts' behaviors

16

under their working reaction processes and is crucial for further developments of advanced catalysts with desirable properties.

A major topic in catalysis development is the synthesis process. It is well known that the catalysts' morphology including shape of nanostructure, size, and orientation relationship regarding to the support are essential for the activity and selectivity. Therefore, understanding how the synthesis processes can be tuned for a better control of catalyst's morphology acts as a key to improve the catalysis performance. Utilizing the ETEM with *in situ* MEMS-based heating holder, transformation of noble metal NPs to single atoms in Ar gas was successfully captured, as shown in Figure 1-5I.[46] It is worth to note that particle sintering involving aggregation and coalescence is a thermodynamically favorable phenomenon during catalyst synthesis, by which a desired size and shape can be obtained. However, this work shows that when temperature is above 900 °C, the atomization process dominates and overcomes the sintering process, leading to the formation of single-atom dispersion of noble metals on the carbon support. It is expected that bonding between Pd and N in carbon support are stronger than the metal Pd-Pd bonding, and thus provide the atomization driving force. In lower temperatures below 900 °C, the sintering process is dominate and particle migration and coalescence are observed. This work shows the temperature can be an essential factor that control the catalysts synthesis process, leading to different morphologies.
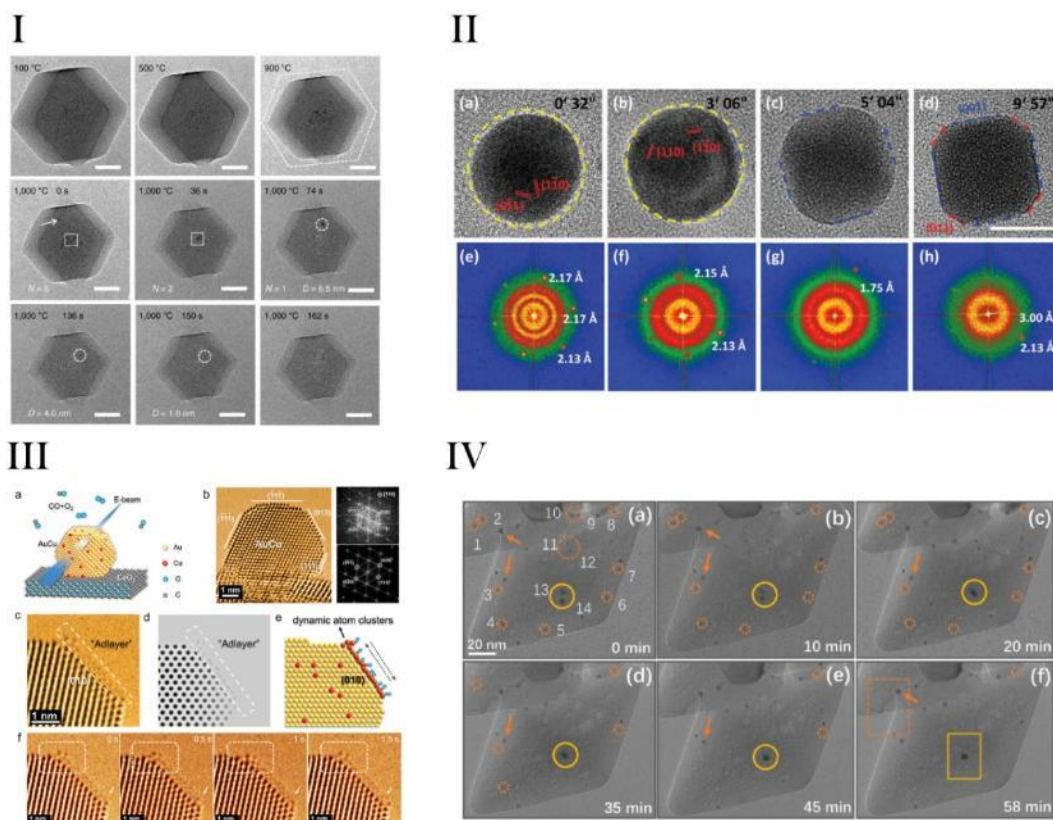
Figure 1-5. (I) *In situ* ETEM image series of Pd NPs in Ar gas at different temperatures. The scale bars are 50 nm. [46]Copyright © 2018, Springer Nature **(II)** HRTEM images and corresponding FFTs of PdCu NPs in atmospheric pressure H_2 at 600 K. [47]© 2016 WILEY−VCH Verlag GmbH & Co. KGaA, Weinheim **(III)** (a) Schematic of ETEM setup to study AuCu NPs supported by CeO_2 in CO and O_2 gases. (b) HRTEM of an AuCu NP with corresponding FFTs. (c-e) HRTEM, simulated HRTEM and schematic of surface reconstruction during CO oxidation. (f) HRTEM image series of the interaction between dynamic atom clusters with AuCu edge sites. Reprinted with permission from [48]. Copyright (2020) American Chemical Society. **(IV)** *In situ* ETEM image series showing the sintering of Au NPs supported by TiO_2 in 0.05 Pa O_2 at 700 °C. Solid and dashed circles marked the NPs underwent PMC and OR, respectively. [49]© 2020 Elsevier Inc. All rights reserved.

18

The catalytic dynamics under reaction conditions is another major aspect that *in situ* gas TEM can be a powerful tool to investigate. When a catalytic reaction happens, the chemical dissociation of gas molecules followed by the adsorption of gas atoms on catalyst surface can alter the shape, size and overall morphology of the catalyst itself. When a catalytic cycle ends, the desorption of gas produce from catalyst surface can change the morphology to its original status. With the help of *in situ* gas TEM technique, the catalysts morphology evolution induced by gases can be resolved in real time with atomic resolution to gain advanced understanding of reaction kinetics and mechanisms during a catalytic cycle. In addition, combing the analytical capability of EDS and EELS, compositional evolution is also possible to be analyzed in a straight-forward manner. For instance, Figure 1-5II shows the PdCu NPs surface reconstruction under atmospheric pressure H_2 at 600 K.[47] From the HRTEM images, it can be seen that the PdCu NPs are spherical initially and gradually developed the facets from {001} and {011} with rotation, resulted in a truncated cube. This phenomenon is further confirmed by the FFT patterns. DFT calculations show that H_2 can improve the stability of (001) facets in PdCu NPs and this is the reason that surface reconstruction was observed that lead to {001} facets dominated truncated cube structure. In another study, dynamic atom clusters were observed to form on AuCu NPs surface during catalytic CO oxidation.[48] As shown in Figure 1-5IIIa-b, ETEM was utilized to capture the dynamic structural evolutions and the HRTEM in Figure 1-5IIIc clearly demonstrates the formation of dynamic atom cluster on the (010) surface of AuCu NP. These clusters are generated from the metal atoms free by gas molecules and are highly mobile to react with edge sites on NPs surface (Figure 1-5IIIf).

19

Moreover, the durability of catalysts is important factor to evaluate the practical application abilities. For most of the catalytic reactions, complex service conditions involving high temperature and exposure to strong oxidizing/reducing environments. *In situ* gas TEM can be an ideal tool to monitor and analysis the catalyst durability in very similar environments compared to the actual service conditions, by allowing the exposure of catalysts to atmospheric gases in elevated temperatures. One of the major catalysis degradation mechanisms, sintering, can be directly captured and analyzed. It is well known that Ostwald ripening and particle migration and coalescence are two main mechanism that guided the particle sintering,[50] where the first involves migration of atom species from smaller NPs to larger NPs, resulting in the loss of small NP but growth of larger NP, and the second mechanism yield migration of whole NPs that finally coalescence into one. In a study of sintering behavior of Au NPs supported by TiO_2 in O_2 gas at 700 °C (Figure 1-5IV), both PMC and OR mechanisms were observed in a same sample region, and similar sintering behavior were identified in O_2 and CO mixed atmosphere. However, the CO gas can inhibit the sintering process because the gas induced surface modification on TiO_2 support suppress the movement of Au NPs.

1.4.2 Oxidation and reduction

Oxidation and reduction are key reactions involved in wide range of chemical processes such as corrosion, catalytic, chemical manufacturing, and environmental protection. For example, the oxidation induced corrosion on materials are one of the major causes of materials degradation during service. Development of corrosion resistance materials as well as the methods to recover from corrosion is attracting significant

20

attentions. Benefiting from the capability of exposing specimen to gas environment, *in situ* gas TEM can provide advance knowledge in the oxidizing and reducing process. Figure 1-6I shows HRTEM image series of Pd NPs surface oxidation in low pressure oxygen induced by electron beam irradiation in room temperature.[51] Based on the analyses on HRTEM and corresponding FFTs, the oxidation was identified to be initiated at step edges of Pd (111) facets and gradually growth into oxide island. The PdO island is not observed to growth on other facets. Therefore, a preferential growth of PdO on {111} Pd surface was concluded. In another study, the oxidation and reduction processes of PtNi rhombic dodecahedron NPs were captured at 400 °C in O_2 and H_2 environments.[43] The morphology and compositional evolutions are shown in Figure 1-6IIa-b and c, as formation of NiO shell in oxidation and strong segregation of Pt during reduction were observed. Further, the interface between metal and oxide were analyzed in detail for Cu_2O/Cu, in reducing environment of H_2 at 350 °C.[52] As shown in Figure 1-6III, HRTEM images focusing at the interface suggest that formation and migration of step edge guides the reduction of process. Moreover, for NiFe alloy NPs oxidation, the morphology and chemical composition evolutions were monitored simultaneously in real-time.[53] Figure 1-6IV shows during the NiFe alloy NPs oxidation in air, Kirkendall voids were formed at metal/oxide interfaces and segregation of Ni and Fe were identified, forming a core-shell structure. The cavity structures are different in terms of pinholes in the alloy NPs, leading to different oxygen penetration abilities and thus different morphology after oxidation.
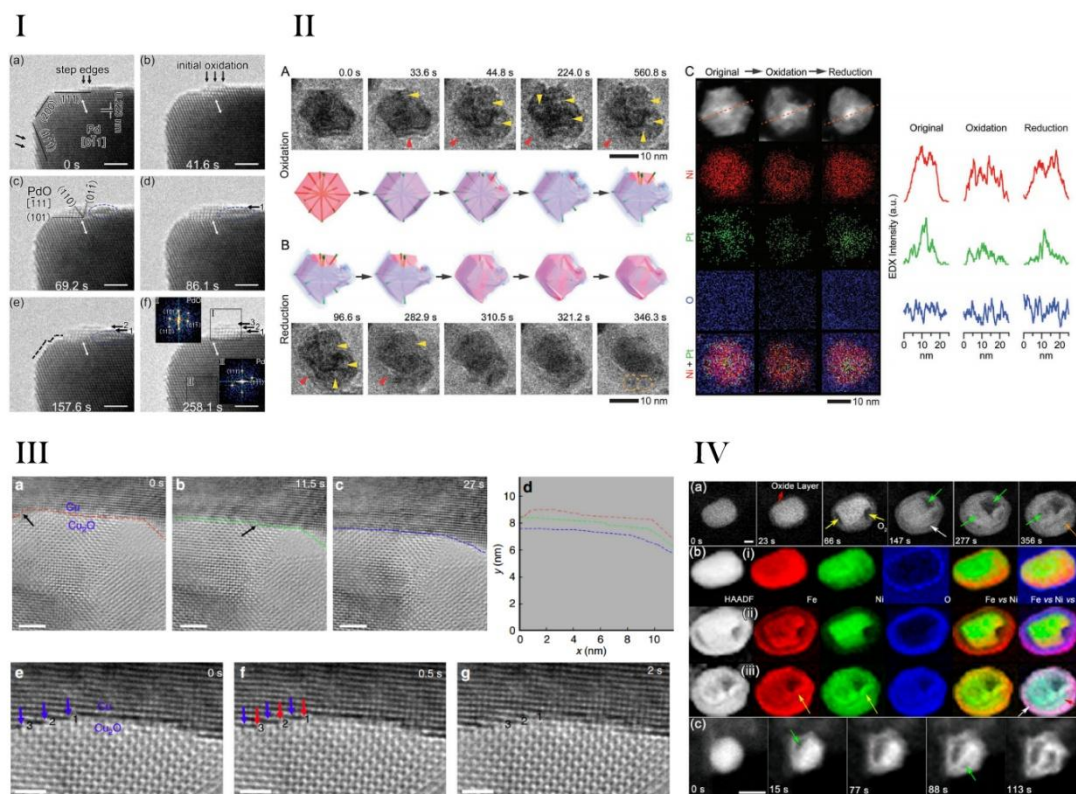
Figure 1-6. (I) *In situ* HRETEM image series of Pd NPs oxidized by electron beam irradiation. The scale bars are 2 nm. [51]Published by The Royal Society of Chemistry. **(II)** (a-b) *In situ* TEM images showing the PtNi rhombic dodecahedron NPs structural evolution in oxidizing and reducing environments at 400 °C. (c) EDS mappings and line scans across an PtNi NP before and after oxidation/reduction. [43]© 2019 WILEY−VCH Verlag GmbH & Co. KGaA, Weinheim **(III)** (a-c) HRTEM images showing the transformation from Cu_2O to Cu at 350 °C in H_2. (d) Evolution of the interface location between Cu_2O and Cu. (e-g) Evolution of interface step edges between Cu_2O and Cu.[52] Copyright © 2017, Springer Nature **(IV)** *In situ* observation of morphology and compositional changes during NiFe oxidation. (a) STEM image series showing the oxidation resulted in formation of porous structure. (b) EELS mapping of Fe, Ni, and O during oxidation. (c) Formation of dual-cavity structure in a NiFe NP. Reprinted with

1.5 Electron beam effects during *in situ* TEM

TEM principles utilize electron beam interactions with specimen for imaging and analytical procedures, so it is crucial to understanding the electron beam effects and be aware of the possible influence on the obtained results. This is essentially important for *in situ* TEM experiments that involve electron interactions with liquids or gases, resulting in complex side effects and may alter the observations. Generally, electron beam effects can be sort into three categories: radiolysis, knock-on and heating effects, as shown in Figure 1-7. The first two are disruptive processes such that crystalline materials may develop defects or even transfer from crystals to amorphous structures. These effects will be discussed individually and the influences for *in situ* TEM experiments will be summarized. In general, electron beam effects can depend on the nature of the materials, thickness and/or orientation of the specimens, temperatures, vacuum conditions and imaging parameters including electron beam energy and electron dose.[54]

In addition, special resolution can be affected because of electron beam effects. For a specific specimen, the resolution of lattice d_s is determined by the Rose equation:

$$d_s = \sqrt{d_i^2 + \frac{(\frac{S}{N})^2}{C^2 D}}$$

where d_i is the resolution of instrument, S/N is the signal-to-noise-ratio (SNR), D is the electron dose and C is the image contrast. As such, the special resolution is not only correlated to the theorical resolution of electron microscopes, but also depending on SNR, electron dose and the contrast after considering the

23

electron beam effects.
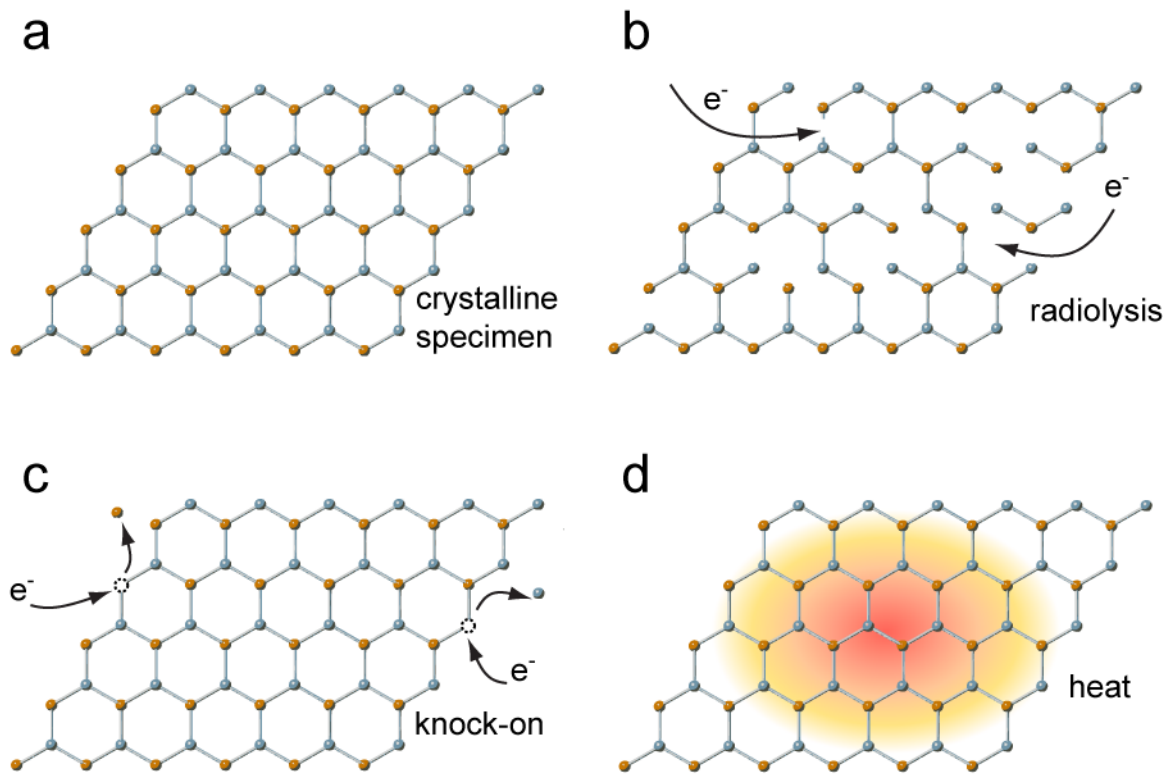
Figure 1-7. Schematic of electron beam effects during TEM experiments. **(a)** Crystalline specimen before electron beam irradiation. **(b)** Radiolysis damage on the specimen introducing the bond breakage. **(c)** Knock-on damage on the specimen introducing the displacement of surface atoms, generating vacancies. **(d)** Electron beam induced heating effect on the specimen resulting in the temperature raise.

1.5.1 Radiolysis or ionization

Radiolysis damage, also called ionization damage, is an electron beam effect when the inelastic scattering damage the chemical bonds of the specimens.[55] The schematic process is shown in Figure 1-7b. This is specially more severe on insulting or semiconductor materials than conducting materials. For conducting

materials, the inelastic scattering happens on conduction bands can be easily refilled by valance band electrons, however in the insulting or semiconducting materials this electron transfer is difficult.[55] Thus, a permanent loss to the conduction band electrons caused by electron beam will result in breaking of chemical bonds in the specimen. It is worth noting that this does not means conducting materials will not suffer from radiolysis damage, but the influence on chemical bond breaking or structural change will be much less significant compared to other electron beam effects such as knock-on effect that will be discussed in the next section. For instance, graphene is a material with very good conductivity, so it is much less suffered from radiolysis damage. However, graphene can be easily damaged by knock-on effect because of the displacement of carbon atoms at the surface. For organic or biological materials, the radiolysis effect is usually the dominate damage mechanism since the chemical bonds are more easily to be break compared to crystalline materials.[55]

1.5.2 Knock-on Damage

Knock-on damage is a displacement effect when electron beam bombarded on materials surfaces.[55] As shown in Figure 1-7c, The atoms close to surface can be displaced from materials surface if the maximum transferred energy E_{trans} caused by electron beam interactions exceeds displacement energy E_{d}, leaving vacancies on the materials surface. The maximum transferred energy is given by the equation as[56]

$$E_{trans} = \frac{E_{beam}(E_{beam} + 2m_e c^2)}{E_{beam} + \frac{1}{2}Mc^2\left(1 + \frac{m_e}{M}\right)^2}$$

where E_{beam} is the incident electron beam energy based on the TEM or STEM instruments; m_e is the

electron rest mass, M is the corresponding atomic mass, and c is the light speed. For each specimen or compound, the threshold displacement energy E_d for a specific element is depend on the physical and chemical properties such as bonding, atomic number, and crystal structures that can be determined by experiments, however, this threshold energy can vary in different compounds for the same element. Oppose to the radiolysis damage, the knock-on damage increases with increasing incident electron beam energy because the maximum transferred energy is proportional to the electron beam energy.[54] In order to reduce the knock-on effect, one can consider lowering the electron beam energy, for example decreasing from 200 keV to 80 keV, such that the maximum energy transferred to the materials can be lower than the threshold energy. The alternative way to minimum knock-on damage is to decrease the electron dose rate during image acquisition. Figure 1-8 shows the relationship between incident electron beam energy and maximum transferred energy for Mo and S in MoS_2 and pristine gold based on equation (1). The dashed horizontal line indicates the corresponding threshold displacement energy for each element. It can be seen that under 200 keV electron beam energy condition Mo and Au are free of knock-on damage, while S in MoS_2 will has knock-on effect because the maximum transferred energy to S atoms can be ~16 eV which is far above the threshold displacement energy (7 eV). Therefore, one can expect the formation of S vacancies on MoS_2 surface due to knock-on damage. To avoid this, a good practice is lower the electron beam energy to less than 90 keV, or using a lower dose rate during the image acquisition.

26
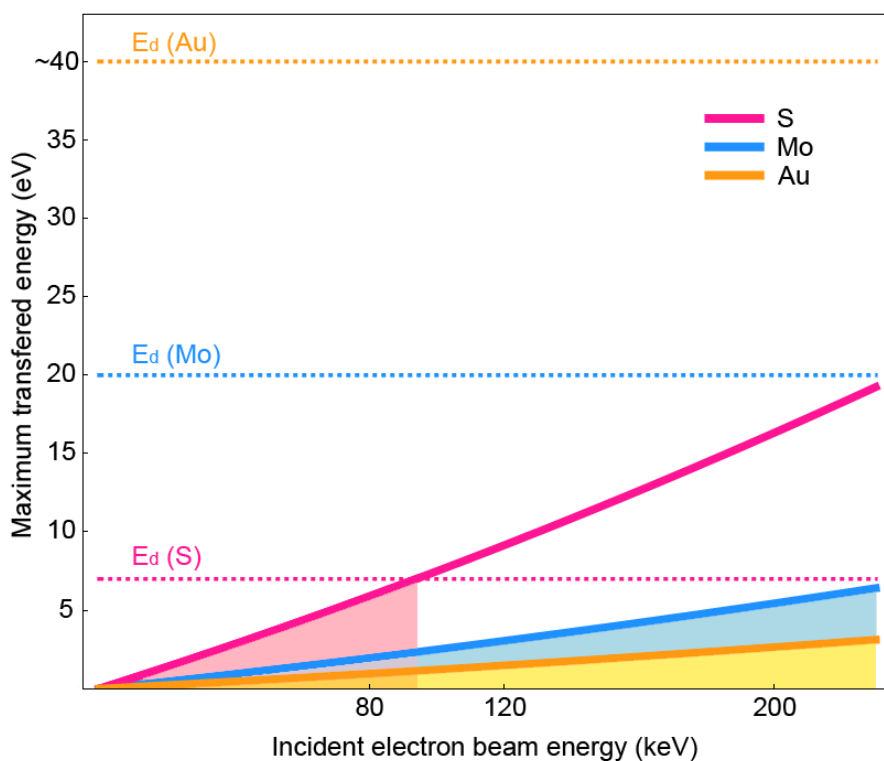
Figure 1-8. Relationship between incident electron beam energy (keV) and maximum transferred energy (eV) for sulfur (pink), molybdenum (blue) from MoS_2 and pristine gold (yellow). Dashed lines show the threshold displacement energy (E_d) for corresponding elements. Shadow areas show the range of incident electron beam energy that will keep the corresponding elements free of displacement. Reproduced from [1] with permission from The Royal Society of Chemistry.

1.5.3 Heating effect

Due to the high energy of incident electron beam, heat may generate during the interactions with specimen. This effect is illustrated in Figure 1-7d. In TEM, the temperature rise due to electron beam can be calculated by:[55]

$$\Delta T \approx \frac{<E> \left(\frac{2R_0}{d}\right)}{4\pi k \lambda_i}$$

where $<E>$ is the mean energy loss due to inelastic scattering, k is the thermal conductivity, λ_i is the inelastic mean free path of transmitted electrons, d is the diameter of electron probe, R_0 is the radial distance that heat is conducted on. Based on this equation, a small electron probe condition will generate only tiny temperature change on the specimen. For example, the temperature rise changes from 0.05 K to 0.15 K when the electron probe diameter change from 1 μm to 1 nm for carbon on TEM grid under 200 keV condition.[55] If the beam current becomes larger, the heating effect can be more notable especially for polymers and organic materials.

1.5.4 Electron beam effects in liquid-phase TEM

Radiolysis in liquid

The electron beam influences on liquid-phase TEM is essential because beside the above discussed effects, there are additional factors that can introduce extra phenomena. One of the key process is the electron beam interaction with the liquid layer surround the specimen. It is known that electron beam irradiation generates radiolysis on most of the liquids, even water, by forming plenty of active radicals. Water molecules can be decomposed into solvated electrons e_{aq}^-, hydrogen radical $H^\bullet$, hydroxyl radical $OH^\bullet$, hydrogen H_2 and oxygen O_2 gases, hydrogen peroxide H_2O_2, hydroxide OH^-, and H_3O^+. Among them, e_{aq}^- and $H^\bullet$ are strong reducing agents while $OH^\bullet$, H_2O_2 are strong oxidizing species. Therefore, the competition between generation of oxidizing and reducing species in aqueous solution will lead to

28

variation of behaviors of specimen including nucleation and growth, dissolution and etching. Although

several parameters can influence the concentration of each species in the solution (liquid thickness, dose

rate, irradiation area), the dose rate is determined to be the key factor that control the concentration. Figure

1-9a shows that increase of electron beam dose rate results in a change of ratio between solvated electrons

and hydroxyl radicals, and thus can alter the crystal etching and growth processes. A stable state can be

achieved by controlling the dose rate to a certain value such that oxidizing and reducing environments are

balanced to maintain a neutral state. In addition, the generation of different species various in speed within

a constant dose rate until they reach equilibrium in the solution. Figure 1-9b shows the concentration of

radiation species as a function of time in water, and it can be concluded that most of the species

increase/decrease in concentration gradually until the equilibrium is reached. Further, increasing or

decreasing the electron beam dose rate, as shown in Figure 1-9c, can alter the steady-state concentration

of radiation species. A general trend can be obtained that almost all species generated from electron beam

irradiation display an increasing in concentration at higher dose rates. Since the variation between

oxidizing and reducing environment can be tuned by controlling the electron beam dose rate, the *in situ*

liquid-phase TEM can act as a reactor to create, write, and even erase nanostructures.[57, 58] Finally,

since ionic species such as H_3O^+ can be generated in the aqueous solution, the pH value will be influenced

as a function of dose rate. This trend is illustrated in Figure 1-9d for water with initial pH as neutral. It can

be seen that a lower dose rate yield less change in the pH value, however as the dose rate increases the pH

can shift to lower value as small as close to 3, creating a significant acid environment. This change can

alter the reaction processes including nucleation, growth, dissolution and etching as well as induce extra
29

impact on the materials morphology. Therefore, careful considerations on the electron beam radiation effects on liquids and control experiments are necessary.
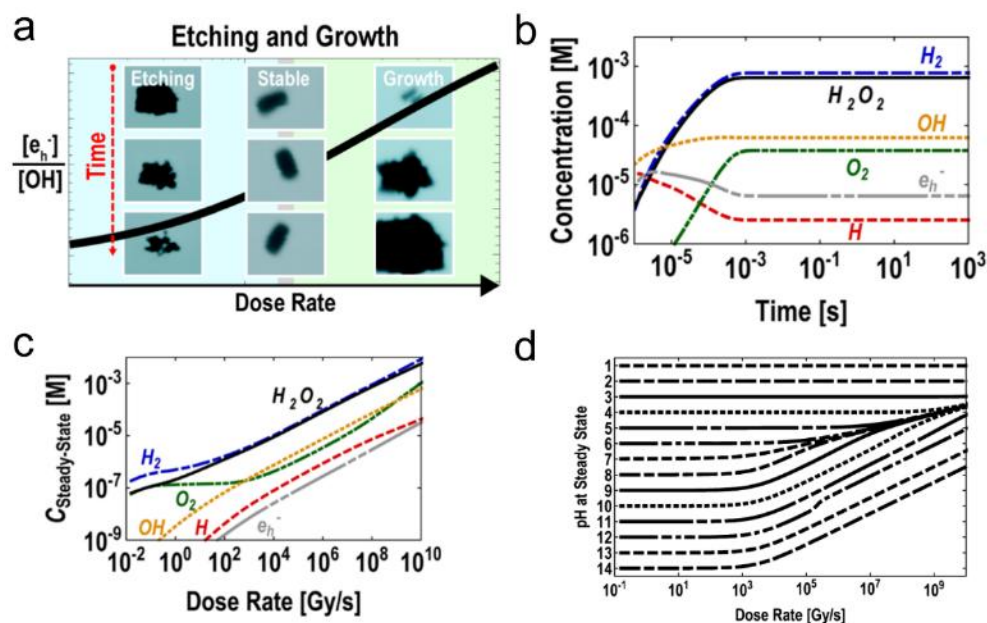
Figure 1-9. (a) Influence of electron beam dose rate on crystal etching and growth in aqueous solution. **(b)** Concentration of radiation species in water as a function of time. **(c)** Steady-state concentration of radiation species in water as a function of dose rate. **(d)** Steady-state pH values in water as a function of dose rate. Reprinted with permission from [59]. Copyright (2014) American Chemical Society.

Effect of Liquid Thickness

The liquid thickness inside the SiN window or graphene layer can significantly affect the imaging spatial resolution. This is due to the multiple scattering of incident electron beam with the liquid layer that produces background in the formed images.[21] Figure 1-10 a and b shows the spatial resolution in STEM

30

and TEM as a function of liquid layer thickness for imaging of Au and carbon, respectively.[60] It can be

seen that for liquid thickness less than 100 nm, STEM can provide better spatial resolution (less than 1

nm) compared to TEM imaging technique. However, as liquid becomes thicker the resolution degradation

gets severe with more than 5 nm for 1 μm thick liquid in STEM mode. In addition, nature of specimen

can affect the spatial resolution such as carbon shown in panel b that the value cannot achieve below 1 nm

for both TEM and STEM mode in the thinnest liquid layer range (10 nm). Panel c and d show the spatial

resolution degradation as a function of liquid thickness when considering the effect of SiN membrane in

dark field and bright field imaging conditions. It can be seen that SiN membrane induce more resolution

degradation especially for dark field STEM imaging, resulting a 0.5 nm decrease for Au and 5 nm decrease

for carbon in a 10 nm thick liquid layer. This effect is less for bright field STEM with degradation of 0.1

nm for Au and 3 nm for carbon. Therefore, thinner liquid thickness is desirable if the imaging resolution

is an essential factor for *in situ* liquid-phase experiments both in TEM and STEM mode, however the

liquid layer cannot be thinner than the thickness of specimen that sandwiched between SiN windows or

graphene layers. It may also necessary to consider the effects of very thin liquid layer, for example the

confined space effect that the reaction pathways are anisotropic compare to thicker liquid layer, therefore

the kinetics of observed phenomena may not reflect the actual application conditions.
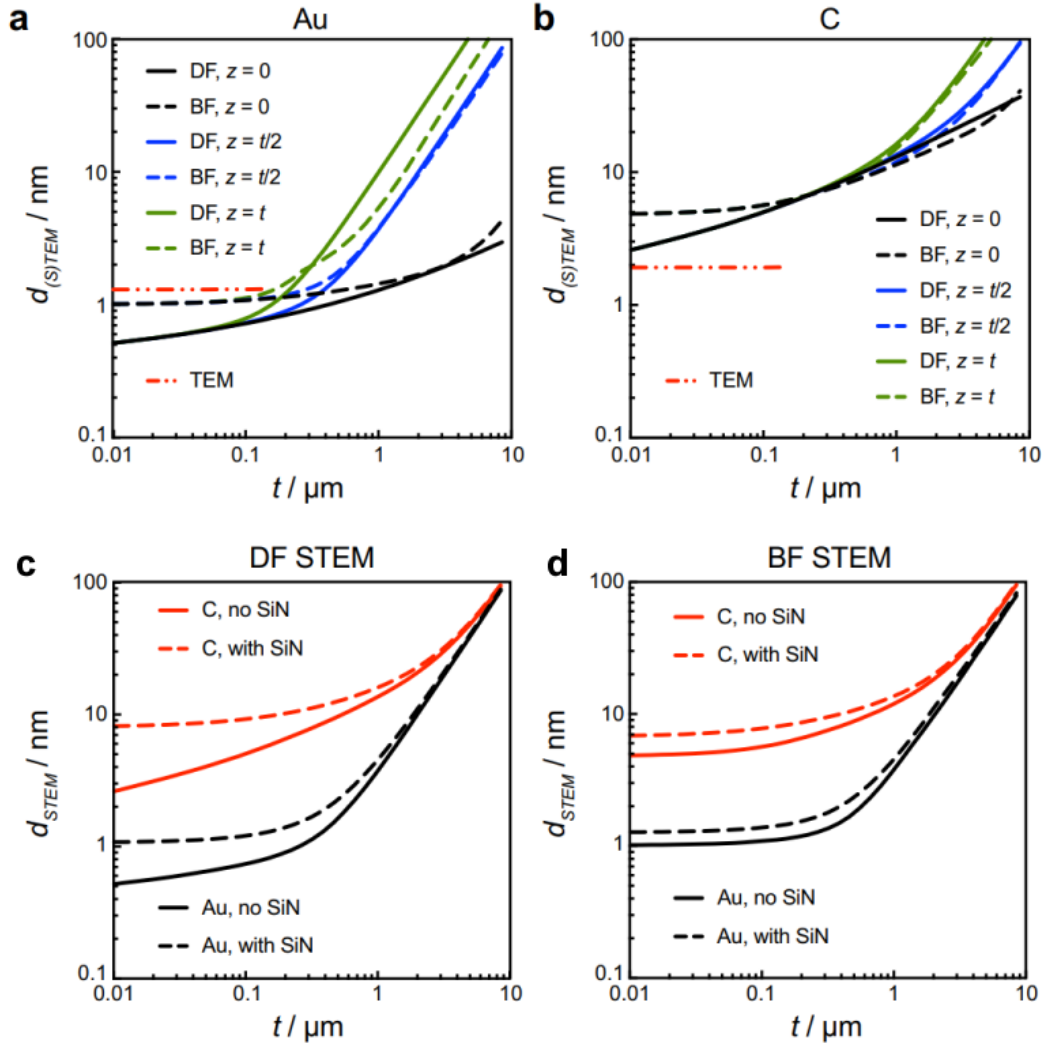
Figure 1-10. (a-b) Spatial resolution as a function of liquid thickness for Au and C. **(c-d)** Spatial resolution as a function of liquid thickness considering the effect of SiN membrane. [60]© 2018 Elsevier B.V. All rights reserved.

In another aspect, the SiN window bulging effects can be a factor that indirectly influence the imaging. This is because of the huge pressure different between the liquid cell and outer vacuum chamber. Bulging increase the liquid layer thickness and therefore can influence the concentration of radiation species in

solution and image resolution. To quantitively characterize the window bulging effect, low-loss EELS were utilized to calculate the liquid layer thickness as a function of distance to the SiN window edge. To do so, inelastic mean free path was determined from the low-loss EELS results based on the equation:[61]

$$\frac{t}{\lambda} = ln\left(\frac{I_{tot}}{I_o}\right)$$

where t is the sample thickness, λ is the inelastic mean free path, I_{tot} and I_o are total spectrum and zero-loss peak integral. This value can be easily determined from the Digital Micrograph software. Then, the λ is approximated by the equation:[61]

$$\lambda = \frac{106FE_0}{E_M \ln\left(\frac{2\beta E_0}{E_M}\right)}$$

where E_0 is acceleration voltage, F is the relativistic factor at a certain electron beam energy, β is the EELS collection semi-angle, and E_M is the factor related to effective atomic number (Z_{eff}) given by:

$$E_M = 7.6Z_{eff}^{0.36}$$

$$Z_{eff} = \frac{\sum f_n Z_n^{1.3}}{\sum f_n Z_n^{0.3}}$$

where f_n is atomic fraction of element and Z_n is atomic number of the element. Figure 1-11a shows the low-loss EELS obtained from different distances related to SiN window edge, and panel b shows the correlated liquid layer thickness. It can be seen that the window bulging effect lead to the increase of liquid thickness from 500 nm at the window edge to close to 1 μm at a distance of 4 μm from window edge.
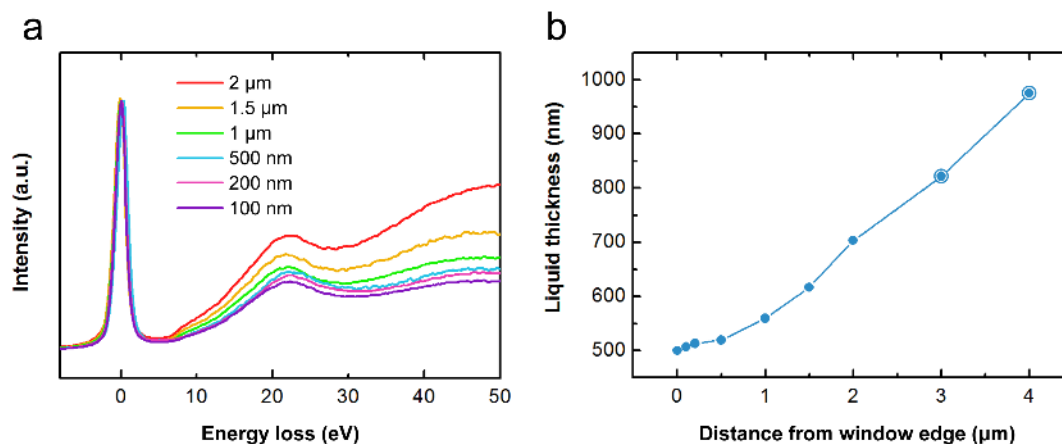
Figure 1-11. (a) EELS collected at different distances from SiN window edge. **(b)** Liquid layer thickness variation calculated from the low-loss EELS in a. Reproduced from [1] with permission from The Royal Society of Chemistry.

In addition, the spatial resolution in liquid-phase TEM can degrade to a great extend especially for MEMS-based liquid cell experiments, and at regions with thicker liquid layer due to the electron scattering in the liquid. As such, imaging is practically being performed at regions closer to the window edge where window bulging effect is less significant.

1.5.5 Electron beam effects in gas cell TEM

Besides the above discussed electron beam effects, special attentions should be paid to the *in situ* gas cell TEM experiments. This is because the electron beam can not only interact with specimen but also with the surrounding gas molecules, introducing the ionization of gases, in some cases can be highly reactive. The reactions of ionized gas molecules with specimen can induce series of phenomena that are difficult to

34

interpret without careful control experiments. For instance, it was found the carbon nanotube can be easily damaged from ionized O_2 gas by attacking the tip regions, as shown in Figure 1-12a to f.[62] The calculated cumulative electron dose for electron beam damage in vacuum and in higher pressure O_2 gas is shown in panel g. The cumulative dose threshold decreases from 1.2×10^6 e^-/A^2 to 1.3×10^4 e^-/A^2 from vacuum to 1 mbar pressure O_2. Therefore, the carbon nanotube can be more prone to be damaged in O_2 gas environment under electron beam irradiation, such that the structural change of the sample has to be carefully evaluated to excludes the electron beam induced effects.
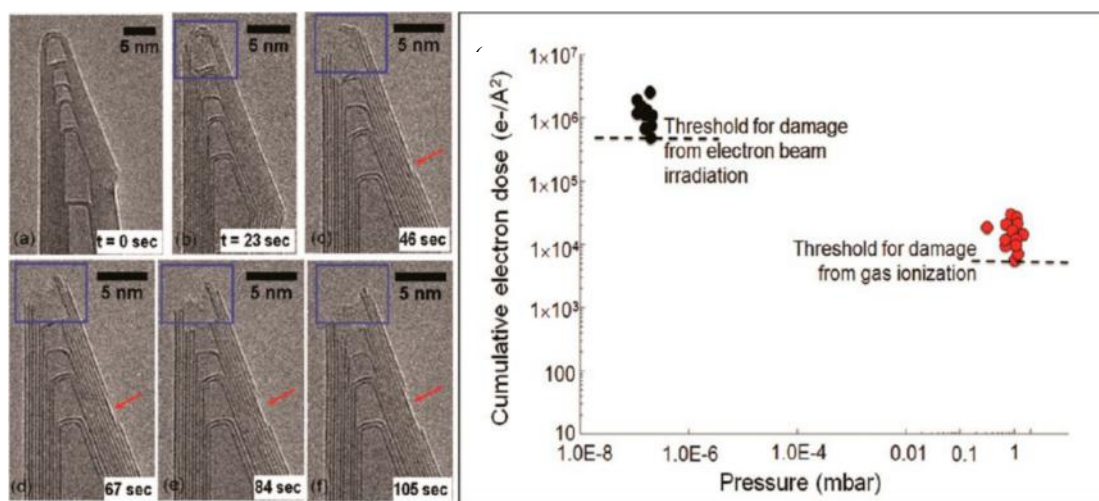
Figure 1-12. (a-f) TEM images of carbon nanotube in 0.7 mbar O_2. Boxed regions highlight the gradually opened nanotube tip. **(g)** Threshold cumulative electron dose for damage of carbon nanotube from electron beam and from gas ionization. Reprinted with permission from [62]. Copyright (2016) American Chemical Society.

As the additional example, Figure 1-13 shows the TEM images and SAED patterns of Au@Pt NPs

35

supported by MoS$_2$ before and after annealing in air at 400 °C.[2] It can be seen that voids formed on MoS$_2$ support and its diffraction spots disappeared, suggesting the MoS$_2$ underwent structural damage with loss of crystallinity. However, this phenomenon is not observed on annealing experiments in vacuum environment and *ex situ* conditions. It is expected that the reaction between ionized O$_2$ and MoS$_2$ caused the structural degradation, which is clearly an electron beam induced effect.
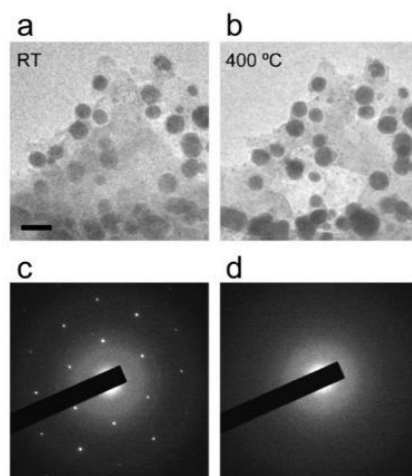
Figure 1-13. Au@Pt NPs annealing in air flow containing 21 vol. % O$_2$. (**a, c**) Transmission electron microscopy (TEM) image and SAED at RT; (**b, d**) TEM and SAED at 400 °C. The scale bar is 10 nm. Reprinted with permission from [2]. Copyright (2020) American Chemical Society.

In addition, spatial resolution decrease due to the contribution of SiN window thickness and gas layer thickness, although not as significant as liquid-phase TEM, is another factor to consider for *in situ* gas TEM experiments. Quantitively, a study analyzed the gas layer influence on the resolution degradation in ETEM.[63] As shown in Figure 1-14a-d of STEM images of amorphous carbon in different gases, the blurring effect becomes obvious once the pressure increases from vacuum (10^{-7} mbar) to 10 mbar. The

36

background changes from darkest to an increase of brightness while the carbon has a decreased brightness. Looking at the intensity and normalized intensity profile in panel e and f in N_2 gas, it is clear that the background intensity has increased from vacuum to high pressure. Panel g and h shows the normalized intensity and signal-to-noise ratio (SNR) of carbon in different gases pressures, and these results show that all gases will induce SNR degradation that negatively impact the image quality when the pressure is high, and Ar shows a stronger effect among the other gases, followed by N_2. Panel i gives the estimation of STEM resolution degradation on a M1 crystal in He and N_2 gas at different pressure. It can be seen that He gas almost have no effect on the resolution degradation even at the highest pressure of 10 mbar, however the N_2 gas can significantly decrease the resolution to more than 0.4 Å at 10 mbar. This is believed to be a reason of gas induced change of probe diameter. The electron beam interaction with the gas layer in the gas cell TEM will cause the broadening of converged beam similar like the interaction with a relatively thick sample. To estimate the probe broadening b, multiple-scattering theory developed by Bothe[64] can be used:

$$b = 1.05 \times 10^3 (\frac{\rho}{W})^{1/2} \frac{Z}{E} (\frac{1+E}{1+E/2}) L^{3/2}$$

where ρ is the mass density, W is the mean molar mass, Z is the mean atomic number of the solid, and E is the accelerating voltage of the microscope being used. The theoretical resolution degradation in panel i is a reason of probe broadening as illustrated in panel j, where N_2 gas induce more broadening compare to He gas at the same pressure.
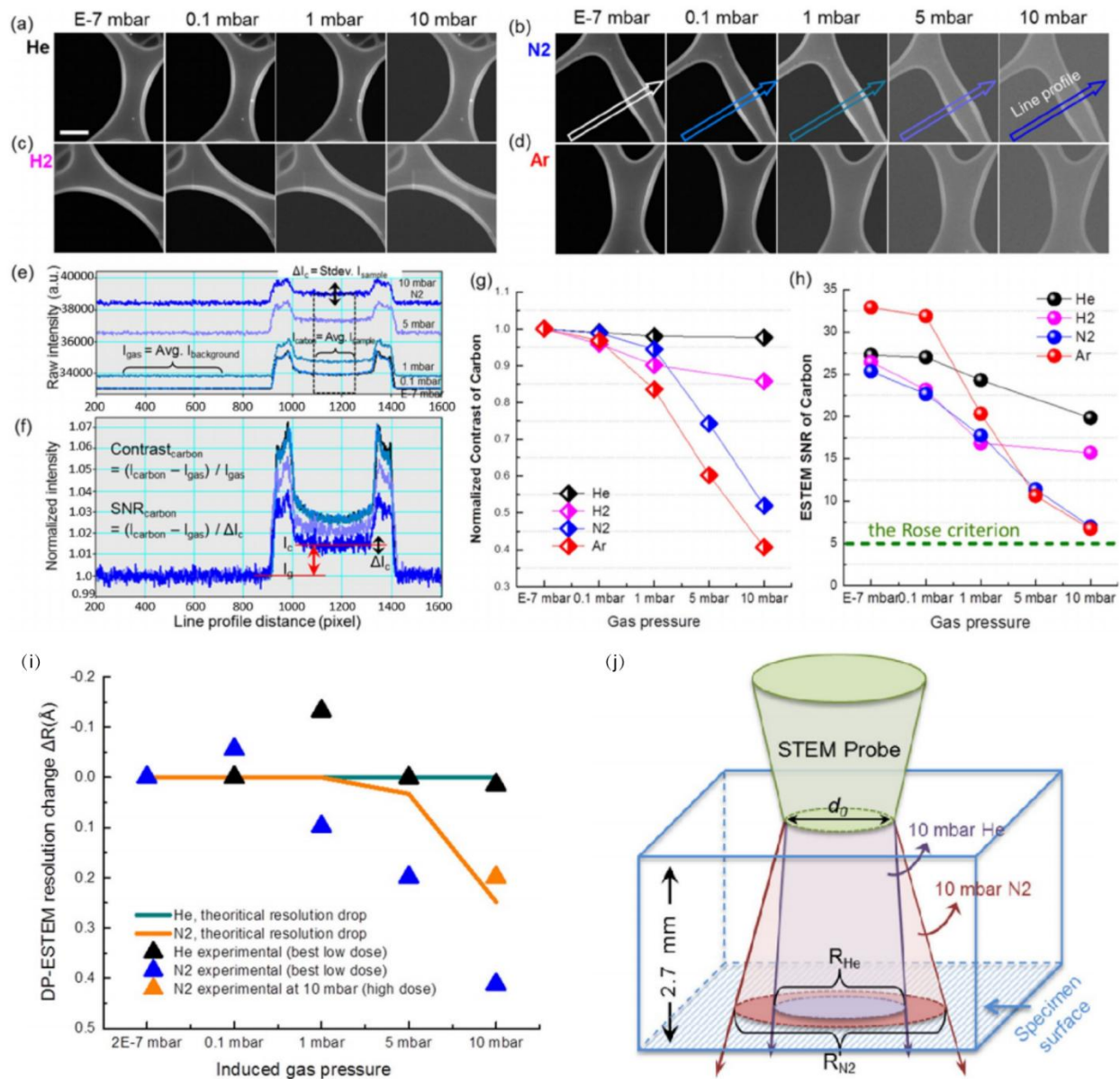
Figure 1-14. (a-d) Environmental STEM images of lacey carbon observed in different pressure of gases. Scale bar is 200 nm. **(e-f)** Intensity and normalized intensity profile of carbon contrast against the background in N_2. **(g-h)** Normalized carbon contrast and SNR in different gases and pressures. All images are reproduced with permission. **(i)** STEM resolution in He and N_2 from calculation and experiments. **(j)** Schematic showing the probe broadening effect due to the gas interaction. [63]© 2017 Wiley−VCH Verlag GmbH & Co. KGaA, Weinheim

Chapter 2 Theories in solid-liquid and solid-gas reactions

2.1 Mechanisms of nucleation and growth in liquid

Nucleation is the process of crystallization of seed nuclei from solution. Nucleation are involved in many chemical synthesis processes, especially for catalysts fabrication. In classical nucleation theory, the crystal is expected to form after the ions in solution overcome the energy barrier such that nuclei being stabilized above a critical radius in the solution. The description of spherical particle nucleation from liquid can be described using the total free energy given by:

$$\Delta G = 4\pi r^2 \gamma + \frac{4}{3}\pi r^3 \Delta G_v$$

where r is the radius of the particle, γ is the surface energy and ΔG_v is the bulk free energy. As the nuclei radius become larger, the surface energy for a specific system is always positive, while bulk free energy is always negative, leading to a maximum free energy for a nucleus at certain radius, as shown in Figure 2-1.[65] This radius, indicated as r_c, is the critical radius above which the nucleus will continue growing without the possibility to be dissolved again into the solution. For nuclei smaller than r_c, they are prone to be dissolved because of the total energy can be lower for smaller size. Thus, for homogeneous nucleation where nuclei form uniformly in the parent phase, in order to form stable particles nucleated from solution, the nuclei need to overcome the energy barrier and reach the critical radius. This is also true for heterogeneous nucleation where nucleation happens at inhomogeneities such as surfaces, but the nucleation barrier can be much lower, making the process easier to happen than homogeneous nucleation.[65]

39
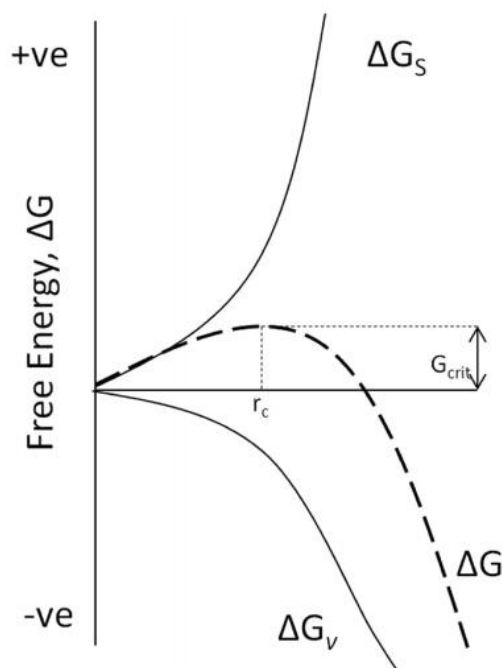
Figure 2-1. Total free energy for a nucleus with different radius in the solution. Image reproduced with permission. Reprinted with permission from [65]. Copyright (2014) American Chemical Society.

The nucleation rate depends on several factors including free energy barrier, supersaturation, and temperatures. In classical nucleation theory, the nucleation rate is described as:[66]

$$J_n = A \exp\left(-\frac{\Delta G}{kT}\right) = A \exp(\frac{-8\pi\omega^2 a^3}{3(kT\sigma)^2})$$

Where A is kinetic constant determined by kinetic barriers including diffusion and steric, ΔG is nucleation free energy barrier, α is the interfacial energy, σ is the supersaturation, ω is the molecular volume, and T is the temperature. Figure 2-2 shows the nucleation rate J_n at different level of supersaturation for calcium phosphate nuclei.[66] The supersaturation from level 1 to 6 increases and thus lead to an increase of the nucleation rate.
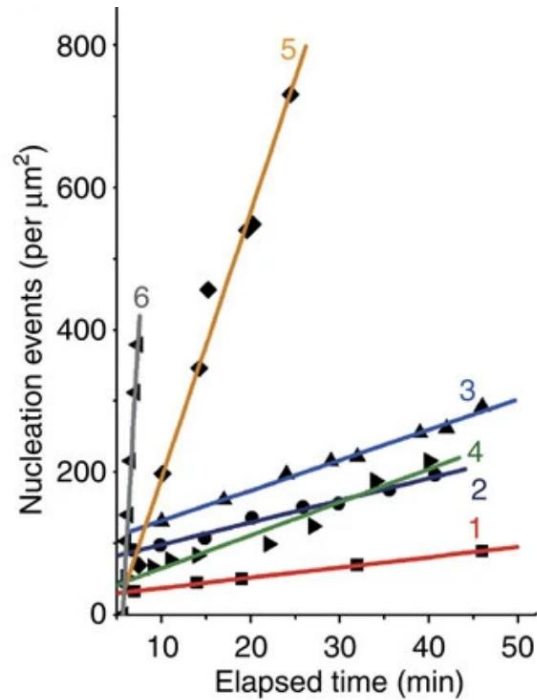
Figure 2-2. Nucleation behavior on the effect of different supersaturations. The nucleation rates are dependent of time. Copyright © 2013, Nature Publishing Group.[66]

The growth of particle in solution are influenced by two factors: the reaction at surface and diffusion of reactant to the surface.[65] As illustrated in schematics of Figure 2-3, the reaction limited growth resulted from the reaction kinetics at growth surface that control the process, while diffusion limited growth is a result of diffusion of monomer toward the surface being the rate controlling factor.
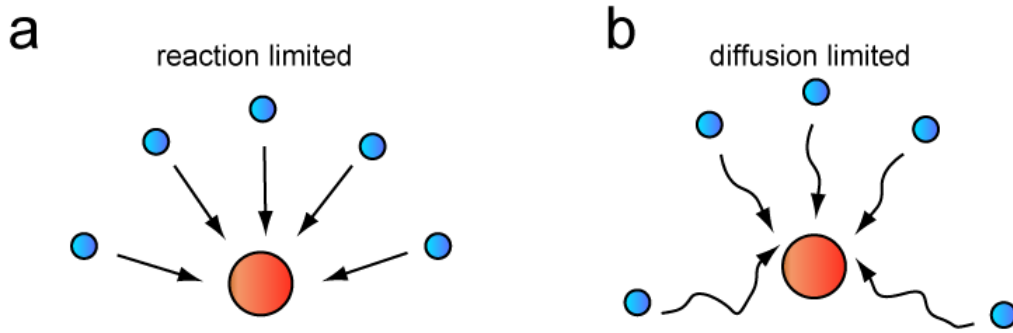
Figure 2-3. Schematic of (a) reaction limited and (b) diffusion limited growth.

To describe the growth phenomena, Fick's law is used for the diffusion process in the form of

$$J = 4\pi x^2 D \frac{dC}{dx}$$

where r is the particle radius, J is the monomers through spherical plane with radius of x, D is the diffusion coefficient, and C is the concentration at distance of x. For the reaction rate at the surface, the process is described by the following equation:

$$J = 4\pi r^2 k(C_i - C_r)$$

where k is the rate of surface reaction, C_i is the concentration of monomers at solid and liquid interface, C_r is the particle solubility. As such, the competition between reaction and diffusion will lead to one of the mechanism being the rate-limiting factor for the growth of particle, or being in between of the two because of other rate-changing parameters such as inhomogeneities, defects, grain boundaries, and so forth.

Models that describe the nucleation and growth processes including the LaMer mechanism, Ostwald ripening, Finke-Watzky mechanism, particle migration and coalescence, oriented attachment, and

intraparticle growth. The LaMer mechanism[67] is known as the first description that distinguish the nucleation and growth process separately. As shown in Figure 2-4, the nucleation and growth process are separated into three stages: the first stage involves increase of concentration of free monomers; the second stage involves rapid nucleation process such that the free monomer concentration begin to decrease; the last stage involves the growth process that the nuclei becomes larger in size. However, there are other models that describe the nucleation and growth process happen simultaneously. One example is Finke-Watzky two step mechanism, where the first step involves slow nucleation and second step involves surface growth.
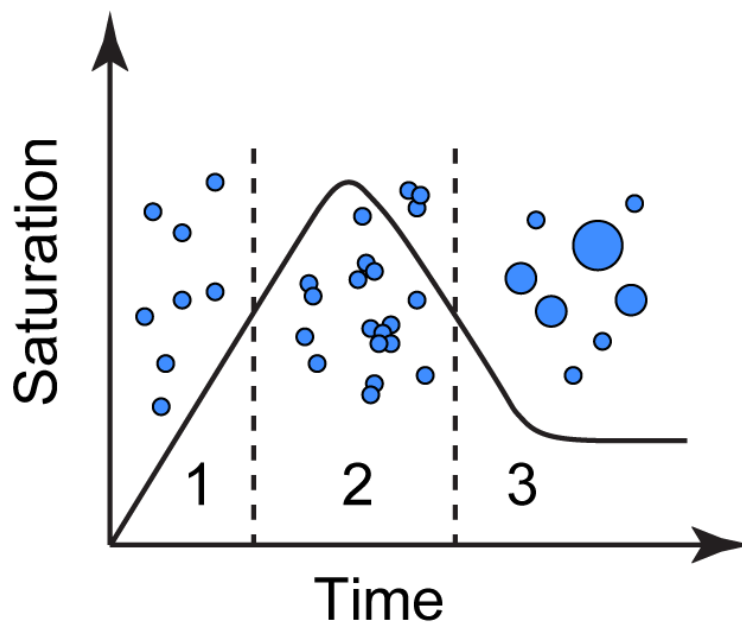
Figure 2-4. LaMer mechanism showing the three stages in nucleation and growth process.

Figure 2-5 shows the schematic of oriented attachment as a model describe the growth process. It involves

coalescence where several nuclei attached together, and rotation of nuclei to align certain crystal facets with each other. This is usually due to the system reducing surface energy to become thermodynamically stable in the solution. Other similar process is the intraparticle growth mechanism, where monomers diffuse along the crystal facets and resulted in surface reconstruction. Because different facets can have different surface energy, the surface reconstruction can lead to preferential growth of lower energy crystal facets while dissolve of higher energy facets.
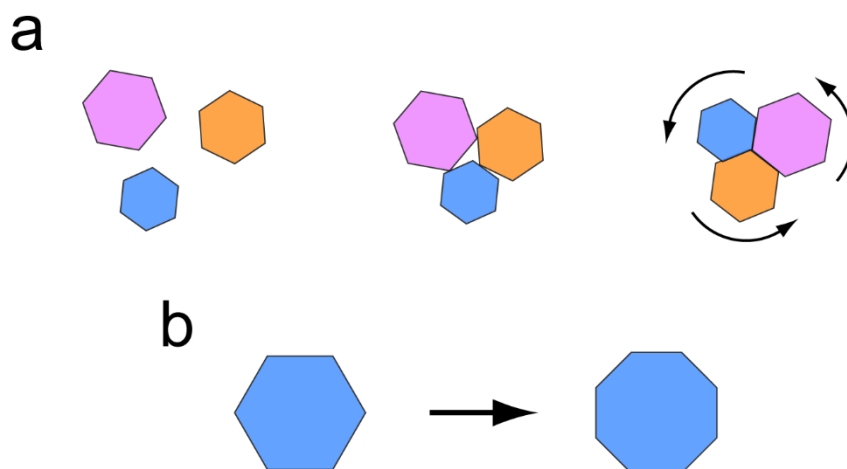
Figure 2-5. Schematic showing the (a) oriented attachment and (b) intraparticle growth.

In addition, mechanisms that guide the growth process including particle migration and coalescence, and Ostwald ripening are well studies. Illustrated in Figure 2-6, particle migration and coalescence means the growth of particle are due to the Brownian motion of free standing particles that leads to the attachment of each other, while Ostwald ripening is a process that adatoms move from smaller particles to larger particles and results in dissolving of smaller ones and growth of larger ones. The Ostwald ripening

44

mechanism is usually due to the increased solubility and surface energy of smaller particles where

detachment of monomer from the surface is easier than for the larger particles.[65]
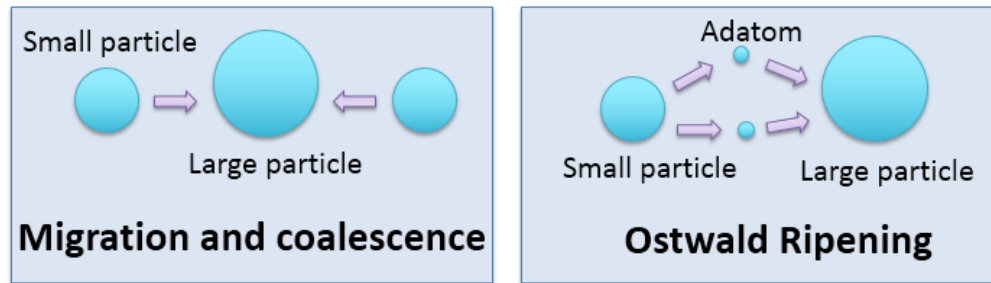
Figure 2-6. Two main mechanisms of growth in solution: particle migration and coalescence, and Ostwald

ripening.

The Ostwald ripening mechanism can be described by Lifshitz-Slyozov-Wagner (LSW) theory,[68]

where the average radius of particles during a diffusion and reaction controlled growth process is

described as:

$$<R>^3 - <R>_0^3 = \frac{8\gamma C_r v^2 D}{9RT} t,$$

and

$$<R>^2 = \frac{64\gamma C_r v^2 k}{81RT} t,$$

suggesting that the average particle radius is correlated to the exponential factor of time (t) with

relationship of $R \sim t^\beta$, where β equals to 1/3 for diffusion limited and 1/2 for reaction limited growth.

If growth process involves both migration and coalescence and Ostwald ripening, the LSW theory are

45

modified by Lifshitz-Slyozov encounter modified (LSEM) theory[69, 70] to enable the accurate description of the process. Compare to LSW theory, the LSEM takes into consideration the particle coalescence during nucleation and growth processes. Based on Gibbs-Thomson relation,

$$C_r = C_e exp\left[\frac{2\gamma\Omega}{R_BT} \cdot \frac{1}{r}\right] \approx C_e\left[1 + \frac{2\gamma\Omega}{R_BT} \cdot \frac{1}{r}\right],$$

where C_e is the solute concentration, C_r is the solubility at surface of a particle with radius r, γ is the specific interfacial energy of matrix-precipitate particle boundary, Ω is the mean atomic volume of particle, R_B is the universal gas constant, T is the absolute temperature. In LSEM model the kinetic equations for average particle radius is as follows,[71]

$$\bar{R}^3(t) - \bar{R}^3(0) = K(Q)t$$

where

$$K = \frac{6\gamma\Omega C_e D\bar{r}'^3}{R_BTY},$$

C_e is the average mole fraction of solute in the matrix, D is the diffusion coefficient, and $\bar{r}'^3$ and Y are parameters that depend on volume fraction of precipitate. In LSW theory $\bar{r}'^3$ and Y are constants with values of 1 and 6.75, while LSEM predicts $\bar{r}'^3$ and Y will change as a function of volume fraction if particle coalescence occurs.[71] This indicates that the combination of particle migration and coalescence and Ostwald ripening in the growth process can lead to the deviation of classical LSW theory.

Besides classical nucleation theory, there are non-classical nucleation pathways being discovered and proposed. Different than the classical theory, non-classical nucleation involves crystallization through metastable or intermediate states before the final stable phase. This means the non-classical nucleation

usually include more than one steps where the system transfer from unstable to stable phase with several intermediate stages instead of directly to the most stable phase. The phase that separated from the solution is usually the one displays lowest free energy barrier.[72] For example, the nucleation process in colloidal systems shows the formation of dense liquid precursor phase before reaching a stable crystal structure.[73] Similar two stage nucleation have been reported in studies of biomineralizations, such as nucleation of calcium carbonate where amorphous calcium carbonate was identified before the crystal mineralization.[74, 75]

2.2 Mechanisms of catalyst behavior and degradation under gas environments

2.2.1 Catalyst degradation

During service, catalysts display dynamic behaviors induced by solid-gas reactions. Among them, catalysts degradation is crucial factor that limit the lifecycle, as illustrated in Figure 2-7[76] for Pt catalyst supported by carbon. During the sintering process where catalytic nanoparticles agglomerate, two mechanisms can be involved as Ostwald ripening and particle migration and coalescence. Both mechanism lead to a growth of particle size and reduce of surface area, leading to a decrease of active catalytic sites.[50]
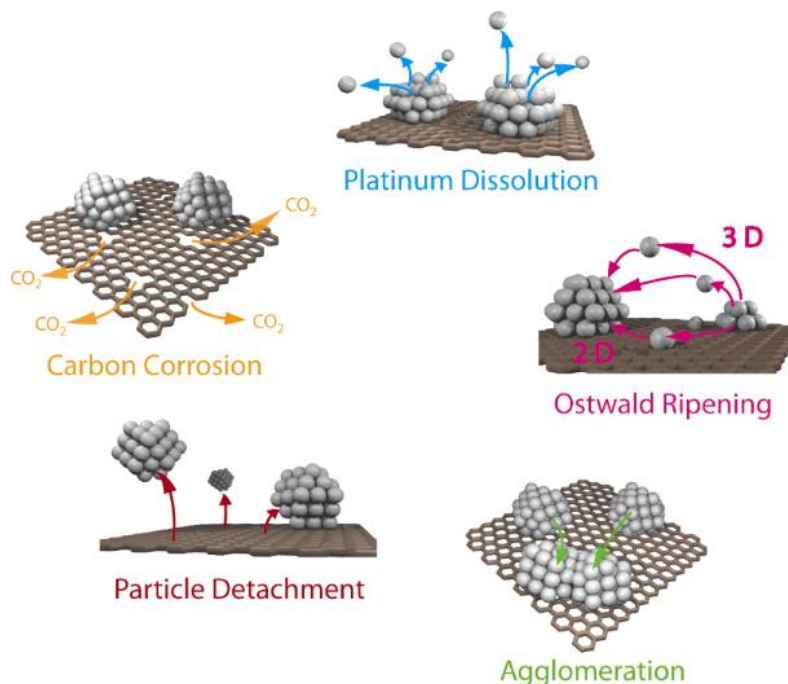
Figure 2-7. Degradation mechanisms of Pt catalyst on carbon support.[76] © 2014 Meier et al; licensee Beilstein-Institut.

Since most of the catalysts are supported, particle migration and coalescence will include the Brownian motion of the NPs on the surface of support. The diffusion of NP is correlated to the Fick's diffusion theory and is usually the reason for the change of particles' center of mass.[50] Smaller particles (diameter less than ~3 nm) are easier to diffuse on the support because of the high mobility of adatoms, while larger particles display decreased mobility during long-term operations. Therefore, for the case of a catalyst system with average large particle size, the particle migration and coalescence mechanism become less possible and Ostwald ripening can be the main mechanism for further sintering.

Similar to particle migration and coalescence, Ostwald ripening also involves the diffusion theory but

48

instead is caused by diffusion of adatoms on the support surface. This is due to the metal-to-metal bonding is less strong than the metal-to-support bonding and thus it is easier for the adatoms to detach from metal NPs surface and diffuse through the environments. Due to the higher surface energy of smaller NPs,[77] adatoms can transfer from surface of smaller NPs towards larger NPs, resulting in the loss of small NPs and growth of large NPs.

The sintering of NPs is qualitatively described by three phases[50]: 1) rapid loss of surface area in early stage caused mainly by Ostwald ripening, resulting in the disappearance of smallest NPs; 2) slowdown of sintering process can be a combination of Ostwald ripening and particle migration and coalescence, resulting in a log-normal like particle size distribution; 3) particles may reach equilibrium dispersion with high stability on the support, depending on the properties of metal, support, temperature, and gas environments.

2.2.2 Oxidation and reduction mechanisms

In catalyst NPs' service conditions, the environments can involve oxidizing and reducing agents such as oxygen (O_2) and hydrogen (H_2). In addition, most catalytic reactions require temperature above room temperature to accelerate the reaction rates. Therefore, understand the high temperature gaseous oxidation and reduction on catalytic NPs are crucial for the development of advanced catalyst. The gaseous oxidation/reduction reactions are also important for applications in gas turbines, power plants, petrochemical and aerospace industries.

49

To determine how easy a specific element is being oxidized, Ellingham diagrams are used where relationships between free energy change and temperature are plotted. As shown in Figure 2-8[78], the free energy change for NiO is negative within the plotted temperature range, suggesting the formation of Ni oxide is spontaneous at the specific temperature. This diagram can be used to compare the stability among different metal oxides, for example, Al_2O_3 shows the most stable oxide while Ag_2O is least stable because the free energy is least compared to other metal oxides.
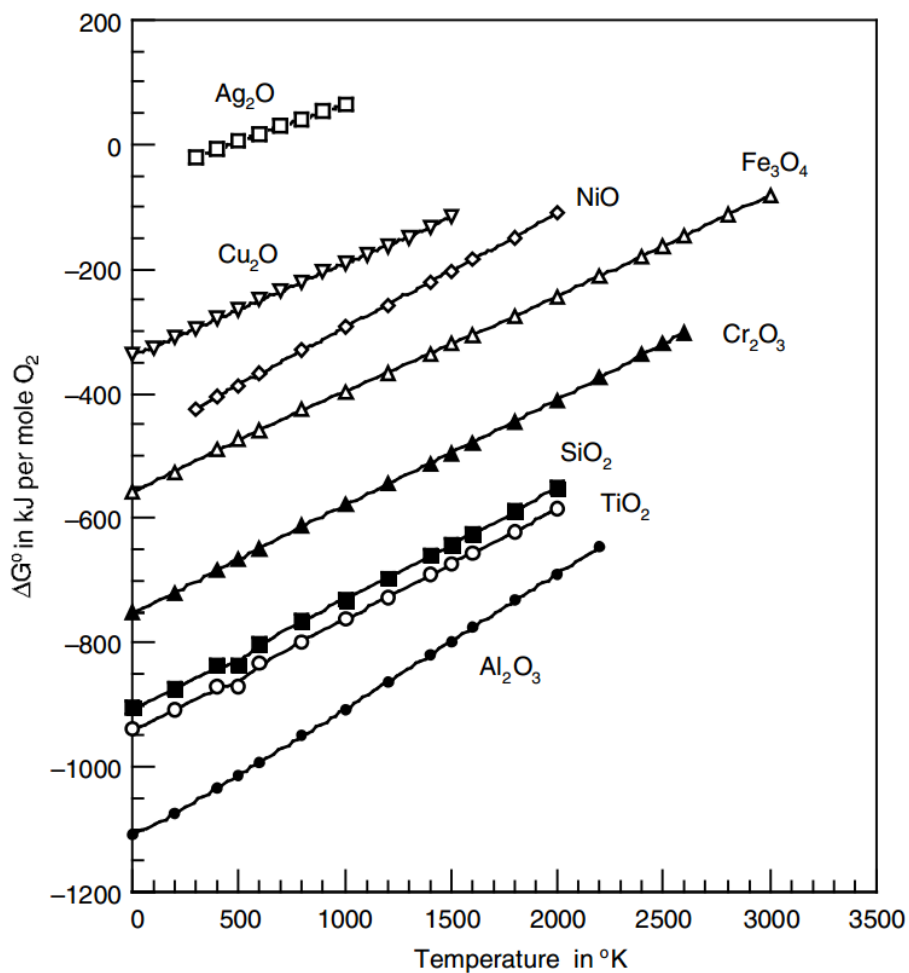
Figure 2-8. Ellingham diagrams showing exemplar elements in oxide form. [78] Copyright Springer-

Verlag New York.

Oxidation theories

For room temperature oxidation, oxidation kinetics are predicted by Cabrera-Mott theory.[79] In this model (Figure 2-9[80]), oxygen dissociation and chemisorption happen on the metal surface, resulting in the formation of a thin oxide layer. Due to the electron tunneling effect, electric field is generated in the oxide layer and thus decrease the activation energy of cation diffusion, providing the driving force for the outward diffusion of metal cations.[79] Since the oxide thickness is inverse to the strength of electric field, the oxidation rate is initially rapid but will decrease dramatically as the oxide layer becomes thicker, and finally reach equilibrium once the electric field are too weak to drive any further cation diffusion. Therefore, the CM model is only valid for thin oxide layers (less than 10 nm) during the initial state of oxidation.[80] In this model, the diffusion of metal ions from metal-oxide interface to the external oxide surface is usually the rate-limiting factor for oxidation kinetics.
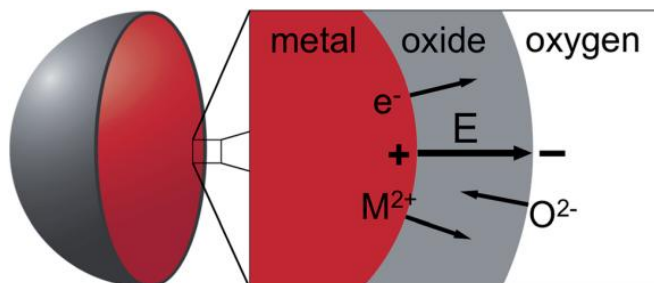
Figure 2-9. Schematic of CM model showing the initial stage of room temperature oxidation of metal NP.

[80] Reproduced by permission of The Royal Society of Chemistry.

In high-temperature oxidation, the CM model is inapplicable since the temperature provides extra effects in activation of diffusion such that the oxide layer can be thicker than the limitation predicted by CM model.[80] Wagner[81] developed the bulk oxidation theory to describe high-temperature oxidation conditions. It assumes a dense and continuous oxide scale and predicts that the diffusion of ions and charges across oxide layer is the rate-limiting factor. Currently, there are several models that modified the Wagner theory to describe the oxidation for spherical NPs instead of planner geometry. For instance, Valensi-Carter's shrinking core model[82] takes the NPs' curvature surface into account and predicts the activation energy of oxidation decrease with decreasing NP size. Another model from Fromhold[83] assuming only surface charge and linear diffusion draws similar conclusion that smaller NPs can be oxidized faster than larger NPs. Therefore, the activation energy for oxidation of smaller size NPs will be less compared to larger size NPs, which has been confirmed by several studies.[84-87]

The oxidation kinetics of metals can be generally described using the electrochemical interpretation (Figure 2-10[78]). The metal surface is the anode, oxide external surface is the cathode, and oxide layer acts as solid electrolyte where both ionic and electronic resistance exist. Metal cations diffuse outward through the oxide layer and oxygen anions can also diffuse inward, following the reactions at metal/oxide interface:

$$M \rightarrow M^{n+} + ne^-$$

$$\frac{n}{4}O_2 + ne^- \rightarrow \frac{n}{2}O^{2-}$$
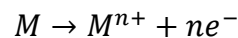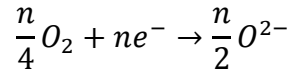
Therefore, the following equation can be used to determine the current I between metal and oxide external surface:[88]

$$I = \frac{E_o}{R + r}$$

Where R is the electronic resistance, r is the electrolytic resistance, and E_0 is the maximum potential difference between the electrodes. The general equation of oxide thickness is:[88]

$$dy/dt = BI$$

Where y is the oxide thickness, t is the time, and B is the constant of proportionality. The rate of oxidation can be derived into the following three categories.
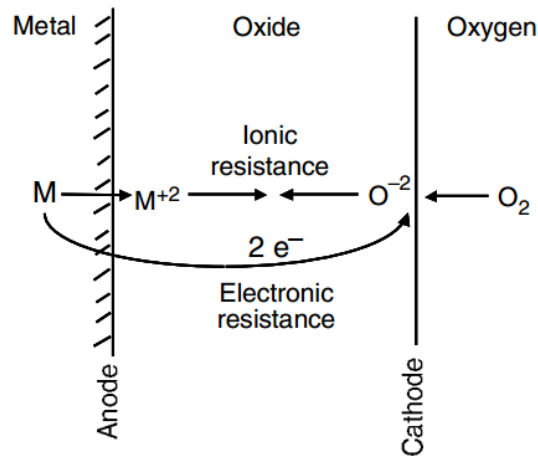
Figure 2-10. Electrochemical interpretation of oxidation of metals. The metal surface and oxide external surface act as anode and cathode, while the oxide layer is the solid electrolyte. [78] Copyright Springer-Verlag New York.

53

In the first case, if the total resistance is small enough such that growth of oxide is controlled by the free diffusion of ions and charges, a linear relationship can be obtained in the following format:[88]

$$y = Kt + A$$

Where K is the rate constant and A is the integration constant. This indicates the oxide grow with a constant rate and will not slow down no matter how thick the oxide layer is. For porous films where the total resistance is relatively small, a liner relationship can be the oxidation kinetics, and it also suggest that the formed oxide will not act as protective layer to prevent further oxidation.

In the second case, when the total resistance is large enough such that diffusion of ions is gradually decreased due to the build thickness of oxide layer, the square of oxide thickness is proportional to time:[78]

$$y^2 = Kt + A$$

This relationship is called parabolic rate law and is in similar format of Fick's diffusion law:[89]

$$L^2 = Dt$$

Where L is the thickness of oxide layer, and D is the diffusion coefficient of metal in the corresponding matrix. For Wagner model, oxidation rates are predicted as parabolic and therefore can be correlated to Fick's diffusion theory where the oxide thickness is proportional to the root square of time. For metal oxidation that forms a continuous oxide layer, Wagner's theory suggests that the diffusion of metal ions control the oxidation process.[81]

In the last case, if polarization exist in the oxide, metal ions can be generated faster than the diffusion

54

across the oxide layer, therefore a counter electric field E is created and the current becomes:[88]

$$I = \frac{E_o - E}{R + r}$$

The rate law of oxide thickness in relationship to time can be expressed as

$$y = K \log(Ct + A)$$

Where K is the rate constant, A and C are integration constants. This logarithmic rate law suggests that the oxidation is controlled by the transfer of electrons due to the existing of electric field in the oxide layer, and is a process that involve combination of electrical and diffusion phenomena.

Figure 2-11[78] shows the plots of linear, parabolic and logarithmic rate law in the condition that all K are equal to 1, C=100 and A=0. These values are arbitrary to show the general trend of three different kinetics. It is clear that both parabolic and logarithmic rate laws indicate the formation of protective oxide layer because of which oxidation is slowed down with time.
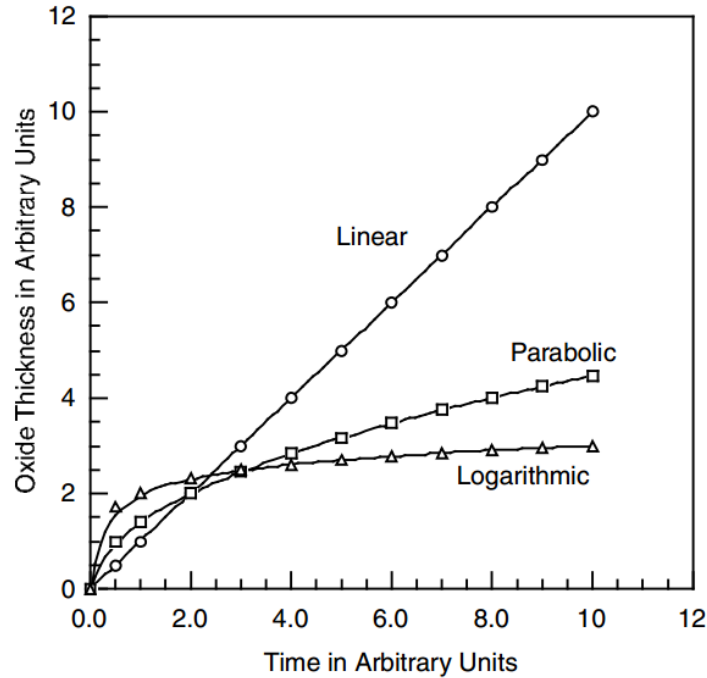
Figure 2-11. Comparison between linear, parabolic, and logarithmic rate law for oxidation. Image reproduced with permission. [78] Copyright Springer-Verlag New York.

Reduction theories

Catalytic oxide NPs exposure in H_2 reduction environment involves the following process: the H_2 molecules dissociate onto metal oxide surface, diffusion of H atom to the reaction site, breakage of the metal-O bonds, formation of metal atoms, nucleation and growth of metallic atoms into clusters and crystalline metallic phase.[90] The kinetics of growth of metallic phase between solid and H_2 can be described according to Avrami relation in:[91]

$$x_{metal\ oxide} = 1 - \exp(-kt^m)$$

where x is the conversion fraction, t is the time, k is the rate constant, and m is exponent factor depends on limiting steps. This is usually for the case where metal clusters grow in two dimensions over the oxide

56

surface, and H_2 can rapidly dissociate on metal surface and into the grain.

For the solid-gas reduction mechanism, the shrinking core model is used to describe the whole process.[92] Illustrated in Figure 2-12[93], as the metal oxide particle reacted with H_2 gas, metallic phase nucleated and growth as thin layer across the oxide, with the oxide shrink into smaller size and finally disappear when fully reduced. During the reduction, H_2 diffuse inward and the reduction product (H_2O) diffuse outward through the metallic layer. The core remains unreacted, but the reaction front moves toward the interior of the particle, resulting in shrinkage of the core to compensate the formation of metallic phase. The outward diffusion of reduction product usually causes the metallic phase to be porous with micro or nanochannels or crystalline grains.
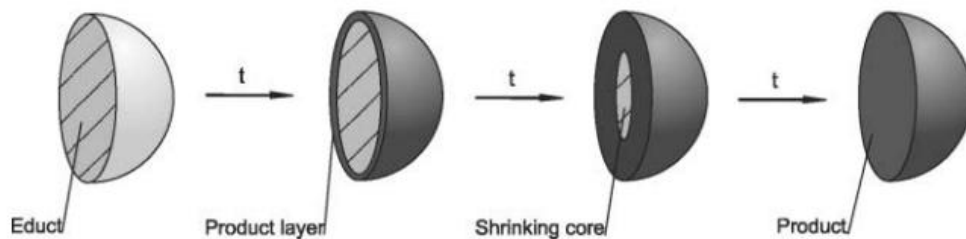
Figure 2-12. Schematic of shrinking core model during reduction reaction. [93] Copyright © 2002 Elsevier Science Ltd. All rights reserved.

57

Chapter 3   *In situ* liquid TEM study of nucleation and growth dynamics of Au nanoparticles on

MoS₂ nanoflakes

(This Chapter is from my published article.[1] The permission is attached in Appendix.)

3.1 Introduction

Catalytic activity of noble metal particles can be optimized by reducing particle size,[94] increasing surface area[95] and tuning orientation.[96] However, obtaining uniformly distributed noble metal nanoparticles with controllable size, shape, and orientation is remaining as the biggest challenge in catalyst design. Over the last decade, supporting noble metal nanoparticles by various substrates have become a promising route where well-chosen substrates can provide a facile way to limit particle size,[97] control orientation[98] and prevent particle aggregation.[99] Recent advances in large scale synthesis of ultrathin 2D materials have attracted tremendous attention for supporting nanomaterials.[100, 101] Besides graphene, many other 2D materials such as transition-metal dichalcogenides (TMDCs) are gaining increased attention since the combination of 2D monolayer form with semiconductor properties.[102] Utilizing TMDCs as templates to grow noble metal nanoparticles opens the possibility of novel composite nanostructures in application of high performance catalyst and electronic devices.[103-106]

The synthesis of noble metal nanoparticles decorated on ultrathin 2D TMDCs has been studied extensively.[107-110] With the help of reducing agents,[108] reducing metal ions from precursors to nanoparticles by chemical reduction is promising because of the relatively low cost and ease of implementation. When the reduction potential of metal ions is more positive compared to the conducting

58

or semiconducting substrate, an electroless deposition called galvanic displacement can occur without any additional reducing agent.[111-113] As an example, when semiconducting MoS_2 is used as substrate, after immersion into aqueous solution containing metal precursors, reduction of metal ions takes place spontaneously by gaining electrons transferred from MoS_2 valence band.[103, 107, 108] This galvanic displacement reaction allows a straightforward synthesis of 2D composite nanostructures decorated with metal nanoparticles. Furthermore, the ability to precisely control the decoration of metal particles on TMDCs is the subject of current interest.[104, 107] Different stabilizers or surface capping agents were added to achieve homogeneously distributed nanoparticles, such as sodium carboxymethyl cellulose[104] and trisodium citrate.[108] Epitaxial growth was also reported for metal nanoparticles such as Pd and Pt that are deposited on MoS_2 with (111) and (101) epitaxial orientations.[108]

Despite that various synthesis strategies for controlling nanoparticles growth on 2D TMDCs are under fast development, the associated mechanism studies mostly relied on theoretical models, which limits an in-depth understanding and exploration of the dynamic essentials. *In situ* (scanning) transmission electron microscopy (S)TEM provides the possibility to directly observe dynamic reaction process in real time with high spatial resolution.[21-23, 26, 114-117] Benefiting from the design of *in situ* liquid cell consisting of two silicon chips with silicon nitride (SiN) viewing windows, liquid solutions can be stored or flowed between chips without influencing the high vacuum in the (S)TEM chamber. The precise control of the liquid thickness allows sub-nanometer imaging of reactions in liquids or at solid-liquid interfaces.[36] Although several studies showed nanoparticle nucleation and growth in liquid-cell (S)TEM,[5, 6, 11, 13, 31, 58, 118-120] to the best of our knowledge, the nucleation and growth of metal nanoparticles on 2D

59

substrates in the liquid cell has not been investigated. Here, we report a combined *in situ* liquid-cell TEM observation and DFT study of the nucleation and growth processes of Au nanoparticles on MoS_2 nanoflakes. We find that MoS_2 nanoflakes play a vital role in controlling the growth mechanism of Au nanoparticles. Due to electrochemical Ostwald ripening, Au nanoparticles on pristine MoS_2 grow with exponent factor of $\beta \sim 0.41$ which is in between diffusion-limited and reaction-limited mechanism. In contrast, sulfur vacancies on MoS_2 induce Au particle diffusion and coalescence during growth process. Additionally, the nanoparticles nucleating along MoS_2 edge have larger size distribution and more orientation variation than those on MoS_2 interior. DFT simulations suggest that MoS_2 edge is very favorable for Au adsorption due to existence of dangling bonds especially at the Mo-terminated side. In addition, S vacancies generate strong nucleation centers that promote diffusion and coalescence of Au nanoparticles.

3.2 Experimental Section

Chemicals. MoS_2 powder (<2 μm, 99%, Sigma-Aldrich) and gold chloride $AuCl_3$ (>99.99%, Sigma-Aldrich) were used as received.

MoS_2 synthesis and exfoliation. Bulk MoS_2 powder was mixed with isopropyl alcohol (IPA) at a concentration of 20 mg/mL. The mixture was sonicated for 5 h in a bath sonicator (Branson 3800, 40kHz, 110W). After that the dispersion was centrifuged at 2000 rpm for 30 min (Thermo Scientific, Legend Micro 21) to remove unexfoliated MoS_2. The obtained supernatant was centrifuged at 1500 rpm for 15

60

min, following by taken out the sediment and re-dispersed in DI water before further characterization.

***Ex situ* deposition of Au nanoparticles on MoS$_2$.** AuCl$_3$ solution was prepared by dissolving powder in DI water with a concentration of 20 mM. 50 μL AuCl$_3$ aqueous solution was added into exfoliated MoS$_2$ dispersion with mild shaking. The resulting solution was sonicated for 5 min before (S)TEM characterization.

***In situ* deposition of Au nanoparticles on MoS$_2$.** A liquid flow TEM holder with pair of silicon microchips (Protochips Inc., Raleigh, NC) was used (Figure 3-1a and b). Each of the microchips has an electron transparent silicon nitride (SiN) viewing window with 50 nm in thickness and $550 \times 20 \ \mu m^2$ in dimension. Spacers with 500 nm thickness (green squares shown in Figure 3-1a) on one microchip were used to ensure a constant distance between two microchips. The O-rings ensured a liquid cell between two microchips with perfect sealing. One droplet (1 μL) of liquid containing MoS$_2$ dispersion was added on the SiN viewing window of one microchip without touching the surface. To create sulfur vacancies on MoS$_2$, the bottom microchip was placed inside the microscope and irradiated under electron beam in vacuum for 3 min, at a dose rate of 90 e$^-$/(Å^2·s). The second microchip was then placed on top of the first one with three screws secured to provide a vacuum sealing. The viewing windows were aligned in parallel to maximize the viewing area.

To flow AuCl$_3$ as precursor into the liquid cell, a microfluid pump was used with Hamilton Syringe containing 1 mL of prepared AuCl$_3$ solution connected to the inlet of PEEK tubing. The microfluid pump

was then started with a constant flow rate at 240 μL/hr. The concentration of Au^{3+} ion was kept the same as it was during *ex situ* experiment. The calculated electron dose rate was approximately 50 $e^-/(Å^2 \cdot s)$ for all *in situ* experiments. Videos were captured using an Orius CCD camera at 30 frames per second with 320×320 resolution. Images were taken with 512×512 scanning resolution. The liquid layer thickness variation due to window bulging effect was calculated using the low-loss EELS data as discussed in Chapter 1.5.4 and Figure 1-11. To minimize the precursor depletion and confinement effect in the liquid cell, continuous flow of $AuCl_3$ solution is ensured and only MoS_2 close to the window edge was used for this study. However, future studies to analyze the effect of different precursor flow rate are worthwhile to be conducted.

   In situ control experiment was performed by presetting imaging condition at a short exposure (0.02s), locate area of interesting, block electron beam and then flow $AuCl_3$ precursor into the holder under same flow rate. Image was taken after five more minutes at same area. Subsequent images were taken with 1 min intervals until no more change is observed.

   Electron microscopy characterization. *Ex situ* deposited Au nanoparticles on MoS_2 was characterized by dropping post-reacted solution on lacy copper grid. TEM images were taken by JEOL JEM-3010 operating at 300 kV. The *in situ* liquid cell experiments were carried out inside a spherical aberration corrected JEOL JEM-ARM200CF STEM with a cold field emission source operating at 200 kV. High angle annular dark field (HAADF) images, as well as energy dispersive spectrometer (EDS) spectrum was acquired by the same microscope. TrueMap was used for all EDS signal collection to correct the

62

overlapping of Mo, S, and Au peaks. Electron energy loss spectra (EELS) were acquired on a Gatan GIF Quantum spectrometer with an entrance aperture of 5 mm.

Density Functional Theory Calculations. DFT calculations were performed with a computational setup similar to previous studies.[121-123] The planewave DFT calculations were carried out using VASP 5.2[124] employing the Perdew, Burke, and Ernzerhof (PBE) Generalized Gradient Approximation (GGA)[125] for the exchange-correlation function and projector augmented wave (PAW) pseudopotentials.[126, 127] The electronic wavefunctions were expanded with planewaves with energy less than 350 eV. The electronic self-consistent loop was terminated when energy changes are less than 1×10^{-6} eV and the ionic relaxations were considered converged when the magnitude of the largest force on any atom is less than 0.01 eV/Å. The $(001)_{MoS2}$ pristine surface and the surface with vacancy was modeled using a 3×3 slab generated from bulk $(001)_{MoS2}$ with lattice constant of 3.18 Å. The Mo-edge/S-edge of MoS_2 were modeled using a nanoribbon of 4×4 extension, exposing four Mo/S sites, respectively. To mitigate the fictitious interactions between the images in the non-periodic directions, we used a supercell approach with more than 12 Å vacuum. For the S-edge NR we had to increase the vacuum spacing to larger than 25 Å to prevent Au from adsorbing at the Mo edge. The Brillouin zone is sampled using the gamma point. We allowed all atoms to relax in all models except for the MoS_2 with S vacancy where we fixed the bottom S layer. Nudge-elastic band (NEB) calculations are carried out to compute the energy barriers.[128, 129] We calculated the nanoparticle binding energy per Au using,

$$E_{BE} = \frac{1}{n}\left(E_{MoS_2+Au_n} - E_{MoS_2} - nE_{Au}\right),$$

63

where n is the number of Au atoms, $E_{MoS_2+Au_n}$ is the energy of the Au$_n$/MoS$_2$ heterostructure in the optimum geometry, E_{MoS_2} is the energy of the MoS$_2$ substrate, and E_{Au} is the energy of an isolated Au atom with $4d^{10}5s^1$ valence according to Hund's rules. The isolated atom was modeled using a large supercell with a cubic lattice of 15 Å side.

3.3 Results and discussion

In this work, *in situ* liquid-cell setup is used to flow AuCl$_3$ solution between two silicon nitride (SiN) membranes. The schematic of the liquid cell device and its cross-section are shown in Figure 3-1a and b, respectively. AuCl$_3$, which is being flowed continuously through the inlet, triggers the following galvanic displacement reactions once in contact with MoS$_2$ nanoflakes:

$$Au^{3+} + 3e^- \rightarrow Au^0;$$

$$MoS_2 \rightarrow (MoS_2)^{n+} + ne^-.$$
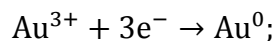
This galvanic displacement takes place spontaneously as the reduction potential (E°) of Au^{3+}/Au is equal to +1.5V versus the standard hydrogen electrode (SHE)[130], which is below the electron affinity (χ = 4.22 eV)[131] of MoS$_2$. Therefore, Au^{3+} will be reduced to Au^0 by gaining electrons transferred from MoS$_2$ substrate.
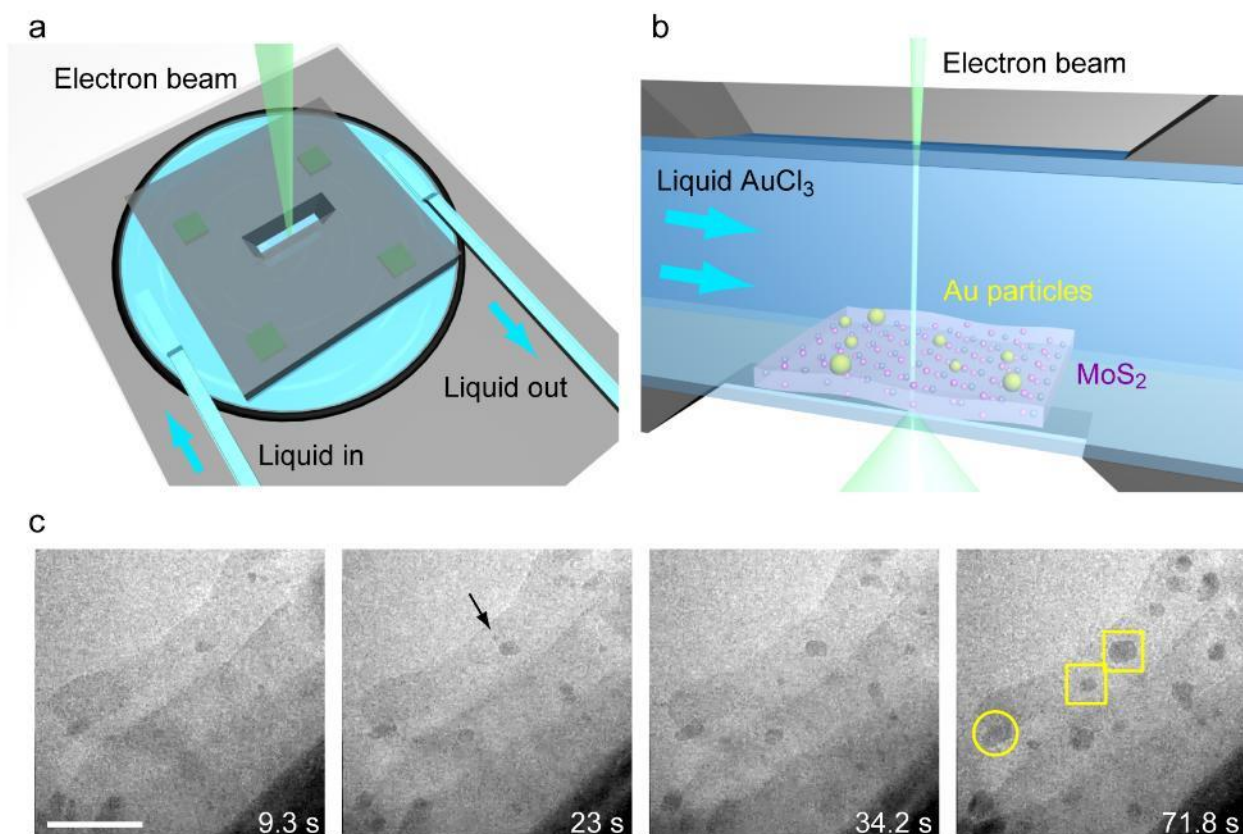
Figure 3-1. (**a**) The schematic of the liquid-cell (S)TEM device used to study the nucleation and growth of nanoparticles. (**b**) The schematic depicts the reaction happens in liquid cell. (**c**) Snapshots from Movie S1 showing the nucleation and growth of Au nanoparticles on MoS_2 interior (yellow squared regions) and edge (yellow circled region). Scale bar is 50 nm.

Movie S1 shows Au nanoparticles nucleation and growth on MoS_2 nanoflake. Snapshots from Movie S1 are shown in Figure 3-1c. As Au^{3+} gains electrons from MoS_2, gold nuclei began to form on MoS_2 interior (yellow squared regions) and along edge (yellow circled region). The nuclei grew into larger nanoparticles as time increases, while nucleation happens at different times and locations. The average particle radius as a function of time is then analyzed and shown in Figure 3-2. The radii were calculated based on $(S/\pi)^{1/2}$ where S is the projection area. Figure 3-2a and b show an example of growth profiles

65

of six Au particles that each can be fitted into a power law function in the form of $R \sim t^{\beta}$, where β is the mean growth exponent. The classic Lifshitz-Slyozov-Wagner (LSW) growth theory predicts two growth mechanisms for average radius of particles where β equals to 1/3 and 1/2 for diffusion-limited and reaction-limited models, respectively.[68] Previous *in situ* TEM studies have shown both consistency[28] and inconsistency[31] compare to the LSW model. Here, the average radius involving all particles in Movie S1 is shown in Figure 3-2c, with β determined to be 0.41. Another example of Au nucleation and growth on MoS$_2$ (Movie S2) is also analyzed with β equals to 0.42. Since the two movies are under the same experimental conditions, the results indicate that the growth of Au on MoS$_2$ yields an exponent of β ~ 0.41 which is in between diffusion-limited and reaction-limited growth mechanisms predicted by the LSW theory.
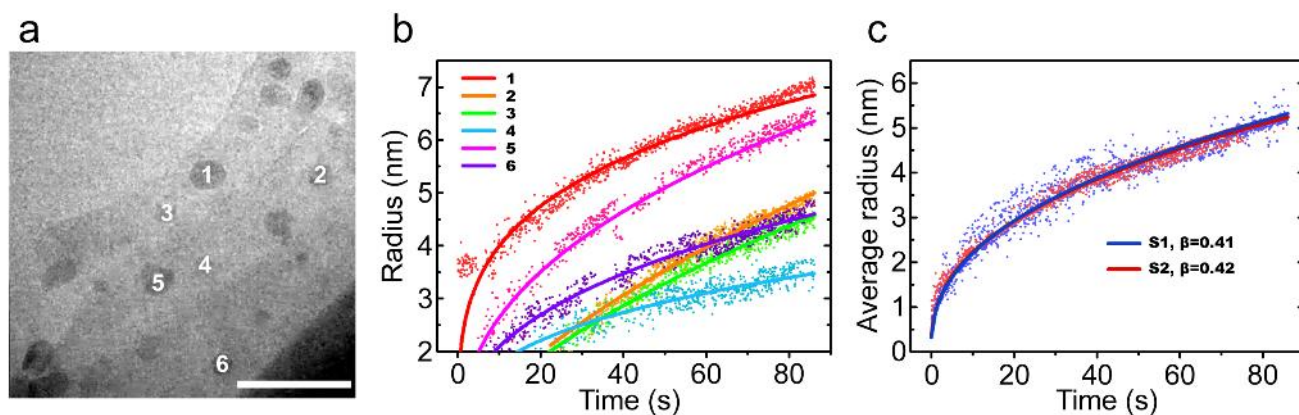
Figure 3-2. (a) Last frame of Movie S1 where the selected particles are numbered. The scale bar is 50 nm. **(b)** Particle radius as function of time obtained from Movie S1 corresponding to the particles numbered in **a**. **(c)** The average radius as function of time obtained from Movie S1 (blue) and Movie S2 (red).

It is also notable that not all the nanoparticles have continuous size increase upon observation, for instance the small nucleus marked by the black arrow in Figure 3-1c disappears within a short time after its nucleation. To further understand this, the surrounding areas of two interior particles (squared regions in Figure 3-1c) and one edge particle (circled region in Figure 3-1c) were analyzed in Figure 3-3a, b and c, respectively. The particles marked in yellow outlines are the largest ones in the selected area, while the ones marked by red outlines are nearby smaller particles. We should clarify that the red outlines show only some examples of the particles, and not all of the particles in the image are outlined. In contrast to the growth of the largest particle, the surrounding smaller ones dissolve soon after nucleation, although a successive nucleation of small nuclei at different locations are observed. The similar phenomenon happened both on the interior and edge particles that the largest one grows while surrounding ones dissolve. As there is no coalescence observed for particles on interior or along edge, this growth mechanism can be attributed to the MoS_2 substrate-induced electrochemical Ostwald ripening. This is a growth process involving migration of ions and electrons instead of atoms from a smaller particle to a larger particle, when a substrate is present. Brus *et al.*[132] first reported the electrochemical Ostwald ripening phenomenon for silver particles on conductive substrates immersed in water. Their observations suggested that smaller silver particles dissolved by releasing Ag^+ into solution while electrons transferred through the conductive substrate and combined with another ion on larger particles, leading to the continuous growth of the larger one. Later on more studies confirmed that the electrochemical Ostwald ripening phenomenon can take place on semiconducting substrates as well.[133] The electron migration driving force is due to the potential difference between the larger and smaller particles, as smaller particles are

67

easily oxidized.[134] Here, the proposed mechanism is shown in Figure 3-3d. At stage Ⅰ, the galvanic displacement resulted in nucleation and initial enlargement of the Au nuclei. At stage Ⅱ, the electrochemical Ostwald ripening is triggered due to the potential difference between small and large nuclei. The presence of electrochemical Ostwald ripening may be the reason that Au nanoparticle growth on MoS$_2$ is bounded by the diffusion-limited and reaction-limited growth mechanisms. To further confirm the electrochemical Ostwald ripening mechanism, more detailed studies utilizing liquid cell setup with better spatial and time resolution are indeed necessary.
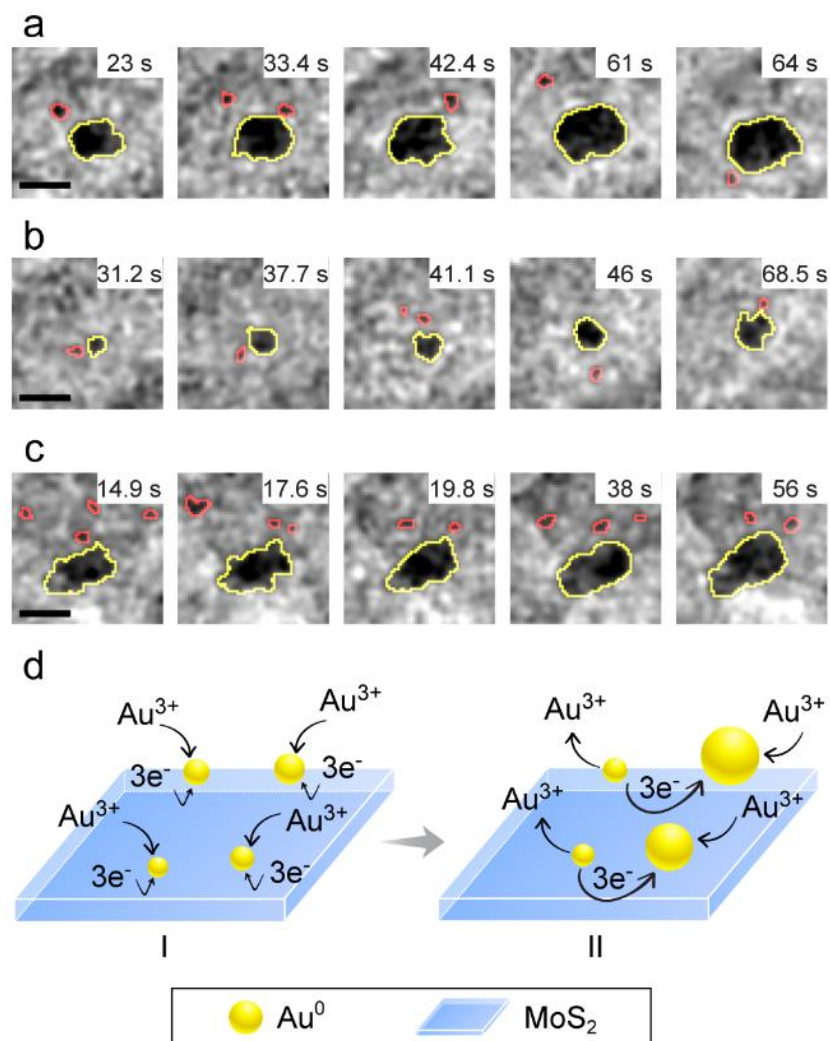
Figure 3-3. (**a-c**) The enlarged surrounding areas of two interior particles (squared regions in Figure 3-1c) and one edge particle (circled region in Figure 3-1c). All scale bars are 10 nm. (**d**) The schematic illustration of galvanic displacement of Au^{3+} on MoS_2 (stage I) and the following electrochemical Ostwald ripening process (stage II).

To better understand this nucleation and growth behavior, the morphology and structure of Au nanoparticles on MoS_2 were further investigated. Figure 3-5a shows the energy dispersive spectrometer

69

(EDS) mapping of Au nanoparticles that formed on MoS_2. The EDS signals of Si and N from SiN viewing window are excluded to reduce color interference. Notably, the Au nanoparticles that grow along MoS_2 edge have remarkably larger diameter compared to those that grow on interior of MoS_2. To quantify the Au nanoparticles size distribution, HAADF images containing more than 1000 Au nanoparticles formed on MoS_2 were statistically analyzed. Figure 3-4 shows an example image of interior and edge Au nanoparticles marked by ImageJ.[135] Quantifications of Au nanoparticles size distribution is shown in Figure 3-5b. It confirms that the diameter of Au nanoparticles formed on MoS_2 interior ($\approx 7 \pm 4$ nm) is smaller than that along MoS_2 edge ($\approx 12 \pm 6$ nm). STEM image in Figure Figure 3-5c shows the uniformly formed Au particles on MoS_2. The corresponding selected area electron diffraction (SAED) pattern is shown in the inset. The diffraction spots of $\{100\}_{MoS2}$ can be identified, indicating that the basal plane of MoS_2 is normal to the electron beam. The inner diffraction ring marked with half dashed circle can be assigned to $1/3\{422\}_{Au}$ planes and outer diffraction ring is from $\{202\}_{Au}$. Amorphous pattern is contributed from SiN viewing window. The appearance of $1/3\{422\}_{Au}$ forbidden spots is probably because the Au thickness along electron pathway is so small that spots from the first Laue zone can be greatly elongated to intercept with Ewald sphere, especially in the case where the number of $\{111\}_{Au}$ layers is not divisible by three, or due to stacking faults along (111) plane.[108, 136] Thereby the zone axis of Au nanoparticles can be confirmed to <111>.
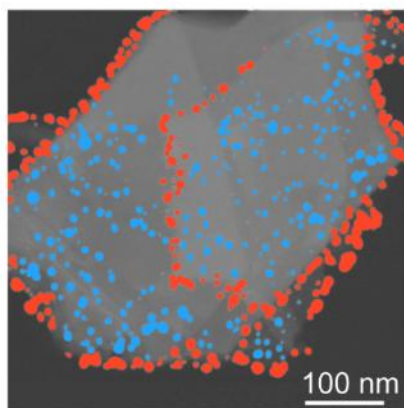
Figure 3-4. Example image for particle size measurement. The Au nanoparticles marked with blue and red correspond to those formed on MoS_2 interior and along MoS_2 edge.
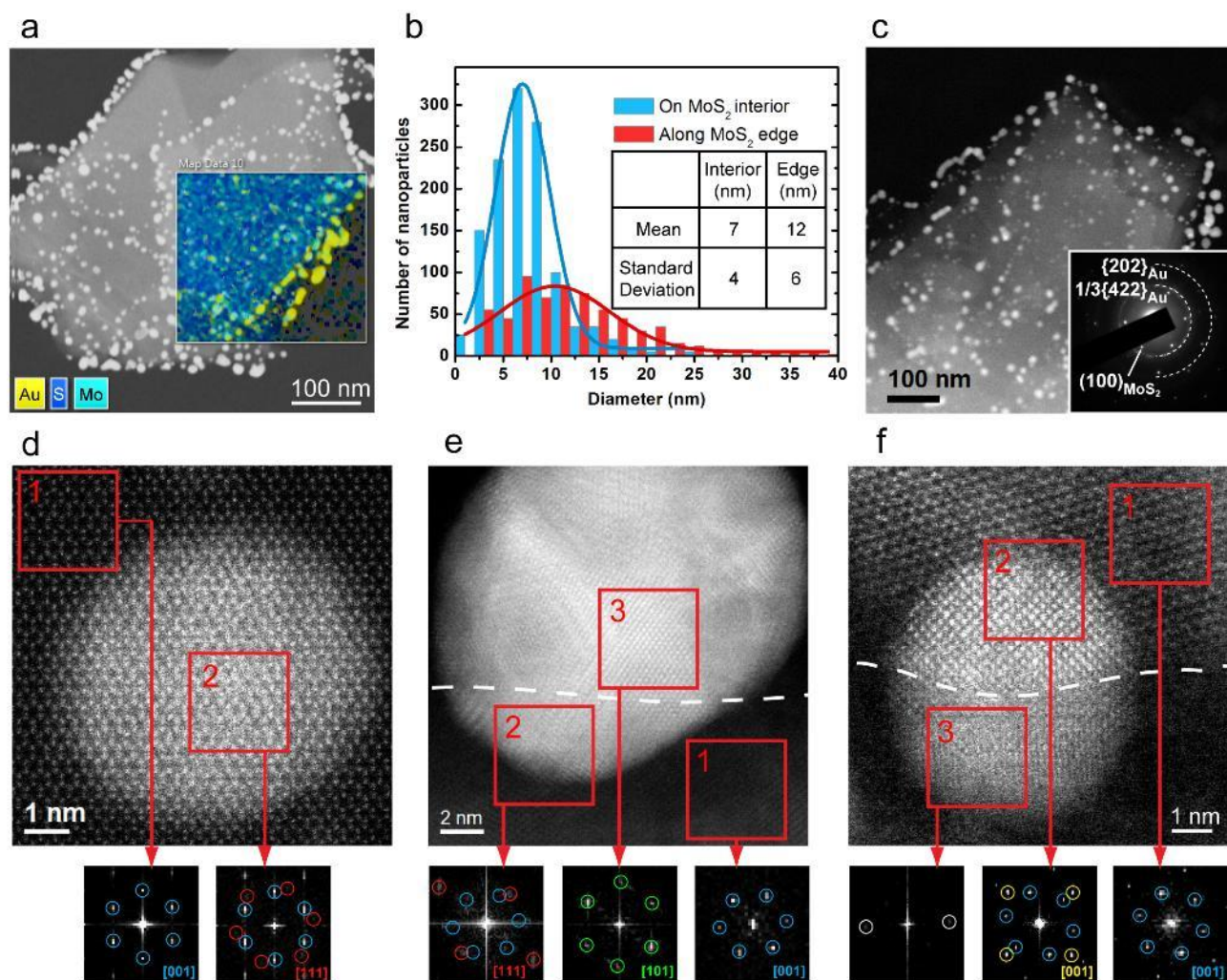
Figure 3-5. (**a**) EDS mapping of Au nanoparticles formed on MoS_2. (**b**) Au nanoparticles size distribution and Gaussian fittings. The inset table lists calculated mean and standard deviation of Au nanoparticles diameter. (**c**) HAADF image of *in situ* grown Au nanoparticles on MoS_2. Inset shows the SAED pattern of hexagonal basal plane of MoS_2 along with $1/3\{422\}_{Au}$ and $\{202\}_{Au}$ diffraction rings. (**d**) HAADF image of an Au nanoparticle formed on MoS_2 interior. Two FFT images were taken from the areas marked with red squares. Spots in blue and red circles are from $(001)_{MoS2}$ and $(111)_{Au}$, respectively. (**e**)(**f**) HAADF images of Au nanoparticles formed along MoS_2 edge (indicated by white dashed line). FFT images were

72

taken from the areas marked with red squares. Spots in blue, red, green and yellow circles are from $(001)_{MoS2}$, $(111)_{Au}$, $(101)_{Au}$, and $(001)_{Au}$, respectively.

The HAADF images of Au nanoparticles formed on MoS_2 interior and along MoS_2 edge are shown in Figure 3-5d and e-f, respectively. In Figure 3-5d, Fast Fourier transform (FFT) image from MoS_2 substrate (Region 1) shows the six diffraction spots in blue circles from $(001)_{MoS2}$ basal plane. FFT from Region 2 shows diffraction spots in red circles from $1/3(4\overline{2}\overline{2})_{Au}$, indicating $(111)_{Au}$ orientation. Figure 3-5e and f show two Au nanoparticles that grown on MoS_2 edge (indicated by white dashed line). Notably, different orientation relationships with MoS_2 basal plane were observed. For instance, Region 3 in Figure 3-5e where part of Au nanoparticle outside MoS_2 shows diffraction spots in green circles from $(11\overline{1})_{Au}$, $(1\overline{1}\overline{1})_{Au}$ and $(020)_{Au}$, suggesting $(101)_{Au}$ orientation. Figure 3-5f shows another example of Au with $(001)_{Au}$ atop MoS_2 while no clear zone axis present for the part outside MoS_2. Previous reports have shown that the low-index facets of FCC metal {111} can grow with preferential orientation on MoS_2 surface.[108] One of the reasons is that Au {111} has the lowest surface energy among low Miller index surfaces,[137] which is generally the case for FCC metals.[138-141] Additionally on $(111)_{Au}$ plane the $[1\overline{1}0]_{Au}$ has the smallest lattice mismatch (9.5%) with $[100]_{MoS2}$.[142] Based on our observations, this preferential orientation can be only observed for the Au nanoparticles formed on MoS_2 interior. Au nanoparticles along edge may have several possible orientation relationships with MoS_2 basal plane, with the possible reason that some particles are polycrystals.
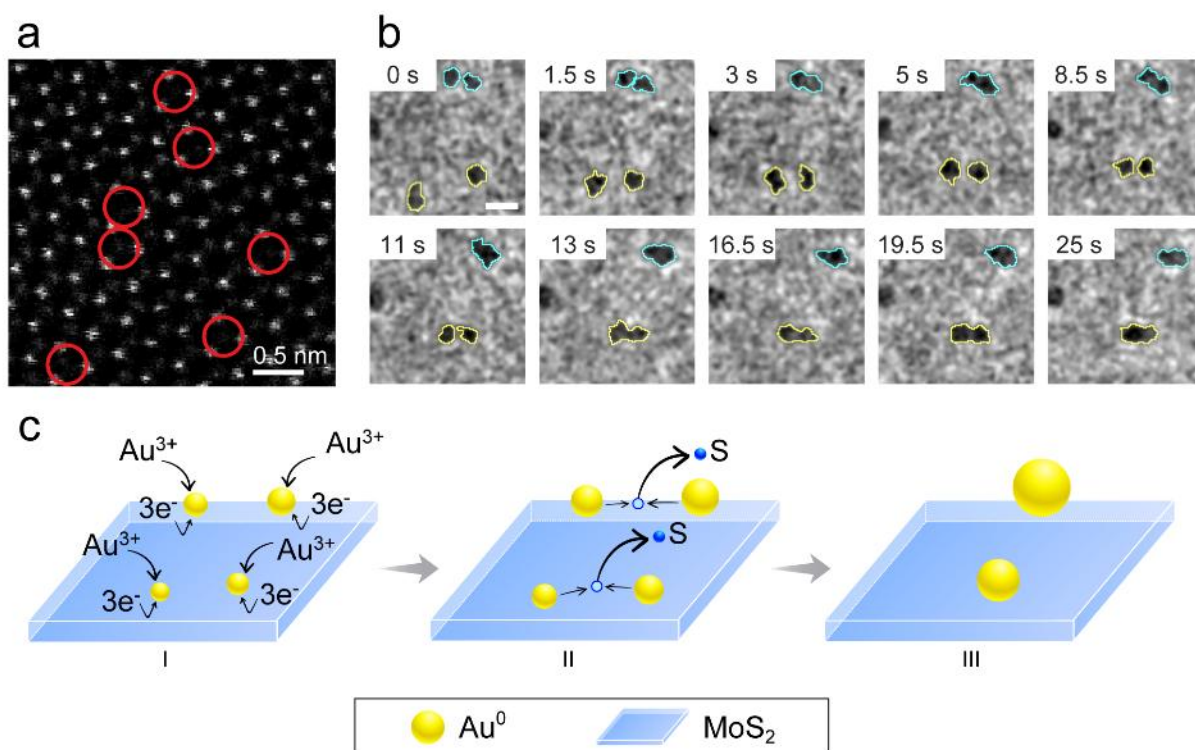
Figure 3-6. (**a**) STEM-HAADF image of MoS_2 surface with sulfur vacancies after electron beam irradiation. (**b**) The snapshots from Movie S3 show the dynamics of Au nanoparticles growth on MoS_2 with sulfur vacancies. Two pairs of nuclei that migrated and coalesced are outlined by blue and yellow lines. The scale bar is 10 nm. (**c**) The schematic illustration of galvanic displacement of Au^{3+} on MoS_2 (stage Ⅰ), diffusion of Au nuclei towards vacancy sites (stage Ⅱ), and particle coalescence mechanism (stage Ⅲ).

In the next step, sulfur vacancies were created on MoS_2 nanoflake and the *in situ* TEM experiment was repeated to analyze the effect of vacancies. The effect of electron beam on generating sulfur vacancies is discussed in Chapter 1.5.2 and Figure 1-8. Figure 3-6a shows exemplary HAADF image of sulfur

74

vacancies on MoS$_2$ surface after electron beam irradiation. The lower intensity indicates the existence of vacancy sites such as the ones marked by red circles. The growth behavior of Au nanoparticles on the area with sulfur vacancies was recorded in Movie S3. The snapshots of Movie S3 focusing on the vacancy area can be found in Figure 3-6b. It is interesting that instead of growth into larger size, the Au nanoparticles have higher mobility to diffuse and coalesce on MoS$_2$ surface. For instance, the two nuclei outlined by yellow lines in Figure 3-6b are well separated at the beginning, however due to increased diffusion the two nuclei migrate towards each other forming a "neck" at around 13 s, and finally they coalesce into a larger particle. Similar phenomenon happens for the two nuclei marked with blue outline. Although galvanic displacement still contributes to the initial nucleation process, most of the particles stop growing at early growth stage (radii $\leq$ 3 nm) compare to the case of pristine MoS$_2$. In addition, the particle diffusion and coalescence are greatly increased. Based on the observation, the possible growth mechanism is illustrated in Figure 3-6c. In stage Ⅰ, the galvanic displacement induces initial Au nuclei. In stage Ⅱ, S vacancies result in localized midgap states[143] in MoS$_2$ electronic structure, and thus induce strong scattering effect.[144] In this circumstance, the galvanic displacement and electrochemical Ostwald ripening are hindered since scattering effect diminishes the electron transfer ability. Furthermore, as S vacancies create new favorable adsorption sites for Au nuclei (see more details in the DFT calculation part), the diffusion towards vacancy sites is greatly enhanced. In the final stage Ⅲ the surrounding Au particles coalesce into larger ones.

To further verify the nucleation and growth differences of Au nanoparticles on MoS$_2$ interior, along

edge, and on MoS_2 with S vacancies, DFT calculations are carried out to illustrate the early stages of the metal adsorption on four different substrate models: 1) pristine MoS_2; 2) MoS_2 nanoribbon (NR) with Mo-exposed edge; 3) MoS_2 NR with S-terminated edge; and 4) $MoS_{2-\eta}$ representing MoS_2 with S vacancies. These models are shown in Figure 3-7. For each model, we have obtained the optimum adsorption configuration of 1-4 Au atoms, similar to the previous study of Pt/MoS_2 system.[121] The binding energies of the most stable adsorption configuration are shown in the inset table in Figure 3-7a. The adsorption configurations are shown in Figure 3-7b-7f and Figure 3-8

For the pristine surface, Au optimum adsorption configuration is atop S site (Figure 3-7b), which is in contrast to most metals on MoS_2 where the favorable adsorption site with the smallest adsorption energy is atop Mo site adopting a four coordinated configuration.[122] The binding energy of the Au monomer is relatively small (0.5-0.6 eV), which is not surprising considering that Au has a deep-lying d-band state and is relatively inert. The small energy difference (less than 0.1 eV) of the monomer between different adsorption sites (atop Mo or in the hollow site) suggests a very shallow potential surface for Au diffusion. This is confirmed with nudged-elastic band (NEB) calculations showing that the Au diffusion barrier is 0.07 eV. The Au_2 dimer (Figure 3-7c) adopts a configuration where the Au_2 bond is perpendicular to the surface atop S site with a strong binding energy of 1.67 eV/atom. The stability of this configuration can be understood due to the $4d^{10}5s^1$ valence of isolated Au atom, and the strength of the Au-Au dimer energy (2.30 eV). Further, the Au-Au bond distance in this vertical configuration is 2.51 Å, which is similar to that of Au_2 dimer of 2.47 Å. In addition to being thermodynamically favorable, NEB calculations show that two isolated Au atoms can diffuse on the surface and form a dimer without any kinetic hindrance.

76

These results, in addition to binding energies of Au_3 and Au_4 in Figure 3-7a, suggest that the dimer is the nucleation seed, and large nanoparticles can easily grow on the surface via Au diffusion and coalescence.

Experimentally, it was seen that Au nanoparticles also nucleate along the edge, and the size of the nanoparticles is larger than those that nucleate on MoS_2 interior. To investigate this, we used an MoS_2 NR with exposed Mo and S edges as shown in Figure 3-7d and e. It was found that the Au adsorption on the Mo-terminated NR is very favorable with an adsorption energy of 3.74 eV/atom. On the other hand, the adsorption of Au on the S-terminated side is less favorable with only 1.8 eV/atom. The difference in bonding of Au to the S-terminated versus Mo-terminated edges can be rationalized by inspecting the bonding configuration. At the Mo edge, Au occupies the bridge site between two neighboring Mo atoms with dangling bonds, while as the bonding on top of sulfur on S-terminated side is not very favorable as sulfur is already bonded to two Mo atoms. Larger Au nanoparticles at the edge site are formed by occupying all available Mo-Mo bridge sites.

Further, we find that the adsorption of Au atop S site on (001) surface near the Mo-terminated edge (~ 1 eV) is less preferable than the edge site but is still larger than the adsorption on (001) surface very far from the edge (~ 0.6 eV). Thus, there is a strong thermodynamic preference for Au nanoparticles to grow at the Mo-terminated MoS_2 edge. Furthermore, it was found that the diffusion of Au from atop site on (001) surface near the Mo-terminated edge to the edge bridge site is barrierless. These results suggest that Au monomers that adsorb on the MoS_2 interior can easily diffuse to the Mo-edge site to nucleate there. In this case, the rate-limiting step is the Au diffusion barrier of 0.07 eV on MoS_2 interior, which is negligible.

For the $MoS_{2-\eta}$ model with one S vacancy (Figure 3-7f), DFT shows that the Au adsorption passivates

77

the S-vacancy in MoS_2, with very favorable adsorption energy of 2.77 eV. Further the hopping of Au atom from the nearest atop-S adsorption configuration that is close to the vacancy site is barrierless (less than 0.02 eV). Thus, the vacancy site will form a strong nucleation center where the Au nanoparticle can be attracted. As seen experimentally, the high mobility of nanometer scale Au particles can be explained by the low diffusion barrier for constituted Au atoms around vacancy sites.

a

$(Au)_n$	MoS_2	MoS_2 NR (Mo-edge)	MoS_2 NR (S-edge)	$MoS_{2-\eta}$
1	0.66	3.72	1.87	2.77
2	1.67	3.80	2.11	2.45
3	1.65	3.65	2.44	2.35
4	1.87	3.65	2.45	2.28

b   c   d   e   f
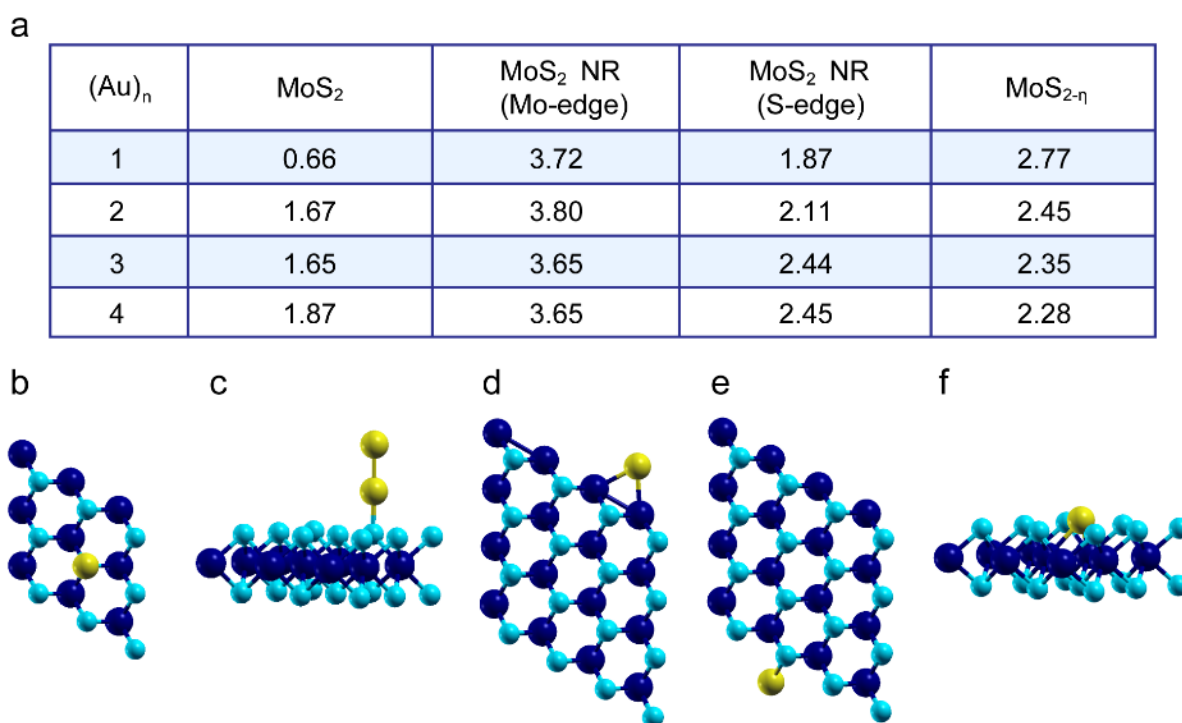
Figure 3-7. (a) Adsorption energies in eV for 1-4 Au atoms on four different MoS_2 substrates. **(b)** Top view of Au configuration on pristine $(001)_{MoS2}$. **(c)** Side view for dimer Au_2 configuration on $(001)_{MoS2}$. **(d)** and **(e)** are top views of Au configuration on Mo-edge and S-edge of MoS_2 nanoribbon. **(f)** Side view of Au configuration on $(001)_{MoS2-\eta}$ with sulfur vacancy. Mo is shown as dark blue, S as blue, and Au as yellow spheres.
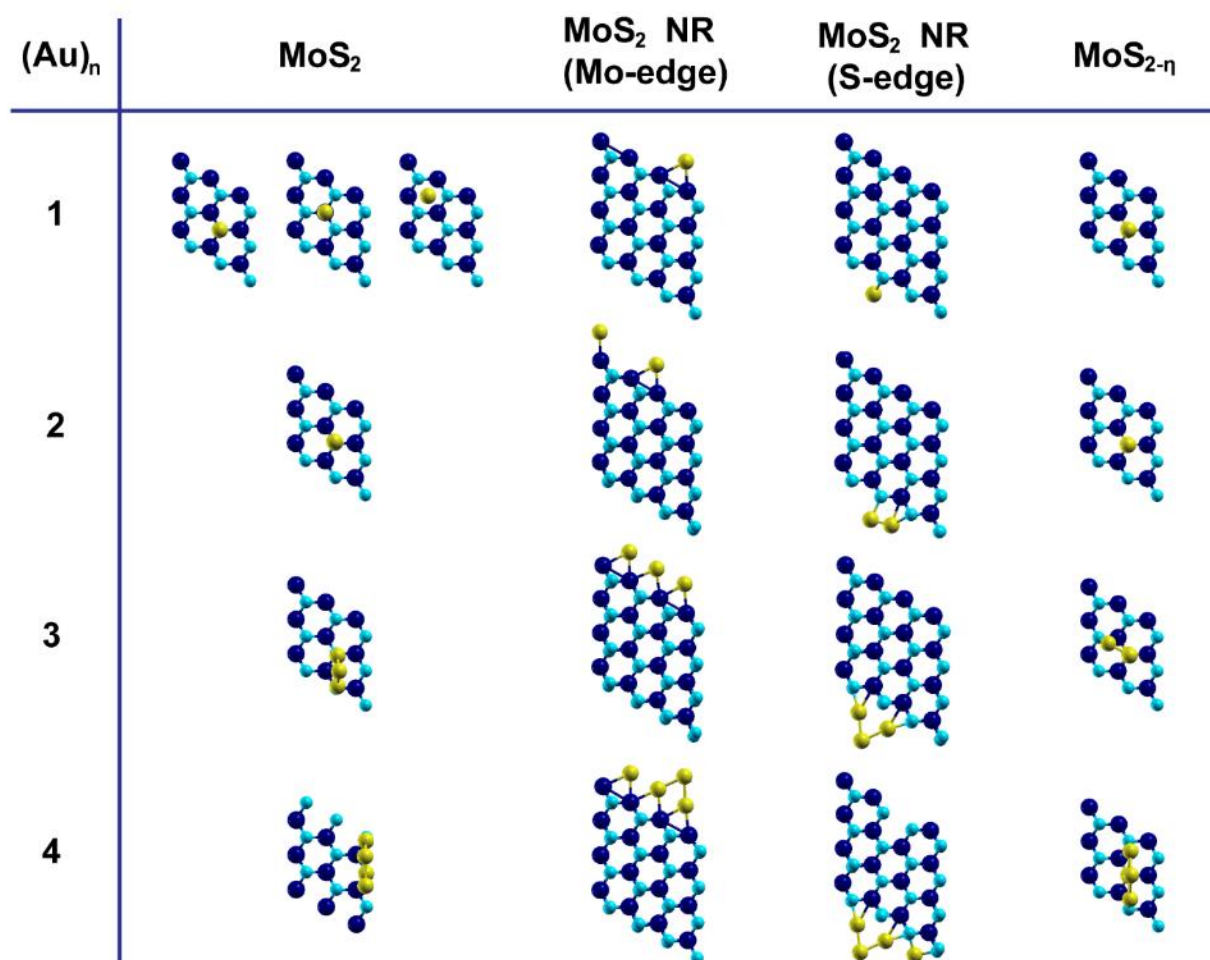
Figure 3-8. Adsorption configuration for 1-4 Au atoms on four different MoS_2 substrates. Mo is shown as dark blue, S as blue, and Au as gold spheres.

Finally, the role of electron beam was analyzed by the *in situ* and *ex situ* control experiments. As AuCl₃ flows into the liquid cell, the electron beam irradiates the viewing area, generates solvated electrons (e_{aq}^-) from the solution[59, 118] and thus creates a reducing environment.[6, 58, 119, 145] The solvated electrons can reduce Au^{3+} ions to Au^0 based on the following reaction $Au^{3+} + 3e_{aq}^- \rightarrow Au^0$, generating Au atoms in the solution. In this scenario, Au atoms may contribute to the growth of Au nanoparticle

79

through conventional chemical Ostwald Ripening instead of the electrochemical Ostwald Ripening. To further understand this, *ex situ* experiments were first carried out to eliminate the influence of electron beam. The morphology of *ex situ* deposited Au nanoparticles on MoS_2 nanoflake is shown in Figure 3-9a. The HRTEM of Au nanoparticles on MoS_2 is shown in Figure 3-9b. The $(100)_{MoS2}$ with lattice spacing of 2.7 Å and $1/3(4\overline{2}\overline{2})_{Au}$ with lattice spacing of 2.5 Å can be clearly identified either from the HRTEM image or from the corresponding FFT shown in the inset. Figure 3-9c shows the EDS line scan data across an *ex situ* grown Au nanoparticle with the distinct energy peaks of Mo, S and Au. Second, the *in situ* control experiment was performed to further verify the formation of Au particles. An example TEM image of Au deposited on MoS_2 with beam blocked is shown in Figure 3-9d. It is obvious that the *ex situ* and *in situ* deposited Au particles on MoS_2 have a good agreement on the morphology. The Au particle size were analyzed and shown in Figure 3-9e, Figure 3-9f for *ex situ* and *in situ* control experiment without electron beam irradiation, respectively. For these two cases, there is no significant difference in terms of either interior or edge particles size distribution. In comparison with *in situ* experiment, around 7% and 12% decrease of mean particle sizes on the interior and edges of MoS_2 can be identified. These results show that the nucleation and growth still happen without electron beam, and the trend that particles along edge are larger still valid. In addition, the slightly larger particle size both on the interior and along edges when electron beam is present suggests that the conventional chemical Ostwald Ripening may also happen due to direct reduction of Au^{3+} ions in the solution. However, the trend that Au particles on MoS_2 edge were larger in comparison to the ones on interior remains the same for both *ex situ* and *in situ* conditions. These results also confirm that the nucleation and growth of Au nanoparticles on MoS_2 still occur without

80

electron beam, which is consistent with the previous *ex situ* studies.[104, 107]
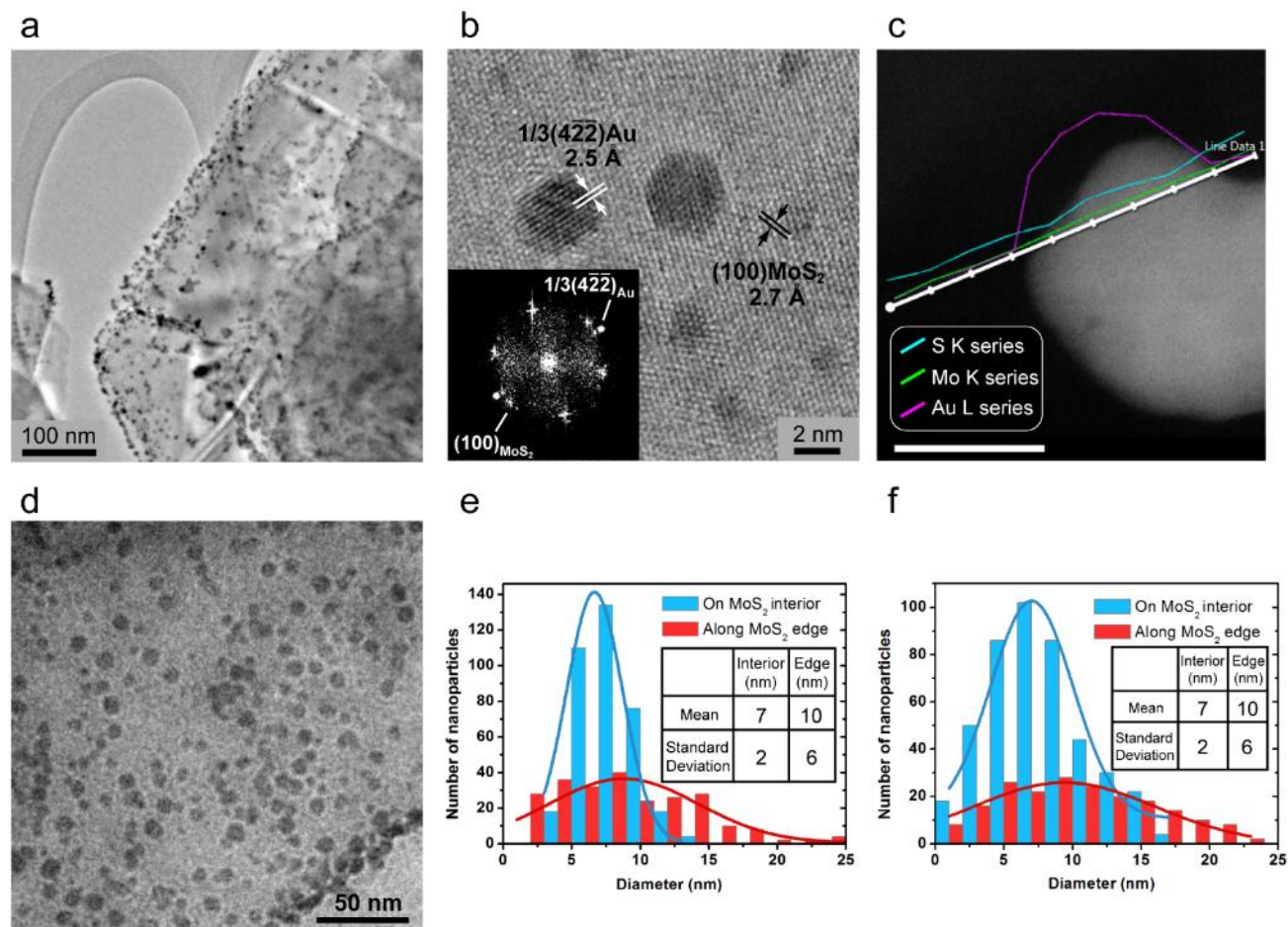
Figure 3-9. (**a**) TEM image of *ex situ* deposited Au nanoparticles on MoS$_2$. (**b**) HRTEM of *ex situ* deposited Au nanoparticles on MoS$_2$ nanoflake. Inset shows corresponding FFT pattern. (**c**) HAADF image of an *ex situ* deposited Au nanoparticle on MoS$_2$. EDS line scan data showing Mo, S, and Au peaks (signals from copper grid were excluded) that overlaid on the image. The scale bar is 10 nm. (**d**) TEM image of Au particles on MoS$_2$ from *in situ* control experiment without electron beam irradiation. (**e**)(**f**) Au nanoparticles size distribution and the Gaussian fitting for the conditions of *ex situ* and *in situ* control

81

experiments without electron beam. The inset tables list calculated mean and standard deviation of Au nanoparticles diameter.

The schematics in Figure 3-10 summarize the Au nucleation and growth processes on MoS_2 nanoflakes based on our observations. The nucleation of Au starts from galvanic displacement of Au ions by accepting electrons from MoS_2 nanoflake at initial stage (Figure 3-10a). Then electrochemical Ostwald ripening is triggered such that the larger nuclei grow even larger by combination of Au ions in solution and electrons transferred from smaller nuclei. Due to the loss of electrons, smaller nuclei dissolve Au ions into solution (Figure 3-10b). In this growth process, if S vacancies are present on MoS_2 surface, electrochemical Ostwald ripening is hindered as the electron transfer pathway will be obstructed by scattering effect. The migration of Au nuclei is then greatly enhanced due to preferable adsorption and low diffusion barriers of the defective S sites. Concomitantly, nuclei with higher surface energy tend to coalesce into larger ones to become more stable (Figure 3-10c).
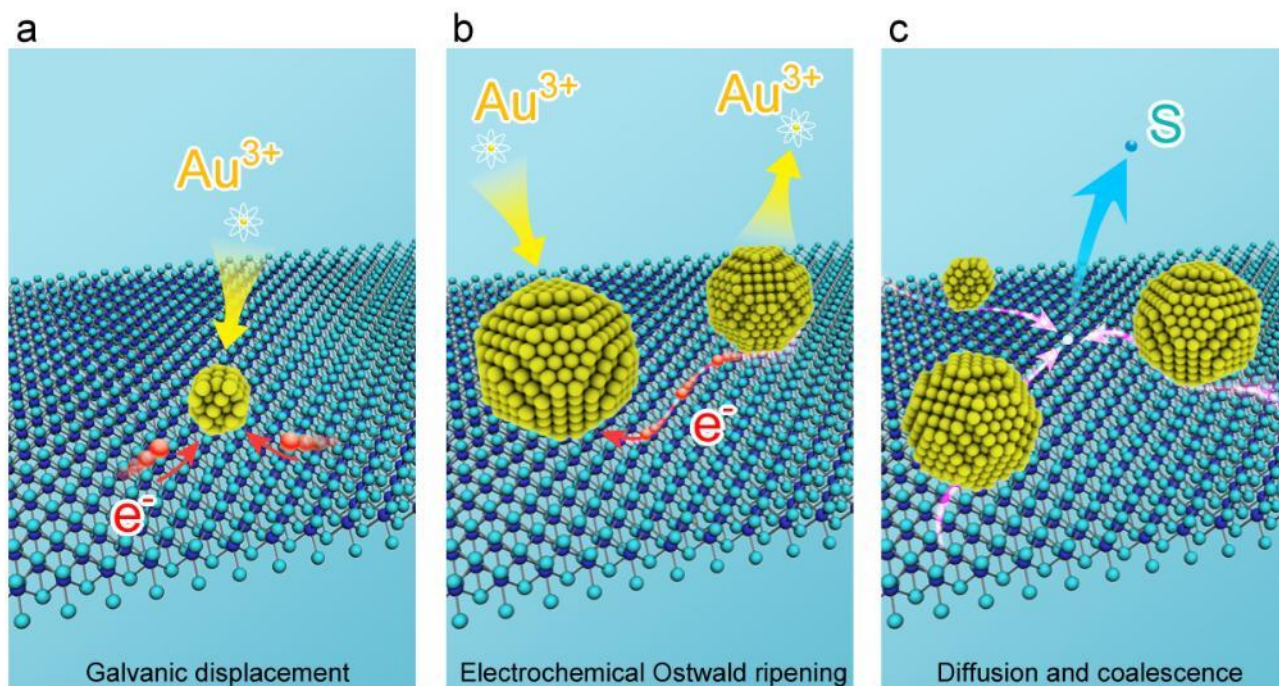
Figure 3-10. Schematic illustration of Au nanoparticle's nucleation and growth on MoS$_2$ nanoflake. (**a**) Galvanic displacement of Au ions to Au nuclei on MoS$_2$ nanoflake. (**b**) Electrochemical Ostwald ripening process leading to the growth of the larger Au particle and dissolution of smaller Au particle on MoS$_2$. (**c**) Diffusion and coalescence of Au particles close to S vacancy site.

3.4 Conclusions

The present work provides real-time observation of nucleation and growth processes of Au nanoparticles on ultrathin MoS$_2$ nanoflakes by *in situ* liquid-cell TEM. The galvanic displacement of Au ions to Au nuclei on MoS$_2$ was observed in real time when AuCl$_3$ flow into the liquid cell. It was found that pristine MoS$_2$ yield a growth mechanism in between diffusion-limited and reaction-limited model, possibly because of electrochemical Ostwald ripening. The growth of Au nanoparticles on interior of MoS$_2$ follows

oriented attachment on {111} facets considering preferable adsorption. Au nanoparticles formed along

MoS_2 edge have a relatively larger size and variety of crystal orientations compared to the ones formed

on the interior of MoS_2. Differ from pristine MoS_2, MoS_2 with S vacancies hinder the electrochemical

Ostwald ripening but promote diffusion and coalescence. The large difference of Au adsorption energy

between edge and interior from DFT calculation explains the tendency of nanoparticles to grow into larger

size at MoS_2 edge. Furthermore, the generation of vacancies on MoS_2 is shown to enhance the coalescence

of nanoparticles due to formation of favorable nucleation center at the defective sites. This work shows

that *in situ* liquid-cell TEM provides a feasible way to investigate the dynamic nucleation and growth

processes of metal nanoparticles on ultrathin substrate. Further, the findings demonstrate how the substrate

can affect the growth of deposited metal nanoparticles, and thus shed new insights on the design of

substrate-supported catalysts.

Chapter 4 *In situ* gas TEM studies on sintering kinetics of MoS$_2$ supported metal nanocatalysts

in atmospheric gas environments

(This Chapter is from my published article.[2] The permission is attached in Appendix.)

4.1 Introduction

Heterostructures formed from 2D substrate and supported nanoparticles have shown promising applications in catalyst,[105, 146-149] sensor,[142, 150-152] and energy storage fields.[153-155] Among the various 2D supports, MoS$_2$ is of increasing interest due to its excellent activity for hydrogen evolution reaction (HER)[108] and chemical sensing.[142] Specifically, the heterostructures of MoS$_2$ supported nano-size metal nanoparticles display better HER activity than commercial Pt/C catalyst, such as Pt-MoS$_2$,[156, 157] Rh-MoS$_2$ composite,[158] Co-doped MoS$_2$,[159] and Ni$_2$P-MoS$_2$,[160] with additional benefit of reducing expensive Pt loading in a catalytic system.

A major challenge in catalysts is the degradation of catalyst nanostructures due to irreversible sintering during service conditions that involve exposure to various gases at elevated temperatures.[161] Such catalyst nanostructure coarsening usually results in loss of active surface area and intended catalytic properties. It is therefore crucial to develop reliable methods to control catalyst size, shape and prevent sintering especially in working environments. There are various examples: Pt decorated Co-Pd core-shell catalyst is shown to have high stability and better oxygen reduction reaction (ORR) activity than commercial Pt catalyst;[162] atomically dispersed dinuclear Ir catalysts anchored on α-Fe$_2$O$_3$ has been reported with good stability against detachment and aggregation;[163] Au-Pt core-shell star-shaped

85

decahedra displays high stability in ORR environments.[164] Further attention is paid on design of substrates to enhance metal-support interactions and inhibit catalyst particle migration,[165] such as spinel $MgAl_2O_4$ for Pt support,[166] porous carbon for Pt and $PtCo_x$,[167] and very recently 2D supports including graphene[168] and MoS_2.[109] However, an in-depth understanding of anchor effects and degradation mechanisms for 2D substrates supported heterogeneous catalysts is still lacking.

Recently various *in situ* experimental techniques are under fast development such as *in situ* X-ray scattering,[169, 170] *in situ* X-ray photoelectron spectroscopy (XPS),[171, 172] and *in situ* TEM[54, 168, 173-182] to overcome the barrier of revealing catalyst dynamics. Among them, advances in the field of *in situ* environmental transmission electron microscopy (ETEM) provide opportunity to obtain both atomic structural and chemical composition information of particle evolution during catalytic reactions. To perform such ETEM studies, either the microscope column can be modified to enable the exposure of specimens to gas environment[183-189] or the specimen holder can be designed to accommodate the microfabricated gas-cell devices.[42, 47, 177, 190-198] The latter setup provides the possibility to observe samples in gases at atmospheric pressure with little resolution degradation, allowing the real time analysis of materials in *operando* conditions. For instance, the CO oxidation reaction on Pt/C was investigated and Pt nanoparticle surface reconstruction was captured in real time.[198] In another work, the transformation of PdCu nanocatalyst from spherical to truncated cubes was observed in H_2 environment.[47] Very recently, formation of NiO shell over Pt-Ni bimetallic nanocatalysts during oxidation and reduction reactions were reported and an enhanced catalytic activity was found in Pt-NiO format.[43]

Despite the extensive research on catalyst evolution in gases environment, how 2D supported catalysts

86

behave in gas and high temperature conditions is not well understood. For example, it is unclear whether a 2D heterostructure catalyst system can maintain good thermal stability against sintering especially during high temperature electrolysis operations that involves H_2 gas.[199] Here, we report an *in situ* environmental gas-cell TEM study of sintering behavior of Pt and Au@Pt core-shell NPs on 2D MoS_2 support from RT to 400 °C in vacuum and N_2, H_2 and air at atmospheric pressure. MoS_2 support exhibits sufficient stability during heating in vacuum, N_2 and H_2, while degradation of MoS_2 is observed when heating in air. We found that sintering of Pt and Au@Pt on MoS_2 in vacuum, N_2 and H_2 were mainly governed by PMC mechanism. More importantly, H_2 plays vital role in controlling the degradation mechanism. High-resolution TEM (HRTEM) results reveal stronger diffusion and rotation of Pt NPs during coalescence in H_2 than in vacuum environment. This is due to the Pt-H interactions that weaken the adhesion of Pt NPs on MoS_2. In contrast, Au@Pt NPs display better stability than Pt in H_2, especially for the smaller size Au@Pt NPs. This is attributed to H_2 adsorption promotes the alloying effect on smaller Au@Pt NPs and results in reduced Pt-H interaction and increase of Pt in contact with MoS_2 that lead to better sintering resistance at elevated temperatures.

4.2 Experimental Section

Chemicals. MoS_2 powder (<2 μm, 99%, Sigma-Aldrich), gold chloride $AuCl_3$ (>99.99%, Sigma-Aldrich) and potassium tetrachloroplatinate K_2PtCl_4 (>99.9%, Sigma-Aldrich) were used as received.

MoS_2 synthesis and exfoliation. Bulk MoS_2 powder was mixed with isopropyl alcohol (IPA) at a

87

concentration of 20 mg/mL. The mixture was first sonicated for 5 h in a bath sonicator (Branson 3800, 40kHz, 110W), and then centrifuged at 2000 rpm for 30 min (Thermo Scientific, Legend Micro 21). The obtained supernatant was collected and centrifuged at 1500 rpm for 15 min. After that the sediment was taken out, washed twice with DI water and re-dispersed in fresh DI water before further characterization.

Deposition of Pt and Au@Pt core-shell NPs on MoS$_2$. Synthesis of Pt NPs on MoS$_2$ is based on the method reported elsewhere[123]. In brief, 20 mM K$_2$PtCl$_4$ was added into MoS$_2$ dispersion, followed by a 10 min UV irritation under an UV lamp (Blak-Ray B-100AP) at full intensity. The obtained MoS$_2$ with Pt was then sonicated for 5 min, centrifuged at 5000 rpm for 10 min, and washed with DI water three times before characterization.

Au@Pt core-shell NPs on MoS$_2$ is based on a two-step seed growth method. 10 μL of 20 mM AuCl$_3$ aqueous solution was added into exfoliated MoS$_2$ dispersion with mild shaking. A galvanic displacement reaction happens resulting in the spontaneously reduction of Au ions to Au seed deposited on MoS$_2$.[1] The obtained solution containing MoS$_2$ with Au seeds was centrifuged and washed with DI water two times before re-disperse in 4 mL DI water. 20 mM K$_2$PtCl$_4$ with 1:1 molar ratio of AuCl$_3$ was then added, followed by UV irradiation for 10 min at full intensity. After 5 min sonication, the resulting solution was centrifuged and washed with DI water three times before any further characterization. Although these methods are ligand-free processes, it is worth mentioning that synthesis conditions may result in different NPs stability, therefore systemic studies are helpful to further elaborate this.

***In situ* gas flow TEM experiment.** A gas-cell TEM holder with pair of silicon microchips (Hummingbird Scientific) was used (Figure 4-4a-c). Each of the microchips has an electron transparent silicon nitride (Si_3N_4) viewing window with 50 nm in thickness and 200×50 μm^2 in dimension. Spacers with 250 nm thickness on one microchip are used to control the top and bottom distance in gas reactor. One droplet containing 1 µL liquid sample dispersion was added on one of the microchips with heater and dried under air. The viewing windows were aligned in parallel to provide a maximized viewing area. For *in situ* heating in vacuum without any gas, the window on small microchip was removed to leave a hole, and then paired with large microchip with sample on that. The gas channels on *in situ* gas holder were blocked to allow the sample stay in vacuum condition. For *in situ* heating in gas environments, 100% pure N_2, H_2 and air (containing ~21 vol. % O_2) flow was introduced through gas channels with constant volumetric flow rate of 0.5 sccm. The pressure inside the cell is approximately 1 atmosphere. Local temperature at the sample area is controlled and monitored in real-time. Figure 4-4d shows the temperature profile for each *in situ* experiment. After loading the holder and flowing gas at RT for 30 min, the temperature was first ramped to 100 °C, followed by a 25°C increase every 5 min. After reaching 400 °C for 5 min the temperature was ramped down back to RT. Images were taken at RT, 100, 150, 200, 250, 300, 350, 400 °C and back to RT, as indicated by red dots in Figure 4-4d. The electron beam was kept blocked except during initial TEM alignment, focusing and image acquisition. Acquisition time for each image was kept within 3s for each imaging period to minimize electron beam effects. All *in situ* experimental parameters were kept consistent except the sample ambience, and were carried out using a field emission JEOL 2100F microscope operated at 200kV. Filtered HRTEM images were obtained by

89

applying band-pass filter in DigitalMicrograph software.

Electron microscopy characterization. The morphology of *in situ* microchips were characterized by a variable pressure SEM Hitachi S-3000N operated at 5 kV. For STEM and EELS characterization, deposited Pt and Au@Pt core-shell NPs on MoS_2 were drop casted on lacy copper grid. *Post situ* sample on microchips were characterized using a self-designed (S)TEM specimen holder (patent pending). STEM images were acquired by a spherical aberration corrected JEOL JEM-ARM 200CF with a cold field emission source operating at 200 kV, at 22 mrad convergence semi-angle. False-color STEM images were obtained by ImageJ.[135] Energy dispersive spectrometer (EDS) spectra were acquired with Oxford X-Max 100TLE windowless silicon drift detector. TrueMap was used for all EDS signal collection to correct the overlapping of Mo, S, Au and Pt signals. Electron energy loss spectra were acquired using a Gatan GIF Quantum spectrometer with an entrance aperture of 5 mm in dual-EELS mode. EELS maps were extracted from Mo $L_{2,3}$ edges, S K edge, Au and Pt $M_{4,5}$ edges using power law fitting background subtraction after energy drift correction and Fourier-ratio deconvolution.

Density functional theory calculations. The DFT calculations are performed using the Vienna *ab initio* simulation package[200-203] with the Perdew-Burke-Ernzerhof (PBE)[204] and projector-augmented wave potentials using a cutoff energy of 400 eV. Dispersion interactions are included using DFT-D2.[205] We also compared the results using Tkatchenko-Scheffler (TS) dispersion.[206, 207] The calculations are carried out using a 7x7 surface supercell for MoS_2 where the Brillouin zone is sampled at the gamma point. The structural optimization is terminated when all force components are less than 0.01

90

eV/Å. The MoS_2/Pt_{20} structure is obtained from our previous study.[123]

4.3 Results and discussion

Before *in situ* experiments, the morphology of synthesized Pt and Au@Pt core-shell NPs on MoS_2 were characterized by atomic resolution scanning transmission electron microscopy (STEM).Figure 4-1a shows false-color high-angle annular dark-field (HAADF) image of pristine MoS_2 nanoflake before metal NPs deposition. The nanoflake is in 2H phase on <001> zone axis with (001) basal plane perpendicular to electron beam. HAADF image in Figure 4-1b shows the Pt NPs grown on MoS_2 support, with epitaxial relationship of $(110)_{Pt}$ parallel to $(001)_{MoS2}$ basal plane. Figure 4-1c shows a lower magnification HAADF image including several Au@Pt NPs. Atomic resolution Au@Pt core-shell NP is shown in Figure 4-1d with fivefold twining on <110> zone axis, suggesting the same epitaxial relationship as Pt. Since the Z (atomic number) contrast difference between Au and Pt in HAADF image is not obvious to differentiate, energy-dispersive X-ray spectroscopy (EDS) and electron energy-loss spectroscopy (EELS) were performed to further determine the elemental distribution. Different from EDS mapping for pristine Pt (Figure 4-2a), mapping for Au@Pt shown in Figure 4-1e indicates an Au core and Pt outer layer. EDS line scan profile in Figure 4-2b and c shows another example of an Au@Pt NP. Similar to EDS, EELS mapping in Figure 4-1f suggests a core-shell structure for Au@Pt by extracting Au and Pt $M_{4,5}$ edges from the core-loss region. Detailed EELS maps including Mo $L_{2,3}$ and S K edge as well as spectra collected at Au core and Pt shell regions are included in Figure 4-3.

91
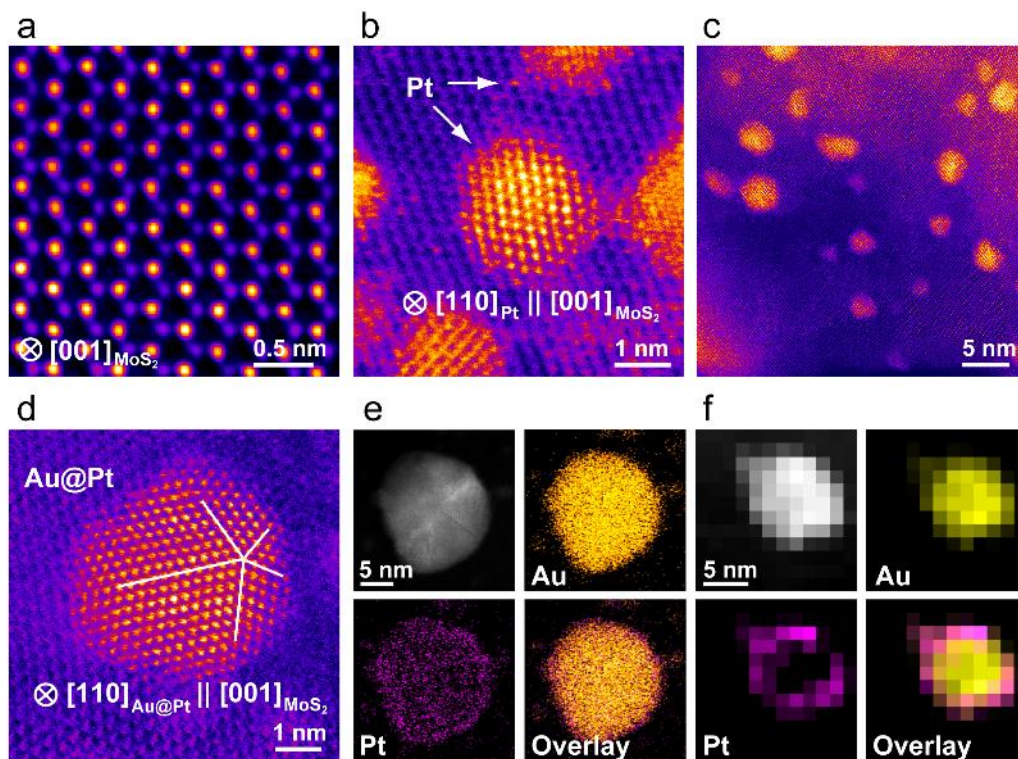
Figure 4-1. Atomic structure and chemical characterization of Pt and Au@Pt core-shell nanoparticles on MoS$_2$ support. False-color atomic HAADF images showing (**a**) MoS$_2$ (**b**) Pt and (**c, d**) Au@Pt core-shell NPs on MoS$_2$ support. The EDS (**e**) and EELS (**f**) mappings of Au, Pt, and the overlaid map. The yellow and magenta colors correspond to Au and Pt, respectively.
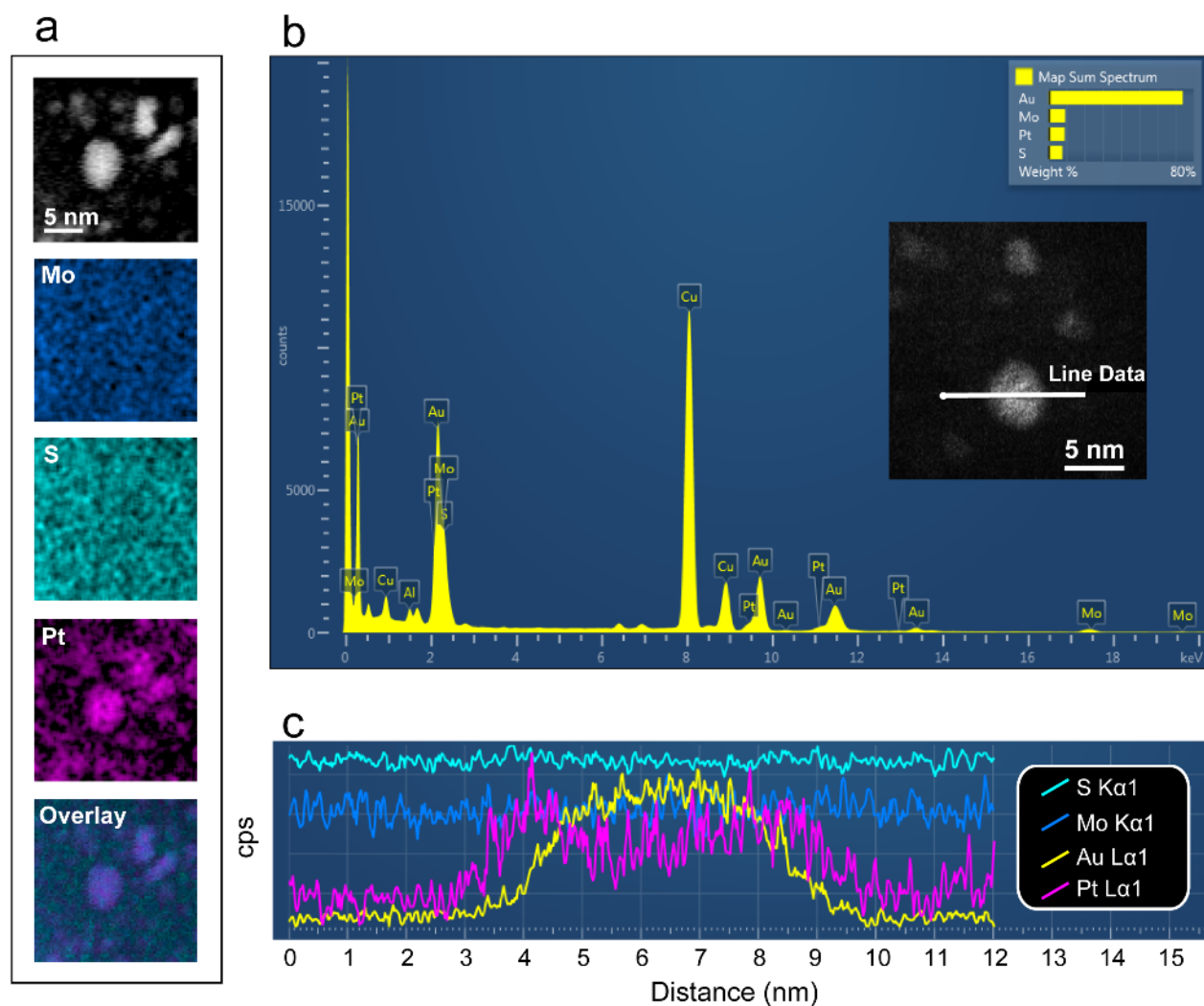
Figure 4-2. Energy-dispersive X-ray spectroscopy (EDS) profiles for Pt and Au@Pt on MoS$_2$ support. (**a**) EDS mapping of Pt NPs on MoS$_2$, showing the Mo, S, Pt and overlaid maps. (**b**) EDS spectrum over an Au@Pt NP. Inset shows the corresponding high-angle annular dark-field (HAADF) image. (**c**) EDS line scan profile with respect to **b**. Mo, S, Au and Pt are shown in blue, cyan, yellow, and magenta, respectively.
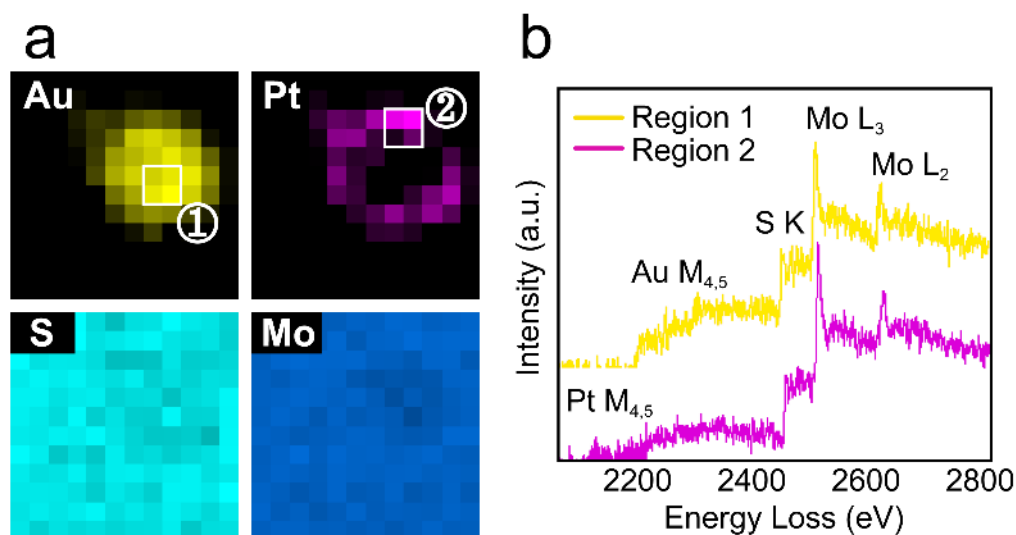
Figure 4-3. (**a**) Electron energy-loss spectroscopy (EELS) mappings of Au, Pt, Mo and S from Au@Pt NP as shown in Figure 1f in main text. (**b**) Core-loss EEL spectra extracted from boxed region 1 (core) and 2 (shell) corresponding to **a**. Mo $L_{2,3}$ edges, S K edge, Au and Pt $M_{4,5}$ edges are marked on the spectra.

For *in situ* environmental gas-cell TEM experiment, a schematic illustration of specimen holder is shown in Figure 4-4a. The isolated environment formed by a pair of microchips allows continuous gas flow at atmospheric pressure inside the cell.[42, 177, 190] The obtained Pt and Au@Pt NPs on MoS_2 were loaded onto one microchip with a heater layer, as shown in scanning electron microscopy (SEM) image in Figure 4-4b. A representative MoS_2 nanoflake is marked by an arrow in higher magnification SEM image (Figure 4-4c). The temperature profile for each *in situ* experiment is shown in Figure 4-4d, with red dots representing the time when images were acquired. It is worth noting that resolution degradation due to window bulging effect for gas-cell TEM is much less than liquid-cell TEM since gases usually have density three orders of magnitude lower than general solutions used for liquid-cell TEM.[42] However,

94

samples located close to the corner and edge of Si_3N_4 window are preferentially selected for imaging to reduce multiple electron scattering and thus ensure a maximized imaging resolution.
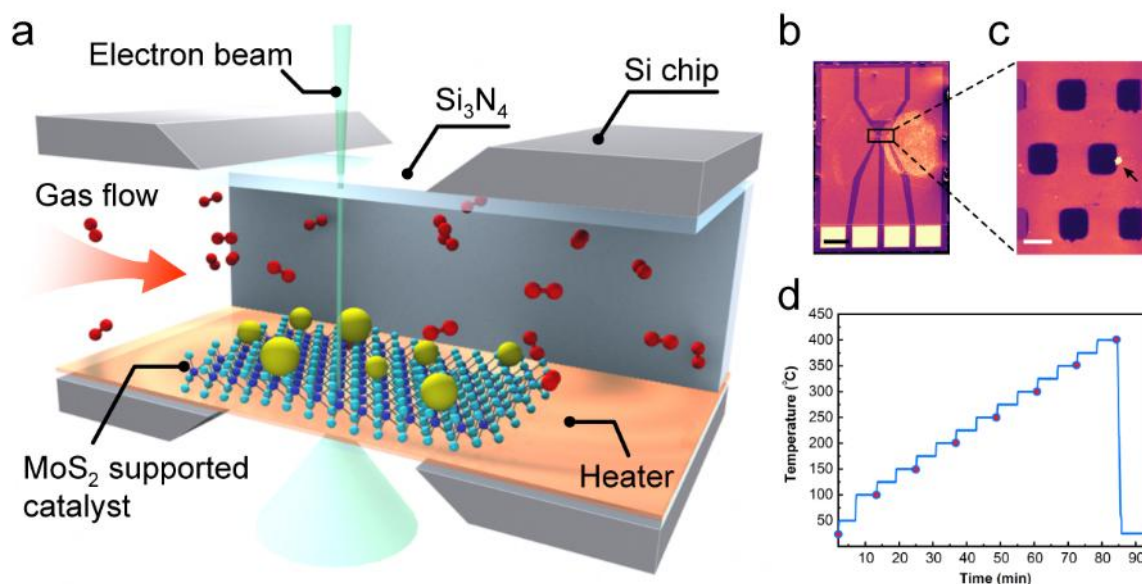
Figure 4-4. *In situ* gas-cell TEM system, microfabricated gas-cell devices and temperature profile. (**a**) Schematic of *in situ* gas-cell TEM to study catalytic reactions. (**b**) SEM image of the microchip with drop-casted sample on it. Scale bar is 0.5 mm. (**c**) Higher magnification SEM image focusing on the Si_3N_4 window area in **b**. The heater area is shown as brighter contrast region. Arrow points to a representative MoS_2 nanoflake with NPs on it. Scale bar is 5 μm. (**d**) Temperature profile for each *in situ* experiment. Red dots represent the time at which image was acquired (more information in Methods).

4.3.1 The effect of environment on nanoparticle degradation

The *in situ* TEM experiments were performed to investigate the effect of environment on nanoparticle-decorated 2D substrates. Firstly, the sintering behavior of Pt in vacuum during heating to 400 °C was investigated and shown in the TEM image sequences as Figure 4-5a. Regions marked with rectangle box

95

highlight exemplar areas where particle sintering happens. The coalescence of some Pt NPs can be seen gradually as temperature rise to 400 °C. When the environment changed to H_2 as shown in Figure 4-5b, the coalescence of Pt NPs is more obvious compare to heating in vacuum.

Next, for Au@Pt NPs on MoS_2, Figure 4-5c depicts the morphological evolution during heating in vacuum. Coalescence is seen to happen clearly at exemplar regions marked with boxes. When heating in H_2 environment (Figure 4-5d), in contrast, fewer evidences of coalescence of Au@Pt NPs were observed. The statistical variation of nanoparticle coalescence in different evaluated system is explained below.

TEM images were collected from repeated experiments to extract statistical information regarding to particle size distribution (PSD), shown as violin plots for Pt in vacuum and H_2 (Figure 4-5e and f) and Au@Pt in vacuum and H_2 (Figure 4-5g and h) at temperatures of RT, 100, 200, 300 and 400 °C. The hollow circle indicates the mean particle size in each distribution. In these violin plots, the vertical distribution shows the size range of nanoparticle, while the horizontal distribution indicates the frequency (or density) of the observed nanoparticles at any particular size.

Both Pt and Au@Pt NPs have narrowed size distribution with a mean particle size of around 4 nm at RT. For Pt NPs heating in vacuum (Figure 4-5e), as temperature increases broadening and a more lognormal-like PSD can be observed accompanied by the increase of mean particle size. It is known that particle sintering is mainly guided by two mechanisms: PMC and Ostwald ripening.[50] It has been reported that the enlargement of extended long tail in larger particle size region serves as direct evidence that sintering process is guided more through PMC than Ostwald ripening,[167, 208] which is similar as what are shown here for Pt NPs heating in vacuum (Figure 4-5e). For Pt NPs heated in H_2 (Figure 4-5f),

the PSD has more extended lognormal-like tail and larger mean particle size than in vacuum, suggesting the same PMC mechanism but more significant sintering.

For Au@Pt NPs in vacuum (Figure 4-5g), the broadening of PSD and extended tail indicate the PMC mechanism leading to sintering process. In contrast, Au@Pt NPs in H_2 (Figure 4-5h) show a much less broadening of PSD and smaller extended tail compare to in vacuum, suggesting much less sintering.

One should note that the MoS_2 substrate did not show evidence of degradation when exposed to temperatures up to 400 °C in vacuum, N_2, and H_2 environments. Figure 4-6 show the selected area electron diffraction (SAED) patterns for Pt (Figure 4-6a) and Au@Pt (Figure 4-6b) on MoS_2 collected at RT, and after heating and cooling to RT in H_2, respectively. Diffraction spots from $\{100\}_{MoS2}$ (marked with hexagonal lines) and $\{110\}_{MoS2}$ remain unchanged in both experiments suggesting a stable MoS_2 under H_2 environment. No significant difference between diffraction rings from $\{111\}$, $\{200\}$ and $\{220\}$ before and after heating for both Pt and Au@Pt (marked with half circles). *In situ* heating in air flow containing 21 vol. % O_2 was also investigated but severe structural degradation of MoS_2 support was observed, as shown in TEM and SAED patterns in Figure 1-13. The reaction between O plasma/O_2 molecule and MoS_2 may explain the structural degradation of MoS_2.[209] Therefore, air flow experiments were not involved in comparison of NPs sintering behaviors due to support degradation.
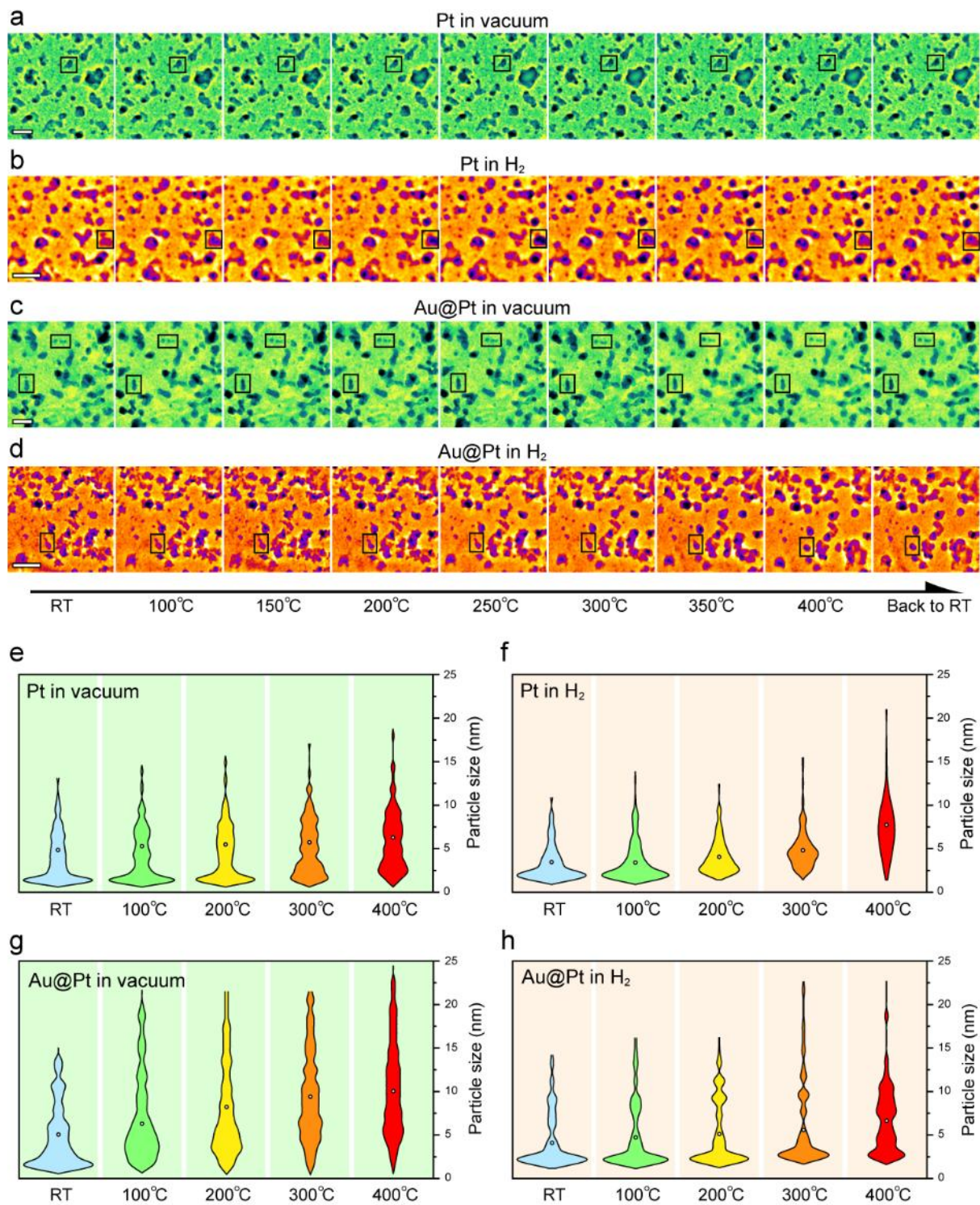
Figure 4-5. Morphological and statistical analysis of Pt and Au@Pt NPs on MoS$_2$ during heating from RT to 400 °C in vacuum and H$_2$. (**a, b**) TEM image sequences of Pt on MoS$_2$ during heating to 400 °C in

98

vacuum and H_2. (**c, d**) TEM image sequences of Au@Pt on MoS_2 during heating to 400 °C in vacuum and H_2. Scale bar is 20 nm for all images. (**e, f**) Violin plots of particle size distribution of Pt NPs during heating in vacuum and H_2. (**g, h**) Violin plots of particle size distribution of Au@Pt NPs during heating in vacuum and H_2. Hollow circles mark the mean particle size in each distribution.
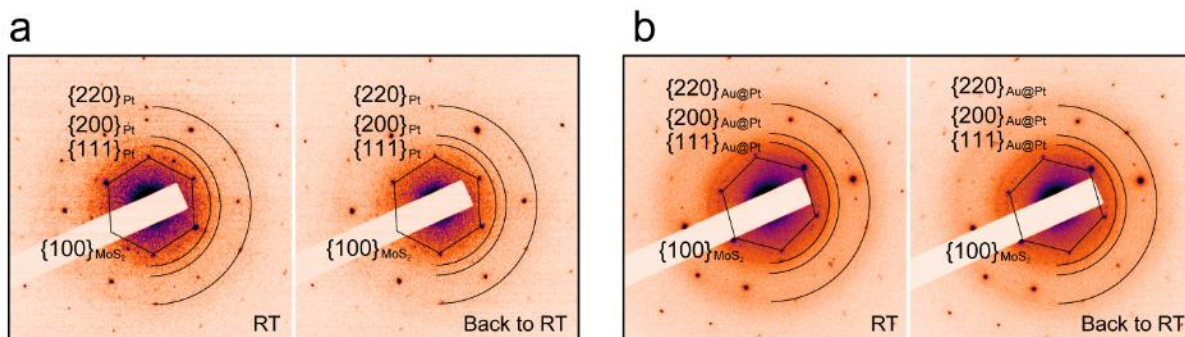
Figure 4-6. Selected area electron diffraction (SAED) patterns at RT, and after annealing in hydrogen (H_2) and cooling down to RT for Pt (**a**) and Au@Pt (**b**) on MoS_2. Diffraction spots from $\{100\}_{MoS2}$ are marked with hexagonal lines. Diffraction rings from metal are marked with half circles.

4.3.2 The effect of composition on nanoparticle degradation

Here, the comparison is focused on the differences between Pt and core-shell Au@Pt NPs behavior under the same environment. For heating in vacuum, the PSD of Au@Pt NPs (Figure 4-5g) broadening and formation of extended long tail happens at relatively lower temperature compare to Pt (Figure 4-5e), suggesting a more obvious sintering process. In contrast, in H_2 environment the Au@Pt NPs (Figure 4-5h) display slightly more sintering resistance than Pt (Figure 4-5f) as the smaller mean particle size.

To further understand such effect of composition, HRTEM imaging was performed *in situ* at each temperature focusing on individual NPs. For heating in vacuum, Pt and Au@Pt are shown in Figure 4-7a and b, respectively. Evidence of diffusion of Pt NPs (Figure 4-7a) can be seen from the shape change of NP #2 and decrease of its distance to NP #1, but without obvious coalescence. This is consistent with the PSD profile that Pt sintering in vacuum is less significant compare to that in H_2. Au@Pt NPs (Figure 4-7b), however, diffuse and coalesce at relatively lower temperature (less than 200 °C) and both small and large NPs have tendency to diffuse on MoS_2 support, as indicated by five NPs numbered 2, 3, 4, 5, 6 coalesced into one from RT to 200 °C. There is not much further morphological change at higher temperatures. These observations are again consistent with the Au@Pt PSD profile containing an extended long tail of larger NPs that indicate PMC. In addition, HRTEMs in Figure 4-8 depict the sintering behaviors of Pt and Au@Pt NPs in atmospheric N_2 gas. Very similar as the condition of annealing in vacuum, in Figure 4-8a smaller Pt NPs (outlines close to particle #1) display migration and coalescence but the overall sintering is less aggressive compare to the condition that in H_2 gas. The behavior of Au@Pt NPs (Figure 4-8b) is also similar as annealing in vacuum that obvious migration and coalescence of smaller NPs can be seen from RT to 200 °C (particle #2 and #3, particle #4 and #5). Since N-N bond is very hard to break, the interactions of N_2 on Pt and Au@Pt NPs are almost negligible compare to H_2 gas. Therefore, there is no anticipated difference in sintering behaviors between annealing in vacuum and in N_2 gas. The consistency of NPs behaviors shown in vacuum and N_2 gas further confirms that N_2 does not induce extra effect on Pt and Au@Pt NPs sintering mechanism.
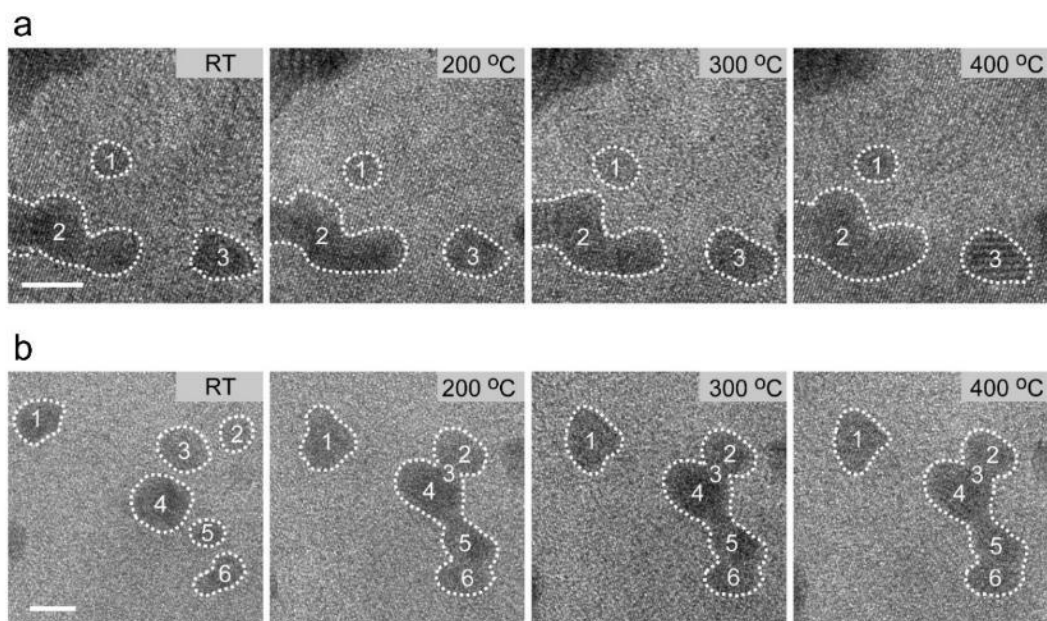
Figure 4-7. Pt and Au@Pt NPs annealing in vacuum condition. (**a**) High-resolution TEM (HRTEM) images of Pt NPs sintering from RT to 400 °C. (**b**) HRTEM images of Au@Pt NPs sintering from RT to 400 °C. Scale bars are 5 nm. Exemplar NPs are outlined and marked with numbers for ease of discussion.
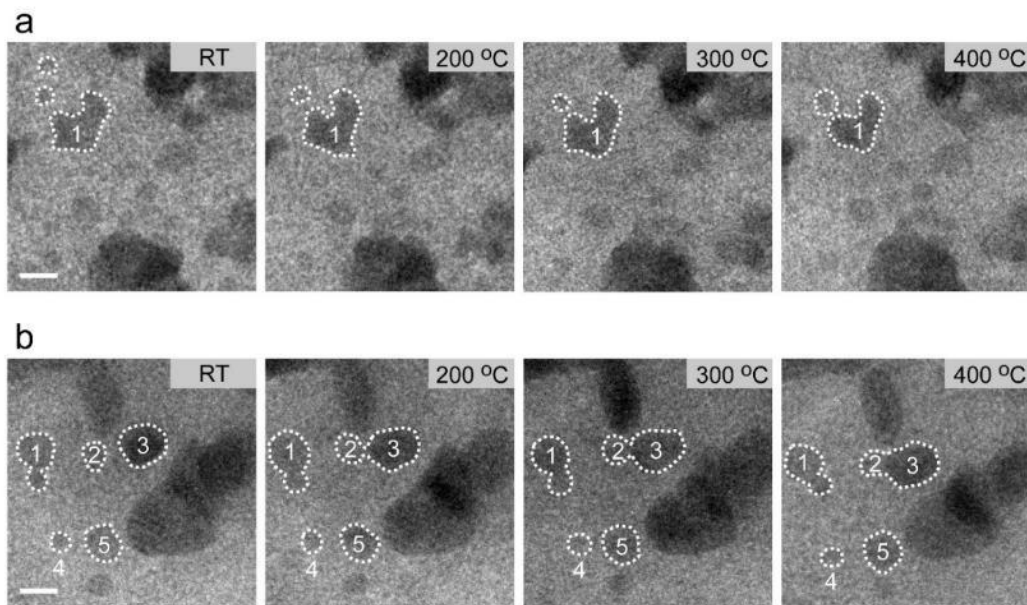
Figure 4-8. Pt and Au@Pt NPs annealing in nitrogen (N$_2$) gas. (**a**) HRTEM images of Pt NPs sintering

from RT to 400 °C. (**b**) HRTEM images of Au@Pt NPs sintering from RT to 400 °C. Scale bars are 5 nm. Exemplar NPs are outlined and marked with numbers for ease of discussion.

For the case of heating in H_2 environment, example of Pt NPs sintering under H_2 (Figure 4-9) clearly depicts the PMC process. In the HRTEM image series (Figure 4-9a) the orientation of three similar size Pt NPs can be resolved (identified as 1, 2, and 3). Particle 2 undergoes partial coalescence with Particle 3 at 250 °C, followed by second coalescence with Particle 1 at 400 °C, as indicated by the outlines in frames #1, 5 and 8. The dot on each particle represents the location of the center of mass and its diameter is proportional to the particle size. Figure 4-9b shows the fast Fourier transform (FFT) patterns at region of particles 1, 2, 3 in frames #1, 5 and 8. The white hexagons indicate diffraction spots from six $<100>_{MoS2}$ directions and also confirms that $(001)_{MoS2}$ basal plane is perpendicular to the viewing direction. These unchanged $\{001\}_{MoS2}$ patterns again suggest the support is stable in the selected temperature range. In each FFT, diffraction spots from $(111)_{Pt}$ and $(200)_{Pt}$ are highlighted by green and yellow circles to analyze the orientation relation with MoS_2 basal plane. It was found that the migration of Pt NPs also involves particle rotation evidenced through the change of $[111]_{Pt}$ and $[200]_{Pt}$ directions. For instance, [200] direction of Particle 1 remains unchanged from RT (frame #1) to 250 °C (frame #5), while at 400 °C (frame #8) this (200) plane disappeared after coalescence with particle 2 and 3, accompanied by formation of new (111) planes. Similarly, particles 2 and 3 both undergo complex rotations and reconstructions involving the change of [111] and [200] directions during coalescence. It is interesting to note that the misalignment angle between $[111]_{Pt}$ and one $[100]_{MoS2}$ direction can change dramatically during particle

102

coalescence, marked as 3°, 27°, 20°, 13° for Particle 2 at RT (frame #1), the right portion of Particle 2 and

3 at 250 °C (frame #5), and the left and right portion of Particle 1, 2 and 3 at 400 °C after coalescence

(frame #8). In addition, the irregular angles between certain [111] and [200] directions indicate the

formation of twining in all coalesced Pt particles. The PMC processes are further shown in Figure 4-9c by

the center of mass evolution of each particle, with the spot diameter proportional to particle size. In

comparison with sintering behavior of Pt NPs in vacuum environment, H_2 is promoting the diffusion and

coalescence by increasing the NPs migration distance. Again, these observations are consistent with the

PSD profile containing an extended long tail of larger NPs that indicates PMC. Although direct evidence

of Ostwald ripening that Pt adatom migrating from small particle towards large particle is beyond

observation capability, it is still more plausible that the Pt sintering under atmospheric pressure H_2 is

guided by PMC because 1) Ostwald ripening usually involves both particle growth and shrinking and 2)

does not induce obvious migration.[185] The slight size increase of each Pt before coalescence suggests

Ostwald ripening may also happen by sacrificing tiny NPs but is less significant.
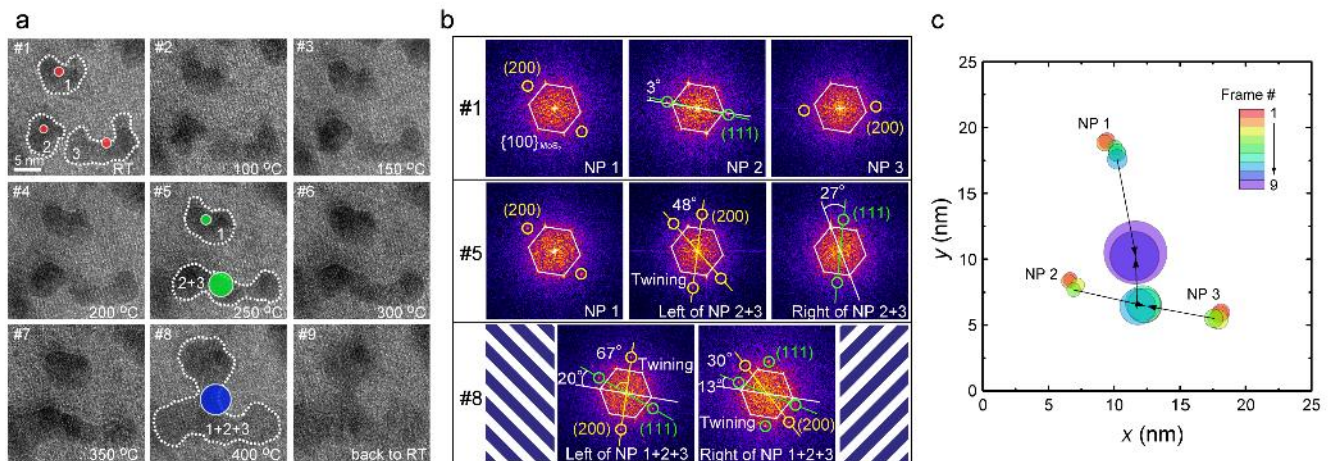
Figure 4-9. HRTEM of Pt NPs crystallinity evolution during sintering. (**a**) HRTEM image sequences of

103

Pt NPs sintering on MoS$_2$ under H$_2$ from RT to 400 °C. Three NPs are identified with dashed outlines and marked as 1, 2, and 3. (**b**) FFT of Pt NPs 1, 2 and 3 in frames #1, #5 and #8 in **a**. Diffraction spots from {100}$_{MoS2}$, (111)$_{Pt}$ and (200)$_{Pt}$ are shown in white, green and yellow, respectively. (**c**) Center of mass evolution of the Pt NPs corresponding to **a**. Arrows indicate the coalescence process.

For the sintering behavior of Au@Pt in H$_2$, it is important to take the size effect into consideration when compare to Pt NPs in H$_2$. Therefore, the discussion will be fully expanded in the subsequent section.

4.3.3 The effect of particle size on nanoparticle degradation

In Figure 4-5f, the PSD of Pt NPs in H$_2$ indicates a gradual loss of smaller Pt NPs at higher temperature. However, it is interesting to note that the PSD for Au@Pt in H$_2$ (Figure 4-5h) shows a heavier density of small particle (< 5 nm) even at 400 °C, resulting in a less symmetric distribution compare to other conditions. This indicates the less loss of smaller Au@Pt NPs in H$_2$ environment.

To fully understand the particle size effect, HRTEM was performed *in situ* on small and larger NPs for both Pt and Au@Pt. For the case of Pt heating in H$_2$, Figure 4-10a shows the evolution of a larger (> 10 nm) Pt NP in the center and several surrounding smaller (<5 nm) NPs during heating. At room temperature, six particles with ~2 nm in diameter are clearly distinguishable around the central Pt particle. As temperature rises, these smaller particles gradually diffuse closer to the central one and merge together. At temperatures above 300 °C all the smaller particles have disappeared. By masking the spots from FFT for each HRTEM, the outline of particles (Figure 4-10b) corresponding to each frame in Figure 4-10a

104

better illustrates the sintering process that involves migration of smaller particles towards central larger particle as well as coalescence when they come in contact. The Pt (200) plane in the central particle is identifiable and can be used to determine crystal domains (pink regions). Contrast between two (200) domains (blue stripes) suggests the necking region. During the coalescence of smaller particles, (200) domains in the central particle slightly enlarged but maintained a fixed direction, suggesting it is relatively more stable than the smaller surrounding Pt particles. These results suggest that smaller Pt NPs are less stable than larger Pt NPs in H_2.
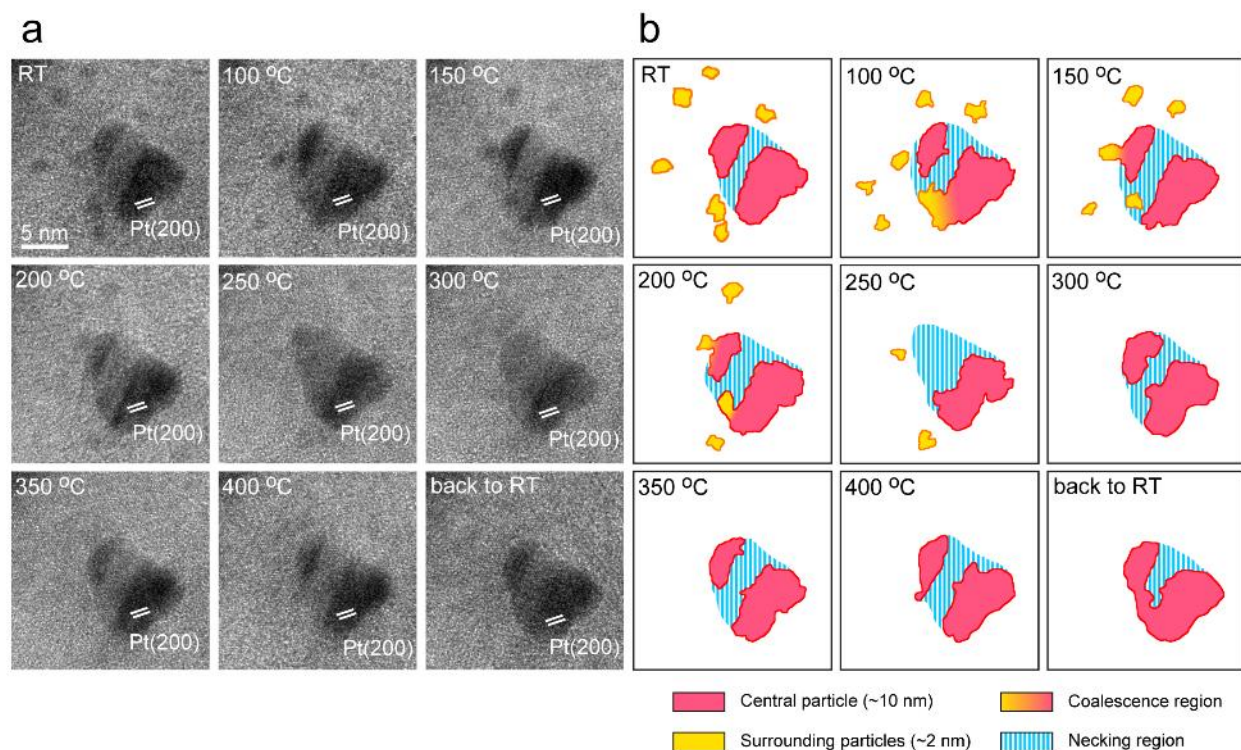
Figure 4-10. HRTEM of Pt NPs sintering with different sizes. (**a**) HRTEM image sequences of Pt NPs on MoS_2 under H_2 from RT to 400 °C. (**b**) Outline of the projected area of Pt NPs corresponding to **a.**

For Au@Pt core-shell NPs in H_2, the sintering behavior is presented in Figure 4-11. The TEM image

series in Figure 4-11a show a relatively larger Au@Pt in 10 nm size during heating, with the center of

mass marked by hollow circles. From RT to 300 °C there is slight surface reconstruction induced particle

shape change, but the migration of the NP is not apparent. When the temperature is above 300 °C,

migration becomes obvious with a clearer change in the center-of-mass location. The particle became

faceted with formation of more distinct corner and edges outlined in the last four frames. By comparing

one of the diagonals, a 69° rotation from 350 °C to 400 °C can be observed, suggesting the migration is

accompanied by particle rotation as well. Similar to Pt on MoS_2, such dynamics happen on Au@Pt NPs

could be the main reason of particle coalescence and size increase. However, in contrast to larger Au@Pt,

the smaller size Au@Pt NPs behave differently as shown in HRTEM image series in Figure 4-11b. The

two outlined particles in size of ~3 nm display no obvious migration from RT to 400 °C. Filtered HRTEM

images in Figure 4-11c give a clearer view of the lattice of $(111)_{Au@Pt}$ in the larger particle, and the distance

between two particles remains 4 nm, indicating the absence of both rotation and migration. FFTs

corresponding to Figure 4-11b shown in Figure 4-11d indicate that there is no change in the misalignment

angle between $[111]_{Au@Pt}$ and one of the $[100]_{MoS2}$ direction, again confirming that such small Au@Pt NP

has no rotation during the whole heating process. This significantly diminished diffusion and coalescence

of small size Au@Pt NPs is consistent with the PSD that heavier density of smaller particles is present at

higher temperatures. In addition, the smaller size Au@Pt display even better stability compare to similar

size Pt NPs, again consistent with the PSD profile in Figure 4-5.
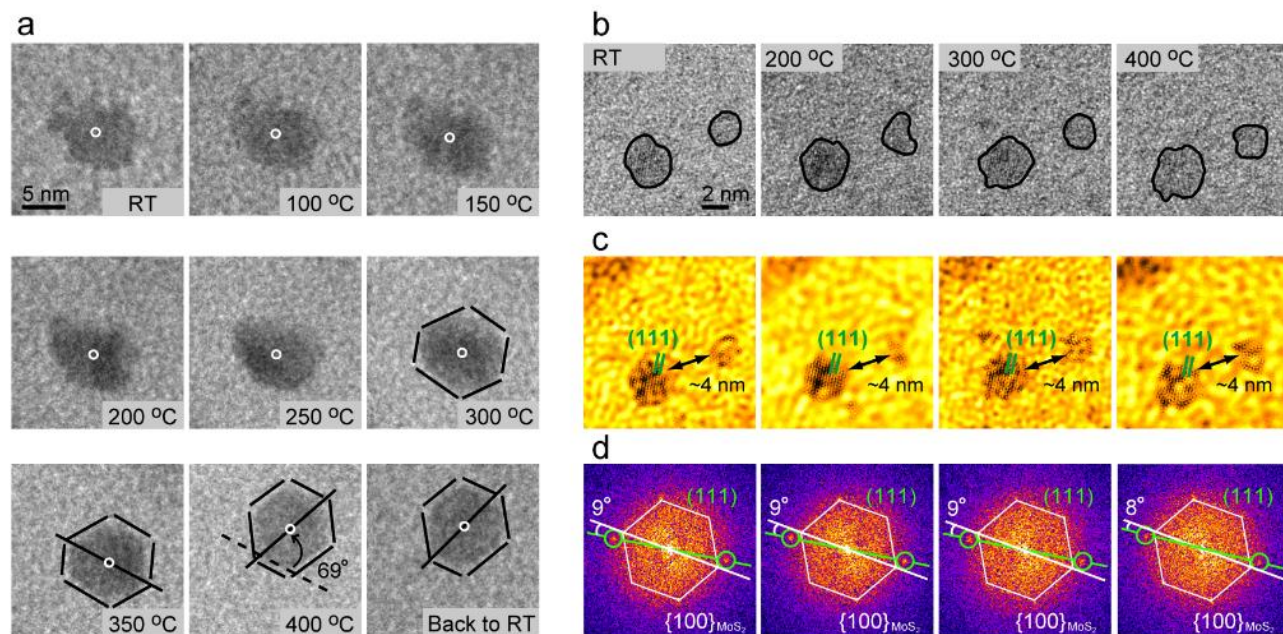
Figure 4-11. TEM and HRTEM analysis of Au@Pt NPs on MoS$_2$ during heating in H$_2$. (**a**) TEM image sequence of a 10 nm Au@Pt NP on MoS$_2$ in H$_2$. Black lines outline the NP boundary and hollow circles mark the location of center of mass. (**b**) HRTEM image sequence of several smaller Au@Pt NPs ($\leq$ 5 nm) on MoS$_2$ in H$_2$. Two exemplar Au@Pt NPs are outlined with black lines. (**c**) Filtered images corresponding to **b**. (111)$_{Au@Pt}$ is marked in green and distance between two NPs marked with arrows (**d**) FFT of TEM image sequence in **b**. Diffraction spots from {100}$_{MoS2}$ and (111)$_{Au@Pt}$ are shown in white and green.

To fully understand the particle size effect, analytical EDS and EELS characterization on *post situ* Au@Pt samples was carried out on smaller and larger Au@Pt NPs on MoS$_2$. Figure 4-12 shows EELS mappings of Au@Pt NPs after heating in vacuum. It can be seen that both smaller (Figure 4-12a) and larger (Figure 4-12b) NPs maintain the core-shell structure after heating, suggesting no significant NPs structural change when there is no H$_2$ gas. In sharp contrast, EDS mappings in Figure 4-14a-b and EELS

107

mappings in Figure 4-13 show that larger NPs maintained roughly core-shell structure after heating in H_2, while these mappings do not seem to reveal a clear core-shell structure for smaller Au@Pt NPs (mostly less than 5 nm). Therefore, it is suggested that these smaller Au@Pt NPs underwent a core-shell to alloy transformation. Based on DFT calculations, the processes of swapping Pt and Au atoms close to the edges of NPs are feasible with low energy barriers of ~ 0.2 eV (Figure 4-15). The observation suggests that smaller Au@Pt NPs are more likely to be alloyed than larger ones in H_2 at elevated temperatures due to shorter diffusion distance of surface Pt toward the core and bottom Au toward the interior of NPs, and H_2 is essentially playing a vital role in promoting the small NPs alloy formation.
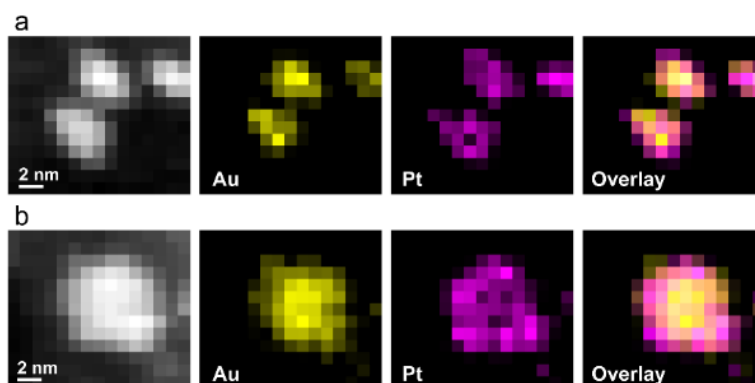
Figure 4-12. *Post situ* EELS mappings of Au@Pt NPs after annealing in vacuum in (**a**) small and (**b**) large size.
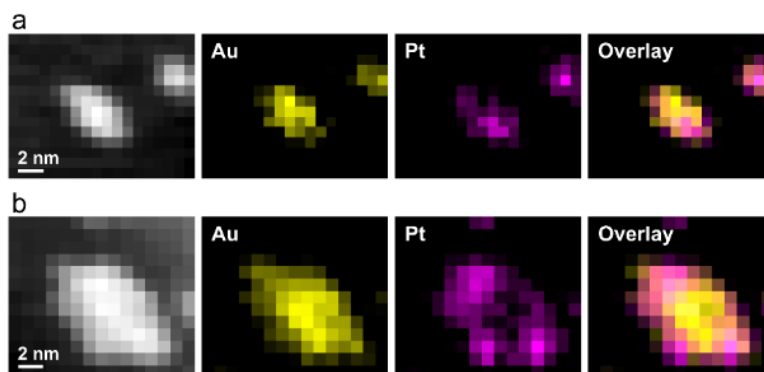
Figure 4-13. *Post situ* EELS mappings of Au@Pt NPs after annealing in H_2 in (**a**) small and (**b**) large size.
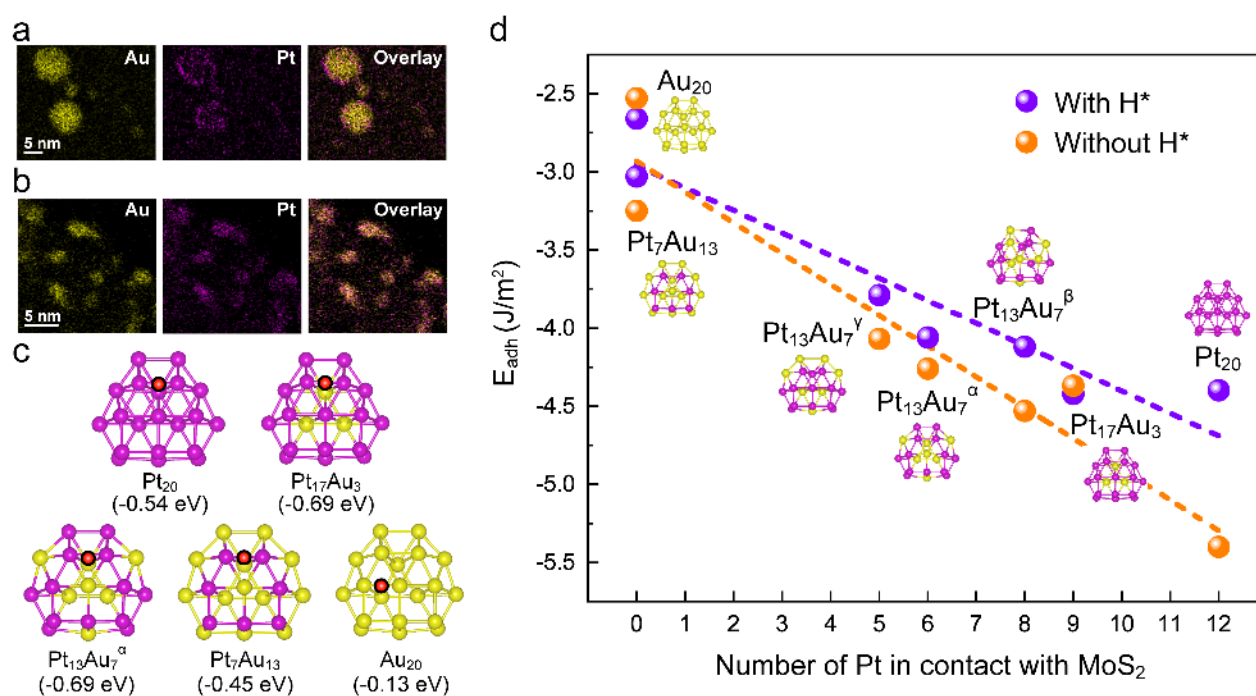
Figure 4-14. (**a**, **b**) *Post situ* EDS analysis on Au@Pt NPs after heating in H_2 in large and small sizes, respectively. (**c**) The MoS_2 supported 20-atom NPs models with different Au/Pt ratios. The strongest H adsorption sites for each structure are indicated by red dots. The ΔG_H of the adsorption sites are listed in parenthesis. (**d**) Adhesion energies of the NPs as function of number of Pt in contact with MoS_2 support. The trends are shown as purple and orange lines for the NPs with and without H^*, respectively.
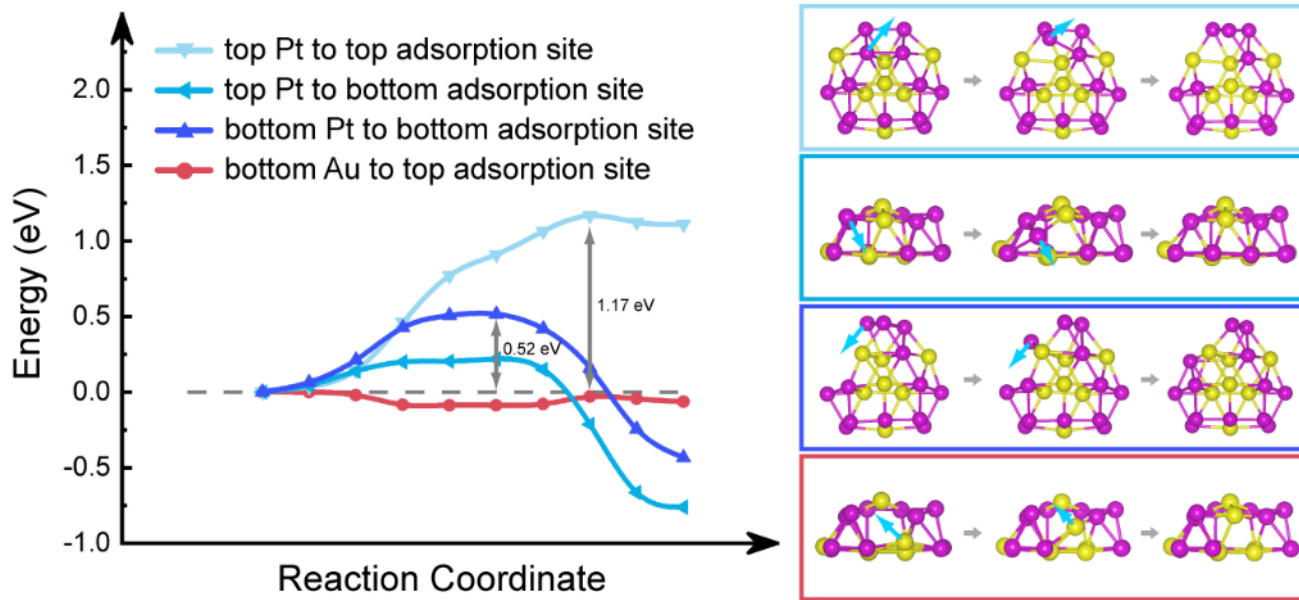
Figure 4-15. The reaction pathways of the diffusion of atoms close to the Au@Pt edge. The reaction details are shown in the corresponding-colored boxes.

To help better understand the effect of H$_2$, composition and size in sintering behaviors of Pt and Au@Pt core-shell NPs on MoS$_2$, DFT calculations were performed to analyze H$_2$ dissociation, H$_2$ → H* + H*, on Pt, Au and Au@Pt NPs surfaces and their effects on NPs stability. The thermodynamic accessibility of H$_2$ dissociation is studied using the hydrogen chemisorption Gibbs free energy $\varDelta G_{\mathrm{H}}$ defined as,

$$\varDelta G_{\mathrm{H}} = \varDelta E_{\mathrm{ads}} + \varDelta E_{\mathrm{ZPE}} - T\varDelta S,$$

with

$$\Delta E_{\mathrm{ads}} = E_{NP/\mathrm{MoS_2}/n\mathrm{H}} - E_{NP/\mathrm{MoS_2}} - 0.5\mathrm{n}E_{\mathrm{H_2(g)}},$$

where $E_{NP/\mathrm{MoS_2}/\mathrm{H}}$ and $E_{NP/\mathrm{MoS_2}}$ are respectively the total energies of a system with n adsorbed

110

hydrogen atom(s) H^* and with no hydrogen. $E_{H_2(g)}$ is the energy of H_2 molecule in vacuum. The difference in zero-point energy ΔE_{ZPE} between H^* and $H_2(g)$ is approximated to 0.04 eV, which is the value obtained on metal surfaces.[210] At $T = 298$ K, experimental results were used to estimate the entropic contribution $T\Delta S = -0.2$ eV.[210] With a positive ΔG_H, hydrogen in gas phase is more stable than in adsorbed state, and *vice versa* for a negative ΔG_H. Next, models of MoS$_2$ supporting 20-atom NPs were employed to study the single hydrogen atom adsorption events, namely the alloys Au$_i$Pt$_j$ at different atomic ratios of i and j as well as pure Au$_{20}$ and Pt$_{20}$ NPs, as shown in Figure 3-7c. Note that Pt$_{13}$Au$_7$ is investigated under three different configurations as shown in Figure 4-16, named as α, β and γ. The strongest H adsorption site is at the bridge sites between two metal atoms. Comparing these systems, ΔG_H is the most negative for Pt$_{17}$Au$_3$ and Pt$_{13}$Au$_7^{\alpha}$ followed by Pt$_7$Au$_{13}$ and Pt$_{20}$, and is the least negative for Au$_{20}$. Such information implies that the hydrogen dissociation is the most thermodynamically favorable on Pt$_{17}$Au$_3$ and Pt$_{13}$Au$_7^{\alpha}$ and the least for Au$_{20}$. In addition, the reaction pathways of hydrogen dissociation (Figure 4-17) on Pt$_{20}$ and Pt$_{13}$Au$_7^{\alpha}$ NPs are barrierless, which is in accordance with the low ΔG_H of -0.54 and -0.69 eV, respectively. In contrast, a relatively high barrier of 0.42 eV is observed on Au$_{20}$ NP with $\Delta G_H = $ -0.13 eV. The density of states (DOS) of the NPs, as shown in Figure 4-18, explain the hydrogen adsorption events. For Au$_{20}$ with the metallic d-band located far below the Fermi level ($E - E_F = 0$), as indicated by the peak of d-band (E_p), its interaction with H^* is relatively weak compare to Pt$_{20}$ and the alloyed NPs with the d-band located close to the Fermi level. This is explained by the d-band theory; upon hydrogen adsorption, the d-band splits into bonding and anti-bonding states located below or above E_p, respectively, and the filling of the anti-bonding states make the system less stable. For Au$_{20}$ that has a

111

lower E_P, its antibonding states are located more closer to E_F thus are more easily to be occupied comparing to Pt$_{20}$ and alloyed NPs which have higher E_p. This suggests that Au is more inert to H$_2$ dissociation compared to Pt and Au@Pt NPs and therefore provides the evidence that the stabilities of Pt and Au@Pt in hydrogen ambient can be affected by structural change induced by hydrogen adsorption. To shows this more, the stabilities of the NPs on MoS$_2$ support are gauged from the adhesion energy defined as, [121, 122]

$$E_{adh} = (E_{NP/MoS_2} - E_{NP} - E_{MoS_2})/A,$$

where E_{NP/MoS_2}, E_{NP} and E_{MoS_2} are the DFT energies of the MoS$_2$ supported NP, non-supported NP and MoS$_2$, respectively, A is the contact surface area between MoS$_2$ and NPs. The impact of hydrogen adsorption on E_{adh} can also be determined where E_{NP/MoS_2} and E_{NP} represent the DFT energies of the MoS$_2$ supported and non-supported NPs with H*. The hydrogen adsorption configurations are obtained by occupying the strong adsorption sites evaluated by single-hydrogen adsorption events, as we have previously shown that H* $-$ H* repulsions have minimal effects on the hydrogen configurations for surfaces with strong hydrogen interaction.[211] Figure 4-14 and the values in Table 4-1 show the decreasing trend of E_{adh} with the increasing number of Pt in contact with MoS$_2$ surface for the NPs with and without H*. It can be concluded that H* decreases NPs stabilities for most of structures. Furthermore, the temperature effect on NPs' stability is also analyzed by calculating temperature-dependent adhesion energies $E_{adh}(T)$ with and without H*. The temperature-dependent adhesion energies are defined as,

$$E_{adh}(T) = E_{adh} + \Delta F^{vib}(T,V)$$

with

$$F^{vib}(T,V) = E_{vib} - TS_{vib}$$

where the phonon energy E_{vib} and entropy S_{vib} are defined as,

$$E_{vib} = \frac{1}{2}\sum_i h\nu_i + \sum_i \frac{h\nu_i e^{-\frac{h\nu_i}{k_\beta T}}}{1 - e^{-\frac{h\nu_i}{k_\beta T}}}$$

$$S_{vib} = k_\beta \sum_i \left(\frac{h\nu_i}{k_\beta T}\right)\frac{e^{-h\nu_i/k_\beta T}}{1 - e^{-h\nu_i/k_\beta T}} - k_\beta \sum_i \ln(1 - e^{-\frac{h\nu_i}{k_\beta T}})$$

Here ν_i is the phonon frequency, and k_β is Boltzmann constant. In Figure 4-19. The $E_{adh}(T)$ of Pt20,

Pt13Au7α and Au20 as a function of temperature. The trends are shown as purple and orange lines for the

NPs with and without H*, respectively., we show the $E_{adh}(T)$ of Pt$_{20}$, Au$_{20}$, and Pt$_{13}$Au$_7^\alpha$ NPs with and

without hydrogen adsorption. On Pt$_{20}$ NP, the $E_{adh}(T)$ increases with increasing temperature, suggesting

that the supported Pt$_{20}$ NP becomes less stable on MoS$_2$ at higher temperature. In contrast, the stability of

Au$_{20}$ and Pt$_{17}$Au$_3^\alpha$ NP shows an opposite trend that its $E_{adh}(T)$ decreases with increasing temperature.

The change of $E_{adh}(T)$ in the interested temperature range of -273 °C to 400 °C is less than 0.1 J/m^2

for all the NPs without hydrogen and for Pt$_{20}$ with hydrogen, and is in between 0.1 ~ 0.2 J/m^2 for

Pt$_{13}$Au$_7^\alpha$ and Au$_{20}$ with hydrogen. As a result, the overall NPs stability affected by temperature is less

significant compare to hydrogen adsorption.

113
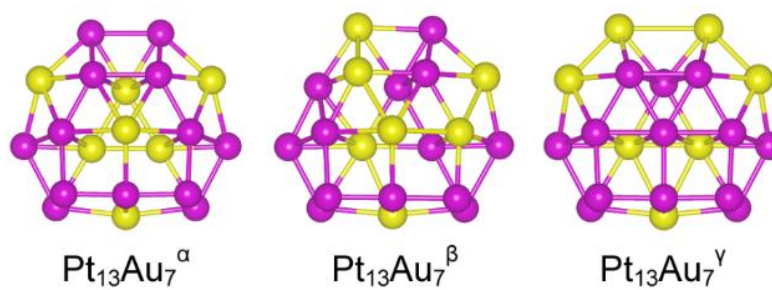
Figure 4-16. The Pt$_{13}$Au$_7$ NPs with different structures named as α，β and γ.
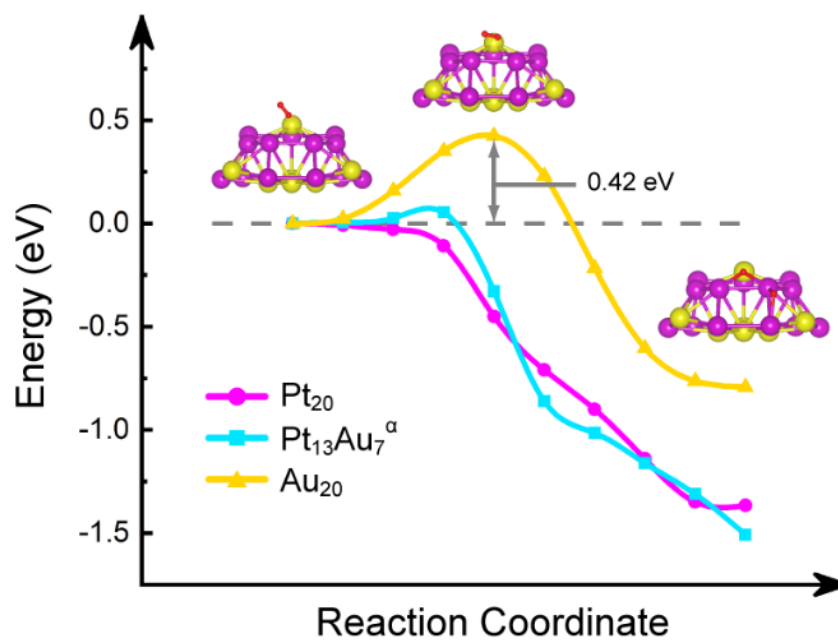
Figure 4-17. The reaction pathways of hydrogen dissociation on Pt$_{20}$, Pt$_{13}$Au$_7^{\alpha}$ and Au$_{20}$. The structures

of the transition states of the three NPs are similar, thus only side view of Pt$_{13}$Au$_7^{\alpha}$ is shown as an example.
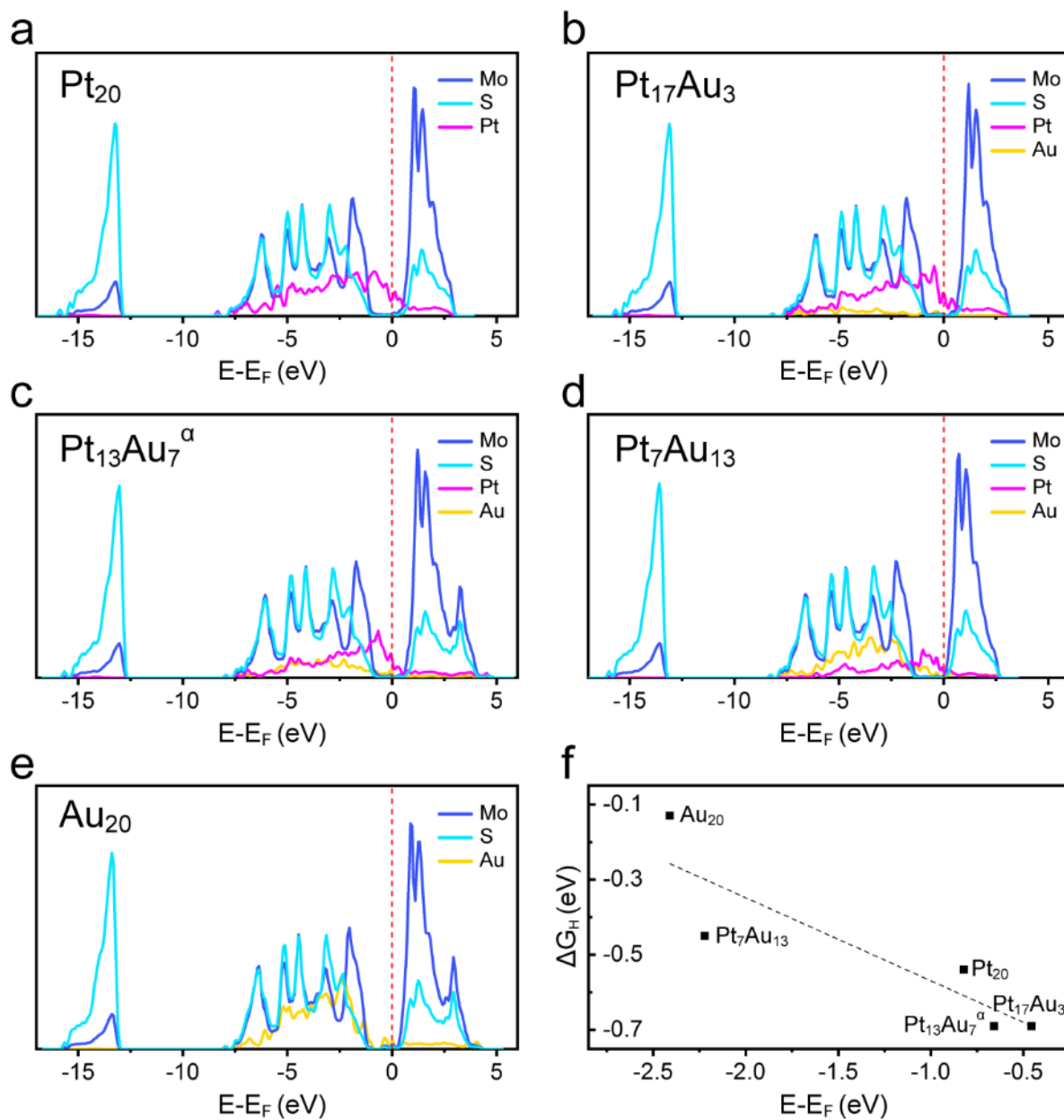
Figure 4-18. (**a-e**) The density of states (DOS) for the structures shown in Figure 4-14c. Fermi level is marked by red dash lines. (f) ΔG_{H} of the structures in Figure 4-14c as a function of metallic d-band peaks. For alloys, the metallic d-band peaks are determined by the sum of the DOS from Au and Pt.

Table 4-1. The stabilities of NPs with and without adsorbed H. The number of adsorbed H and the number of Pt/Au in contact with MoS$_2$ are provided.

	Pt/Au with MoS$_2$	J/m^2 (without H)	J/m^2 (with H)	# of H*
Pt$_{20}$	12/0	-5.40	-4.40	19
Pt$_{17}$Au$_3$	9/3	-4.37	-4.42	21
Pt$_{13}$Au$_7{}^{\alpha}$	6/6	-4.26	-4.06	13
Pt$_{13}$Au$_7{}^{\beta}$	8/4	-4.53	-4.12	13
Pt$_{13}$Au$_7{}^{\gamma}$	5/7	-4.07	-3.79	13
Pt$_7$Au$_{13}$	0/12	-3.25	-3.03	15
Au$_{20}$	0/12	-2.53	-2.66	9
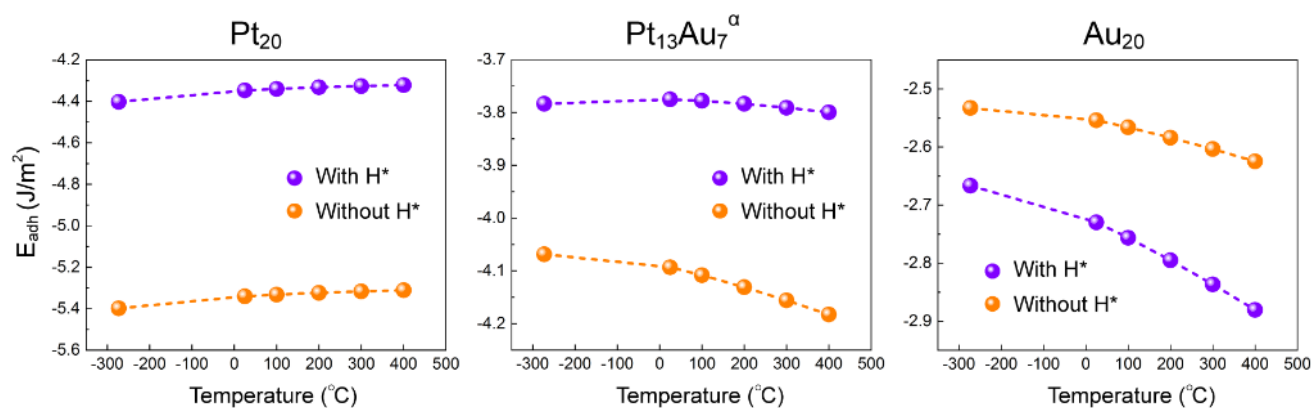
Figure 4-19. The $E_{adh}(T)$ of Pt$_{20}$, Pt$_{13}$Au$_7{}^{\alpha}$ and Au$_{20}$ as a function of temperature. The trends are shown as purple and orange lines for the NPs with and without H*, respectively.
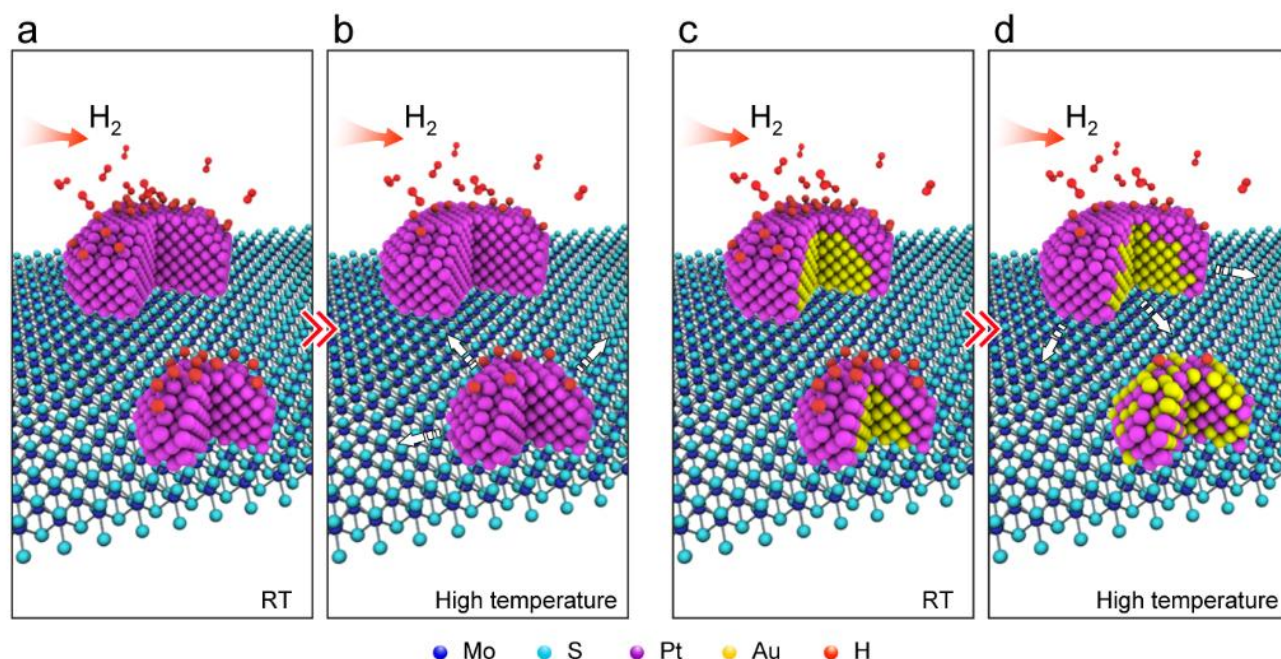
Figure 4-20. Schematic illustration of (**a**, **b**) Pt and (**c**, **d**) Au@Pt core-shell NPs behavior on MoS$_2$ at RT and higher temperature up to 400 °C in H$_2$ environment.

Combining all the experimental and theorical analysis, the NPs degradation kinetics on MoS$_2$ can be schematically illustrated in Figure 4-20. Schematic illustration of (a, b) Pt and (c, d) Au@Pt core-shell NPs behavior on MoS2 at RT and higher temperature up to 400 °C in H2 environment.. Overall, the NPs stability is affected by surface reaction with ambient atmosphere and interaction with the support.[165] Under vacuum or N$_2$ environments, the NP-support interaction is a critical factor that control sintering behaviors. In this case, the Au@Pt NPs display less stability compare to Pt NPs on MoS$_2$, due to less Pt in contact with MoS$_2$. For Pt NPs on MoS$_2$ in H$_2$ (Figure 4-20a and b), hydrogen adsorption weakens NPs adhesion with MoS$_2$ at RT and elevated temperatures, resulted in more diffusion and migration of NPs on the support. In contrast, Au@Pt NPs in H$_2$ display better sintering resistance compare to Pt in H$_2$

117

environment. This can be explained by H_2 induced size-dependent structural change in Au@Pt NPs (Figure 4-20c and d). As temperature rises, small NPs are easier to transform into alloy than large NPs due to H_2 dissociation, resulting in a decrease of surface Pt atoms and an increase of Pt in contact with MoS_2 support. Therefore, such H_2 promoted alloying kinetics enhances the stability of small size Au@Pt NPs due to two reasons: 1) the decrease of surface Pt mitigates the metal-H interactions and thus reduces the hydrogen adsorption induced weakening of adhesion with MoS_2, and 2) the increase of Pt in contact with MoS_2 strengthens the anchoring of NPs on MoS_2 support. Experimentally, this is seen as relatively stable small Au@Pt while rotation and diffusion of similar size Pt NPs under H_2 gas. Furthermore, it is worthwhile to mention that the physical properties of support materials, such as surface morphology, can also influence the degradation mechanism. This can be seen from the sintering behaviors of commercial Pt/C under H_2 gas as shown in Figure 4-21. The circles highlighted regions that Pt NPs undergo very complex dynamics involving migration and coalescence and possibly Ostwald ripening due to both movement and diminish of small NPs. In addition, morphology change of carbon indicates the support is not stable at elevated temperature under H_2 and thus will have extra impact on sintering mechanisms. It has been reported that porous carbon support such as high surface area carbon can constrain the NPs and enhance the sintering resistance compared to solid carbon such as Vulcan.[167] Correspondingly, a flat support allows more free movements of NPs and thus tend to enhance the mobility. In our condition, MoS_2 provides a smoother 2D surface than carbon support so the NPs rotation and migration can be easier when particle-support adhesion is weak for the case of Pt in H_2 and thus allow further oriented attachment for particle coalescence. As such, Pt and Au@Pt NPs sintering behavior on MoS_2 can be more possibly guided

118

by PMC.
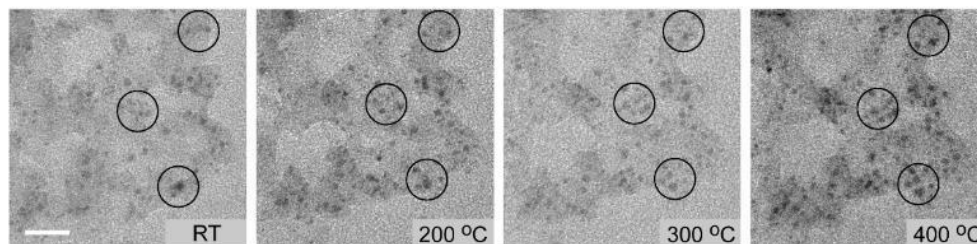
Figure 4-21. TEM images of Pt/C annealing in H_2 flow from RT to 400 °C. The scale bar is 20 nm. Circular outlines highlight the exemplar regions where sintering happens.

4.4 Conclusions

The present work provides study of catalysts sintering dynamics of Pt and Au@Pt on MoS_2 nanoflakes under vacuum and various gases environment including N_2, H_2 and air by *in situ* gas-cell TEM approach. It is found that type of environment, size of NPs, and composition modification (core-shell design) are important factors in controlling the degradation mechanism over MoS_2 substrates. The observations are summarized as: **Effect of environment:** while it was found that PMC was the main mechanism that led to Pt and Au@Pt NPs degradation under vacuum, N_2 and H_2 environments, the degradation of MoS_2 substrate was prominent under exposure to air at high temperatures. In addition, the Pt NPs were less stable under H_2 environment when compared with the Pt NPs under vacuum or N_2. This was explained by Pt-H interactions that weakens the adhesion of Pt with MoS_2. **Effect of NP composition:** under H_2, the stability of Au@Pt NPs was higher in comparison to Pt NPs. This phenomenon was attributed to H_2

119

interactions with metals by promoting the alloying of Pt-Au thus reducing the number of Pt at the surface (reducing H_2 dissociation) and increasing Pt atoms in contact with MoS_2. **Effect of particle size:** The alloying effect promoted by H_2 was more pronounced in small size Au@Pt NPs resulting in higher sintering resistance in comparison to large size Au@Pt NPs and similar size Pt NPs. Therefore, how Au@Pt core-shell structure influence the thermal degradation of NPs in atmospheric gas environment are demonstrated. These findings suggest that although H_2 decreases sintering resistant of Pt NPs on MoS_2, the core-shell NPs can be stabilized by carefully designing their structure and composition taking advantage of metal-gas interactions. In addition, insights on how 2D supports influence degradation behaviors of pristine and bimetallic core-shell NPs could benefit the future design of substrate-supported catalyst with better sintering resistance. We believe the presented *in situ* study is crucial for understanding catalyst behaviors in condition that closer to real applications such as at elevated temperatures and with exposure to various atmospheric gases.

120

Chapter 5   *In situ* gas TEM studies of redox-induced phase segregation in high-entropy alloy

nanoparticles

(Partial of this Chapter is from my published article [3]. The permission is attached in Appendix.)

5.1 Introduction

Corrosion, the oxidation between materials and their service environments involving interfacial chemical

or electrochemical reactions, is one of the most common causes of material failure during service resulting

in an annually global cost of 2.5 trillion US dollars.[212] The raising awareness of corrosion and the

problem that it causes is attracting significant efforts focusing on development of corrosion resistance

materials as well as strategies for corrosion removal. Understanding the involved key reactions including

how oxidation and reduction happens at materials and environments interface serves as essential guidance

for exploring advanced corrosion resistance materials. Based on the conventional principle of alloying

lower concentration secondary element(s) to form passive protective layer and thus preventing further

reaction with oxidant, existing designs focus mainly on binary or ternary compound and alloys such as

stainless steel,[213] aluminum alloys,[214] and nickel alloys[215]. Although some satisfying corrosion

resistance can be achieved,[216-219] the recent fast developed industries have been calling for

extraordinary structural and high temperature properties especially in applications of aerospace and energy

related fields. High-entropy alloys (HEAs), an emerging alloy compound involving five or more principle

elements in the form of homogeneous mixed disordered solid solutions, is attracting increased attention

because of their superior properties compared to conventional alloys including high mechanical strength,

high thermal stability, and better corrosion resistance[220-223]. The successful fabrication of such HEAs have emerged rapidly over the last two decades involving bulk melting[224, 225], solid-state processing[226-228], physical vapor deposition[229], and additive manufacturing[230-232]. Notably, the lately developed carbothermal shock method[233] allows incorporating multiple metal elements into single HEA nanoparticles (HEA NPs) and thus opens wide possible applications in catalysis, electronics, structural alloys, and so forth. The recently developed scalable aerosol synthesis[234] method takes a further step towards production of HEA NPs in bulk manufacturing quantities with full potential for industrial applications.

Similar to conventional alloys, industrial service environments for HEAs usually involve critical conditions such as exposure to high-temperature and oxidizing/reducing gases, acidic and chloride-containing solutions[235]. Several studies have been devoted to understand the corrosion behaviors of HEAs such as oxidation in air[236-240]and oxygen-containing atmospheres.[241] However, these studies are focused on bulk HEAs and there is still very limited knowledge of how HEA NPs behave under such environments. One of the key challenges for such nanometer-size HEA NPs is in obtaining structural and compositional information at the atomic scale, which requires advanced characterization techniques including transmission electron microscopy (TEM). Recently, the development of *in situ* environmental TEM (ETEM) with capability of exposing sample into gas environments opens the possibility to study materials behavior under realistic application conditions. Among of the two approaches of ETEM where either electron microscope's column is modified to allow sample exposure to gas environments[52, 53, 122

188, 189, 242] or specialized holder is utilized for a sealable gas-cell[42, 43, 47, 193, 194, 196], the latter enables observation of the sample in atmospheric pressure gas environments that closely mimic actual application conditions. Material behavior under redox reactions are captured including facet evolution of Pt NPs[196] and PdCu[47], phase segregation in bimetallic Pt-Ni NPs[43] and PdCu[193], and sintering of Co NPs[194], Pt and core-shell NPs[2]. Benefiting from the *in situ* gas-cell TEM, we studied the high temperature oxidation and reduction behaviors of $Fe_{0.28}Co_{0.21}Ni_{0.20}Cu_{0.08}Pt_{0.23}$ HEA NPs in atmospheric air and H_2 environments. The structural and compositional evolution during redox reactions at 400°C are captured in real time through (S)TEM imaging, EDS and EELS analyses. It was found that the HEA NPs are oxidized with logarithmic rate constants and are guided by Kirkendall effect involving outward diffusion of transition metals including Fe, Co, Ni and Cu. Anisotropic oxidation is observed on adjacent HEA NPs in a way that oxide initiate at connecting interface. The oxide layer is found to have a disordered mixture of Fe^{3+}, Co^{2+}, Ni^{2+} and Cu^{2+} in oxidation states with detected localized ordering belonging to Fe_2O_3, CoO, NiO and CuO crystal lattices. Hybrid Monte Carlo/ molecular dynamics simulations based on first-principles calculations support these findings and show that under oxidizing conditions there is a preferential surface segregation of Fe, Co, Ni, and Cu while Pt remains in the core of the NP. In reduction environments, the oxide layer expanded and transformed to porous structure as H_2 takes away oxygen. Oxidized Cu can be fully reduced into Cu NPs while Fe, Co, and Ni are rarely fully reduced. Lastly, we show that thermal pretreatment in H_2 environment can serve as an effective strategy in preventing further oxidation of HEA NPs.

123

5.2 Experimental Section

HEA NPs synthesis. HEA NPs containing Fe, Co, Ni, Cu, and Pt were synthesized based on the method in previous study[234] and stored in glove box under Ar. The as-prepared sample were dispersed in ethanol and sonicated for 2 min in a bath sonicator (Branson 3800, 40kHz, 110W) before TEM experiments.

In situ **TEM experiment in vacuum.** A furnace based heating holder (Gatan, Inc.) is used for heating experiments in vacuum condition. HEA sample dispersion is drop-casted onto Mo grid and then inserted into a spherical aberration corrected JEOL JEM-ARM 200CF with cold field emission source operating at 200 kV. Temperature was ramped up from RT to 400 °C with a 100 °C interval every 1 hr, and ramped down to RT after another 1 hr staying at 400 °C.

In situ **gas flow TEM experiment.** A gas-cell TEM holder with pair of silicon microchips (Hummingbird Scientific) was used (Figure 5-3a). Each of the microchips has an electron transparent silicon nitride (Si_3N_4) viewing window with 50 nm in thickness and 200×50 μm^2 in dimension. Spacers with 250 nm thickness on one microchip are used to control the top and bottom distance in gas reactor. One droplet containing 1 μL HEA sample dispersion was added on one of the microchips with heater and dried under air. The viewing windows were aligned in parallel to provide a maximized viewing area. For *in situ* annealing in gas environments, 100% pure N_2, air (containing ~21 vol. % O_2) and 100% pure H_2 was introduced through gas channels with constant volumetric flow rate of 0.5 sccm. The pressure inside

124

the cell is approximately 1 atmosphere. Local temperature at the sample area is controlled and monitored in real-time. After loading the holder and flowing gas at RT for 30 min, the temperature was ramped up to 400 °C within 2 min and kept constant afterwards. When finished the temperature was ramped down back to RT within 1 min. Unless otherwise specified, the electron beam was kept blocked at all time except initial TEM alignment, focusing and image acquisition to minimize electron beam effects. All *in situ* TEM experiments were carried out using a field emission JEOL 2100F microscope operated at 200kV. The three-window method was employed to map the Fe and O distribution by EFTEM. For Fe L-edge, the three windows were taken at 644 eV, 684 eV and 728 eV with energy slit of 40 eV. For O K-edge, the three windows were taken at 484 eV, 514 eV and 547 eV with energy slit of 30 eV. Backgrounds were subtracted by power-law fitting model after spatial drift correction.

***In situ* gas flow STEM experiment.** The *in situ* STEM and EDS experiments were performed using spherical aberration corrected JEOL JEM-ARM 200CF with a cold field emission source operating at 200 kV combined with a gas-cell TEM holder (Protochips, Inc). The spacer distance between two microchips was 5 μm. The holder was assembled after drop-casted HEA samples onto one of the microchips. Gas channels were first opened to allow sample expose in air environment for oxidation, then connected to H_2 tank for reduction process. The local temperature was kept constant at 400 °C. EDS maps were collected on the same sample region at RT and every 5 min at 400 °C.

***Ex situ* annealing experiment in air.** *Ex situ* oxidation were performed in two different methods. In

125

the first method, HEA NPs were firstly drop-casted onto Mo grid. The grid was placed onto a hot plate in air atmosphere with temperature preset to 400 °C for 1 hr. Then the grid is cool down in air before (S)TEM characterization. In the second method, the gas-cell TEM holder was assembled with HEA NPs but was not inserted into the microscope. The holder was then flowed with air and temperature ramped up in same way as *in situ* TEM experiment. After finished and cool down to RT, the HEA NPs on microchip is characterized directly by (S)TEM.

Electron microscopy characterization. *Post situ* sample on microchips were characterized using a self-designed (S)TEM specimen holder (patent pending). STEM images were acquired by a spherical aberration corrected JEOL JEM-ARM 200CF with a cold field emission source operating at 200 kV, at 22 mrad convergence semi-angle. *Post situ* Energy dispersive spectrometer (EDS) maps were acquired with Oxford X-Max 100TLE windowless silicon drift detector. *In situ* EDS maps were acquired with JEOL dual silicon drift detectors. The area of a single detector is 100 mm^2 and the solid angle for this dual EDS system is 1.8 sr. Electron energy loss spectra (EELS) were acquired using a Gatan GIF Quantum spectrometer with an entrance aperture of 5 mm in dual-EELS mode. EELS maps were extracted from transition metals $L_{2,3}$-edges, O K-edge using power law fitting background subtraction after energy drift correction and Fourier-ratio deconvolution. Transition metal L_3/L_2 white-line intensity ratio was determined by applying Hartree-Slater cross section step-functions following the methods reported elsewhere[243].

Density functional theory calculations. First-principles DFT calculations are employed using the Perdew-Burke-Ernzerhof[125] exchange-correlational functional to solve the Kohn-Sham equations. The electronic self-consistent loops are terminated with energy-change tolerance of 1×10^{-8} eV. Bulk calculations for the alloy or for the elementary metals, or their oxides and hydrides are carried out using the Vienna ab initio simulation package (VASP)[244-246] with a planewave cutoff of 400 eV. For these calculations, a dense gamma-centered k-grid with 0.24 Å^{-1} spacing between k-points were used. This is equivalent to 8 x 8 x 8 mesh for bulk metals with conventional four atom FCC unit cell. The projector augmented wave (PAW) method implemented in VASP was used to describe the electron-nucleus interactions.[127] The hybrid Monte Carlo/molecular dynamics simulations are carried out using VASP computed energies and forces. For these calculations, we employed softer PAW potentials, a 300 eV planewave cutoff, and gamma point sampling of the Brillouin zone. We find that equilibrium is reached by conducting a total of 1000 steps where each hybrid step corresponds to a potential MC swap between two random metal atoms followed by 40 molecular dynamics steps with a 1 femtosecond timestep.[247] The ab initio molecular dynamics simulations for the slabs models or for isolated nanoparticles are carried our using CP2K using DZVP-MOLOPT-SR-GTH basis sets and GTH norm-conserving potentials.[248, 249] All of our calculations are done within the spin-averaged approximation. For bulk FCC random alloy model, we checked that spin-polarized calculations yield a lattice constant 3.67Å that is close to the value obtained from spin-unpolarized calculations of 3.61Å.

127

5.3 Results and discussion

In the first step, the atomic ordering and chemical composition of the as-synthesized HEA NPs were studied. The NPs were prepared *via* aerosol synthesis method as reported in our earlier work.[234] The morphology and chemical composition of synthesized HEA NPs were characterized by STEM, EDS and EELS. High-angle annular dark-field (HAADF) image in Figure 5-1a shows that the HEA NPs are mostly spherical with particle size ranging from 50 to 200 nm. Figure 5-1b is a low-angle annular dark-field (LAADF) image focused on an individual NP with facetted edges. The boxed region was selected for atomic resolution HAADF and annular bright-field (ABF) imaging as shown in Figure 5-1c. The lattice distortion and random atom-to-atom contrast variation suggests a homogeneous mixing of Fe, Co, Ni, Cu and Pt at the atomic level. Inset in the ABF image shows the fast Fourier transform (FFT) patterns in <100> zone axis with $(00\bar{2})$ and (022) planes highlighted, confirming the successfully synthesized single-phase HEA NPs with face-centered cubic (FCC) crystal structure, which is consistent with our previous reported X-ray powder diffraction (XRD) results.[234] The composition uniformity was confirmed by both STEM-EELS and STEM-EDS mappings. STEM-EELS mapping was performed on a NP in <110> zone axis as shown in Figure 5-1d. The crystal contains regions with appreciable twining as suggested in FFT and marked by dashed lines. The EELS mappings in red shadowed region from Fe, Co, Ni, Cu *L*-edges and Pt *M*-edge are shown in Figure 5-1e. In all cases, Fe, Co, Ni, Cu and Pt are found to be distributed homogeneously. In addition, elemental distribution from STEM-EDS mapping in the sample region of Figure 5-1a is shown in Figure 5-1f. These further confirm that all the synthesized NPs, irrespective of their sizes, have well-mixed elemental compositions. The composition of each HEA NP is obtained from
128

EDS analysis (Figure 5-2) and the averaged HEA composition is determined to be $Fe_{0.28}Co_{0.21}Ni_{0.20}Cu_{0.08}Pt_{0.23}$.
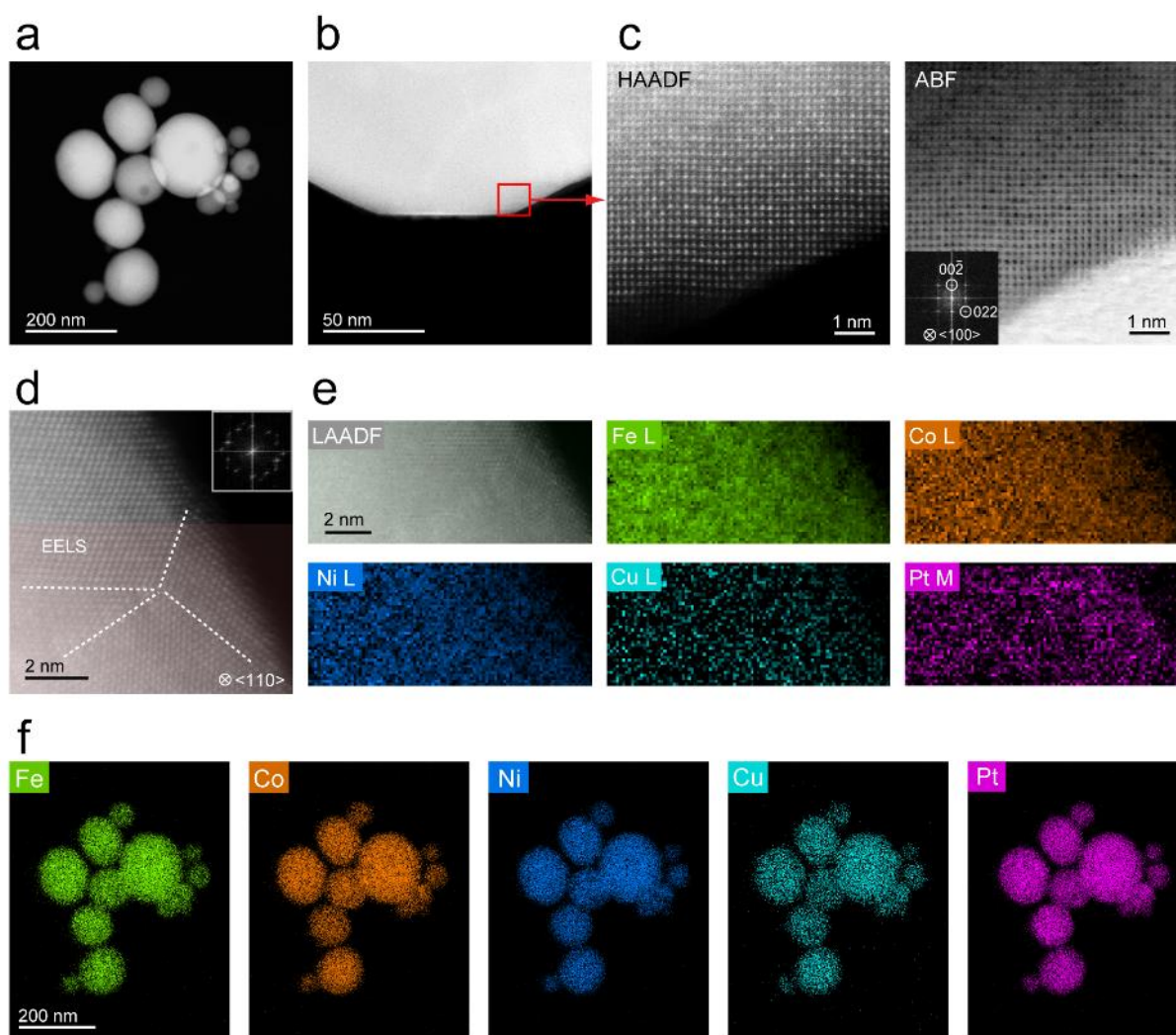
Figure 5-1. Atomic structure and chemical characterization of HEA NPs. (**a**) HAADF image showing the as-synthesized HEA NPs. (**b**) LAADF image focusing on the edge of an individual HEA NP. (**c**) HAADF and ABF images from the boxed region in **b**, showing the atomic structure of HEA in <100> zone axis. The inset in ABF image is the corresponding FFT with highlighted diffraction spots from $(00\bar{2})$ and (022)

129

planes. (**d**) LAADF image of HEA in <110> zone axis with twining marked with dashed lines. The inset

shows the corresponding FFT with multiple diffraction spots from twining. Red shadowed region marks

the EELS mappings area. (**e**) EELS mappings from region in **d**. Signals are extracted from *L*-edges of Fe,

Co, Ni, Cu and *M*-edge of Pt. (**f**) EDS mappings of the HEA NPs in **a**.

Result Type	Atomic %								
Spectrum Label	1	2	3	4	6	7	8	9	10
O	0.00	2.66	3.67	4.84	5.30	0.86	4.12	3.68	8.42
Fe	26.17	22.90	23.36	24.19	22.24	24.22	22.36	24.50	20.20
Co	20.29	22.60	21.75	15.59	22.02	21.10	22.18	18.60	19.17
Ni	21.27	21.33	20.63	20.22	20.22	22.36	20.58	18.97	19.98
Cu	5.52	6.84	6.22	5.26	8.01	6.80	7.12	7.35	8.57
Pt	26.75	23.66	24.36	29.89	22.20	24.67	23.64	26.89	23.66
Total	100.00	100.00	100.00	100.00	100.00	100.00	100.00	100.00	100.00

Total average	Fe	Co	Ni	Cu	Pt
Average	27.80	21.13	19.60	7.98	23.50
Standard Deviation	2.71	2.01	2.08	2.57	4.89

Figure 5-2. As-prepared HEA NPs composition obtained from EDS analysis. Left: exemplar HAADF

image showing the EDS profile from individual HEA NPs highlighted with circles. Right: EDS

atomic % of O, Fe, Co, Ni, Cu, and Pt extracted from circular regions in HAADF image, together with

total averaged HEA composition including Fe, Co, Ni, Cu and Pt extracted from more than 30

nanoparticles.

5.3.1 Oxidation of HEA NPs in air

Figure 5-3a shows a schematic illustration of specimen holder employed for the *in situ* gas-cell TEM

experiments. Atmospheric pressure can be maintained inside the cell with continuous gas flow benefiting

from the isolated environment formed by a pair of microchips.[2, 42, 177, 190] The *in situ* experiment is firstly performed in air environment as shown in Movie S1. The beginning of the movie is exactly at the same time of starting the heating process. Snapshots from Movie S1 are shown in Figure 5-3b. The HEA NPs underwent oxidation in atmospheric air and oxide layer can be seen to grow gradually covering the NPs, shown as the lighter contrast layer on HEA NPs. Interestingly, the oxidation is particle-size dependent. The largest HEA NP ~130 nm at the center display a large-scale contrast originating from oxide starting at ~13.3 min (highlighted by blue arrows), while such contrast cannot be observed for smaller NPs (exemplar region highlighted by purple arrows). To present this more visibly, the zoomed-in images of the boxed regions in the first frame are shown in Figure 5-3c and d, with purple box corresponding to one small NP (less than 100 nm) and blue box focusing on top surface of the larger NP. Again, the small NP has a thin and isotropic oxide layer, while the oxide layer on large NPs are thick and not uniform that becomes noticeable starting from ~13.3 min. Compared to monometallic NPs in similar or milder oxidation conditions, for instance Co NPs at 200°C and Ni NPs at 400 °C,[87, 250] transformation from solid NPs to hollow structures can be seen in less than one hour due to the Kirkendall effect. Moreover, bimetallic alloy NPs were also observed to show fast oxidation in less than 30 mins forming porous and hollow structures such as NiFe NPs in air[53] and NiCr NPs in low pressure (1 mbar) O_2,[189] as well as the formation of obvious voids for NiCo NPs accompanied by the outward diffusion of Ni and Co.[251] For HEA NPs presented here, formation of voids and hollow structures in similar size range are not observed, suggesting that the overall oxidation kinetics can be slower than mono and bimetallic alloy NPs with similar principle elements. The oxide layer thickness d_{OX} was measured following the same

131

direction as indicated in the arrows in Figure 5-3c and d, and are plotted in Figure 5-3e. For the small NP, oxidation kinetics can be perfectly fitted with a logarithmic law $d_{OX} = K \ln(t - A)$ with oxidation rate K determined to be 1.72. The oxidation kinetics follow logarithmic law rather than parabolic predicted by Wagner theory,[81] suggesting that the growth of oxide layer is governed by combined effects involving electric field and lattice diffusion. The reason can be that Wagner's theory assumes a planar geometry, while for HEA NPs considering the spherical geometry with surface curvature, the oxidation kinetics can be altered by surface charge and space charge distribution. Since there is much stronger polarization in spherical NP than planar surface,[252] the electromagnetic field[88] across the oxide in radial direction[86] will result in faster growth rate compared to parabolic relationship in the initial stage and slower rate in longer time range that fits into the logarithmic law. The larger NP, again follows logarithmic law with K_1 equal to 1.46 in the first 10.7 min but has a burst of oxide growth starting at ~13.3 min. The oxidation kinetics afterwards can also be fitted with a logarithmic function with $K_2 = 6.87$, indicating a much faster oxidation rate. This anomalous two-stage oxidation kinetics seems to happen selectively at the region where two HEA NPs are adjacent (highlighted by blue arrows in Figure 5-3b), while the surface without adjacent NPs displays only one-stage oxidation kinetics (purple arrows in Figure 5-3b). Existing high-temperature oxidation models[80] (Valensi-Carter and Fromhold) taking into consideration of spherical geometry predict that smaller NPs can be oxidized faster than larger NPs, which is consistent with experimental observation within first ~10.7 min. The much increased oxidation rate after 13.3 min for large NP in its second oxidation stage may be attributed to the sintering induced atomic surface diffusive flux close to the interfaces where HEA NPs are in contact,[253] resulting in a change of electric-field

132

induced concentration gradient in initial oxide and provide extra driving force for metal outward diffusion.[84, 253, 254] To further understand the mechanism, after *in situ* oxidation the HEA NPs were characterized by STEM-EDS as shown in Figure 5-3f. HAADF and LAADF images show the same HEA NP region while the LAADF image show more clearly the oxide region with a brighter contrast. In the STEM-EDS maps, transition metals of Fe, Co, Ni and Cu are all seen to present in the oxide layer, while Pt is the only metal that does not segregate to the surface. The last two rows showing the overlaid maps illustrate more explicitly that 1) in the region without oxygen, HEA NPs still show a homogeneous mixing of Fe, Co, Ni, Cu and Pt; 2) Fe, Co, Ni and Cu can be found in the region with oxygen; and 3) Cu is the most widely dispersed in the oxide region. Further, quantitative EDS analysis were extracted from the maps in the two boxed regions focusing on the large NP and are shown in Figure 5-3g and h. The boxed regions were aligned with the plots with corresponding colors. The NP surface is defined as the boundary of the brightest contrast in LAADF images (marked by dashed lines) so the outward direction indicates oxide region. The two plots show same trends where Fe, Co, Ni and Cu diffuse out to react with oxygen while Pt does not display outward segregation and is not present in the oxide. Among the transition metals, Co is more accumulated in the oxide region closer to HEA surface within ~20 nm, and Cu is more presented in the region farther away; Fe and Ni are distributed in a more monotonic decreasing manner in the oxide. These results show the oxidation of HEA NPs is guided by Kirkendall effects, where metals diffuse outward at different rates to react with oxygen and lead to a composition variation in the formed oxide and HEA core.

133
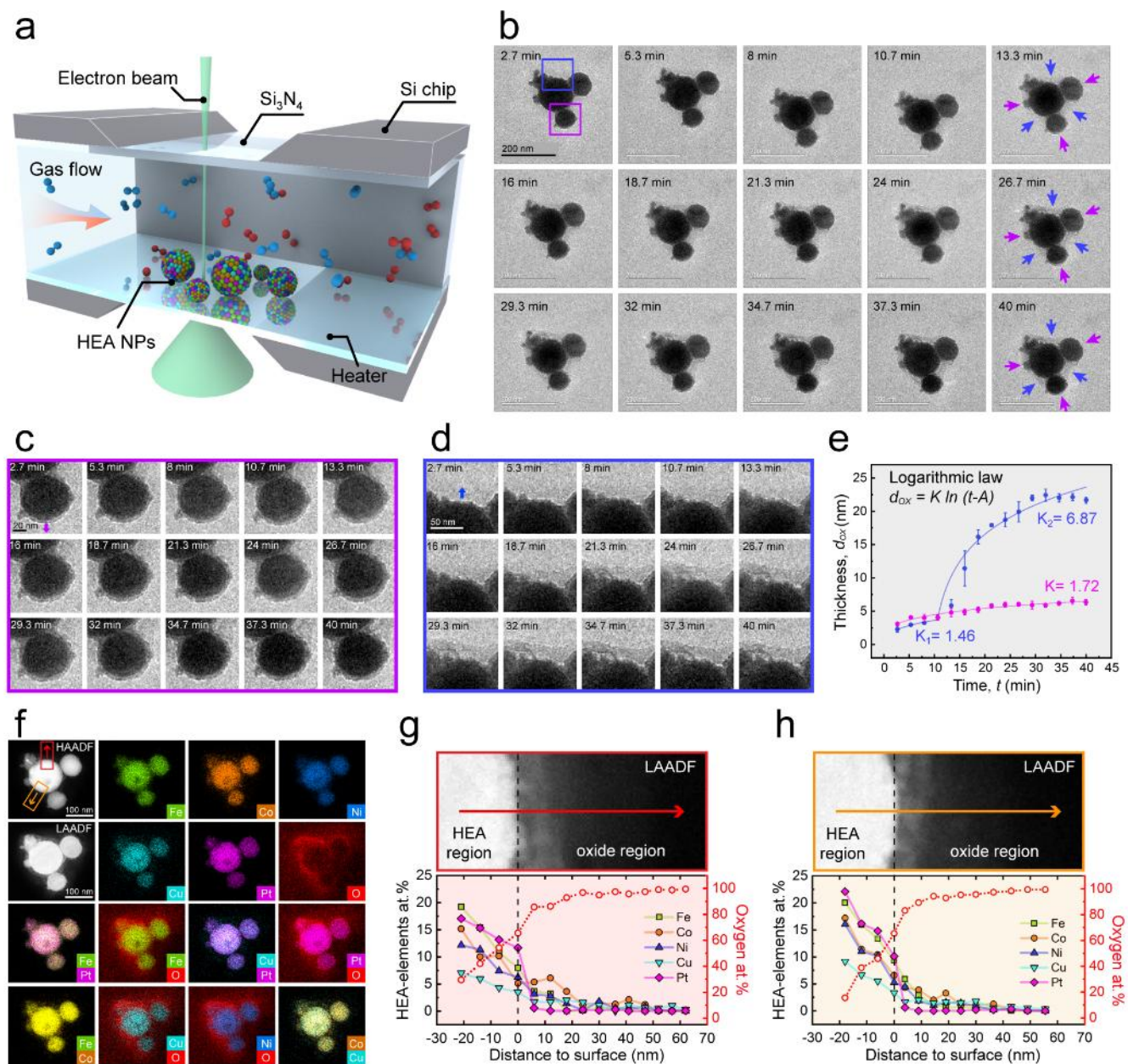
Figure 5-3. Oxidation of HEA NPs in air. (**a**) Schematic of the *in situ* gas-cell (S)TEM device to study the redox reactions of HEA NPs. (**b**) *In situ* TEM image sequences of HEA NPs during annealing in air. (**c, d**) TEM image sequences focused on the two boxed regions in **b** during annealing in air. (**e**) Oxide thickness as a function of time measured from the direction highlighted in **c** and **d**. (**f**) *Post situ* HAADF and LAADF images of the same HEA NPs after *in situ* oxidation, followed by EDS mappings of Fe, Co,

134

Ni, Cu, Pt and O and selected overlaid mappings. (**g, h**) LAADF images from two boxed regions in **f** and

corresponding at. % distribution of Fe, Co, Ni, Cu, Pt and O extracted from EDS maps. The arrows in

LAADF images indicate the same directions as the arrows in **f**. The zero in the horizontal axis (distance

to surface) represent the edge of NP marked by dash lines, while positive values stand for outward

directions.

Considering the electron beam effects during the *in situ* oxidation process in Figure 5-3, HEA NPs on

other regions without the electron beam exposure were also characterized and shown in Figure 5-4. The

HAADF and LAADF images (Figure 5-4a) show several HEA NPs of different sizes after oxidation. The

NPs on the left portion of the image are all less than 100 nm and show the same behavior as the smaller

NPs in Figure 5-3, with uniformly formed oxide layers. The largest NP of ~ 200 nm in size, however,

displays obvious voids between the HEA and oxide layers (exemplary marked by red arrows in LAADF

image). This phenomenon has not been observed in particle sizes less than 200 nm, and is suggestive that

the Kirkendall effect happens more significantly on larger NPs. Such process induces more large-scale

voids because the outward diffusion of Fe, Co, Ni, Cu are less compensated due to longer required

diffusion distances from the NPs interior. From a composition point of view, the EDS maps in Figure 5-4b

and c show almost the same elemental distribution compared to the EDS in Figure 5-3f. Figure 5-4d-f

show atomic distribution (at. %) of three boxed regions from Figure 5-4a with corresponding LAADF

images, covering regions with voids (red and orange box in Figure 5-4d and e) and without voids (blue

box in Figure 5-4f). Similar to the distributions in Figure 5-3g and h, outward diffusion of Fe, Co, Ni and
135

Cu guided by Kirkendall effect are observed, with Cu displaying the farthest diffusion distance from HEA surface. In addition, there is no distinguishable difference in terms of atomic distribution between void and non-void regions.
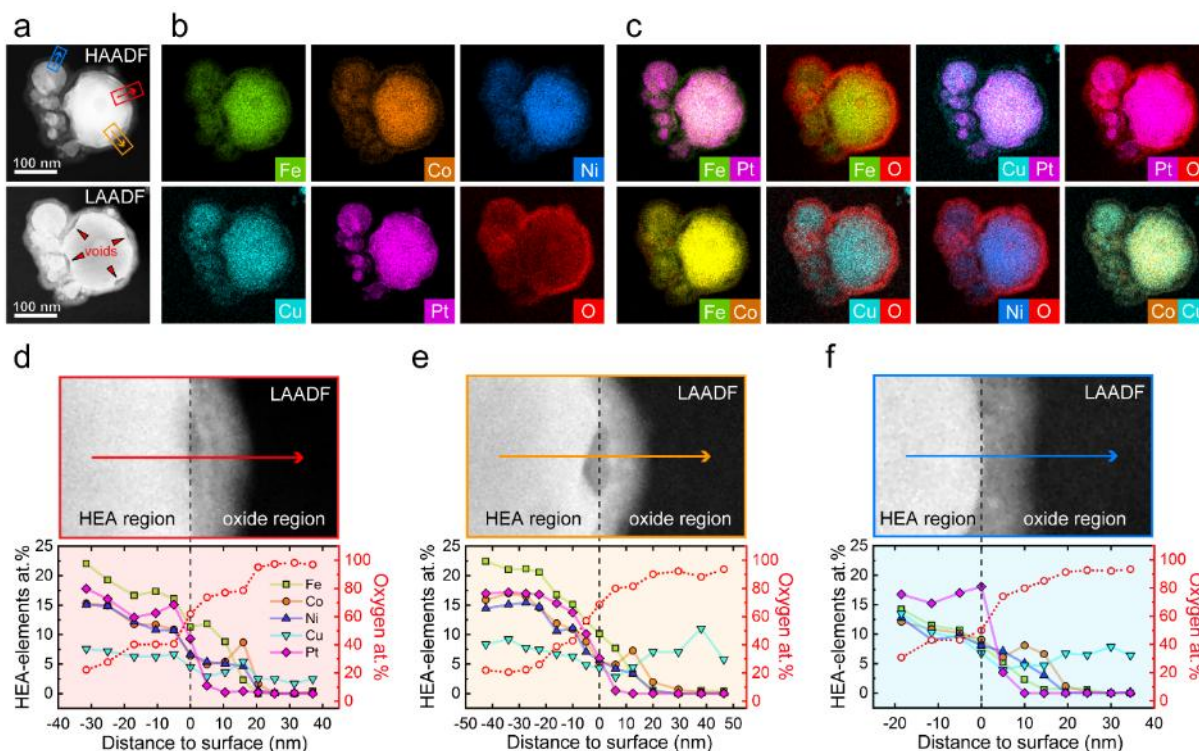
Figure 5-4. Oxidation of HEA NPs in air in the region without electron beam. (**a**) *Post situ* HAADF and LAADF images showing different sizes of NPs after oxidation. Red arrows in LAADF image mark exemplar regions with void formation. (**b**) EDS mappings of Fe, Co, Ni, Cu, Pt and O corresponding to **a**. (**c**) Overlaid EDS maps of selected elements. (**d-f**) LAADF images from three boxed regions in **a** and corresponding at. % distribution of Fe, Co, Ni, Cu, Pt and O extracted from EDS maps. The arrows in LAADF images indicate the same directions as the arrows in **a**. The zero in the horizontal axis (Distance to surface) represent the edge of NP marked by dash lines, while positive values stand for outward directions.

Due to the interference of the SiN window on the microchip and the single-tilt limitation of *in situ* TEM holder, extracting atomic information is challenging. Nevertheless, HRTEM images were successfully obtained on HEA NPs in Movie S1 and Figure 5-3 after oxidation. The first row in Figure 5-5a-c show exemplar HRTEM images with HEA and oxide region highlighted. The corresponding FFTs are shown in the second row, with diffraction spots marked with *d*-spacings. Since the largest *d*-spacing in FCC HEA NPs is 0.214 nm from {111} planes, any observed *d*-spacing larger than that should originate from the oxides. As such, in FFTs the diffraction spots are labeled as the most possible crystal planes from HEA or oxide compounds. Examples are shown as $\{111\}_{CoO}$ in Figure 5-5a, $\{111\}_{NiO}$ in b, $\{110\}_{Fe2O3}$ or $\{002\}_{CuO}$, $\{006\}_{Fe2O3}$ or $\{200\}_{CoO}$ in c. To present the oxides more obvious, IFFTs were shown in both Figure 5-5a-c by masking each pair of diffraction spots. As seen, starting from third row in Figure 5-5a, for instance, $\{111\}_{HEA}$ are only from HEA region, while $\{111\}_{CoO}$ are mostly in the oxide layer. Following the same trend, Figure 5-5b and c show that crystal planes from oxide compounds are only presented in oxidized regions. After carefully analysis of all the HRTEMs, the lattice *d*-spacings not likely to belong to HEA are plotted as dashed signs in Figure 5-5d. The *d*-spacings from planes in HEA and some oxide compounds are shown as reference. The first and second columns named HEA_T and HEA_X are data from (S)TEM and XRD analysis, respectively. Those *d*-spacings not belonging to HEA are likely from oxides including Fe_2O_3, CoO, NiO, and CuO. There also possibilities that these localized ordered lattices originate from complex oxides involving more than one metal element, however it is not possible to properly index them due to the lack of standard lattice parameters. The results further suggest that although

137

the oxide lattices are not observed to be homogeneous in all oxide regions, clearly there is localized ordering in the disordered oxide matrix containing Fe, Co, Ni, Cu and O. While principle elements including Fe, Co, Ni and Cu typically form crystalline oxide under similar oxidation conditions, the observed disordered oxide with only localized oxide crystallites can be ascribed to two factors that lower the total Gibbs free energy of disordered oxide compared to crystalline oxide: 1) built-in high entropy in the HEA NPs that lower the positive contribution of interfacial energy between HEA and disordered oxide interface,[255] and 2) the huge strain induced lattice mismatch between an epitaxial HEA and crystalline metal oxide interface at curvature regions that increase the interfacial energy contribution.[32] Therefore, compared to single elements, the special properties in HEANPs allow them yield formation of thermodynamically stable disordered oxides. Since disordered oxide is expected to serve as diffusion barrier and thus provide better corrosion resistance,[256] it is possible to be the reason that HEA NPs display slower oxidation kinetics compared to monometallic or bimetallic NPs.
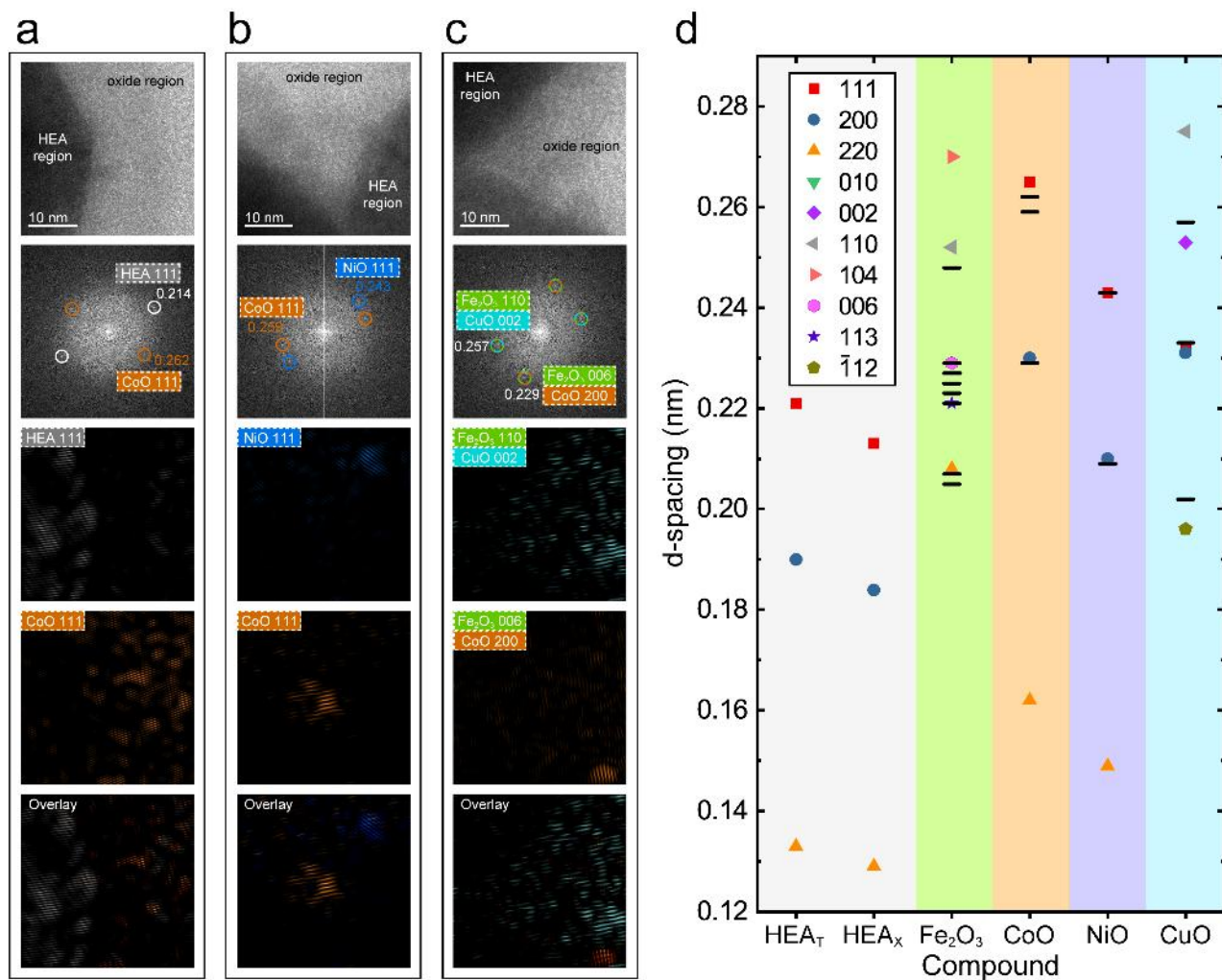
Figure 5-5. HRTEM analysis of HEA NPs after oxidation in air. (**a-c**) Three exemplar HRTEM images and the corresponding FFTs of HEA NPs after *in situ* oxidation in air. In the FFTs, diffraction spots are highlighted according to the most possible crystal planes in HEA or oxide phases. The last three rows show the IFFT of masked diffraction spots with corresponding phases and the overlaid image. (**d**) Portion of d-spacings in different crystal planes in as-prepared HEA and various oxide compounds. Dash signs in oxide compounds mark the d-spacings obtained from HRTEM analysis. HEA_T stands for information extracted from (S)TEM analysis and HEA_X are obtained from XRD results. For oxide compounds, only

139

d-spacings larger than 0.195 nm are shown to avoid overlapping of data points.

To gain more understanding at the atomic level for the HEA NPs after oxidation, *ex situ* oxidation on HEA NPs was performed and is shown in Figure 5-6a-h (first method, details in Method section). LAADF image in Figure 5-6a shows the oxide layer on HEA NPs after oxidation, and the EELS mappings from small red boxed region (Figure 5-6b) again confirm that the oxide layer contains Fe, Co, Ni and Cu. EEL spectra from the mapping region is then extracted following the direction of the rainbow arrow and are plotted in Figure 5-6c. Although subtle changes of transition metal $L_{2,3}$-edges are hard to discern in the current energy resolution, there are obvious variations on O K-edge especially the pre-peak intensity and energy separation between pre-peak and main peak when it is closer to NP surface, as highlighted by red arrows. Further, with a larger EELS mapping area (larger boxed region in Figure 5-6a) covering the whole HEA NP, multiple linear least squares (MLLS) fitting results is shown in Figure 5-6d. The fitting is performed using L-edges reference spectra of as-prepared HEA, Fe_2O_3, CoO, NiO and CuO[257-262], and is shown in the same sequence. The last image is a directly extracted O-K map for the ease of comparison. These MLLS fitting results serve as valence state maps of Fe, Co, Ni and Cu. It can be seen that Fe^{3+}, Co^{2+}, Ni^{2+}, and Cu^{2+} are all presented in the oxide layer region, suggesting that in the oxides Fe is in 3+ state while Co, Ni and Cu are in 2+ state. In addition, the results show consistency with previous HRTEM analyses on *in situ* HEA NPs that localized ordering from lattices of Fe_2O_3, CoO, NiO and CuO are observed. Figure 5-6e shows energy loss near edge fine structure (ELNES) of L_3/L_2 white-line intensity ratio for Fe and Co and O-K on another similar size HEA NP. It is known that the transition metal L_3/L_2

140

white-line ratio is directly correlated with *3d* orbital occupancy that a higher ratio indicates increased

oxidation state for Fe[263] while a lower ratio indicates higher oxidation state[243, 264] for Co. Here, Fe

L_3/L_2 white-line ratio displays an increase in the external oxide (positive distance to surface) region

suggesting a more oxidized Fe state compared to the interior of HEA NP. Likewise, Co L_3/L_2 white-line

ratio gradually decreases from NP interior to surface and drop further in external oxide region, suggesting

an upward gradient of Co oxidation state. The third plot in Figure 5-6e shows distance of O *K*-edge pre-

peak to main peak (energy separation, ΔE) as a function of distance to HEA surface. Although the ELNES

of O K-edge contains metal-oxygen bonding information contributed by four transition metals involving

Fe, Co, Ni and Cu, an increase of ΔE from interior to surface can still be identified indicating the higher

overall oxidation states in the oxide region.[265] Figure 5-6f shows an ABF image of a HEA NP after *ex*

situ oxidation. The oxide layer can be seen in the lower contrast region close to the HEA surface. Plenty

of voids of less than 10 nm in size are clearly observed and exemplar of them marked by red arrows.

Larger voids are expected to form after these tiny ones accumulate and coalesce. Figure 5-6g shows a pair

of HAADF and ABF images of HEA NP in <110> zone axis. FFT (inset in ABF image) indicates an FCC

pattern of HEA NP. While no lattice can be resolved in the oxide layer region, apparently the HEA NP

maintains its FCC structure as evident through the same atomic arrangement in comparison to as-prepared

sample (Figure 1d). This is true even at the void regions (marked by red arrows) suggesting that the atomic

outward diffusion during oxidation does not break the FCC crystal structure. Again, this is consistent with

HRTEM in Figure 5-6a that $\{111\}_{HEA}$ can be clearly resolved. Pair of HAADF and ABF images in Figure

5-6h show another HEA NP in <110> zone axis with identifiable twining (marked by dashed lines).
141

Although it is not clear whether the twining existed initially or formed after oxidation, the FCC structure in HEA NP is confirmed to remain unchanged. Lastly, to make sure the *ex situ* oxidation reflects exactly the actual condition of *in situ* experiments, another *ex situ* oxidation (second method, details in Method section) was performed and shown in Figure 5-6i and j. The morphology of as-prepared HEA NPs and after oxidation (Figure 5-6i) indicates the formation of similar oxide layer surrounding the NPs as observed in *in situ* oxidation experiment, exemplary marked by red arrows. Figure 5-6j shows three HRTEM images on HEA and oxide interfaces after oxidation. Insets are FFTs from a larger region covering all three images, with corresponding diffraction spots highlighted with circles. The HRTEM images and FFTs resolve the lattice of 0.214 nm from $\{111\}_{HEA}$, further confirms the preserved FFC structure of HEA NPs after oxidation.
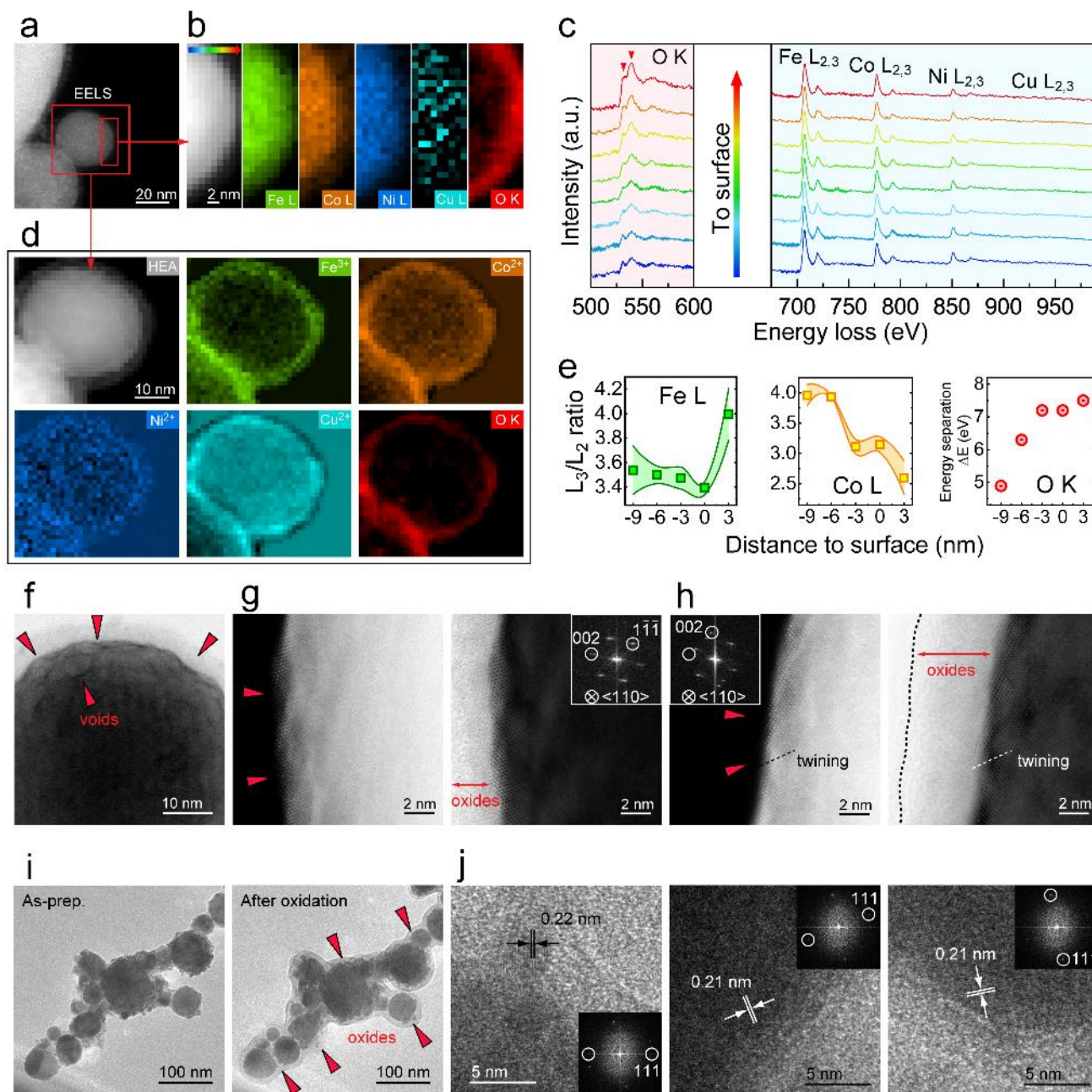
Figure 5-6. Oxidation of HEA NPs in air without electron beam. (**a**) LAADF images showing HEA NPs after *ex situ* oxidation in air. (**b**) Spectrum image corresponding to smaller red boxed region in **a** and EELS maps extracted from Fe, Co, Ni, Cu $L_{2,3}$-edges and O K-edge. (**c**) EEL spectra extracted from the spectrum image in **b** in the direction marked by rainbow arrow. The O pre-peak and main peak maximum marked

with red arrows are highlighted with dash lines. (**d**) EELS MLLS fitting showing the valence state map from larger red boxed region in **a**. The maps are displayed in sequence of fitting results from reference spectra of as-prepared HEA, Fe_2O_3, CoO, NiO and CuO. The last map was extract directly from O K-edge. (**e**) Fe and Co L_3/L_2 white-line intensity ratio as function of distance to surface obtained from another HEA NP after oxidation. Zero in horizontal axis represent the edge of NP, while positive values stand for outward directions. The third plot shows energy difference between O K-edge pre-peak and main peak (energy separation, ΔE) as function of distance to HEA surface. (**f**) ABF image of a HEA NP after *ex situ* oxidation showing plenty of voids less than 10 nm in length. (**g**) Atomic resolution HAADF and ABF image of a HEA NP edge after oxidation. Exemplar voids are marked by red arrows. The oxide layer is highlighted. Inset in ABF image is the corresponding FFT showing the NP in <110> zone axis. (**h**) Atomic resolution HAADF and ABF image of a HEA NP in <110> zone axis. Exemplar voids are marked by red arrows and oxide layer is highlighted. A twining can be observed in both images marked with dash lines, as well as in the FFT (inset in HAABF image) with two pairs of (002) diffraction spots. (**i**) TEM images showing the HEA NPs before (as-prepared) and after *in situ* oxidation in air without electron beam. Some of the formed oxide layers are highlighted by red arrows. (**j**) HRTEM images of HEA NPs after *in situ* oxidation in air without electron beam. The inset in each image shows FFT with corresponding highlighted HEA (111) planes (d ~ 0.21 nm). Note that the three FFTs are identical because they are from a larger region covering all three HRTEM images.

5.3.2 Reduction of HEA NPs in H_2

Next, *in situ* reduction on HEA NPs is shown as TEM image series in Figure 5-7. The process involves two steps: first *in situ* oxidation with same condition as previously discussed (in red box) and then *in situ* reduction in H_2 environment (in grey box). Since the individual HEA NP at left corner and three HEA NPs at top behave differently, zoomed in images focusing on different regions are displayed separately in Figure 5-8 and Figure 5-9. As shown in Figure 5-8a, in the oxidation process of individual HEA NP, oxide layer grows uniformly around the HEA NP similar to the NP in Figure 5-3c. Zoomed-in TEM images focusing on right edge of the NP (Figure 5-8b) in frame 1, 2 and 3 show the growth of oxide layer with thickness d_{OX} defined by difference between center of HEA NP to HEA surface (R_1) and center of HEA NP to oxide external surface (R_2). Evolution of d_{OX} in two directions and diameter D of the NP (marked in Figure 5-8a) is plotted in Figure 5-8c. Similar to oxidation kinetics of the NP in Figure 5-3c, logarithmic oxidation with rate constants K equal to 2.84 and 2.53 on left and right directions are identified, suggesting isotropic oxidation. The HEA diameter D does not show significant change as oxidation progresses. In the followed reduction progress, within 10 more min in H_2 (first frame in grey box, t= 80 min), the oxide layer becomes porous and cracks can be observed at interface between oxides and the HEA core. The oxide layer in both directions expand from ~10 nm to ~20 nm in thickness after H_2 penetration, accompanied by shrinkage of the HEA diameter from ~178 nm to ~173 nm. The expanded porous structure of oxide layer is further shown in the zoomed in TEM images in Figure 5-8d focusing on left edge of NP in first and last frame (numbered 4 and 5 in Figure 5-8a) during reduction progress. The *post situ* STEM-EDS mappings in Figure 5-8e show clearly that after H_2 reduction the HEA segregated into a reduced size HEA core with all five elements and an oxide layer containing Fe, Co, and Ni. The Cu

145

element, which is shown to be present in the oxide after oxidation, is not concentrated in the oxide after reduction but instead dispersed widely around the HEA core, suggesting that oxidized Cu has been mostly reduced by H_2. In contrast, Fe, Co, and Ni are not fully reduced and still preserved in the oxide region. The at. % distribution in boxed region on HAADF image shown in Figure 5-8f further indicates Fe, Co, and Ni are present both in and outside of the oxide, while Cu are present only outside the oxide external surface. The results suggest that during reduction all transition metals in the oxide react with H_2 and resulted in expansion of the oxide layer; simultaneously, the HEA core slightly shrinks and collapses due to the outward diffusion of transition metals and associated vacancies, leaving a gap between HEA core and the oxide internal surface.
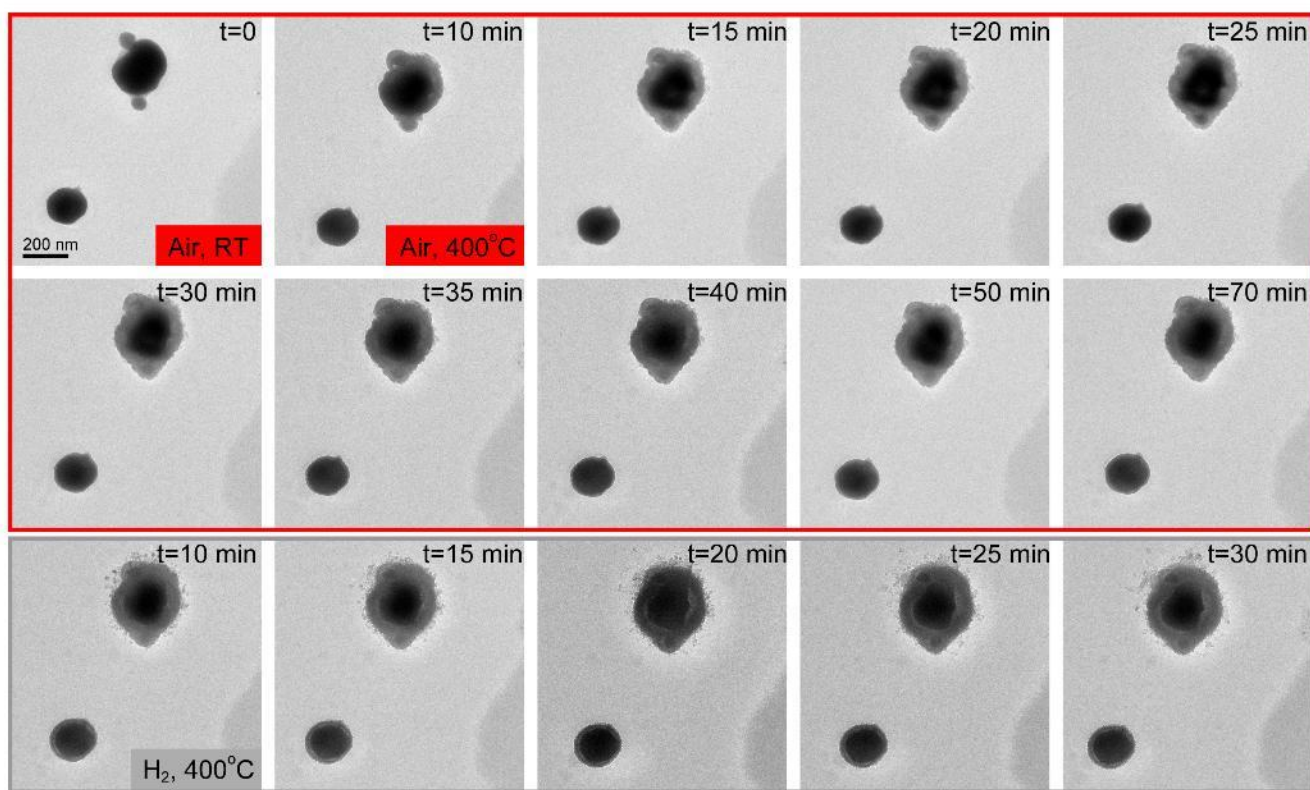
Figure 5-7. *In situ* TEM image series of HEA NPs annealing in air (red box, first two rows) and H_2 (grey

146
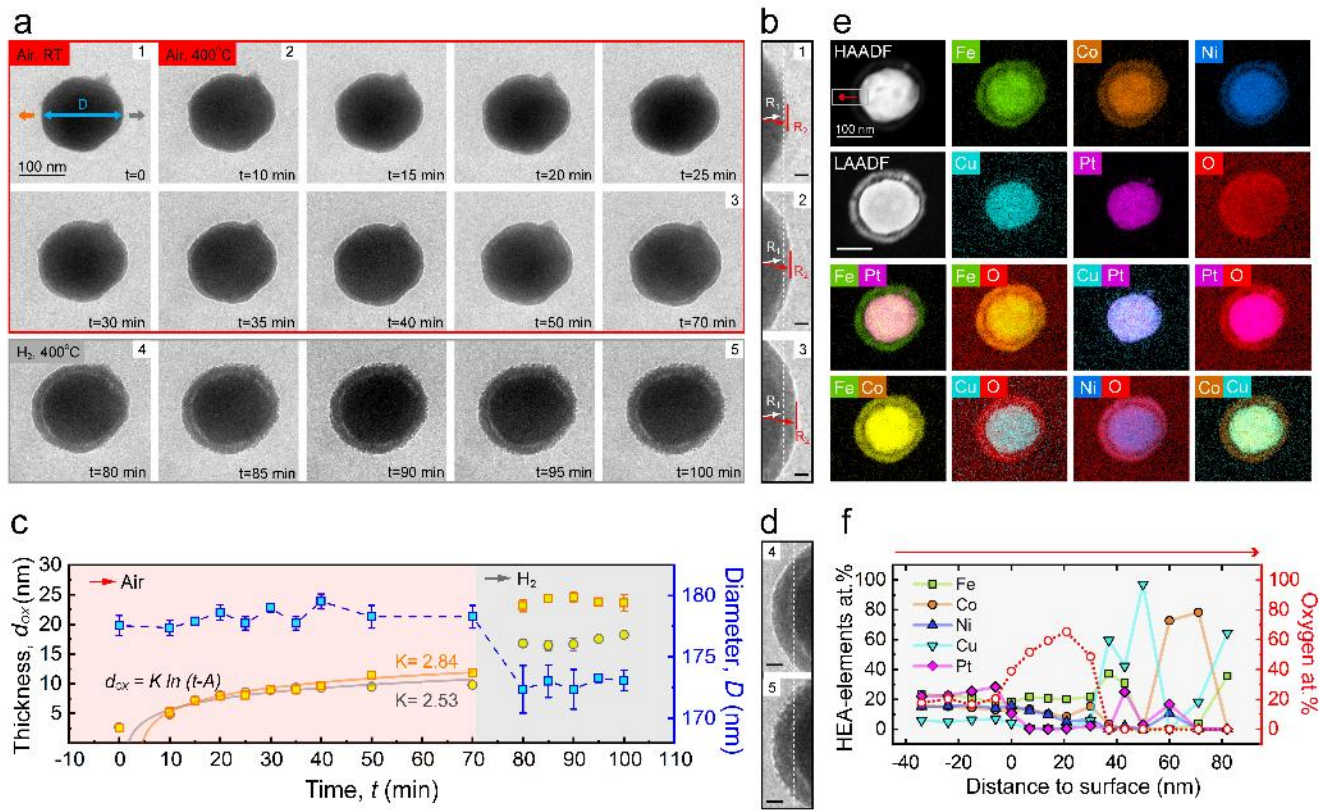
Figure 5-8. Oxidation and reduction of an individual HEA NP. (**a**) *In situ* TEM image sequences of HEA

NP during annealing in air (red box) and then H_2 (grey box). The temperature is RT in first frame and

400 °C in all other frames. (**b**) Zoom in of TEM images numbered 1, 2 and 3 in **a** focusing on the NP right

edge, showing the growth of oxide layer during annealing in air. The oxide thickness d_{OX} is defined by

R_2-R_1. The scale bars are 10 nm. (**c**) Oxide thickness d_{OX} and HEA NP diameter D as a function of time

measured from the direction marked in **a**. The diameter is shown in blue while oxide thickness is shown

in orange and grey in left and right directions. (**d**) Zoomed in of TEM images numbered 4 and 5 in **a**

focusing on the NP left edge, showing the formation of porous structure during annealing in H_2. The scale

147

bars are 20 nm. (**e**) *Post situ* HAADF and LAADF images of the same HEA NP after *in situ* experiment, EDS mappings of Fe, Co, Ni, Cu, Pt and O and selected overlaid EDS mappings. (**f**) At. % distribution of Fe, Co, Ni, Cu, Pt and O extracted from EDS. The arrow indicates the same directions as the arrows in HAADF image in **e**. Zero in the horizontal axis (distance to surface) represent the NP edge, while positive values stand for outward directions.

Figure 5-9 shows the oxidation and reduction process of the larger HEA NP in center and two adjacent smaller NPs. The oxidation seems significantly different compared to what has been shown in Figure 5-8, with very thick oxide layer formed nonuniformly within the first 10 min. Highlighted in the second frame with red arrows, the oxide is observed to initiate at the connecting regions between center large NP and small NP, and then grows rapidly into thick layer surrounding the whole particle. This phenomenon is consistent with what has been discussed in Figure 5-3 that adjacent HEA NPs display two-stage oxidation kinetics. At t= 40 min in the frame with dashed outline, energy-filtered transmission electron microscopy (EFTEM) was performed to further confirm the metals' outward diffusion. The EFTEM maps shown in Figure 5-9b include Fe L-edge, O K-edge and the overlaid image, suggesting that Fe is diffusing out to contribute to the oxide growth. The maps for other metals are not shown due to a decreased signal to noise ratio as their L-edges onset are in higher energy ranges for such *in situ* EFTEM. Figure 5-9c shows the oxide thickness d_{OX} and the center HEA NP diameter D as a function of time measured from the direction marked in Figure 5-9a. The diameter is shown in blue while oxide thickness is shown in orange in left direction. Accompanying the oxidation with K equals to 13.24, the NP diameter decreases from the

148

beginning. Compared to the individual smaller HEA NP shown in Figure 5-8, the faster oxidation rate leads to more voids formation and finally results in the voids collapse. This is observed as the HEA core diameter decreases and change of NP's shape. The oxide layer at the end of the oxidation process (t=70 min) are much thicker on the center large NP (~ 50 nm) than the two adjacent small NPs (~ 20 nm), again consistent with the results discussed in Figure 5-3. Since the center HEA NP has an initial size of ~ 245 nm that is larger than any of the ones shown in Figure 5-3 and Figure 5-4, it is expected that this NP displays the most significant oxidation including formation of voids and faster growth of oxide layer. In addition, this HEA NP has adjacent NP that may also increase the oxidation rate similarly to the case shown in Figure 5-3. Next, in the following reduction process, a slight expansion of the oxide layer and further shrinkage of HEA NP can be observed in Figure 5-9c, which is consistent with what has been discussed on the smaller individual HEA NP in Figure 5-8. Formation of porous structures can also be observed as shown in the enlarged TEM images in Figure 5-9d. The images are focused on the left edge of center HEA NP, with frame number the same as shown in Figure 5-9a. From the last frame of HEA in air (frame 1) to the first frame of HEA in H_2 (frame 2), the oxide layer transformed to porous-like and plenty of NP seeds can be seen to form on oxide external interface, as highlighted by grey arrows. These seeds, ranging from few to tens of nm, seems not to be stable as their location can change in time (frame 2-6). In order to understand their composition, *post situ* STEM and EDS results are shown in Figure 5-9e-g. HAADF and LAADF images in Figure 5-9e show clearly that the HEA NPs have segregated into a HEA core with reduced size and a porous oxide layer with some NP seed-features close to interface. EDS maps and overlaid elemental distribution in Figure 5-9f-g show that the seed-features are all non-oxidized

149

or pristine Cu NPs, while Fe, Co, and Ni mainly display a homogeneous mixing with oxygen. These indicate that Cu is the only element that has been reduced and segregated into Cu NPs from the oxide while the other three transition metals are not fully reduced and partially remain in the oxidized phase. The HEA core, although shrank, consists of all five elements Fe, Co, Ni, Cu and Pt. Further, atomic % distributions are extracted from the rectangle regions highlighted in HAADF image and shown in Figure 5-9h-j with same color. Similarly like the individual NP in Figure 5-8f, Cu are mostly present outside of the oxide layer rather than in the oxide, confirming the oxidized Cu have been reduced into Cu and segregated outward from external oxide interface. Furthermore, the HEA core of the center larger NP displays condensed Pt with atomic ratio more than 23.5 % while significant reduced amount of Fe (12%) and Co (8%) that resulted from the outward diffusion of Fe, Co, Ni and Cu, which is not obvious on the small NPs shown in Figure 5-8f with the less significant collapse (21% Pt, 22% Fe, 18% Co, 18% Ni, 7% Cu).
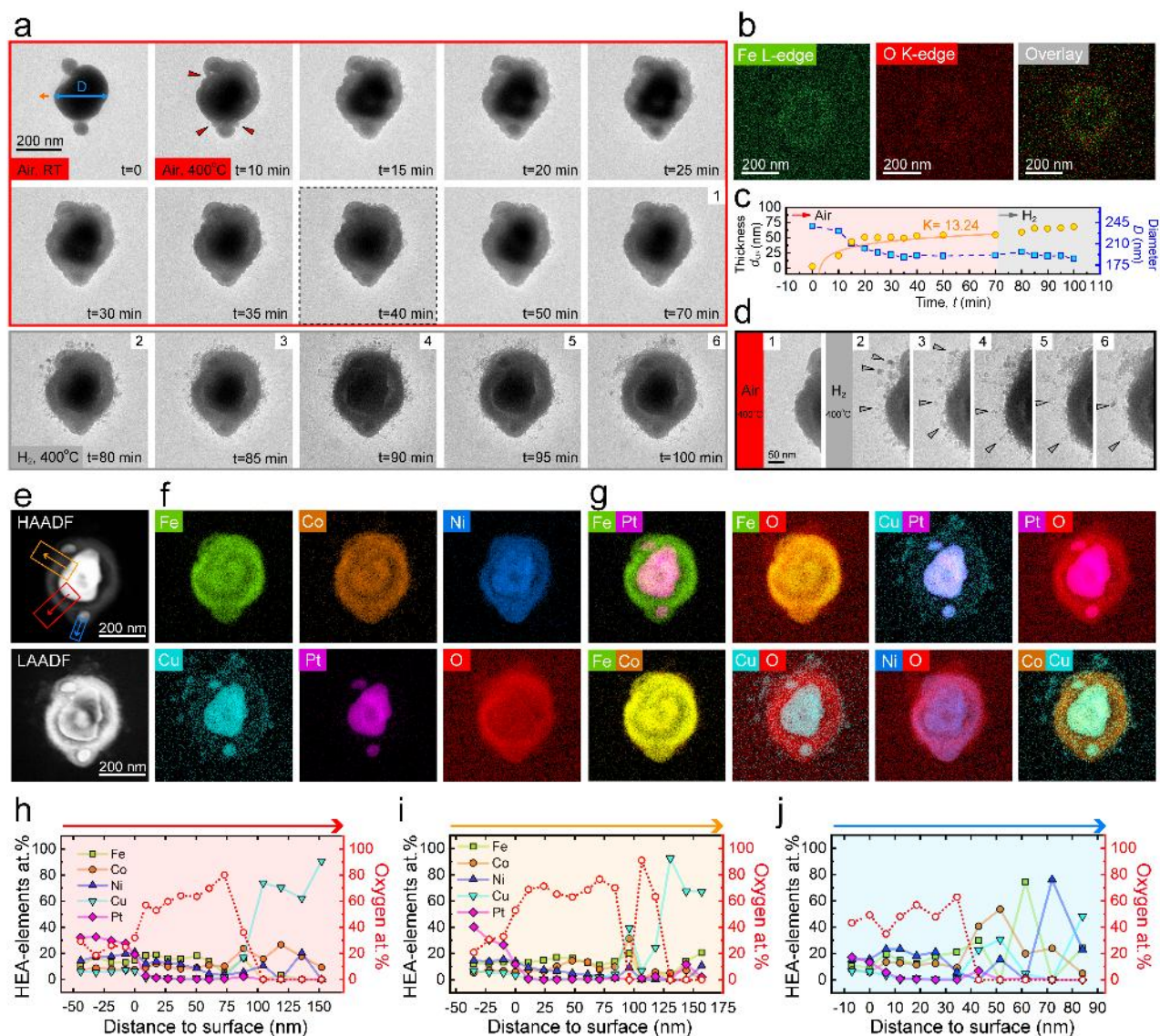
Figure 5-9. Oxidation and reduction of HEA NPs. (**a**) *In situ* TEM image sequences of HEA NPs during annealing in air (red box) and then H_2 (grey box). The temperature is RT in first frame and 400 °C in all other frames. (**b**) *In situ* EFTEM mappings obtained at the frame with dashed outline in **a** (t=40 min) showing Fe L-edge, O K-edge and the overlaid image. (**c**) Oxide thickness d_{OX} and the center HEA NP diameter D as a function of time measured from the direction marked in **a**. The diameter is shown in blue while oxide thickness is shown in orange in left direction. (**d**) Zoom in of TEM images numbered 1-6 in

151

a focusing on the left edge of largest NP, showing the formation of porous structures during annealing in H$_2$. Exemplar nuclei are highlighted with grey arrows. (**e**) *Post situ* HAADF and LAADF images of the same HEA NPs after *in situ* experiment. (**f**) EDS mappings of Fe, Co, Ni, Cu, Pt and O. (**g**) Selected overlaid EDS mappings. (**h-j**) At. % distribution of Fe, Co, Ni, Cu, Pt and O extracted from EDS. The arrow in each plot indicates the same directions as the arrows in HAADF image in **e**. The zero in the horizontal axis (Distance to surface) represent the edge of NP, while positive values stand for outward directions.

5.3.3 *In situ* EDS during oxidation and reduction

During *in situ* redox experiments, analytical methods like EELS are challenging due to the interference of SiN windows. To further understand the compositional evolution, *in situ* STEM-EDS are performed and shown in Movie S2. The HEA NP in the upper left corner is zoomed in and shown in Figure 5-10 and Figure 5-11 for oxidation and reduction process, respectively. ABF and HAADF images are displayed together with EDS maps for Fe, Co, Ni, Cu and O at different time. Outlines of HEA and the formed oxide are also shown in the last column. At RT, the HEA NPs show homogeneous mixing of all five elements with 2-3 nm native oxide covering the surface. The oxide is expected to originate from initial stage of oxidation driven by the Mott electric field between HEA surface and oxide layer, as predicted by the Cabrera-Mott model[79]. After 2 min at 400 °C, the oxide layer begins to grow and is denser on left side where two adjacent NPs are present. The gradual outward diffusion of Fe, Co, Ni and Cu evidenced through EDS maps suggests that the oxidation is guided by a Kirkendall effect. This outward diffusion of

152

transition metals results in voids formation close to HEA surface and voids collapse as vacancy diffusion, and finally lead to the shrinkage of HEA NP and notable segregation of Fe, Co, Ni, Cu to the outer oxide. In the followed reduction progress, it is obvious that the oxide layer is expanding as Fe, Co, Ni and Cu are reduced from oxidized form. Additionally, further outward diffusion of Fe, Co, Ni and Cu can be observed, resulting in a concertation gradient in the oxide, which is poor in Fe, Co, Ni and Cu at the internal surface but rich in them at external oxide surface. This leads to a deficiency of elements between HEA core and the internal oxide surface. Based on the Ellingham diagrams, Cu oxide is the least stable among other metal oxides at 400 °C and is thus preferable to be reduced. These observations are consistent with previously discussed oxidation and reduction behaviors. In addition, the *in situ* EDS analyses suggest that the outward diffusion of transition metals happens almost simultaneously from the beginning at 400 °C due to atomic homogeneity of as-prepared HEA, thus the composition gradient in the formed oxide are mainly induced by different diffusion rates among transition metals. Figure 5-12 shows the Arrhenius plots of diffusion coefficients for Fe, Co, Ni and Cu in their oxides. Fe has the highest diffusibility at 400 °C followed by Cu, Co and Ni, which is in partial agreement with experimental observations that outward diffusion of Fe and Cu are more notable than Co and Ni. However, the diffusion coefficient cannot explain why Cu shows the farthest diffusion distance from HEA surface among all transition metals, suggesting future investigations of metal diffusibility in different oxide matrices are indeed necessary.
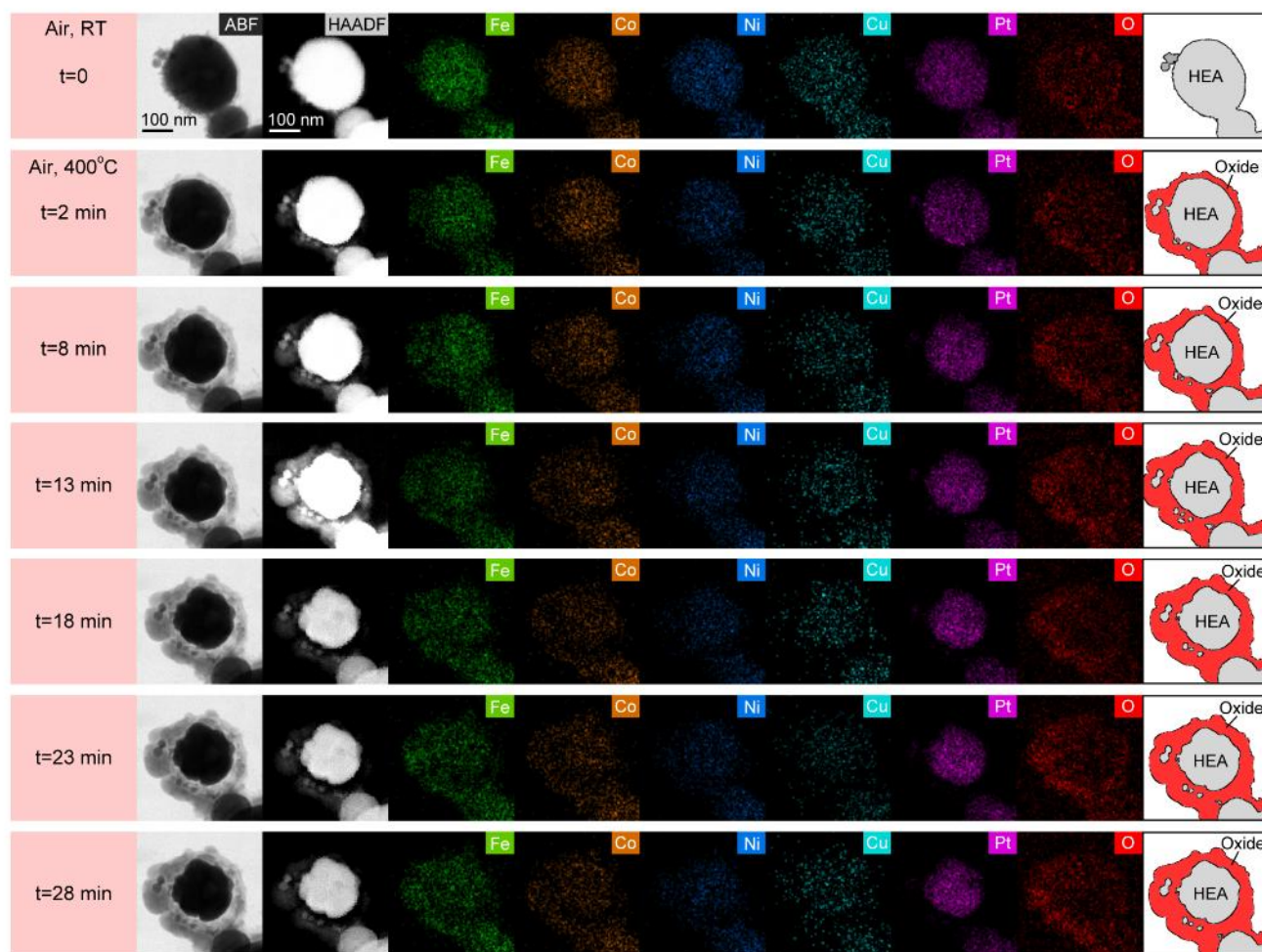
Figure 5-10. *In situ* EDS analysis on HEA NPs annealing in air. First column: time stamps; Second column: ABF images of HEA NPs annealing in air. From third column: HAADF images of the HEA NPs and corresponding EDS maps of Fe, Co, Ni, Cu, Pt and O. Last column: outlines of HEA NP and the formed oxides extracted from ABF images. The first row (t=0) corresponding to the condition at RT and is right before temperature ramping up to 400 ℃.
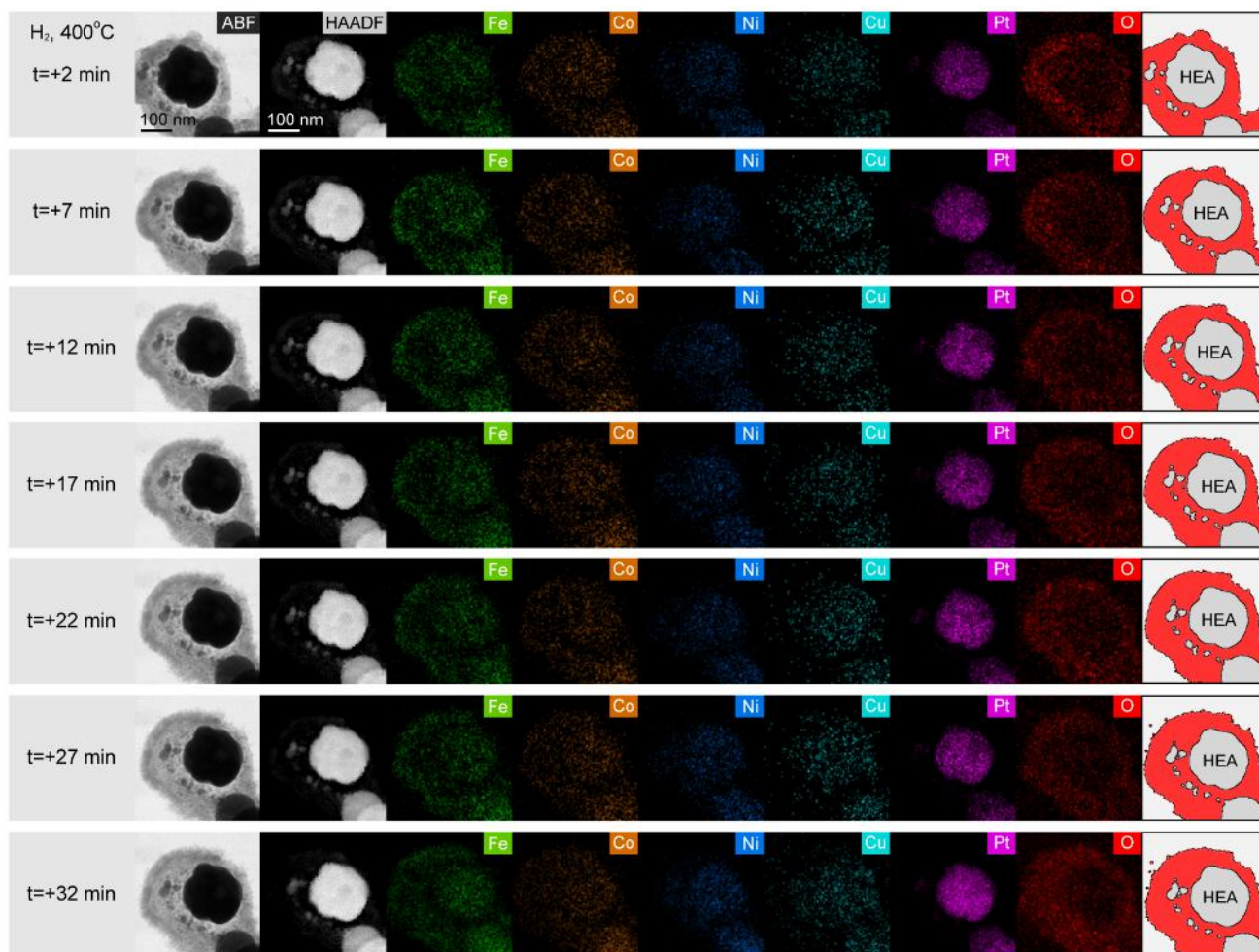
Figure 5-11. *In situ* EDS analysis on same HEA NPs annealing in H_2 right after oxidation shown in Figure 5-10. First column: time stamps; Second column: ABF images of HEA NPs annealing in H_2. From third column: HAADF images of the HEA NPs and corresponding EDS maps of Fe, Co, Ni, Cu, Pt and O. Last column: outlines of HEA NP and the oxides extracted from ABF images.

155
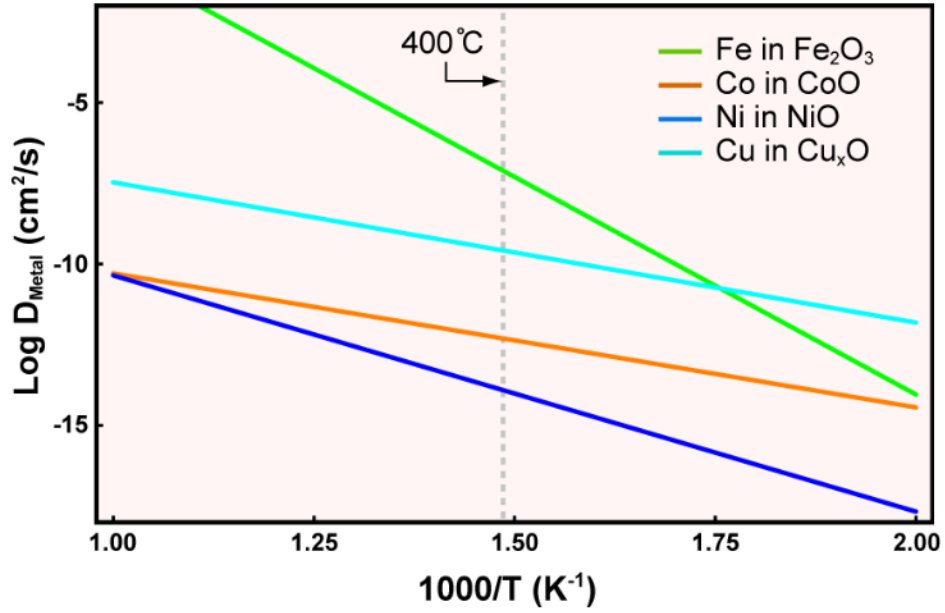
Figure 5-12. Arrhenius plots for diffusion coefficient D_{Metal} with temperature. Data of Fe in α-Fe_2O_3[266], Co in CoO[267], Ni in NiO[268], and Cu in Cu_xO[269] are from previous reports. Dashed line marks the experimental temperature condition equal to 400 °C.

Lastly, to confirm that the phase segregation is only induced by gases, results of *in situ* annealing of HEA NPs in vacuum environment are shown in Figure 5-13. The lower magnification HAADF images (Figure 5-13a) shows HEA NPs from RT to 400 °C and back to RT, with no observable change in particle size, shape, and evidence of oxidation during the whole process. Only slight movement of few small NPs can be seen as highlighted with arrows. The higher magnification HAADF images (Figure 5-13b) focusing on fewer HEA NPs on another region suggest the same behavior that no observable phase segregation is present. These results indicate the phase segregation is induced by oxidizing/reducing environments instead of electron beam effect.

156
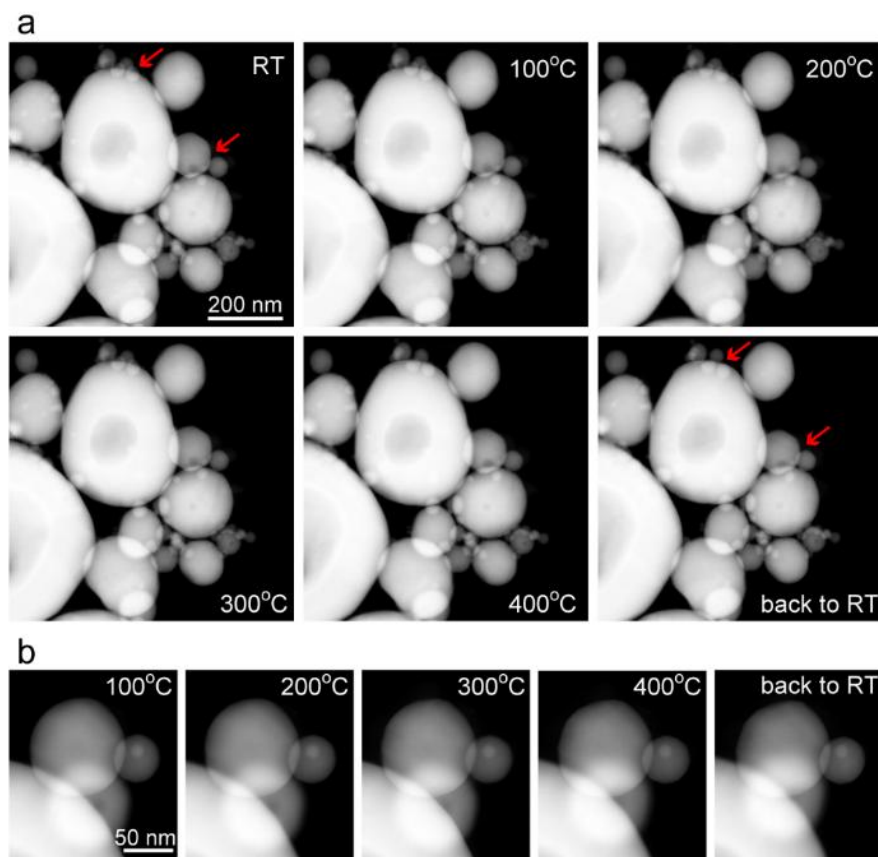
Figure 5-13. *In situ* annealing of HEA NPs in vacuum environment. (**a**) HAADF image series of HEA NPs from RT to 400 °C. Red arrows marked exemplar NPs that underwent slight movements. (**b**) HAADF image series focused on several smaller HEA NPs from RT to 400 °C.

5.3.4 Molecular Modeling of Oxidation and Reduction

We carried out density functional theory (DFT) calculations to further understand the oxidation/reduction processes of the HEA NPs. First, we investigated the stability of a bulk random alloy consistent with the $Fe_{0.28}Co_{0.21}Ni_{0.20}Cu_{0.08}Pt_{0.23}$ chemical composition that is inferred experimentally.

157

Using a single random realization of the alloy, we compared the energies of two models of the alloy with FCC or BCC lattice symmetry. After a full optimization including atomic positions and lattice constant, we find that the FCC system is 0.05 eV/atom lower in energy than the BCC one. We obtained similar results using different random samples of the FCC and BCC alloys. Thus, the alloy has an FCC symmetry that agrees with the experimental results. In addition, the optimum lattice constant of the FCC lattice is found to be 3.61 Å that correlates to a d-spacing of 2.1 Å for {111} planes, which is very close to the experimentally determined d-spacing of the same planes.

DFT simulations using few models of the alloy do not capture the configurational entropy that is key for the stability of HEAs. To address this shortcoming, we carried out calculations using a hybrid Monte Carlo (MC)/molecular dynamics (MD) approach based on energies and forces computed using DFT. This scheme involves short *ab initio* molecular dynamics runs and random exchange between atoms at different locations, in which the last configuration is accepted or rejected using a standard Metropolis algorithm.[270][247] There are several advantages of MC/MD; it automatically accounts for impurity-impurity or impurity-host interactions, temperature, mixing entropy, and atomic vibrations. Following the MC/MD simulations, we find that in equilibrium the alloy has a uniform distribution of the elements. Also, consistent with the static full optimization calculations, the HEA with FCC symmetry is found to be ~0.05 eV/atom lower in energy than that of the BCC one at all investigated temperatures 100 - 900 °C (Figure 5-14).
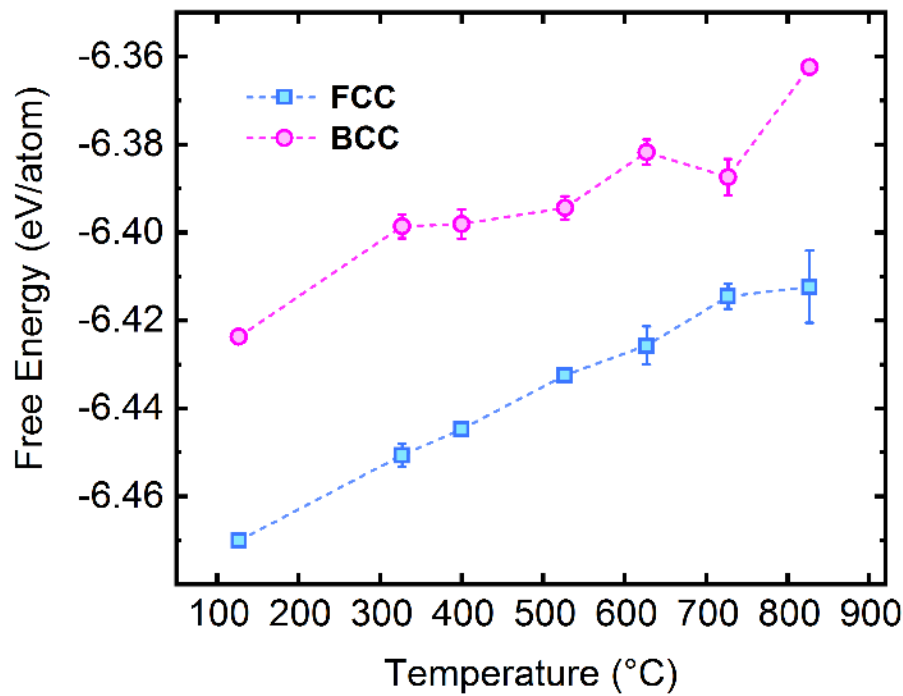
Figure 5-14. Comparison between the FCC and BCC energies of the HEA as obtained from MC/MD simulations.

Next, we studied the impact of oxidation and reduction on the stability of the HEAs. First, we examined stabilization energies due to potential segregation under oxidizing/reducing conditions. We constructed 5 alloy models that differ in the identity of the element enriching the top layer but is random otherwise, in addition to three different alloy models with complete random distribution. In these studies, we employed surface slab models well representing the large ~ 50 - 200 nm NPs that are seen experimentally. Further, we also verified that a smaller ~1 nm NP (Figure 5-15, Figure 5-16, and Figure 5-17) displays similar energy preferences. The oxidizing/reduction conditions are modeled by adsorbing oxygen or hydrogen on the top surface.[271-274] Starting from the initial configuration constructed using

159

FCC with lattice constant 3.61 Å, we relaxed the atomic positions to ground state equilibrium structure at T = 0 Kelvin, and then conducted a 4 pico-second (ps) *ab initio* molecular dynamic trajectory within NVT ensemble (constant number of particles, volume and temperature) at T = 400 °C. Figure 5-18a shows the energies of the different models averaged over the last 2 ps, as measured with respect to the random alloy model. Here Fe, Co and Pt segregated surfaces have high energies due to their large surface energies compared to that of Ni and Cu.[275] It is noted that the high entropy of mixing is not included in the energies of Figure 5-18a, and hence models that have lower energies than the random alloy one such as the Cu rich surface are not indicative that segregation is preferable for the pristine surface. For instance, based on ideal mixing of the elements, the configuration entropy $-k_B \sum_{i=0}^{5} x_i \ln x_i$ (k_B is Boltzmann constant and x_i is metals concentration) lowers the free energies by ~ 0.09 eV/atom for the alloy at 400°C. As we will show later, we do not have any elements segregation for the pristine HEA surfaces when configurational entropy is accounted for by employing the hybrid MC/MD approach.

160
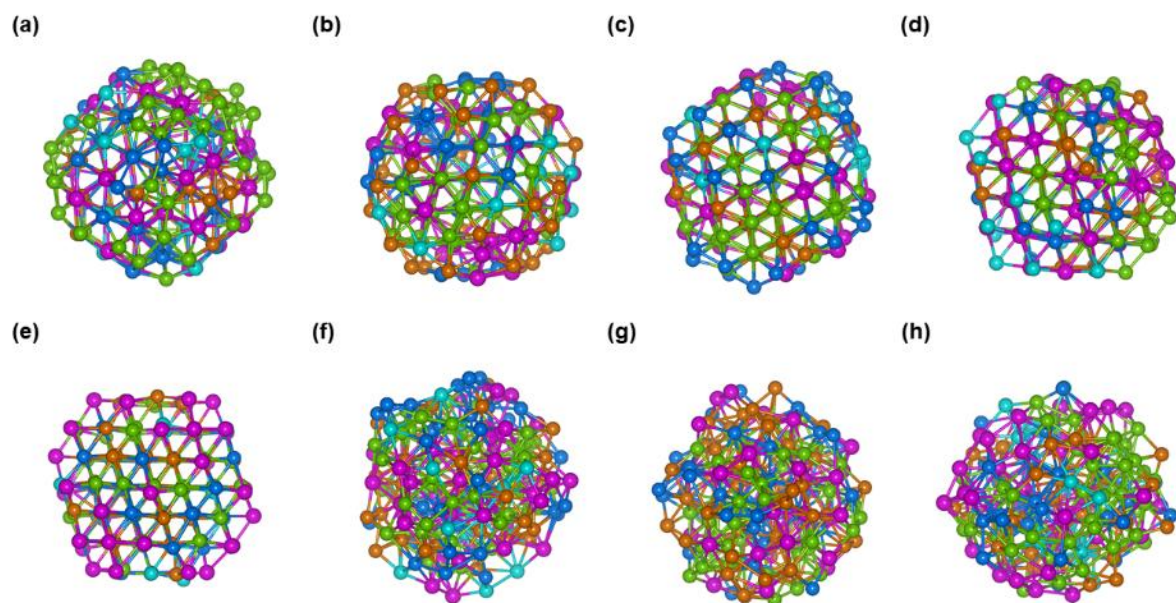
Figure 5-15. Alloy models for a 7 Å NP with (**a**) Fe (**b**) Co, (**c**) Ni, (**d**) Cu, and (**e**) Pt surface segregation, and (**f-h**) homogenous alloying. In the segregated models, the surfaces are rich in different elements while the core is random.
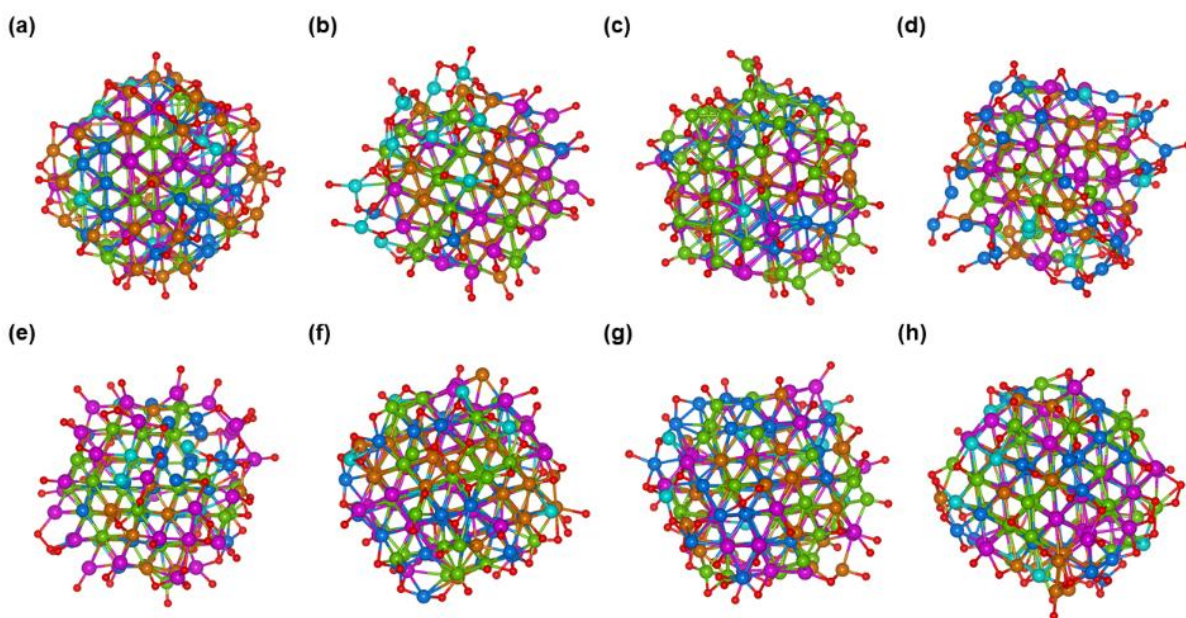
Figure 5-16. Corresponding models as in Figure S11 after oxidation with ~ 60 oxygen atoms.
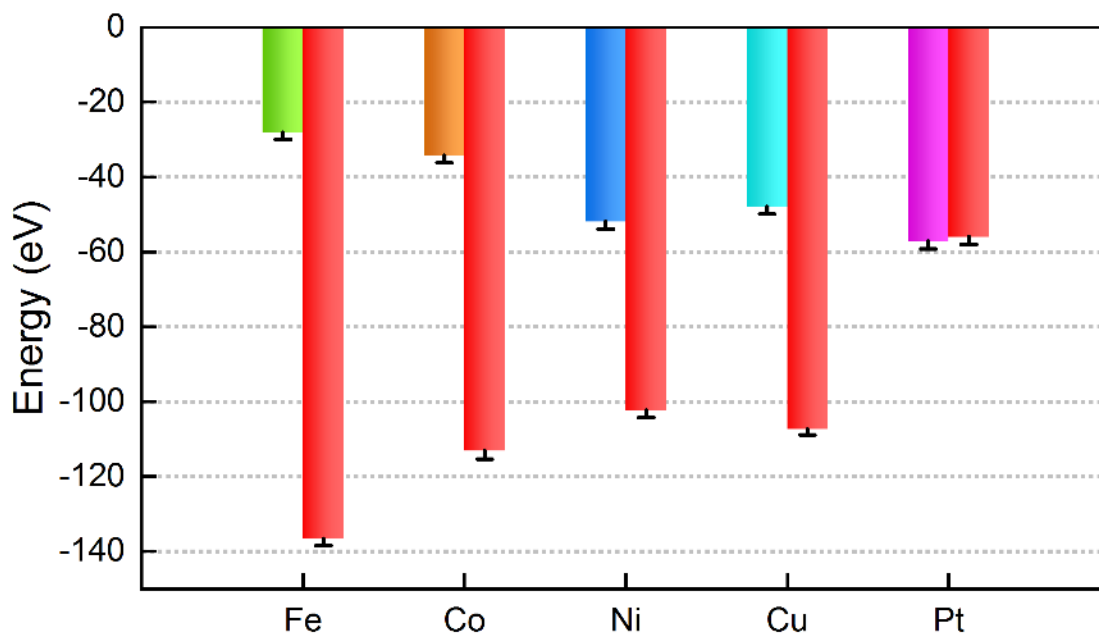
Figure 5-17. Normalized energies for the NP models shown in Figure S11 and Figure S12 compared to the random alloy model. For each element, we show the corresponding energy of the oxidized (red) NP.

As seen from the energies in Figure 5-18a, oxidation significantly stabilizes surfaces that are rich in Fe and Co compared to the random alloy, and to a lesser extent surfaces rich in Ni and Cu. However, Pt-rich surfaces have significantly higher energy compared to the random alloy surface. Thus, under oxidation, surfaces of the NPs are expected to be poor in the noble metal Pt but rich in Fe, Co and to a lesser extent Cu and Ni. In contrast, as seem from the figure, hydrogen does not induce any strong segregation preferences in agreement with experimental results shown in Figure S7. The obtained energy trends for the oxidized/reduced slab models can be understood by examining the formation energies of the corresponding bulk oxides and hydrides. For the metal oxides, the order of the formation energies is Fe

162

(1.7), Co (1.3), Cu (1.0), Ni (0.9), and Pt (0.6) with the numbers in parenthesis showing the DFT formation energies in eV/atom. Thus, Fe forms the most stable oxide with a formation energy of 1.7 eV/atom and Pt is the least stable one with 0.6 eV/atom. Similar conclusions can also be reached by inspecting the Ellingham diagrams of these oxides. In contrast, the corresponding metal hydrides are all significantly less stable than the oxides with formation energies that vary between 0.1 - 0.2 eV/atom, and with Ni the most stable followed by Fe, Co, Cu and Pt.

MC/MD simulations are then carried for the slab models to determine their equilibrium composition while accounting for temperature and entropy effects. Figure 5-18b shows a layer-by-layer surface decomposition obtained by analyzing equilibrium configurations from the MC/MD simulations. An exemplary configuration is shown in Figure 5-18c. As seen from the figure, while we have a relatively uniform distribution of the elements for the bare or hydrogen-reduced surfaces, there is a strong segregation preference for some elements to the top layers under oxidation conditions. For instance, compared to the bare surface, we see a notable enrichment of Fe and Co in the top exposed layers but a significant reduction of Pt. This is also consistent with the trends inferred from the energies of the segregated models of Figure 5-18a. Further, the oxidation process increases the thickness of the substrate resulting in the formation of an additional layer. As seen in Figure 5-18c, an equilibrium configuration during the oxidation shows formation of vacancies in subsurface layers due to a Kirkendall effect from the inequivalent inner/outer diffusion of oxygen/metal. Also, the oxidized slab models retain FCC symmetry away from the surface, again consistent with the experimentally observed FCC lattices after

163

oxidation. Although the slab models are relatively small to show the formation of any nanocrystalline

oxides, we see from Bader charge analysis in Table 5-1 that the chemical environment of the metals in the

oxide layer are similar to the corresponding Fe_2O_3, CoO, NiO and CuO oxides that are inferred

experimentally.
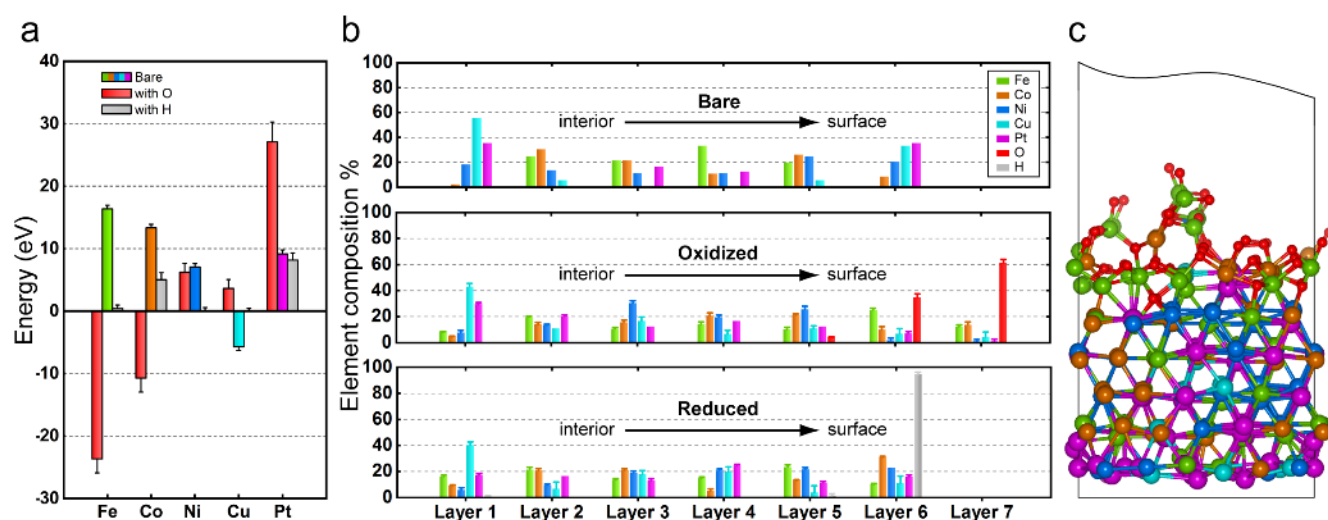
Figure 5-18. (**a**) Total energies for slab models with different elements segregation compared to the

random alloy model. For each model, we show the corresponding energy of the oxidized (red) or reduced

surface with hydrogen (gray). Negative values indicate enhanced stability compared to random alloy

without accounting for configurational entropy. Statistical errors for the energies extracted from molecular

trajectory are shown. (**b**) Equilibrium layer-by-layer surface composition for bare, oxidized and hydrogen-

reduced surfaces at 400 °C. The error bars indicate statistical errors from equilibrium structures obtained

from MC/MD. Oxidation increases the thickness of the slab and leads to the formation of an extra layer.

(**c**) Exemplary atomic model for an oxidized slab from the MC/MD ensemble after equilibration.

164

Table 5-1. Bader charge analysis. The average number of valence electron of the metal atom M (Fe, Co, Ni and Cu) far from the surface (core-metal) and on the surface for the HEA slab model. For comparison, we show the charge of the corresponding oxides Fe_2O_3, CoO, CuO, and NiO in the last column.

M type	Core-metal	Surface-metal	M_xO_y
Fe	7.7	7.0	6.6
Co	8.8	8.1	7.9
Ni	9.9	9.0	8.8
Cu	10.8	10.0	10

5.4 Conclusions

The present work provides *in situ* TEM observation and DFT study of phase segregation in HEA NPs during high temperature redox reactions. The oxidation of HEA NPs in air is guided by Kirkendall effects with logarithmic rate constants that will prevent further oxidation. Analytical EDS, EELS and HRTEM provide direct evidence of transition metals segregation by outward diffusion and disordered oxide layer formation. In addition, localized ordering is identified in the oxide layer that possibly belong to lattices from Fe_2O_3, CoO, NiO and CuO crystallites. In H_2 reducing environment, expansion of oxide layer and transformation into porous structures are observed as H_2 takes away oxygen. The oxidized Cu can be fully reduced and further segregated into Cu NPs while Fe, Co, and Ni are rarely fully reduced. Simulations using hybrid Monte Carlo/molecular dynamics simulations based on DFT energies and forces confirm the

165

stabilization of the alloy solution for the bare and hydrogen reduced surfaces, and show that oxidation drive Fe, Co, Ni and Cu segregation to the top layers in agreement with experimental results. The present study is crucial for understanding HEA behavior in oxidation and reduction environments and provide insights in designing high corrosion resistance alloys for various applications.

Chapter 6   Future work

6.1 *In situ* TEM of HEA NPs catalytic reaction with gas composition analyzer

6.1.1 Overview

High-entropy alloys (HEA), an emerging material compound involving five or more principle elements in a single phase solid solution, is being recognized as promising materials for applications in catalysis and structural alloys. Recently the successful synthesis of HEA NPs via thermal shock[233] and aerosol[234] methods has made the scale up fabrication possible for industrial applications. The use of HEA NPs as catalysts for wide range catalytic reactions have been predicted by theoretical calculations and some of them studied by experiments involving oxygen reduction and evolution, hydrogen evolution, CO oxidation, ammonia oxidation and decomposition,[276] and methanol oxidation, and CO_2 reduction.[277]

During the working condition of HEA NPs under such catalytic reactions, the structural and chemical status of working HEA NP catalysts remains unknown due to the challenge of obtaining nanoscale information regarding to the typical few nanometer sizes of HEA NPs. Such information is used to be obtained by bulk phase analytical methods such as XRD and TGA. *In situ* gas-cell TEM, benefiting from its high spatial and temporal resolution, serves as an ideal method to bridge the gap between bulk and nano-scale characterizing especially during catalytic reactions. Here, we propose to investigate the structural and chemical evolution in HEA NP catalysts subjected to gas environments and elevated temperatures with *in situ* monitoring of gas compositions.

6.1.2 Experimental setup

Figure 6-1a shows the schematic of *in situ* TEM setup, with *in situ* gas-cell TEM holder being used and connected with a residual gas analyzer (RGA) system with capability of analyzing gas composition in real-time. Figure 6-1b shows the specimen region inside the gas cell reaction, including a pair of Si microchips with HEA NPs sample on the side with heater. The distance between two Si microchips can range between 50 nm and 5 μm to accommodate different specimen thickness. Gases can be flowed into the cell with a volumetric flow rate of 0.5 sccm or less. Gas type includes air, N_2, H_2, CO_2, water vapor, and CO, CH_4, etc. The gas flow controller has the capability of flowing one type of gas or a combination of several gases at the same time. The pressure inside the cell is approximately 1 atmosphere. A temperature controller is used to set the temperature from RT to 1000 °C without the need for any external cooling system. The *in situ* gas-cell allows atomic resolution imaging at both room and elevated temperatures. Figure 6-1c shows an example HRTEM image of HEA NP oxidized in air environment at 400 °C, with corresponding FFT shown in d. The lattices from HEA (111) plane and from oxide can be clearly resolved, demonstrating the atomic resolution imaging capability of the *in situ* gas-cell setup.
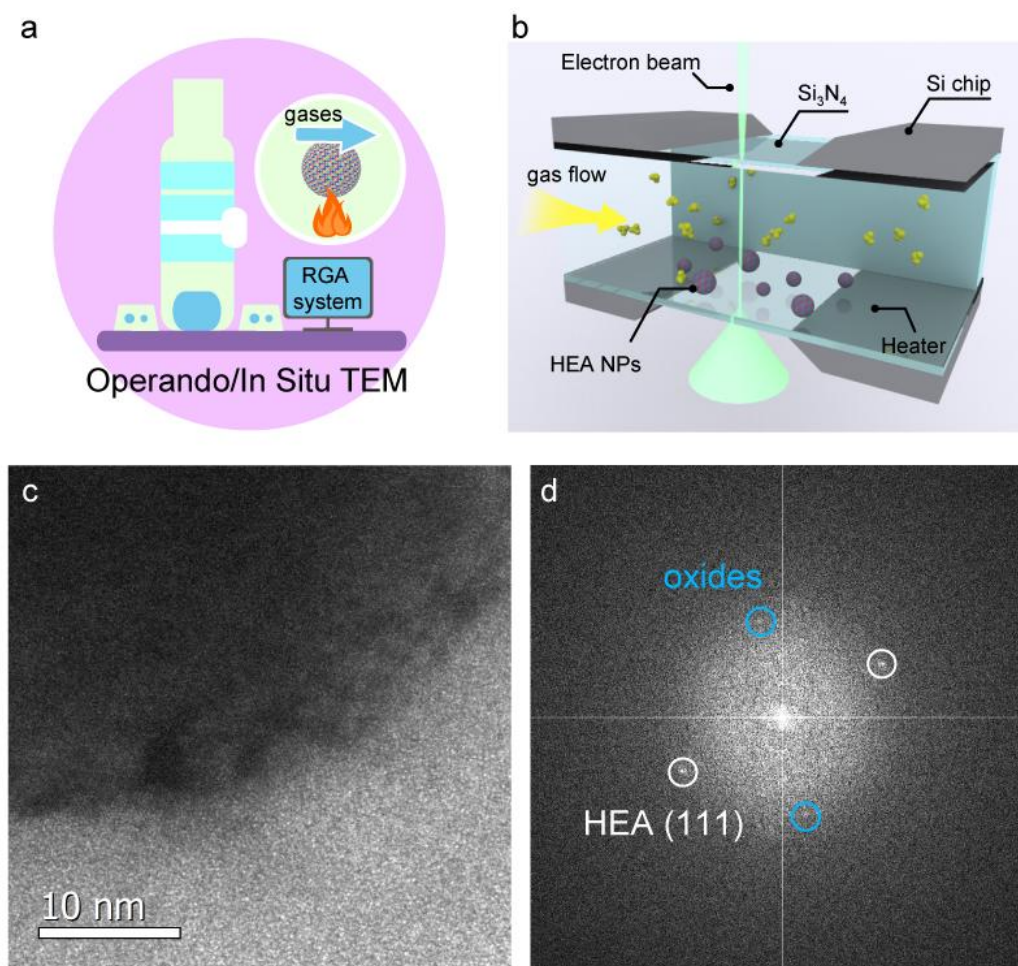
Figure 6-1. (a) Schematic showing the *in situ*/operando TEM experiments on HEA catalytic reactions. A residual gas analyzer (RGA) system is attached to the specimen holder for real-time analyze of gas compositions. **(b)** Schematic showing the specimen region in gas cell TEM holder. **(c)** HRTEM image of HEA NPs oxidized in air at 400 °C for about 1 hour. **(d)** The corresponding FFT of c showing diffraction spots from HEA and oxide planes.

In situ gas cell experiments is carried out using a field emission JEOL 2100F microscope operated at 200kV at Center for Nanoscale Materials, Argonne National Laboratory. Additionally, with same *in situ*

169

gas-cell holder available at Northwestern University combined with aberration corrected JEOL ARM-200CF microscope, advanced Z-contrast STEM imaging can be done such as HAADF, LAADF, ABF, which further extend the capability. Atomic resolution EDS and EELS mapping focusing locally on less than 50 nm HEA NPs is achievable, allowing the investigation of structure and composition in sub-angstrom manner. In addition, the EDS and EELS both can be done *in situ* simultaneously with imaging, allowing extracting both structural and chemical information in a time-resolved manner.

6.1.3 Structural analyses of HEA NP evolution

In situ TEM provides direct observation of the morphology changes of samples inside the gas cell, with sub-nanometer spatial resolution. The *in situ* gas cell TEM holder is capable of tilting in α direction and thus atomic resolution imaging is achievable. By looking at a desired amount of HEA NPs on the microchip, it is very possible to locate NPs that is on zone, resolving their atomic structures. In addition, the morphology evolution during HEA NPs catalytic reactions in service environments such as high temperature air, water vapor, H_2, CO_2, CH_4, NH_3, and many other gas environments can be realized in real time by combined HRTEM imaging and diffraction analyses. Further, such evolution can be captured in whole during the reactions as videos. Formation of new layers over HEA NPs, surface reconstruction, and phase segregation during reactions can be investigated through HRTEM, HAADF, LAADF, ABF imaging techniques.

6.1.4 Analytical studies of HEA composition evolution

The energy loss near edge fine structure (ELNES) and extended energy loss fine structure (EXELFS) analyses for oxygen K edge and several transition metal $L_{2,3}$, $M_{4,5}$ edges can be performed within a single collection at 0.5 eV energy resolution, allowing a detailed understanding of products composition.

6.1.5 Analytical studies of gas composition evolution

The composition of gas input through the inlet channel on gas-cell holder can be monitored in real-time by a gas controller, simultaneously, the gas residual flowing out from the outlet channel can be analyzed through a residual gas analyzer (RGA) very close to the reaction chamber. This system equipped with software-controlled ability to detect and analyze real-time gas products between and after *in situ* gas-cell TEM experiments, allowing detailed information regarding reaction kinetics and products. The connection with the TEM holder is short to ensure a quick response time in detecting the gas composition, usually in less than a few seconds. Therefore, a correlation between *in situ* imaging/video recording and gas composition evolution can be made. For HEA catalytic properties, the following reactions will be focused: CO oxidation and methanol oxidation. Gases phase CO and methanol are flowed into the gas cell while maintaining a high temperature in the HEA NPs catalysts region. When gas molecules reach the surface of HEA NPs, dissociation of the gas molecules and chemisorption of gas atoms onto the metals will generate metal-gas species. Different than monometallic NPs, the chemisorption may happen selectively on fewer kind of metal atoms, resulting in the catalytic active site becomes anisotropic. For instance, CO adsorption on AuCu alloy NPs show preferable activated surface and dynamic atom clusters on (010) facets. In O_2 environment, oxidation and segregation of Cu were observed and formed Cu_2O at AuCu

171

interface.[48] Such surface reconstruction induced by chemisorption of gas molecules on HEA NPs can be captured in real-time, while the residual gas composition can be analyzed with correlation to the same time scale during the *in situ* experiments. For instance, the amount of formed carbon dioxide during the catalytic reactions are detected by RGA such that the reaction kinetics can be determined and correlated with morphology changes of HEA NPs.

6.1.6 Post situ analyses of HEA NPs

Post situ analysis on HEA NPs can be done using a specialized designed holder with high resolution tomography, EDS and EELS ability, with less interference from Si_3N_4 window. The structural information is obtained by combined imaging techniques including HRTEM, HAADF, LAADF, ABF and diffraction.

Compositional-wise, the dual EELS setup at University of Illinois at Chicago is especially powerful to analysis the chemical composition of HEA NPs due to the simultaneous collection of two energy ranges, including any combination of zero loss peak, low-loss region and high-loss region. The energy loss near edge fine structure (ELNES) and extended energy loss fine structure (EXELFS) analysis for oxygen K edge and several transition metal $L_{2,3}$, $M_{4,5}$ edges can be performed within a single collection at 0.5 eV energy resolution, allowing a detailed understanding of reaction products composition. In addition, the chemical state of different transition metals in HEA NPs can be obtained from EELS white-line intensity ratio analysis, such as Ti, Cr, Mn, Fe, Co, Ni $L_{2,3}$ edges and Nb, Mo $M_{4,5}$ edges. The edge onset for these transition metals are shown in Table 6-1.[278] The chemical composition of reconstructed HEA surface is also achievable through combined EELS analysis via dual EELS setup.

172

Table 6-1. Energy onset of L and M edges for exemplar transition metals.

	L_3/L_2 (eV)	$M_{4,5}$ (eV)
Ti	456/462	-
Cr	575/584	-
Mn	640/651	-
Fe	708/721	-
Co	779/794	-
Ni	855/872	-
Nb	-	205
Mo	-	227

6.2 *In situ* nucleation and growth studies of HEAs using liquid TEM

6.2.1 Overview

Although HEA NPs have been reported by various synthesis method such as bulk melting,[224, 225] solid-state processing,[226-228] physical vapor deposition,[229] additive manufacturing,[230-232] carbothermal shock[233], and aerosol synthesis, [234] little is known of how the multiple elements combined together to form well-mixed single phase solid solution alloys. Insights of the nucleation and growth process of such HEA NPs during their initial fabrication stage can shed light on further design of highly stable alloy systems, and help further improve the properties in structural, thermal, corrosion-resistance and catalytic activity/durability.

In situ liquid-phase TEM can be an ideal method to directly observe the initial nucleation and growth of HEA NPs with high spatial and temporal resolution. The whole process can be monitored in real-time and reaction kinetics can be obtained by analyzing the movies frame-by-frame. Combining the *in situ*

173

analytical EDS capability, one can extract chemical composition information during reaction process and link such compositional evolution with structural dynamics. Here, we target combining two *in situ* TEM techniques for such study: *in situ* graphene liquid cell TEM and *in situ* liquid-flow TEM. The former one is especially ideal for atomic resolution imaging and EDS on nucleation and growth process of HEA NPs in liquid phase, providing high pressure inside the graphene liquid cell to trigger nucleation process. The latter method is ideal for statistical analysis of overall behavior by looking at HEA NPs in relatively lower-magnifications. In addition, the *in situ* liquid-flow method allow the introduction of liquid into the reaction chamber such that the influence of external reaction agents on nucleation and growth process can be studied.

6.2.2 Experimental setup

Liquid-flow TEM holder

Figure 6-2a shows the schematic of *in situ* liquid holder. The idea of liquid-flow TEM method is isolated metal salt precursor solutions by one pair of microchips. Liquid metal salt precursor solutions are drop-casted onto one of the microchips and the other microchip sealed the liquid cell before the solution dry-out. Electron transparent Si_3N_4 windows are on both side of Si microchips to allow real time observation. The window on each microchip has 50 nm thickness and a dimension of 550×20 μm^2. Windows can be aligned in either parallel or perpendicular to provide maximized or confined viewing area. The *in situ* liquid-cell holder allow either static or flowing liquid conditions, with a maximum flow rate of 350 μL/h. This allows the study of how external metal salt precursor influence the nucleation and growth process. 174

TEM, HRTEM and (S)TEM imaging and video recording can be done during the whole *in situ* experiment.
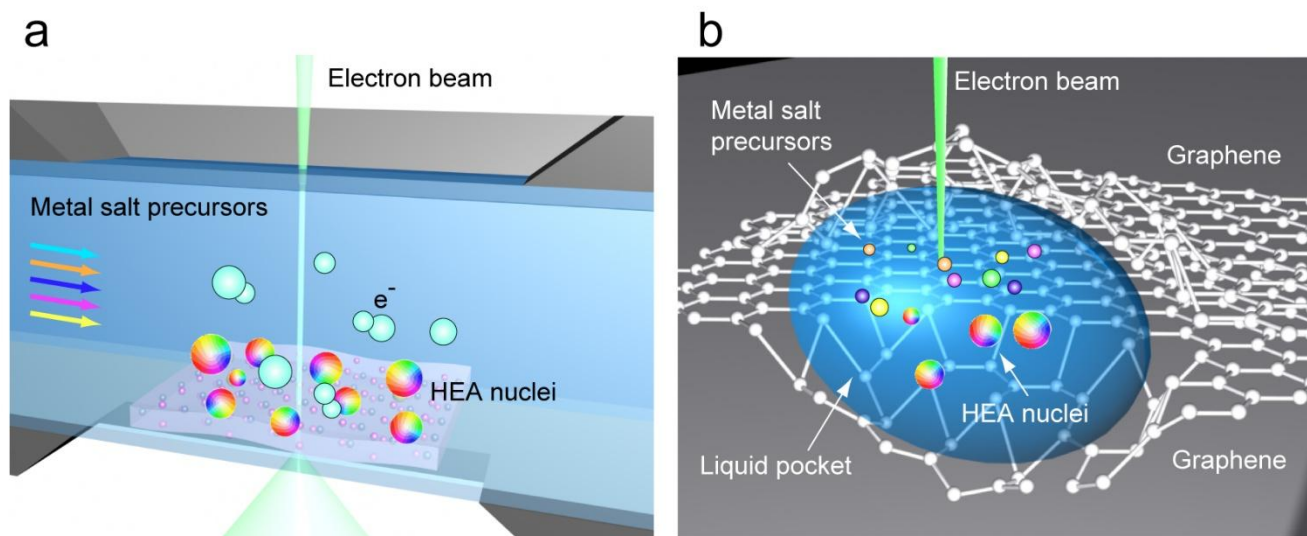
Figure 6-2. (a) Schematic of *in situ* liquid-cell (S)TEM to study nucleation and growth of HEA NPs in aqueous solution. **(b)** Schematic of GLC for study of HEA nucleation and growth in liquid.

Graphene liquid cell (GLC)

The schematic of GLC is shown in Figure 6-2b.[25] To prepare GLC, a general method is involved including fabrication of single or few-layer high quality graphene, transfer the graphene layer onto TEM grid, loading metal salt precursor solutions onto the graphene layer and final isolate the liquid cell by putting another graphene layer on top of the bottom graphene. The fabricated GLC can be loaded directly to conventional TEM holders without the need for specialized *in situ* holders. In comparison to liquid-flow TEM holder, GLC provide advantages including ensure a much better spatial resolution in imaging/video recording as well as much better SNR in analytical techniques like EELS/EDS. However, the short comes of GLC are specific to lack of the ability of flowing liquid in/out from the cell that are

necessary to observe the reaction starting from the initial stage. Therefore, one can expect to extract the most information from structural and chemical aspects by combing the two *in situ* techniques together.

6.2.3 Structural analyses of HEA NP evolution

The morphological evolution of HEA NPs are captured in real-time via liquid-flow TEM method. Staying at a relatively lower magnification, one can ensure a larger filed-of-view to include as much of nucleation center as possible to extract statistical information. By measuring the particle size and shape evolution as a functional of time, critical radius of nuclei formation can be determined. It is expected that the critical radius of HEA nuclei is determined by the total free Gibbs energy discussed in Chapter 2.1:

$$\Delta G = 4\pi r^2 \gamma + \frac{4}{3}\pi r^3 \Delta G_v$$

but the value of radius can be different compared to the nucleation of monometallic element since both the bulk free energy and surface energy can varies. It is proposed that during the initial nucleation stage where the metal with highest positive reduction potential is reduced first, while the nucleation of secondary element will change the surface energy and thus alter the critical radius. Therefore, it is expected that the nucleation radius is a dynamic process that varies based on different steps of reduced metals, and an ultrafast imaging system is ideal to capture the initial nucleation process.

In addition, growth kinetics can be identified by measuring the average radius as a function of time. As discussed in Chapter 2.1, the growth process is determined by factors involving reaction at the surface and diffusion of reactant to the surface. In order to estimate the rate-limiting factor, the diffusion coefficients

of different metals in aqueous solution need to be compared. If there is significant difference between diffusion of metals, the growth process will involve inhomogeneous deposition of certain metals and lead to phase segregation in the obtained HEA NPs. Therefore, the initial concentrations of metal precursors are expected to be adjusted accordingly based on the diffusion coefficients. For the growth mechanism, it is proposed that the process can involve both particle migration and coalescence and Ostwald ripening, with the first one being the dominant mechanism. This is because of the build-in entropy and strong metal-to-metal bonds in HEA nuclei making adatoms hard to leave the surface and diffuse toward others, while the Brownian motion of free standing nuclei and the following attachment is less influenced by the intrinsic properties of HEA NPs.

The structural evolution of HEA NPs are captured in real-time via GLC method by staying at relatively higher magnification so that atomic information can be resolved. The possible amorphous to crystal transformation during nucleation and growth process are expected to be observed by real-time HRTEM imaging combined with FFT analyses. Information regarding the transformation of amorphous to crystalline in aqueous precursor solution, growth of crystal lattice and orientation evolution, particle migration and coalescence in liquid during oriented attachment are expected to be analyzed through HRTEM imaging and FFT interpretation. Since the reaction kinetics maybe fast in aqueous solution with few seconds or minutes, MEMS-based liquid-flow holder is used where flow of precursor solution into the liquid cell can be controlled such that *in situ* video recordings are allowed to avoid missing any process at the initial stage. In addition, MEMS-based liquid-flow holder is advanced in providing larger field of

177

view compared to GLC, so the overall nucleation and growth processes of larger number of HEA NPs can be captured at same time, allowing straight-forward statistical analysis.

6.2.4 Analytical studies of HEA composition evolution

GLC provides an ideal environment to perform *in situ* EDS and EELS during the nucleation and growth process of HEA NPs due to the thin layer of graphene and low atomic number of carbon. Therefore, both EDS and EELS can be performed on aqueous solution without significant loss of SNR. The chemical distribution in a field of view is easily obtained. Figure 6-3a and b shows the EELS mappings obtained on ferritin samples in GLC and on monolayer graphene.[32] The protein shell containing N and O over the ferritin particle can be identified, and further valance state analysis of Fe was performed on L_2/L_3 ratio and O K-edge analyses. For HEA NPs with principle elements including transition metals, the higher atomic number compared to soft ferritin materials can provide better signal for EDS and EELS analysis.
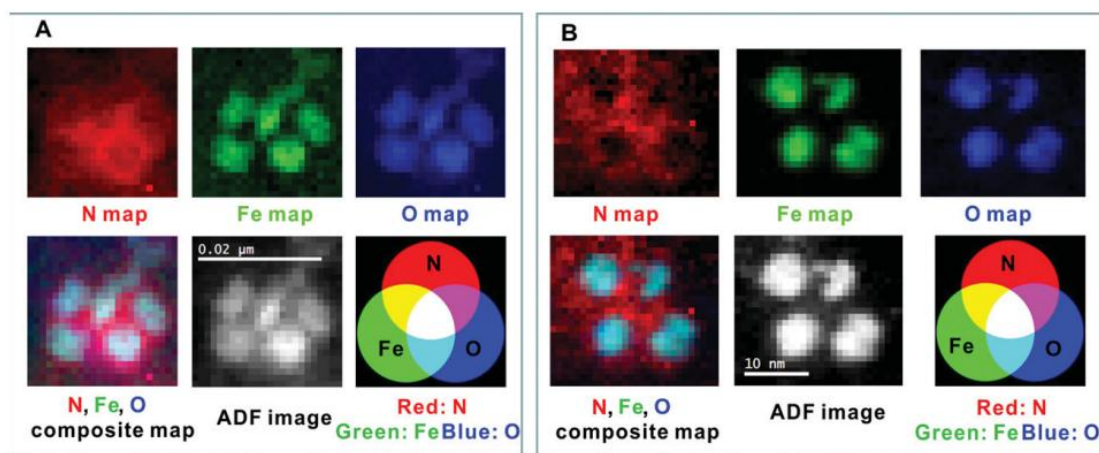
Figure 6-3. EELS mappings of N, O, and Fe on ferritin samples **(a)** in GLC and **(b)** on monolayer graphene layer. [32]© 2014 WILEY−VCH Verlag GmbH & Co. KGaA, Weinheim.

178

The reduction potential of metal ions in aqueous solution are listed in Table 6-2.[130] It can be seen that noble metals such as Au^{3+} and Pt^{2+} are very easy to be reduced to Au and Pt to form metallic atoms in aqueous solution, while transition metals are harder to be reduced since their reduction potentials are mostly negative. This also means that for the co-existence of several metal elements, the ones with more negative reduction potentials will be oxidized by others into ionic phase, preventing the simultaneous formation of metal atoms. Therefore, it is important to control the electron beam conditions such that the solvated electrons in liquid can be sufficiently generated for the reduction of different metals. In particular, EELS has the capability to analyze the valance state of metals and thus can provide insight on the formation composition of metallic HEA NPs.

Table 6-2. Reduction potential for exemplar metals in aqueous solution at room temperature.[130]

Half reaction	Reduction potential
$Au^{3+} + 3e^- \rightarrow Au$	+1.40 V
$Pt^{2+} + 2e^- \rightarrow Pt$	+1.20 V
$Cu^{2+} + 2e^- \rightarrow Cu$	+0.34 V
$Fe^{3+} + 3e^- \rightarrow Fe$	-0.04 V
$Ni^{2+} + 2e^- \rightarrow Ni$	-0.23 V
$Co^{2+} + 2e^- \rightarrow Co$	-0.28 V

$Cr^{2+} + 2e^- \rightarrow Cr$	-0.91 V
$Mn^{2+} + 2e^- \rightarrow Mn$	-1.18 V

6.2.5 *Post situ* analyses of HEA NPs

Post situ analyses of HEA NPs formed via liquid-flow TEM method can be done by using a self-designed multifunctional specimen holder that allow loading of one microchip with sample after liquid-phase reactions. Structurally, HRTEM and STEM imaging can be achieved to fully resolve the formed HEA NPs from liquid phase nucleation and growth processes. Compositional wise, EDS and EELS can be done at the same sample region after nucleation/growth process to further confirm the composition of HEA NPs, as well as the valance state distribution of multiple elements. Phase segregation, if happened, are expected to be identified by EDS and EELS analyses.

Post situ analyses of HEA NPs formed via GLC method can be done by directly imaging the same sample region after nucleation and growth process. Since the graphene layer is thin enough in reducing the electron scattering, it is straight-forward to obtain atomic resolution HRTEM and STEM images to extract crystallinity information. In addition, EDS and EELS can be done with a better SNR than liquid-flow TEM method such that quantitative analyses are possible.

6.3 *In situ* TEM of calcination and sintering in high entropy alloys and oxides

6.3.1 Overview

High entropy oxides (HEO), a form of homogeneous mixed oxide involving more than five principle metal
180

elements with oxygen, is attracting increased attentions in application of energy related materials and structural oxides. Calcination, a key process widely involved in materials synthesis with desired properties in ceramics, thin films and structural oxides, can be utilized to produce industrial quantity of HEO. Understanding the key processes involved in the calcination of HEA to form HEO is essential for the high-efficiency, low-cost production of the materials. Here, the *in situ* TEM technique are used to investigate the calcination behavior of HEA to HEO. The mechanism can be explored with two steps, sintering behavior of HEA NPs at high temperature in vacuum and gases environments; and calcination of HEO NPs in air environments.

6.3.2 Experimental setup

To investigate the sintering behaviors of HEA NPs in vacuum condition, the MEMS-based heating TEM holder is used. The holder is assembled after drop-casted HEA NPs onto the microchip. In microscope, the local temperature at HEA specimen region can be controlled from room temperature to any value up to 1000 °C in one millisecond. The dynamic processes in HEA sintering can be monitored with atomic resolution.

To investigate the calcination process of HEA NPs, the *in situ* gas TEM technique is utilized where HEA NPs are isolated in air environments and high temperatures for a specified period of time. Then real-time imaging/video are performed to capture the whole process. During the experiments, analytical methods using EDS can be done to further obtained the compositional information of the transformation of HEA into HEO NPs.

181

6.3.3 Structural and compositional analyses

During the *in situ* TEM experiments, sintering of the HEA NPs can be captured in real-time, including the possible dynamic processes like rotation, migration, oriented attachment, formation of necking regions between NPs, formation of dislocations during the coalescence, and formation and evolution of surface curvatures. Due to the much improved thermal stability of MEMS-based *in situ* heating instrument, atomic resolution imaging can be performed at the sintering region to extract the structural information. Compositional probing based on EDS and EELS is achievable such that the elemental distribution evolution during sintering can be analyzed.
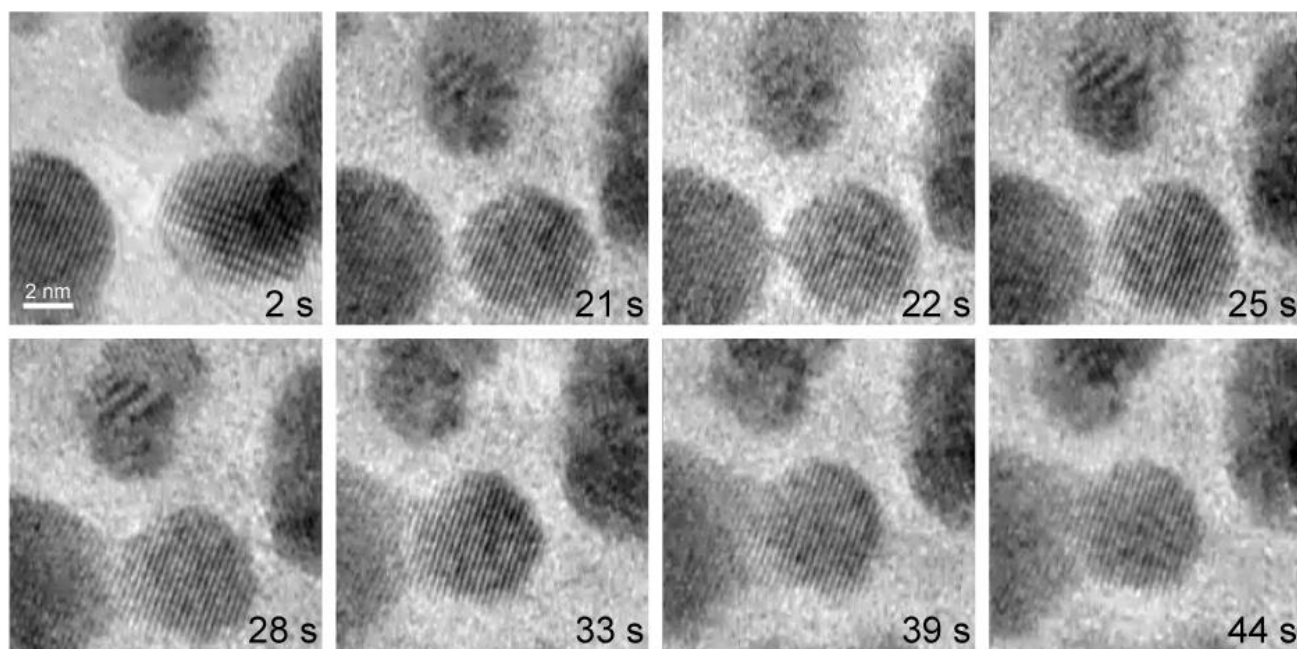
Figure 6-4. Au NPs coalescence process on h-BN support in vacuum condition at RT.

Figure 6-5 shows the sintering process of HEA NPs at 400 °C in N₂ gas. When temperature rises from RT to 400 °C, the smaller NPs (highlighted by red and yellow arrows) gradually migrate and coalesce with the adjacent larger NPs, and the size of smaller NPs is reducing due to the diffusion of atoms towards the larger NPs lattice. This sintering process is accompanied with reduce of surface curvature (as shown by the blue arrows) to minimize the surface energy at the necking interface. Therefore, the necking region transform from large surface curvature into a smoothed spherical surface at the end of sintering process.
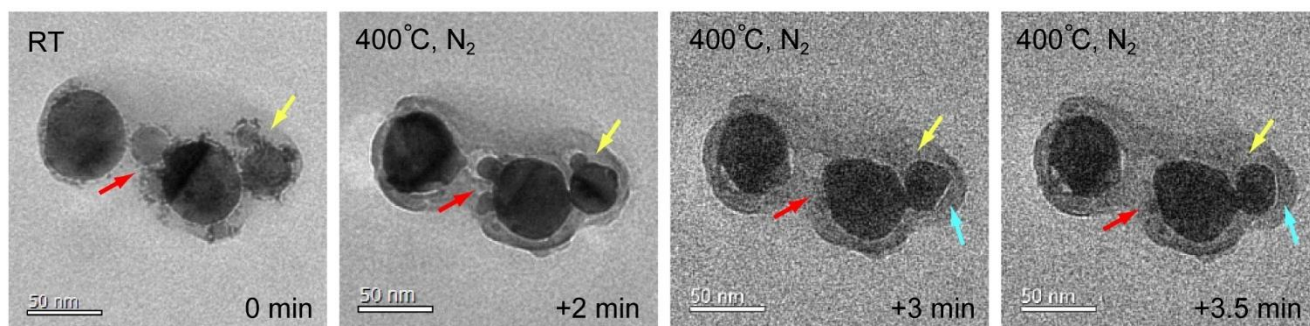
Figure 6-5. Time series TEM images showing the HEA NPs sintering at 400 °C in N₂ gas. First frame corresponding to the condition at RT and is right before temperature rises to 400 °C. The arrows in red, and yellow highlight the region that sintering is happening. Blue arrows highlight the sintering induced evolution of surface curvature.

During sintering process, defects such as dislocations, twin boundaries are expected to form because the thermodynamic equilibrium drives the reduce of interfacial energy between different grain boundaries. For example, Figure 6-6a shows atomic resolution ABF image of adjacent Au NPs on h-BN support. The upper NP is in <111> zone axis, and the bottom one in <110> zone axis. There is no rotation observed

during the image acquisition. Figure 6-6b is enlarged image in dashed boxed region in a and the corresponding atomic illustration shows in c. The Au atoms can be seen as darker contrast from both the upper and bottom NPs, with a stabilized grain boundary interface in between that prevent coalescence.
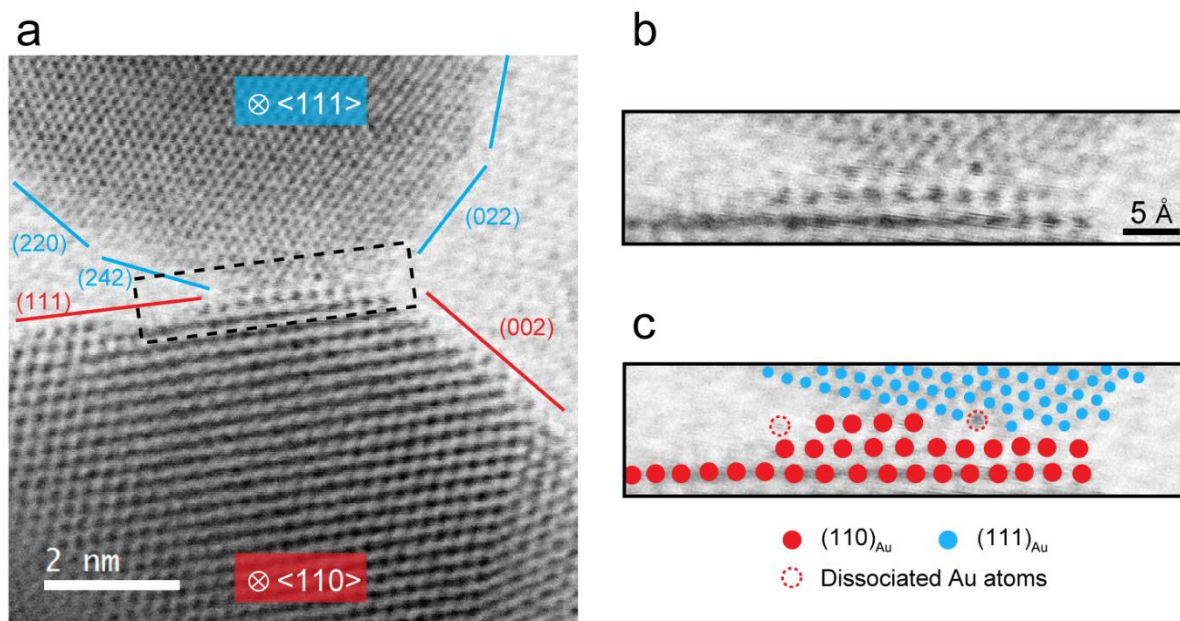
Figure 6-6. (a) Interface between two adjacent Au NPs on h-BN support. The upper NP is in <111> zone axis while the bottom one in <110> zone axis. **(b)** Enlarged image from dashed boxed region in (a) showing the interface between upper and bottom Au NP. **(c)** Atomic illustration of the Au atoms at the interface forming grain boundary.

Similar process can be captured and analyzed for HEA NPs to provide insights for their sintering resistance compare to mono or bimetallic NPs. Figure 6-7a shows the atomic resolution ABF image of HEA NPs with adjacent smaller NPs during the coalescence process. Dislocation at the particle-particle interface were formed and is highlighted in Figure 6-7b. The atomic columns from the smaller NPs and close to the

184

dislocation interface are highlighted as well. Further experiments capturing the whole process of

dislocation evolution including migration and diffusion are helpful to provide deeper insights regarding

the mechanical properties of HEA NPs.
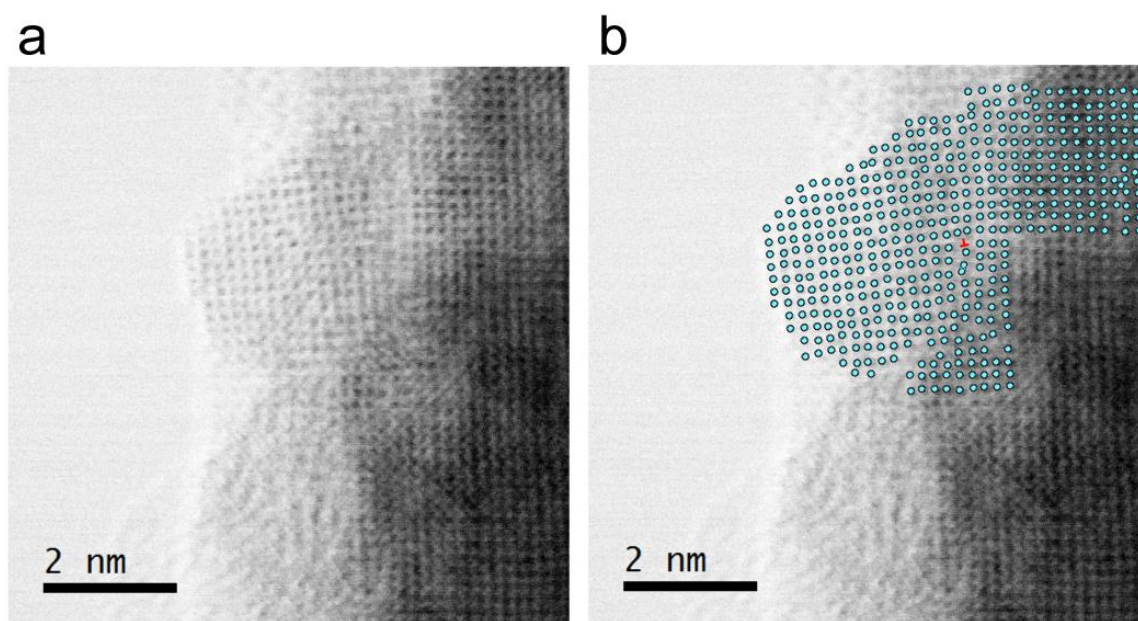
Figure 6-7. (a) ABF image of HEA NPs structural change during coalescence. **(b)** Atomic locations

extracted from (a) highlighting the formation of edge dislocation at the particle interface.

For *in situ* calcination experiments using gas TEM, atomic resolution imaging is also possible if the HEA

and HEO NPs are on zone axis; In addition, EDS can be done through the SiN viewing window benefiting

from the recent novel design of *in situ* gas TEM holder.

185

Chapter 7 Conclusions

(Partial of this Chapter is from my published articles.[1-3] The permission is attached in Appendix.)

In situ TEM can be a powerful tool for studying materials dynamics in their service conditions. The conclusions from the presented research projects are summarized here.

In the first project, *in situ* liquid phase TEM is utilized to investigate the nucleation and growth processes in synthesis of 2D supported heterogeneous catalysts. Specifically, the visualization of dynamic nucleation and growth processes of gold nanoparticles on ultrathin MoS_2 nanoflakes by *in situ* liquid-cell transmission electron microscopy (TEM) are presented. The galvanic displacement resulting in Au nuclei formation on MoS_2 was observed in real time inside the liquid cell. The growth mechanism of Au particles on pristine MoS_2 is found to be in between diffusion-limited and reaction-limited, possibly due to presence of electrochemical Ostwald ripening. Differ from pristine MoS_2, sulfur vacancies on MoS_2 induce Au particle diffusion and coalescence during growth process. The size difference is because the exposed molybdenum atoms at the edge with dangling bonds can strongly interact with Au atoms, whereas sulfur atoms on MoS_2 interior have no dangling bonds and weakly interact with gold atoms. In addition, S vacancies on MoS_2 generate strong nucleation centers that can promote diffusion and coalescence of Au nanoparticles. Therefore, the role of 2D materials in controlling the size and orientation of noble metal nanoparticles vital to the design of next generation catalysts is better understood.

186

In the second project, key insights into the parameters affecting the catalyst degradation mechanisms on 2D supports are obtained. Specifically, the degradation behavior of Pt and bimetallic Au-core Pt-shell NPs on MoS_2 supports at high temperatures under vacuum, N_2, H_2, and air environments by *in situ* gas-cell TEM are presented. The key observations are summarized as: Effect of environment: while PMC was the main mechanism that led to Pt and Au@Pt NPs degradation under vacuum, N_2 and H_2 environments, the degradation of MoS_2 substrate was prominent under exposure to air at high temperatures. Pt NPs were less stable in H_2 environment when compared with the Pt NPs under vacuum or N_2, due to Pt-H interactions that weakened the adhesion of Pt on MoS_2. Effect of nanoparticle composition: under H_2, the stability of Au@Pt NPs was higher in comparison to Pt NPs. This is because H_2 promotes the alloying of Pt-Au, thus reducing the number of Pt at the surface (reducing H_2 interactions) and increasing Pt atoms in contact with MoS_2. Effect of nanoparticle size: The alloying effect promoted by H_2 was more pronounced in small size Au@Pt NPs resulting in their higher sintering resistance in comparison to large size Au@Pt NPs and similar size Pt NPs.

In the third project, efforts have been devoted to answer a range of challenging questions related to alloy oxidation and reduction mechanisms that are hard to be resolved at atomic scale and in real-time. This is especially true for high-entropy alloys (HEAs) in the form of single-phase nanoparticles (NPs) displaying promising properties in catalysis, electronics, and energy storage fields. Specifically, the oxidation and reduction behaviors of FeCoNiCuPt HEA NPs in atmospheric pressure air and H_2 environments are investigated by *in situ* gas-cell TEM. Combined with real-time imaging and analytical characterizations,
187

the oxidation of HEA NPs is found to be Kirkendall effect governed co-segregation process with logarithmic rate constants. In reducing environment, the oxide layer expands and transforms into porous structures, with oxidized Cu being fully reduced to Cu NPs while Fe, Co, and Ni remain in the oxides. Revealing the oxidation and reduction behaviors of HEA NPs helps the development of advanced multicomponent alloys for wide applications possibilities.

REFERENCES

1. Song, B., He, K., Yuan, Y., Sharifi-Asl, S., Cheng, M., Lu, J., Saidi, W. A., and Shahbazian-Yassar, R.: In situ study of nucleation and growth dynamics of Au nanoparticles on MoS2 nanoflakes. *Nanoscale*, 10: 15809-15818, 2018.

2. Song, B., Yang, T. T., Yuan, Y., Sharifi-Asl, S., Cheng, M., Saidi, W. A., Liu, Y., and Shahbazian-Yassar, R.: Revealing Sintering Kinetics of MoS2-Supported Metal Nanocatalysts in Atmospheric Gas Environments via Operando Transmission Electron Microscopy. *ACS Nano*, 14: 4074-4086, 2020.

3. Song, B., Yang, Y., Rabbani, M., Yang, T. T., He, K., Hu, X., Yuan, Y., Ghildiyal, P., Dravid, V. P., Zachariah, M. R., Saidi, W. A., Liu, Y., and Shahbazian-Yassar, R.: In Situ Oxidation Studies of High-Entropy Alloy Nanoparticles. *ACS Nano*: 2020.

4. Parsons, D.: Structure of wet specimens in electron microscopy. *Science*, 186: 407-414, 1974.

5. Parent, L. R., Robinson, D. B., Woehl, T. J., Ristenpart, W. D., Evans, J. E., Browning, N. D., and Arslan, I.: Direct in situ observation of nanoparticle synthesis in a liquid crystal surfactant template. *ACS Nano*, 6: 3589-96, 2012.

6. Woehl, T. J., Evans, J. E., Arslan, I., Ristenpart, W. D., and Browning, N. D.: Direct in situ determination of the mechanisms controlling nanoparticle nucleation and growth. *ACS Nano*, 6: 8599-610, 2012.

7. Patterson, J. P., Abellan, P., Denny, M. S., Jr., Park, C., Browning, N. D., Cohen, S. M., Evans, J. E., and Gianneschi, N. C.: Observing the growth of metal-organic frameworks by in situ liquid cell transmission electron microscopy. *J. Am. Chem. Soc.*, 137: 7322-8, 2015.

8. Kraus, T., and de Jonge, N.: Dendritic gold nanowire growth observed in liquid with transmission electron microscopy. *Langmuir*, 29: 8427-32, 2013.

9. Alloyeau, D., Dachraoui, W., Javed, Y., Belkahla, H., Wang, G., Lecoq, H., Ammar, S., Ersen, O., Wisnet, A., Gazeau, F., and Ricolleau, C.: Unravelling kinetic and thermodynamic effects on the

growth of gold nanoplates by liquid transmission electron microscopy. *Nano Lett.*, 15: 2574-81, 2015.

10. Evans, J. E., Jungjohann, K. L., Browning, N. D., and Arslan, I.: Controlled growth of nanoparticles from solution with in situ liquid transmission electron microscopy. *Nano Lett.*, 11: 2809-13, 2011.

11. Woehl, T. J., Park, C., Evans, J. E., Arslan, I., Ristenpart, W. D., and Browning, N. D.: Direct observation of aggregative nanoparticle growth: kinetic modeling of the size distribution and growth rate. *Nano Lett.*, 14: 373-8, 2014.

12. Smeets, P. J., Cho, K. R., Kempen, R. G., Sommerdijk, N. A., and De Yoreo, J. J.: Calcium carbonate nucleation driven by ion binding in a biomimetic matrix revealed by in situ electron microscopy. *Nat Mater*, 14: 394-9, 2015.

13. Liao, H. G., Zherebetskyy, D., Xin, H., Czarnik, C., Ercius, P., Elmlund, H., Pan, M., Wang, L. W., and Zheng, H.: Facet development during platinum nanocube growth. *Science*, 345: 916-9, 2014.

14. Mehdi, B. L., Qian, J., Nasybulin, E., Park, C., Welch, D. A., Faller, R., Mehta, H., Henderson, W. A., Xu, W., Wang, C. M., Evans, J. E., Liu, J., Zhang, J. G., Mueller, K. T., and Browning, N. D.: Observation and quantification of nanoscale processes in lithium batteries by operando electrochemical (S)TEM. *Nano Lett.*, 15: 2168-73, 2015.

15. Sacci, R. L., Black, J. M., Balke, N., Dudney, N. J., More, K. L., and Unocic, R. R.: Nanoscale imaging of fundamental li battery chemistry: solid-electrolyte interphase formation and preferential growth of lithium metal nanoclusters. *Nano Lett.*, 15: 2011-8, 2015.

16. Zeng, Z., Zhang, X., Bustillo, K., Niu, K., Gammer, C., Xu, J., and Zheng, H.: In Situ Study of Lithiation and Delithiation of MoS2 Nanosheets Using Electrochemical Liquid Cell Transmission Electron Microscopy. *Nano Lett.*, 15: 5214-20, 2015.

17. Wu, J., Gao, W., Yang, H., and Zuo, J. M.: Dissolution Kinetics of Oxidative Etching of Cubic and Icosahedral Platinum Nanoparticles Revealed by in Situ Liquid Transmission Electron Microscopy. *ACS Nano*, 11: 1696-1703, 2017.

18. Egawa, M., Ishida, T., Jalabert, L., and Fujita, H.: In-situ realtime monitoring of nanoscale gold

electroplating using micro-electro-mechanical systems liquid cell operating in transmission electron microscopy. *Appl. Phys. Lett.*, 108: 023104, 2016.

19. Chee, S. W., Pratt, S. H., Hattar, K., Duquette, D., Ross, F. M., and Hull, R.: Studying localized corrosion using liquid cell transmission electron microscopy. *Chem Commun (Camb)*, 51: 168-71, 2015.

20. O'Regan, C., Zhu, X., Zhong, J., Anand, U., Lu, J., Su, H., and Mirsaidov, U.: CTAB-Influenced Electrochemical Dissolution of Silver Dendrites. *Langmuir*, 32: 3601-7, 2016.

21. Ross, F. M.: Opportunities and challenges in liquid cell electron microscopy. *Science*, 350: aaa9886, 2015.

22. de Jonge, N., and Ross, F. M.: Electron microscopy of specimens in liquid. *Nat. Nanotechnol.*, 6: 695-704, 2011.

23. Wu, F., and Yao, N.: Advances in sealed liquid cells for in-situ TEM electrochemial investigation of lithium-ion battery. *Nano Energy*, 11: 196-210, 2015.

24. Wang, C.-M.: In situ transmission electron microscopy and spectroscopy studies of rechargeable batteries under dynamic operating conditions: A retrospective and perspective view. *J. Mater. Res.*, 30: 326-339, 2014.

25. Yuk, J. M., Park, J., Ercius, P., Kim, K., Hellebusch, D. J., Crommie, M. F., Lee, J. Y., Zettl, A., and Alivisatos, A. P.: High-Resolution EM of Colloidal Nanocrystal Growth Using Graphene Liquid Cells.pdf. *Science*, 336: 2012.

26. Zheng, H., Meng, Y. S., and Zhu, Y.: Frontiers of in situ electron microscopy. *MRS Bull.*, 40: 12-18, 2015.

27. Sasaki, Y., Kitaura, R., Yuk, J. M., Zettl, A., and Shinohara, H.: Efficient preparation of graphene liquid cell utilizing direct transfer with large-area well-stitched graphene. *Chem. Phys. Lett.*, 650: 107-112, 2016.

191

28. Zheng, H., Smith, R. K., Jun, Y. W., Kisielowski, C., Dahmen, U., and Alivisatos, A. P.: Observation of single colloidal platinum nanocrystal growth trajectories. *Science*, 324: 1309-12, 2009.

29. Jungjohann, K. L., Bliznakov, S., Sutter, P. W., Stach, E. A., and Sutter, E. A.: In situ liquid cell electron microscopy of the solution growth of Au-Pd core-shell nanostructures. *Nano Lett.*, 13: 2964-70, 2013.

30. Wu, J., Gao, W., Wen, J., Miller, D. J., Lu, P., Zuo, J. M., and Yang, H.: Growth of Au on Pt icosahedral nanoparticles revealed by low-dose in situ TEM. *Nano Lett.*, 15: 2711-5, 2015.

31. Qin, F., Wang, Z., and Wang, Z. L.: Anomalous Growth and Coalescence Dynamics of Hybrid Perovskite Nanoparticles Observed by Liquid-Cell Transmission Electron Microscopy. *ACS Nano*, 10: 9787-9793, 2016.

32. Wang, C., Qiao, Q., Shokuhfar, T., and Klie, R. F.: High-resolution electron microscopy and spectroscopy of ferritin in biocompatible graphene liquid cells and graphene sandwiches. *Adv. Mater.*, 26: 3410-4, 2014.

33. Narayanan, S., Shahbazian-Yassar, R., and Shokuhfar, T.: In Situ Visualization of Ferritin Biomineralization via Graphene Liquid Cell-Transmission Electron Microscopy. *ACS Biomaterials Science & Engineering*, 6: 3208-3216, 2020.

34. Gu, M., Parent, L. R., Mehdi, B. L., Unocic, R. R., McDowell, M. T., Sacci, R. L., Xu, W., Connell, J. G., Xu, P., Abellan, P., Chen, X., Zhang, Y., Perea, D. E., Evans, J. E., Lauhon, L. J., Zhang, J. G., Liu, J., Browning, N. D., Cui, Y., Arslan, I., and Wang, C. M.: Demonstration of an electrochemical liquid cell for operando transmission electron microscopy observation of the lithiation/delithiation behavior of Si nanowire battery anodes. *Nano Lett.*, 13: 6106-12, 2013.

35. Beermann, V., Holtz, M. E., Padgett, E., de Araujo, J. F., Muller, D. A., and Strasser, P.: Real-time imaging of activation and degradation of carbon supported octahedral Pt–Ni alloy fuel cell catalysts at the nanoscale using in situ electrochemical liquid cell STEM. *Energy Environ. Sci.*, 12: 2476-2485, 2019.

36. He, K., Bi, X., Yuan, Y., Foroozan, T., Song, B., Amine, K., Lu, J., and Shahbazian-Yassar, R.: Operando liquid cell electron microscopy of discharge and charge kinetics in lithium-oxygen

batteries. *Nano Energy*, 49: 338-345, 2018.

37. Ortiz Peña, N., Ihiawakrim, D., Han, M., Lassalle-Kaiser, B., Carenco, S., Sanchez, C., Laberty-Robert, C., Portehault, D., and Ersen, O.: Morphological and Structural Evolution of Co3O4 Nanoparticles Revealed by in Situ Electrochemical Transmission Electron Microscopy during Electrocatalytic Water Oxidation. *ACS Nano*, 13: 11372-11381, 2019.

38. Lu, Y., Yin, W.-J., Peng, K.-L., Wang, K., Hu, Q., Selloni, A., Chen, F.-R., Liu, L.-M., and Sui, M.-L.: Self-hydrogenated shell promoting photocatalytic H 2 evolution on anatase TiO 2. *Nat. Commun.*, 9: 1-9, 2018.

39. Hashimoto, H., Naiki, T., Eto, T., and Fujiwara, K.: High temperature gas reaction specimen chamber for an electron microscope. *Jpn. J. Appl. Phys.*, 7: 946, 1968.

40. Hwang, S., Chen, X., Zhou, G., and Su, D.: In Situ Transmission Electron Microscopy on Energy-Related Catalysis. *Advanced Energy Materials*, 10: 1902105, 2019.

41. Kawasaki, T., Ueda, K., Ichihashi, M., and Tanji, T.: Improvement of windowed type environmental-cell transmission electron microscope for in situ observation of gas-solid interactions. *Rev. Sci. Instrum.*, 80: 113701, 2009.

42. Xin, H. L., Niu, K., Alsem, D. H., and Zheng, H.: In situ TEM study of catalytic nanoparticle reactions in atmospheric pressure gas environment. *Microsc. Microanal.*, 19: 1558-68, 2013.

43. Tan, S. F., Chee, S. W., Baraissov, Z., Jin, H., Tan, T. L., and Mirsaidov, U.: Real-Time Imaging of Nanoscale Redox Reactions over Bimetallic Nanoparticles. *Adv. Funct. Mater.*, 29: 1903242, 2019.

44. DeRita, L., Resasco, J., Dai, S., Boubnov, A., Thang, H. V., Hoffman, A. S., Ro, I., Graham, G. W., Bare, S. R., Pacchioni, G., Pan, X., and Christopher, P.: Structural evolution of atomically dispersed Pt catalysts dictates reactivity. *Nature Materials*, 18: 746-751, 2019.

45. He, B., Zhang, Y., Liu, X., and Chen, L.: In-situ Transmission Electron Microscope Techniques for Heterogeneous Catalysis. *ChemCatChem*, 12: 1853-1872, 2020.

193

46. Wei, S., Li, A., Liu, J. C., Li, Z., Chen, W., Gong, Y., Zhang, Q., Cheong, W. C., Wang, Y., Zheng, L., Xiao, H., Chen, C., Wang, D., Peng, Q., Gu, L., Han, X., Li, J., and Li, Y.: Direct observation of noble metal nanoparticles transforming to thermally stable single atoms. *Nat Nanotechnol*, 13: 856-861, 2018.

47. Jiang, Y., Li, H., Wu, Z., Ye, W., Zhang, H., Wang, Y., Sun, C., and Zhang, Z.: In Situ Observation of Hydrogen-Induced Surface Faceting for Palladium–Copper Nanocrystals at Atmospheric Pressure. *Angew. Chem. Int. Ed.*, 55: 12427-12430, 2016.

48. Luo, L., Chen, S., Xu, Q., He, Y., Dong, Z., Zhang, L., Zhu, J., Du, Y., Yang, B., and Wang, C.: Dynamic Atom Clusters on AuCu Nanoparticle Surface during CO Oxidation. *J. Am. Chem. Soc.*, 142: 4022-4027, 2020.

49. Li, G., Fang, K., Chen, Y., Ou, Y., Mao, S., Yuan, W., Wang, Y., Yang, H., Zhang, Z., and Wang, Y.: Unveiling the gas-dependent sintering behavior of Au-TiO2 catalysts via environmental transmission electron microscopy. *J. Catal.*, 388: 84-90, 2020.

50. Hansen, T. W., Delariva, A. T., Challa, S. R., and Datye, A. K.: Sintering of catalytic nanoparticles: particle migration or Ostwald ripening? *Acc. Chem. Res.*, 46: 1720-30, 2013.

51. Zhang, D., Jin, C., Tian, H., Xiong, Y., Zhang, H., Qiao, P., Fan, J., Zhang, Z., Li, Z. Y., and Li, J.: An In situ TEM study of the surface oxidation of palladium nanocrystals assisted by electron irradiation. *Nanoscale*, 9: 6327-6333, 2017.

52. Zou, L., Li, J., Zakharov, D., Stach, E. A., and Zhou, G.: In situ atomic-scale imaging of the metal/oxide interfacial transformation. *Nat Commun*, 8: 307, 2017.

53. Xia, W., Yang, Y., Meng, Q., Deng, Z., Gong, M., Wang, J., Wang, D., Zhu, Y., Sun, L., Xu, F., Li, J., and Xin, H. L.: Bimetallic Nanoparticle Oxidation in Three Dimensions by Chemically Sensitive Electron Tomography and in Situ Transmission Electron Microscopy. *ACS Nano*, 12: 7866-7874, 2018.

54. Taheri, M. L., Stach, E. A., Arslan, I., Crozier, P. A., Kabius, B. C., LaGrange, T., Minor, A. M., Takeda, S., Tanase, M., Wagner, J. B., and Sharma, R.: Current status and future directions for in situ transmission electron microscopy. *Ultramicroscopy*, 170: 86-95, 2016.

55.   Egerton, R. F.: Control of radiation damage in the TEM. *Ultramicroscopy*, 127: 100-8, 2013.

56.   Garcia, A., Raya, A. M., Mariscal, M. M., Esparza, R., Herrera, M., Molina, S. I., Scavello, G., Galindo, P. L., Jose-Yacaman, M., and Ponce, A.: Analysis of electron beam damage of exfoliated MoS(2) sheets and quantitative HAADF-STEM imaging. *Ultramicroscopy*, 146: 33-8, 2014.

57.   Park, J. H., Steingart, D. A., Kodambaka, S., and Ross, F. M.: Electrochemical electron beam lithography: Write, read, and erase metallic nanocrystals on demand. *Science advances*, 3: e1700234, 2017.

58.   Unocic, R. R., Lupini, A. R., Borisevich, A. Y., Cullen, D. A., Kalinin, S. V., and Jesse, S.: Direct-write liquid phase transformations with a scanning transmission electron microscope. *Nanoscale*, 8: 15581-8, 2016.

59.   Schneider, N. M., Norton, M. M., Mendel, B. J., Grogan, J. M., Ross, F. M., and Bau, H. H.: Electron–Water Interactions and Implications for Liquid Cell Electron Microscopy. *J. Phys. Chem. C*, 118: 22373-22382, 2014.

60.   de Jonge, N.: Theory of the spatial resolution of (scanning) transmission electron microscopy in liquid water or ice layers. *Ultramicroscopy*, 187: 113-125, 2018.

61.   Malis, T., Cheng, S., and Egerton, R.: EELS log‑ratio technique for specimen‑thickness measurement in the TEM. *Microsc. Res. Tech.*, 8: 193-200, 1988.

62.   Koh, A. L., Gidcumb, E., Zhou, O., and Sinclair, R.: Oxidation of Carbon Nanotubes in an Ionizing Environment. *Nano Lett.*, 16: 856-63, 2016.

63.   Zhu, Y., and Browning, N. D.: The Role of Gas in Determining Image Quality and Resolution During In Situ Scanning Transmission Electron Microscopy Experiments. *ChemCatChem*, 9: 3478-3485, 2017.

64.   Reimer, L. 2013. *Transmission electron microscopy: physics of image formation and microanalysis*. Vol. 36: Springer.

195

65. Thanh, N. T., Maclean, N., and Mahiddine, S.: Mechanisms of nucleation and growth of nanoparticles in solution. *Chem. Rev.*, 114: 7610-30, 2014.

66. Habraken, W. J. E. M., Tao, J., Brylka, L. J., Friedrich, H., Bertinetti, L., Schenk, A. S., Verch, A., Dmitrovic, V., Bomans, P. H. H., Frederik, P. M., Laven, J., van der Schoot, P., Aichmayer, B., de With, G., DeYoreo, J. J., and Sommerdijk, N. A. J. M.: Ion-association complexes unite classical and non-classical theories for the biomimetic nucleation of calcium phosphate. *Nat. Commun.*, 4: 1507, 2013.

67. LaMer, V. K., and Dinegar, R. H.: Theory, production and mechanism of formation of monodispersed hydrosols. *J. Am. Chem. Soc.*, 72: 4847-4854, 1950.

68. Lifshitz, I. M., and Slyozov, V. V.: The kinetics of precipitation from supersaturated solid solutions. *J. Phys. Chem. Solids*, 19: 35-50, 1961.

69. Davies, C., Nash, P., and Stevens, R. N.: The effect of volume fraction of precipitate on Ostwald ripening. *Acta Metall.*, 28: 179-189, 1980.

70. Davies, C., Nash, P., and Stevens, R.: Precipitation in Ni-Co-Al alloys. *J. Mater. Sci.*, 15: 1521-1532, 1980.

71. Baldan, A.: Review progress in Ostwald ripening theories and their applications to nickel-base superalloys Part I: Ostwald ripening theories. *J. Mater. Sci.*, 37: 2171-2202, 2002.

72. Stranski, I., and Totomanow, D.: Keimbildungsgeschwindigkeit und Ostwaldsche Stufenregel. *Z. Phys. Chem.*, 163: 399-408, 1933.

73. Zhang, T. H., and Liu, X. Y.: How does a transient amorphous precursor template crystallization. *J. Am. Chem. Soc.*, 129: 13520-13526, 2007.

74. Gebauer, D., Völkel, A., and Cölfen, H.: Stable prenucleation calcium carbonate clusters. *Science*, 322: 1819-1822, 2008.

75. Pouget, E. M., Bomans, P. H., Goos, J. A., Frederik, P. M., and Sommerdijk, N. A.: The initial stages

of template-controlled CaCO3 formation revealed by cryo-TEM. *Science*, 323: 1455-1458, 2009.

76. Meier, J. C., Galeano, C., Katsounaros, I., Witte, J., Bongard, H. J., Topalov, A. A., Baldizzone, C., Mezzavilla, S., Schüth, F., and Mayrhofer, K. J.: Design criteria for stable Pt/C fuel cell catalysts. *Beilstein journal of nanotechnology*, 5: 44-67, 2014.

77. Challa, S. R., Delariva, A. T., Hansen, T. W., Helveg, S., Sehested, J., Hansen, P. L., Garzon, F., and Datye, A. K.: Relating rates of catalyst sintering to the disappearance of individual nanoparticles during Ostwald ripening. *J. Am. Chem. Soc.*, 133: 20672-20675, 2011.

78. McCafferty, E. 2010. *Introduction to corrosion science*: Springer Science & Business Media.

79. Cabrera, N., and Mott, N. F.: Theory of the oxidation of metals. *Rep. Prog. Phys.*, 12: 163-184, 1949.

80. Anderson, B. D., and Tracy, J. B.: Nanoparticle conversion chemistry: Kirkendall effect, galvanic exchange, and anion exchange. *Nanoscale*, 6: 12195-216, 2014.

81. Wagner, C.: Beitrag zur theorie des anlaufvorgangs. *Z. Phys. Chem.*, 21: 25-41, 1933.

82. Valensi, G.: Kinetics of the oxidation of metallic spherules and powders. *Compt. Rend*, 202: 309-12, 1936.

83. Fromhold Jr, A.: Growth rate of low-space-charge oxides on spherical metal particles. *J. Phys. Chem. Solids*, 49: 1159-1166, 1988.

84. Rai, A., Park, K., Zhou, L., and Zachariah, M. R.: Understanding the mechanism of aluminium nanoparticle oxidation. *Combustion Theory and Modelling*, 10: 843-859, 2006.

85. Zhou, L., Rai, A., Piekiel, N., Ma, X., and Zachariah, M. R.: Ion-Mobility Spectrometry of Nickel Nanoparticle Oxidation Kinetics: Application to Energetic Materials. *J. Phys. Chem. C*, 112: 16209-16218, 2008.

86. Henz, B. J., Hawa, T., and Zachariah, M. R.: On the role of built-in electric fields on the ignition of oxide coated nanoaluminum: Ion mobility versus Fickian diffusion. *J. Appl. Phys.*, 107: 024901,

197

2010.

87. Railsback, J. G., Johnston-Peck, A. C., Wang, J., and Tracy, J. B.: Size-dependent nanoscale kirkendall effect during the oxidation of nickel nanoparticles. *ACS Nano*, 4: 1913-20, 2010.

88. Miley, H. A.: Theory of Oxidation and Tarnishing of Metals. *Transactions of The Electrochemical Society*, 81: 391, 1942.

89. Bird, R. B., Stewart, W. E., Lightfoot, E. N., and Meredith, R. E.: Transport phenomena. *J. Electrochem. Soc.*, 108: 78C, 1961.

90. Richardson, J.: X-ray diffraction study of nickel oxide reduction by hydrogen. *Applied Catalysis A: General*, 246: 137-150, 2003.

91. Avrami, M.: Interfacial electrochemistry: theory: experiment, and applications. *J. Chem. Phys*, 7: 103, 1939.

92. Yagi, S., and Kunii, D.: 5th Symposium (International) on Combustion. *Reinhold, New York*, 231: 1955.

93. Schulmeyer, W. V., and Ortner, H. M.: Mechanisms of the hydrogen reduction of molybdenum oxides. *Int. J. Refract. Met. Hard Mater.*, 20: 261-269, 2002.

94. Salehi-Khojin, A., Jhong, H.-R. M., Rosen, B. A., Zhu, W., Ma, S., Kenis, P. J., and Masel, R. I.: Nanoparticle silver catalysts that show enhanced activity for carbon dioxide electrolysis. *J. Phys. Chem. C*, 117: 1627-1632, 2013.

95. Lu, Q., Rosen, J., Zhou, Y., Hutchings, G. S., Kimmel, Y. C., Chen, J. G., and Jiao, F.: A selective and efficient electrocatalyst for carbon dioxide reduction. *Nat. Commun.*, 5: 3242, 2014.

96. Yamada, Y., Miyamoto, K., Hayashi, T., Iijima, Y., Todoroki, N., and Wadayama, T.: Oxygen reduction reaction activities for Pt-enriched Co/Pt (111), Co/Pt (100), and Co/Pt (110) model catalyst surfaces prepared by molecular beam epitaxy. *Surf Sci.*, 607: 54-60, 2013.

97. Zhang, P., Qiao, Z.-A., Jiang, X., Veith, G. M., and Dai, S.: Nanoporous ionic organic networks: stabilizing and supporting gold nanoparticles for catalysis. *Nano Lett.*, 15: 823-828, 2015.

98. Hoque, M. A., Hassan, F. M., Higgins, D., Choi, J. Y., Pritzker, M., Knights, S., Ye, S., and Chen, Z.: Multigrain Platinum Nanowires Consisting of Oriented Nanoparticles Anchored on Sulfur-Doped Graphene as a Highly Active and Durable Oxygen Reduction Electrocatalyst. *Adv. Mater.*, 27: 1229-1234, 2015.

99. Fu, C., Song, B., Wan, C., Savino, K., Wang, Y., Zhang, X., and Yates, M. Z.: Electrochemical growth of composite hydroxyapatite coatings for controlled release. *Surf. Coat. Technol.*, 276: 618-625, 2015.

100. Tan, C., and Zhang, H.: Epitaxial growth of hetero-nanostructures based on ultrathin two-dimensional nanosheets. *J. Am. Chem. Soc.*, 137: 12162-74, 2015.

101. Bai, S., and Shen, X.: Graphene–inorganic nanocomposites. *RSC Adv.*, 2: 64-98, 2012.

102. Lee, Y. H., Zhang, X. Q., Zhang, W., Chang, M. T., Lin, C. T., Chang, K. D., Yu, Y. C., Wang, J. T. W., Chang, C. S., and Li, L. J.: Synthesis of Large-Area MoS2 Atomic Layers with Chemical Vapor Deposition. *Adv. Mater.*, 24: 2320-2325, 2012.

103. Kim, J., Byun, S., Smith, A. J., Yu, J., and Huang, J.: Enhanced Electrocatalytic Properties of Transition-Metal Dichalcogenides Sheets by Spontaneous Gold Nanoparticle Decoration. *J. Phys. Chem. Lett.*, 4: 1227-32, 2013.

104. Yuwen, L., Xu, F., Xue, B., Luo, Z., Zhang, Q., Bao, B., Su, S., Weng, L., Huang, W., and Wang, L.: General synthesis of noble metal (Au, Ag, Pd, Pt) nanocrystal modified MoS2 nanosheets and the enhanced catalytic activity of Pd-MoS2 for methanol oxidation. *Nanoscale*, 6: 5762-9, 2014.

105. Yin, Z., Chen, B., Bosman, M., Cao, X., Chen, J., Zheng, B., and Zhang, H.: Au nanoparticle-modified MoS2 nanosheet-based photoelectrochemical cells for water splitting. *Small*, 10: 3537-43, 2014.

106. Lampeka, Y. D., and Tsymbal, L. V.: Nanocomposites of Two-Dimensional Molybdenum and Tungsten Dichalcogenides with Metal Particles: Preparation and Prospects for Application. *Theor.*

Exp. Chem., 51: 141-162, 2015.

107. Shi, Y., Huang, J. K., Jin, L., Hsu, Y. T., Yu, S. F., Li, L. J., and Yang, H. Y.: Selective decoration of Au nanoparticles on monolayer MoS2 single crystals. *Sci. Rep.*, 3: 1839, 2013.

108. Huang, X., Zeng, Z., Bao, S., Wang, M., Qi, X., Fan, Z., and Zhang, H.: Solution-phase epitaxial growth of noble metal nanostructures on dispersible single-layer molybdenum disulfide nanosheets. *Nat. Commun.*, 4: 1444, 2013.

109. Su, S., Zhang, C., Yuwen, L., Liu, X., Wang, L., Fan, C., and Wang, L.: Uniform Au@Pt core-shell nanodendrites supported on molybdenum disulfide nanosheets for the methanol oxidation reaction. *Nanoscale*, 8: 602-8, 2016.

110. Cheng, Z., He, B., and Zhou, L.: A general one-step approach for in situ decoration of MoS2 nanosheets with inorganic nanoparticles. *J. Mater. Chem. A*, 3: 1042-1048, 2015.

111. Porter, L. A., Choi, H. C., Ribbe, A. E., and Buriak, J. M.: Controlled Electroless Deposition of Noble Metal Nanoparticle Films on Germanium Surfaces. *Nano Lett.*, 2: 1067-1071, 2002.

112. Sayed, S. Y., Wang, F., Malac, M., Meldrum, A., Egerton, R. F., and Buriak, J. M.: Heteroepitaxial growth of gold nanostructures on silicon by galvanic displacement. *ACS Nano*, 3: 2809-17, 2009.

113. Alia, S. M., Yan, Y. S., and Pivovar, B. S.: Galvanic displacement as a route to highly active and durable extended surface electrocatalysts. *Catal. Sci. Technol.*, 4: 3589-3600, 2014.

114. de Jonge, N., Peckys, D. B., Kremers, G. J., and Piston, D. W.: Electron microscopy of whole cells in liquid with nanometer resolution. *Proc. Natl. Acad. Sci. U. S. A.*, 106: 2159-64, 2009.

115. Ramachandramoorthy, R., Bernal, R., and Espinosa, H. D.: Pushing the envelope of in situ transmission electron microscopy. *ACS Nano*, 9: 4675-85, 2015.

116. Holtz, M. E., Yu, Y., Gunceler, D., Gao, J., Sundararaman, R., Schwarz, K. A., Arias, T. A., Abruna, H. D., and Muller, D. A.: Nanoscale imaging of lithium ion distribution during in situ operation of battery electrode and electrolyte. *Nano Lett.*, 14: 1453-9, 2014.

117. Zeng, Z., Liang, W.-I., Liao, H.-G., Xin, H. L., Chu, Y.-H., and Zheng, H.: Visualization of electrode–electrolyte interfaces in LiPF6/EC/DEC electrolyte for lithium ion batteries via in situ TEM. *Nano Lett.*, 14: 1745-1750, 2014.

118. Loh, N. D., Sen, S., Bosman, M., Tan, S. F., Zhong, J., Nijhuis, C. A., Kral, P., Matsudaira, P., and Mirsaidov, U.: Multistep nucleation of nanocrystals in aqueous solution. *Nat. Chem.*, 9: 77-82, 2017.

119. Park, J. H., Schneider, N. M., Grogan, J. M., Reuter, M. C., Bau, H. H., Kodambaka, S., and Ross, F. M.: Control of Electron Beam-Induced Au Nanocrystal Growth Kinetics through Solution Chemistry. *Nano Lett.*, 15: 5314-20, 2015.

120. Ievlev, A. V., Jesse, S., Cochell, T. J., Unocic, R. R., Protopopescu, V. A., and Kalinin, S. V.: Quantitative Description of Crystal Nucleation and Growth from in Situ Liquid Scanning Transmission Electron Microscopy. *ACS Nano*, 9: 11784-91, 2015.

121. Saidi, W. A.: Density Functional Theory Study of Nucleation and Growth of Pt Nanoparticles on MoS2(001) Surface. *Cryst. Growth Des.*, 15: 642-652, 2015.

122. Saidi, W. A.: Trends in the Adsorption and Growth Morphology of Metals on the MoS2(001) Surface. *Cryst. Growth Des.*, 15: 3190-3200, 2015.

123. Shi, Y., Song, B., Shahbazian-Yassar, R., Zhao, J., and Saidi, W. A.: Experimentally Validated Structures of Supported Metal Nanoclusters on MoS2. *J. Phys. Chem. Lett.*, 9: 2972-2978, 2018.

124. Kresse, G., and Furthmüller, J.: Efficient iterative schemes forab initiototal-energy calculations using a plane-wave basis set. *Phys. Rev. B*, 54: 11169-11186, 1996.

125. Perdew, J. P., Burke, K., and Ernzerhof, M.: Generalized Gradient Approximation Made Simple. *Phys. Rev. Lett.*, 77: 3865-3868, 1996.

126. Blochl, P. E.: Projector augmented-wave method. *Phys. Rev. B*, 50: 17953-17979, 1994.

127. Kresse, G., and Joubert, D.: From ultrasoft pseudopotentials to the projector augmented-wave method. *Phys. Rev. B*, 59: 1758-1775, 1999.

201

128. Henkelman, G., and Jónsson, H.: Improved tangent estimate in the nudged elastic band method for finding minimum energy paths and saddle points. *J. Chem. Phys*, 113: 9978-9985, 2000.

129. Henkelman, G., Uberuaga, B. P., and Jónsson, H.: A climbing image nudged elastic band method for finding saddle points and minimum energy paths. *J. Chem. Phys*, 113: 9901-9904, 2000.

130. Lide, D., and Haynes, W. 2009. *CRC handbook of chemistry and physics: a ready-reference book of chemical and physical data-/editor-in-chief, David R. Lide; ass. ed. WM"Mickey"Haunes*: Boca Raton, Fla: CRC.

131. Zhong, H., Quhe, R., Wang, Y., Ni, Z., Ye, M., Song, Z., Pan, Y., Yang, J., Yang, L., Lei, M., Shi, J., and Lu, J.: Interfacial Properties of Monolayer and Bilayer MoS2 Contacts with Metals: Beyond the Energy Band Calculations. *Sci Rep*, 6: 21786, 2016.

132. Redmond, P. L., Hallock, A. J., and Brus, L. E.: Electrochemical Ostwald Ripening of Collodial Ag particles on conductive substrates. *Nano Lett.*, 5: 131-135, 2005.

133. Ghosh, T., Karmakar, P., and Satpati, B.: Electrochemical Ostwald ripening and surface diffusion in the galvanic displacement reaction: control over particle growth. *RSC Adv.*, 5: 94380-94387, 2015.

134. Plieth, W.: Electrochemical properties of small clusters of metal atoms and their role in the surface enhanced Raman scattering. *The Journal of Physical Chemistry*, 86: 3166-3170, 1982.

135. Schneider, C. A., Rasband, W. S., and Eliceiri, K. W.: NIH Image to ImageJ: 25 years of image analysis. *Nat. Methods*, 9: 671-675, 2012.

136. Reyes-Gasga, J., Gomez-Rodriguez, A., Gao, X., and Jose-Yacaman, M.: On the interpretation of the forbidden spots observed in the electron diffraction patterns of flat Au triangular nanoparticles. *Ultramicroscopy*, 108: 929-36, 2008.

137. Liu, S.-H., Saidi, W. A., Zhou, Y., and Fichthorn, K. A.: Synthesis of {111}-Faceted Au Nanocrystals Mediated by Polyvinylpyrrolidone: Insights from Density-Functional Theory and Molecular Dynamics. *J. Phys. Chem. C*, 119: 11982-11990, 2015.

138. Saidi, W. A., Feng, H., and Fichthorn, K. A.: Adsorption of polyvinylpyrrolidone on Ag surfaces: insight into a structure-directing agent. *Nano Lett.*, 12: 997-1001, 2012.

139. Saidi, W. A., Feng, H., and Fichthorn, K. A.: Binding of Polyvinylpyrrolidone to Ag Surfaces: Insight into a Structure-Directing Agent from Dispersion-Corrected Density Functional Theory. *J. Phys. Chem. C*, 117: 1163-1171, 2013.

140. Chen, M., Wu, B., Yang, J., and Zheng, N.: Small adsorbate-assisted shape control of Pd and Pt nanocrystals. *Adv. Mater.*, 24: 862-79, 2012.

141. Wu, J., Li, P., Pan, Y.-T. F., Warren, S., Yin, X., and Yang, H.: Surface lattice-engineered bimetallic nanoparticles and their catalytic properties. *Chem. Soc. Rev.*, 41: 8066-8074, 2012.

142. Lu, J., Lu, J. H., Liu, H., Liu, B., Gong, L., Tok, E. S., Loh, K. P., and Sow, C. H.: Microlandscaping of Au nanoparticles on few-layer MoS2 films for chemical sensing. *Small*, 11: 1792-800, 2015.

143. Ghorbani-Asl, M., Enyashin, A. N., Kuc, A., Seifert, G., and Heine, T.: Defect-induced conductivity anisotropy in MoS2monolayers. *Phys. Rev. B*, 88: 2013.

144. Rutter, G. M., Crain, J., Guisinger, N., Li, T., First, P., and Stroscio, J.: Scattering and interference in epitaxial graphene. *Science*, 317: 219-222, 2007.

145. Jungjohann, K., Bliznakov, S., Sutter, P., Stach, E., and Sutter, E.: In situ liquid cell electron microscopy of the solution growth of Au–Pd core–shell nanostructures. *Nano Lett.*, 13: 2964-2970, 2013.

146. Julkapli, N. M., and Bagheri, S.: Graphene supported heterogeneous catalysts: An overview. *Int. J. Hydrogen Energy*, 40: 948-979, 2015.

147. Zeng, Z., Tan, C., Huang, X., Bao, S., and Zhang, H.: Growth of noble metal nanoparticles on single-layer TiS2and TaS2nanosheets for hydrogen evolution reaction. *Energy Environ. Sci.*, 7: 797-803, 2014.

148. Wang, Y., Zhang, X., Luo, Z., Huang, X., Tan, C., Li, H., Zheng, B., Li, B., Huang, Y., Yang, J.,

Zong, Y., Ying, Y., and Zhang, H.: Liquid-phase growth of platinum nanoparticles on molybdenum trioxide nanosheets: an enhanced catalyst with intrinsic peroxidase-like catalytic activity. *Nanoscale*, 6: 12340-4, 2014.

149. Deng, D., Novoselov, K. S., Fu, Q., Zheng, N., Tian, Z., and Bao, X.: Catalysis with two-dimensional materials and their heterostructures. *Nat. Nanotechnol.*, 11: 218-230, 2016.

150. Cai, Q., Mateti, S., Watanabe, K., Taniguchi, T., Huang, S., Chen, Y., and Li, L. H.: Boron Nitride Nanosheet-Veiled Gold Nanoparticles for Surface-Enhanced Raman Scattering. *ACS Appl. Mater. Interfaces.*, 8: 15630-15636, 2016.

151. Sun, H., Chao, J., Zuo, X., Su, S., Liu, X., Yuwen, L., Fan, C., and Wang, L.: Gold nanoparticle-decorated MoS2 nanosheets for simultaneous detection of ascorbic acid, dopamine and uric acid. *RSC Adv.*, 4: 27625, 2014.

152. Jasuja, K., and Berry, V.: Implantation and growth of dendritic gold nanostructures on graphene derivatives: electrical property tailoring and Raman enhancement. *ACS Nano*, 3: 2358-66, 2009.

153. Yang, X., Liu, W., Xiong, M., Zhang, Y., Liang, T., Yang, J., Xu, M., Ye, J., and Chen, H.: Au nanoparticles on ultrathin MoS2sheets for plasmonic organic solar cells. *J. Mater. Chem. A*, 2: 14798-14806, 2014.

154. Yue, W., Yang, S., Ren, Y., and Yang, X.: In situ growth of Sn, SnO on graphene nanosheets and their application as anode materials for lithium-ion batteries. *Electrochim. Acta*, 92: 412-420, 2013.

155. Asadi, M., Kumar, B., Liu, C., Phillips, P., Yasaei, P., Behranginia, A., Zapol, P., Klie, R. F., Curtiss, L. A., and Salehi-Khojin, A.: Cathode Based on Molybdenum Disulfide Nanoflakes for Lithium-Oxygen Batteries. *ACS Nano*, 10: 2167-75, 2016.

156. Hou, D., Zhou, W., Liu, X., Zhou, K., Xie, J., Li, G., and Chen, S.: Pt nanoparticles/MoS2 nanosheets/carbon fibers as efficient catalyst for the hydrogen evolution reaction. *Electrochim. Acta*, 166: 26-31, 2015.

157. Yang, T. T., Tan, T. L., and Saidi, W. A.: High Activity toward the Hydrogen Evolution Reaction on the Edges of MoS2-Supported Platinum Nanoclusters Using Cluster Expansion and Electrochemical

Modeling. *Chem. Mater.*, 32: 1315-1321, 2020.

158. Cheng, Y., Lu, S., Liao, F., Liu, L., Li, Y., and Shao, M.: Rh-MoS2 Nanocomposite Catalysts with Pt-Like Activity for Hydrogen Evolution Reaction. *Adv. Funct. Mater.*, 27: 1700359, 2017.

159. Bose, R., Jin, Z., Shin, S., Kim, S., Lee, S., and Min, Y.-S.: Co-catalytic effects of CoS2 on the activity of the MoS2 catalyst for electrochemical hydrogen evolution. *Langmuir*, 33: 5628-5635, 2017.

160. Kim, M., Anjum, M. A. R., Lee, M., Lee, B. J., and Lee, J. S.: Activating MoS2 Basal Plane with Ni2P Nanoparticles for Pt-Like Hydrogen Evolution Reaction in Acidic Media. *Adv. Funct. Mater.*, 29: 1809151, 2019.

161. Argyle, M., and Bartholomew, C.: Heterogeneous catalyst deactivation and regeneration: a review. *Catalysts*, 5: 145-269, 2015.

162. Dai, S., Chou, J.-P., Wang, K.-W., Hsu, Y.-Y., Hu, A., Pan, X., and Chen, T.-Y.: Platinum-trimer decorated cobalt-palladium core-shell nanocatalyst with promising performance for oxygen reduction reaction. *Nat. Commun.*, 10: 440, 2019.

163. Zhao, Y., Yang, K. R., Wang, Z., Yan, X., Cao, S., Ye, Y., Dong, Q., Zhang, X., Thorne, J. E., Jin, L., Materna, K. L., Trimpalis, A., Bai, H., Fakra, S. C., Zhong, X., Wang, P., Pan, X., Guo, J., Flytzani-Stephanopoulos, M., Brudvig, G. W., Batista, V. S., and Wang, D.: Stable iridium dinuclear heterogeneous catalysts supported on metal-oxide substrate for solar water oxidation. *Proceedings of the National Academy of Sciences*, 115: 2902-2907, 2018.

164. Bian, T., Zhang, H., Jiang, Y., Jin, C., Wu, J., Yang, H., and Yang, D.: Epitaxial Growth of Twinned Au-Pt Core-Shell Star-Shaped Decahedra as Highly Durable Electrocatalysts. *Nano Lett.*, 15: 7808-15, 2015.

165. Campbell, C. T., and Sellers, J. R.: Anchored metal nanoparticles: effects of support and size on their energy, sintering resistance and reactivity. *Faraday Discuss.*, 162: 9-30, 2013.

166. Li, W. Z., Kovarik, L., Mei, D., Liu, J., Wang, Y., and Peden, C. H.: Stable platinum nanoparticles on specific MgAl2O4 spinel facets at high temperatures in oxidizing atmospheres. *Nat. Commun.*,

4: 2481, 2013.

167. Padgett, E., Yarlagadda, V., Holtz, M. E., Ko, M., Levin, B. D. A., Kukreja, R. S., Ziegelbauer, J. M., Andrews, R. N., Ilavsky, J., Kongkanand, A., and Muller, D. A.: Mitigation of PEM Fuel Cell Catalyst Degradation with Porous Carbon Supports. *J. Electrochem. Soc.*, 166: F198-F207, 2019.

168. Jin, Z., Nackashi, D., Lu, W., Kittrell, C., and Tour, J. M.: Decoration, Migration, and Aggregation of Palladium Nanoparticles on Graphene Sheets. *Chem. Mater.*, 22: 5695-5699, 2010.

169. Gilbert, J. A., Kariuki, N. N., Wang, X., Kropf, A. J., Yu, K., Groom, D. J., Ferreira, P. J., Morgan, D., and Myers, D. J.: Pt Catalyst Degradation in Aqueous and Fuel Cell Environments studied via In-Operando Anomalous Small-Angle X-ray Scattering. *Electrochim. Acta*, 173: 223-234, 2015.

170. Matos, J., Ono, L. K., Behafarid, F., Croy, J. R., Mostafa, S., DeLaRiva, A. T., Datye, A. K., Frenkel, A. I., and Roldan Cuenya, B.: In situ coarsening study of inverse micelle-prepared Pt nanoparticles supported on gamma-Al2O3: pretreatment and environmental effects. *PCCP*, 14: 11457-67, 2012.

171. Wang, L., Zhang, W., Wang, S., Gao, Z., Luo, Z., Wang, X., Zeng, R., Li, A., Li, H., Wang, M., Zheng, X., Zhu, J., Zhang, W., Ma, C., Si, R., and Zeng, J.: Atomic-level insights in optimizing reaction paths for hydroformylation reaction over Rh/CoO single-atom catalyst. *Nat. Commun.*, 7: 14036, 2016.

172. Bonifacio, C. S., Carenco, S., Wu, C. H., House, S. D., Bluhm, H., and Yang, J. C.: Thermal Stability of Core–Shell Nanoparticles: A Combined in Situ Study by XPS and TEM. *Chem. Mater.*, 27: 6960-6968, 2015.

173. Chi, M., Wang, C., Lei, Y., Wang, G., Li, D., More, K. L., Lupini, A., Allard, L. F., Markovic, N. M., and Stamenkovic, V. R.: Surface faceting and elemental diffusion behaviour at atomic scale for alloy nanoparticles during in situ annealing. *Nat. Commun.*, 6: 8925, 2015.

174. Cichocka, M. O., Zhao, J., Bachmatiuk, A., Quang, H. T., Gorantla, S. M., Gonzalez-Martinez, I. G., Fu, L., Eckert, J., Warner, J. H., and Rümmeli, M. H.: In situ observations of Pt nanoparticles coalescing inside carbon nanotubes. *RSC Adv.*, 4: 49442-49445, 2014.

175. Yuk, J. M., Jeong, M., Kim, S. Y., Seo, H. K., Kim, J., and Lee, J. Y.: In situ atomic imaging of

coalescence of Au nanoparticles on graphene: rotation and grain boundary migration. *Chemical Communications (Cambridge)*, 49: 11479-81, 2013.

176. Liu, Y., and Sun, Y.: Electron beam induced evolution in Au, Ag, and interfaced heterogeneous Au/Ag nanoparticles. *Nanoscale*, 7: 13687-93, 2015.

177. Li, Y., Zakharov, D., Zhao, S., Tappero, R., Jung, U., Elsen, A., Baumann, P., Nuzzo, R. G., Stach, E. A., and Frenkel, A. I.: Complex structural dynamics of nanocatalysts revealed in Operando conditions by correlated imaging and spectroscopy probes. *Nat. Commun.*, 6: 7583, 2015.

178. Chen, H., Yu, Y., Xin, H. L., Newton, K. A., Holtz, M. E., Wang, D., Muller, D. A., Abruña, H. D., and DiSalvo, F. J.: Coalescence in the Thermal Annealing of Nanoparticles: An in Situ STEM Study of the Growth Mechanisms of Ordered Pt–Fe Nanoparticles in a KCl Matrix. *Chem. Mater.*, 25: 1436-1442, 2013.

179. Li, J., Wang, Z., Chen, C., and Huang, S.: Atomic-scale observation of migration and coalescence of Au nanoclusters on YSZ surface by aberration-corrected STEM. *Sci. Rep.*, 4: 5521, 2014.

180. Gao, W., Tieu, P., Addiego, C., Ma, Y., Wu, J., and Pan, X.: Probing the dynamics of nanoparticle formation from a precursor at atomic resolution. *Science Advances*, 5: eaau9590, 2019.

181. Vara, M., Roling, L. T., Wang, X., Elnabawy, A. O., Hood, Z. D., Chi, M., Mavrikakis, M., and Xia, Y.: Understanding the Thermal Stability of Palladium-Platinum Core-Shell Nanocrystals by In Situ Transmission Electron Microscopy and Density Functional Theory. *ACS Nano*, 11: 4571-4581, 2017.

182. Chen, Q., He, K., Robertson, A. W., Kirkland, A. I., and Warner, J. H.: Atomic Structure and Dynamics of Epitaxial 2D Crystalline Gold on Graphene at Elevated Temperatures. *ACS Nano*, 10: 10418-10427, 2016.

183. Simonsen, S. B., Chorkendorff, I., Dahl, S., Skoglundh, M., Sehested, J., and Helveg, S.: Ostwald ripening in a Pt/SiO2 model catalyst studied by in situ TEM. *J. Catal.*, 281: 147-155, 2011.

184. Simonsen, S. B., Chorkendorff, I., Dahl, S., Skoglundh, M., Sehested, J., and Helveg, S.: Direct Observations of Oxygen-induced Platinum Nanoparticle pipening studied by in situ TEM. *J. Am. Chem. Soc.*, 132: 2010.

207

185. Simonsen, S. B., Wang, Y., Jensen, J. O., and Zhang, W.: Coarsening of carbon black supported Pt nanoparticles in hydrogen. *Nanotechnology*, 28: 475710, 2017.

186. Lawrence, E. L., and Crozier, P. A.: Oxygen Transfer at Metal-Reducible Oxide Nanocatalyst Interfaces: Contrasting Carbon Growth from Ethane and Ethylene. *ACS Applied Nano Materials*, 1: 1360-1369, 2018.

187. Lin, P. A., Gomez-Ballesteros, J. L., Burgos, J. C., Balbuena, P. B., Natarajan, B., and Sharma, R.: Direct evidence of atomic-scale structural fluctuations in catalyst nanoparticles. *J. Catal.*, 349: 149-155, 2017.

188. Zhu, Y., Sushko, P. V., Melzer, D., Jensen, E., Kovarik, L., Ophus, C., Sanchez-Sanchez, M., Lercher, J. A., and Browning, N. D.: Formation of Oxygen Radical Sites on MoVNbTeOx by Cooperative Electron Redistribution. *J. Am. Chem. Soc.*, 139: 12342-12345, 2017.

189. Wang, C.-M., Genc, A., Cheng, H., Pullan, L., Baer, D. R., and Bruemmer, S. M.: In-Situ TEM visualization of vacancy injection and chemical partition during oxidation of Ni-Cr nanoparticles. *Sci. Rep.*, 4: 3683, 2014.

190. Wu, Y. A., Li, L., Li, Z., Kinaci, A., Chan, M. K., Sun, Y., Guest, J. R., McNulty, I., Rajh, T., and Liu, Y.: Visualizing Redox Dynamics of a Single Ag/AgCl Heterogeneous Nanocatalyst at Atomic Resolution. *ACS Nano*, 10: 3738-46, 2016.

191. Dai, S., Hou, Y., Onoue, M., Zhang, S., Gao, W., Yan, X., Graham, G. W., Wu, R., and Pan, X.: Revealing surface elemental composition and dynamic processes involved in facet-dependent oxidation of Pt3Co nanoparticles via in situ transmission electron microscopy. *Nano Lett.*, 17: 4683-4688, 2017.

192. Matsubu, J. C., Zhang, S., DeRita, L., Marinkovic, N. S., Chen, J. G., Graham, G. W., Pan, X., and Christopher, P.: Adsorbate-mediated strong metal–support interactions in oxide-supported Rh catalysts. *Nat. Chem.*, 9: 120, 2017.

193. Prestat, E., Kulzick, M. A., Dietrich, P. J., Smith, M. M., Tien, M. E. P., Burke, M. G., Haigh, S. J., and Zaluzec, N. J.: In Situ Industrial Bimetallic Catalyst Characterization using Scanning Transmission Electron Microscopy and X‑ray Absorption Spectroscopy at One Atmosphere and

Elevated Temperature. *ChemPhysChem*, 18: 2151-2156, 2017.

194. Dembélé, K., Bahri, M., Melinte, G., Hirlimann, C., Berliet, A., Maury, S., Gay, A. S., and Ersen, O.: Insight by In Situ Gas Electron Microscopy on the Thermal Behaviour and Surface Reactivity of Cobalt Nanoparticles. *ChemCatChem*, 10: 4004-4009, 2018.

195. Zhang, X., Meng, J., Zhu, B., Yu, J., Zou, S., Zhang, Z., Gao, Y., and Wang, Y.: In situ TEM studies of the shape evolution of Pd nanocrystals under oxygen and hydrogen environments at atmospheric pressure. *Chemical Communications (Cambridge)*, 53: 13213-13216, 2017.

196. Altantzis, T., Lobato, I., De Backer, A., Béché, A., Zhang, Y., Basak, S., Porcu, M., Xu, Q., Sánchez-Iglesias, A., Liz-Marzán, L. M., Van Tendeloo, G., Van Aert, S., and Bals, S.: Three-Dimensional Quantification of the Facet Evolution of Pt Nanoparticles in a Variable Gaseous Environment. *Nano Lett.*, 19: 477-481, 2019.

197. Stach, E. A., Li, Y., Zhao, S., Gamalski, A., Zakharov, D., Tappero, R., Chen-Weigart, K., Thieme, J., Jung, U., Elsen, A., Wu, Q., Orlov, A., Chen, J., Nuzzo, R. G., and Frenkel, A.: Characterizing Working Catalysts with Correlated Electron and Photon Probes. *Microsc. Microanal.*, 21: 563-564, 2015.

198. Avanesian, T., Dai, S., Kale, M. J., Graham, G. W., Pan, X., and Christopher, P.: Quantitative and Atomic-Scale View of CO-Induced Pt Nanoparticle Surface Reconstruction at Saturation Coverage via DFT Calculations Coupled with in Situ TEM and IR. *J. Am. Chem. Soc.*, 139: 4551-4558, 2017.

199. Sapountzi, F. M., Gracia, J. M., Weststrate, C. J., Fredriksson, H. O. A., and Niemantsverdriet, J. W.: Electrocatalysts for the generation of hydrogen, oxygen and synthesis gas. *Prog. Energy Combust. Sci.*, 58: 1-35, 2017.

200. Kresse, G., and Furthmuller, J.: Efficient iterative schemes for ab initio total-energy calculations using a plane-wave basis set. *Physical review. B, Condensed matter*, 54: 11169-11186, 1996.

201. Kresse, G., and Furthmüller, J.: Efficiency of ab-initio total energy calculations for metals and semiconductors using a plane-wave basis set. *Computational Materials Science*, 6: 15-50, 1996.

202. Kresse, G., and Hafner, J.: Ab initio molecular dynamics for liquid metals. *Physical review. B,*

209

Condensed matter, 47: 558-561, 1993.

203. Kresse, G., and Hafner, J.: Ab initio molecular-dynamics simulation of the liquid-metal-amorphous-semiconductor transition in germanium. *Physical review. B, Condensed matter*, 49: 14251-14269, 1994.

204. Perdew, J. P., Burke, K., and Ernzerhof, M.: Generalized gradient approximation made simple. *Physical review letters*, 77: 3865, 1996.

205. Grimme, S.: Accurate description of van der Waals complexes by density functional theory including empirical corrections. *Journal of computational chemistry*, 25: 1463-1473, 2004.

206. Tkatchenko, A., and Scheffler, M.: Accurate Molecular Van Der Waals Interactions from Ground-State Electron Density and Free-Atom Reference Data. *Physical review letters*, 102: 073005, 2009.

207. Al-Saidi, W., Voora, V. K., and Jordan, K. D.: An assessment of the vdW-TS method for extended systems. *Journal of Chemical Theory and Computation*, 8: 1503-1513, 2012.

208. Granqvist, C.: Size distributions for supported metal catalysts *1Coalescence growth versus ostwald ripening. *J. Catal.*, 42: 477-479, 1976.

209. Ye, G., Gong, Y., Lin, J., Li, B., He, Y., Pantelides, S. T., Zhou, W., Vajtai, R., and Ajayan, P. M.: Defects Engineered Monolayer MoS2 for Improved Hydrogen Evolution Reaction. *Nano Lett.*, 16: 1097-103, 2016.

210. Nørskov, J. K., Bligaard, T., Logadottir, A., Kitchin, J. R., Chen, J. G., Pandelov, S., and Stimming, U.: Trends in the Exchange Current for Hydrogen Evolution. *Journal of The Electrochemical Society*, 152: J23-J26, 2005.

211. Yang, T. T., and Saidi, W. A.: Tuning the hydrogen evolution activity of β-Mo2C nanoparticles via control of their growth conditions. *Nanoscale*, 9: 3252-3260, 2017.

212. Koch, G., Varney, J., Thompson, N., Moghissi, O., Gould, M., and Payer, J.: International measures of prevention, application, and economics of corrosion technologies study. *NACE International*: 216,

2016.

213. Evans, H. E., Hilton, D. A., Holm, R. A., and Webster, S. J.: Influence of silicon additions on the oxidation resistance of a stainless steel. *Oxid. Met.*, 19: 1-18, 1983.

214. Huang, L. P., Chen, K. H., Li, S., and Song, M.: Influence of high-temperature pre-precipitation on local corrosion behaviors of Al–Zn–Mg alloy. *Scripta Mater.*, 56: 305-308, 2007.

215. Schnaas, A., and Grabke, H. J.: High-temperature corrosion and creep of Ni-Cr-Fe alloys in carburizing and oxidizing environments. *Oxid. Met.*, 12: 387-404, 1978.

216. Orlov, D., Ralston, K. D., Birbilis, N., and Estrin, Y.: Enhanced corrosion resistance of Mg alloy ZK60 after processing by integrated extrusion and equal channel angular pressing. *Acta Mater.*, 59: 6176-6186, 2011.

217. Gu, C., Lian, J., He, J., Jiang, Z., and Jiang, Q.: High corrosion-resistance nanocrystalline Ni coating on AZ91D magnesium alloy. *Surf. Coat. Technol.*, 200: 5413-5418, 2006.

218. Zhao, S., Xie, X., Smith, G. D., and Patel, S. J.: Research and Improvement on structure stability and corrosion resistance of nickel-base superalloy INCONEL alloy 740. *Materials & Design*, 27: 1120-1127, 2006.

219. Dai, J., Zhu, J., Chen, C., and Weng, F.: High temperature oxidation behavior and research status of modifications on improving high temperature oxidation resistance of titanium alloys and titanium aluminides: A review. *J. Alloys Compd.*, 685: 784-798, 2016.

220. Tsai, M.-H., and Yeh, J.-W.: High-Entropy Alloys: A Critical Review. *Materials Research Letters*, 2: 107-123, 2014.

221. Ye, Y. F., Wang, Q., Lu, J., Liu, C. T., and Yang, Y.: High-entropy alloy: challenges and prospects. *Mater. Today*, 19: 349-362, 2016.

222. Chen, J., Zhou, X., Wang, W., Liu, B., Lv, Y., Yang, W., Xu, D., and Liu, Y.: A review on fundamental of high entropy alloys with promising high–temperature properties. *J. Alloys Compd.*, 760: 15-30,

2018.

223. George, E. P., Raabe, D., and Ritchie, R. O.: High-entropy alloys. *Nature Reviews Materials*, 4: 515-534, 2019.

224. Yeh, J. W., Chen, S. K., Lin, S. J., Gan, J. Y., Chin, T. S., Shun, T. T., Tsau, C. H., and Chang, S. Y.: Nanostructured High-Entropy Alloys with Multiple Principal Elements: Novel Alloy Design Concepts and Outcomes. *Adv. Eng. Mater.*, 6: 299-303, 2004.

225. Otto, F., Yang, Y., Bei, H., and George, E. P.: Relative effects of enthalpy and entropy on the phase stability of equiatomic high-entropy alloys. *Acta Mater.*, 61: 2628-2638, 2013.

226. Fu, Z., Chen, W., Wen, H., Zhang, D., Chen, Z., Zheng, B., Zhou, Y., and Lavernia, E. J.: Microstructure and strengthening mechanisms in an FCC structured single-phase nanocrystalline $Co_{25}Ni_{25}Fe_{25}Al_{7.5}Cu_{17.5}$ high-entropy alloy. *Acta Mater.*, 107: 59-71, 2016.

227. Sriharitha, R., Murty, B. S., and Kottada, R. S.: Alloying, thermal stability and strengthening in spark plasma sintered $Al_xCoCrCuFeNi$ high entropy alloys. *J. Alloys Compd.*, 583: 419-426, 2014.

228. Fang, S., Chen, W., and Fu, Z.: Microstructure and mechanical properties of twinned $Al_{0.5}CrFeNiCo_{0.3}C_{0.2}$ high entropy alloy processed by mechanical alloying and spark plasma sintering. *Materials & Design (1980-2015)*, 54: 973-979, 2014.

229. Zou, Y., Wheeler, J. M., Ma, H., Okle, P., and Spolenak, R.: Nanocrystalline High-Entropy Alloys: A New Paradigm in High-Temperature Strength and Stability. *Nano Lett.*, 17: 1569-1574, 2017.

230. Brif, Y., Thomas, M., and Todd, I.: The use of high-entropy alloys in additive manufacturing. *Scripta Mater.*, 99: 93-96, 2015.

231. Fujieda, T., Shiratori, H., Kuwabara, K., Kato, T., Yamanaka, K., Koizumi, Y., and Chiba, A.: First demonstration of promising selective electron beam melting method for utilizing high-entropy alloys as engineering materials. *Mater. Lett.*, 159: 12-15, 2015.

232. Gorsse, S., Hutchinson, C., Gouné, M., and Banerjee, R.: Additive manufacturing of metals: a brief

212

review of the characteristic microstructures and properties of steels, Ti-6Al-4V and high-entropy alloys. *Science and Technology of Advanced Materials*, 18: 584-610, 2017.

233. Yao, Y., Huang, Z., Xie, P., Lacey, S. D., Jacob, R. J., Xie, H., Chen, F., Nie, A., Pu, T., Rehwoldt, M., Yu, D., Zachariah, M. R., Wang, C., Shahbazian-Yassar, R., Li, J., and Hu, L.: Carbothermal shock synthesis of high-entropy-alloy nanoparticles. *Science*, 359: 1489-1494, 2018.

234. Yang, Y., Song, B., Ke, X., Xu, F., Bozhilov, K. N., Hu, L., Shahbazian-Yassar, R., and Zachariah, M. R.: Aerosol Synthesis of High Entropy Alloy Nanoparticles. *Langmuir*, 36: 1985-1992, 2020.

235. Shi, Y., Yang, B., and Liaw, P.: Corrosion-Resistant High-Entropy Alloys: A Review. *Metals*, 7: 43, 2017.

236. Daoud, H. M., Manzoni, A. M., Völkl, R., Wanderka, N., and Glatzel, U.: Oxidation Behavior of Al8Co17Cr17Cu8Fe17Ni33, Al23Co15Cr23Cu8Fe15Ni15, and Al17Co17Cr17Cu17Fe17Ni17Compositionally Complex Alloys (High-Entropy Alloys) at Elevated Temperatures in Air. *Adv. Eng. Mater.*, 17: 1134-1141, 2015.

237. Kai, W., Li, C. C., Cheng, F. P., Chu, K. P., Huang, R. T., Tsay, L. W., and Kai, J. J.: Air-oxidation of FeCoNiCr-based quinary high-entropy alloys at 700–900 °C. *Corros. Sci.*, 121: 116-125, 2017.

238. Butler, T. M., and Weaver, M. L.: Oxidation behavior of arc melted AlCoCrFeNi multi-component high-entropy alloys. *J. Alloys Compd.*, 674: 229-244, 2016.

239. Laplanche, G., Volkert, U. F., Eggeler, G., and George, E. P.: Oxidation Behavior of the CrMnFeCoNi High-Entropy Alloy. *Oxid. Met.*, 85: 629-645, 2016.

240. Gorr, B., Azim, M., Christ, H. J., Mueller, T., Schliephake, D., and Heilmaier, M.: Phase equilibria, microstructure, and high temperature oxidation resistance of novel refractory high-entropy alloys. *J. Alloys Compd.*, 624: 270-278, 2015.

241. Kai, W., Li, C. C., Cheng, F. P., Chu, K. P., Huang, R. T., Tsay, L. W., and Kai, J. J.: The oxidation behavior of an equimolar FeCoNiCrMn high-entropy alloy at 950°C in various oxygen-containing atmospheres. *Corros. Sci.*, 108: 209-214, 2016.

242. Jeangros, Q., Hansen, T. W., Wagner, J. B., Damsgaard, C. D., Dunin-Borkowski, R. E., Hébert, C., Van herle, J., and Hessler-Wyser, A.: Reduction of nickel oxide particles by hydrogen studied in an environmental TEM. *J. Mater. Sci.*, 48: 2893-2907, 2013.

243. Wang, Z. L., Yin, J. S., and Jiang, Y. D.: EELS analysis of cation valence states and oxygen vacancies in magnetic oxides. *Micron*, 31: 571-580, 2000.

244. Kresse, G., and Hafner, J.: Ab initio molecular dynamics for liquid metals. *Phys. Rev. B*, 47: 558, 1993.

245. Kresse, G., and Hafner, J.: Ab initio molecular dynamics for open-shell transition metals. *Phys. Rev. B*, 48: 13115, 1993.

246. Kresse, G., and Hafner, J.: Ab initio molecular-dynamics simulation of the liquid-metal–amorphous-semiconductor transition in germanium. *Phys. Rev. B*, 49: 14251, 1994.

247. Widom, M., Huhn, W. P., Maiti, S., and Steurer, W.: Hybrid Monte Carlo/Molecular Dynamics Simulation of a Refractory Metal High Entropy Alloy. *Metallurgical and Materials Transactions A*, 45: 196-200, 2013.

248. Goedecker, S., Teter, M., and Hutter, J.: Separable dual-space Gaussian pseudopotentials. *Phys. Rev. B*, 54: 1703-1710, 1996.

249. VandeVondele, J., Krack, M., Mohamed, F., Parrinello, M., Chassaing, T., and Hutter, J.: Quickstep: Fast and accurate density functional calculations using a mixed Gaussian and plane waves approach. *Comput. Phys. Commun.*, 167: 103-128, 2005.

250. Ha, D.-H., Moreau, L. M., Honrao, S., Hennig, R. G., and Robinson, R. D.: The Oxidation of Cobalt Nanoparticles into Kirkendall-Hollowed CoO and Co3O4: The Diffusion Mechanisms and Atomic Structural Transformations. *J. Phys. Chem. C*, 117: 14303-14312, 2013.

251. Han, L., Meng, Q., Wang, D., Zhu, Y., Wang, J., Du, X., Stach, E. A., and Xin, H. L.: Interrogation of bimetallic particle oxidation in three dimensions at the nanoscale. *Nat Commun*, 7: 13335, 2016.

214

252. Zhdanov, V. P., and Kasemo, B.: Cabrera–Mott kinetics of oxidation of nm-sized metal particles. *Chem. Phys. Lett.*, 452: 285-288, 2008.

253. Grammatikopoulos, P., Sowwan, M., and Kioseoglou, J.: Computational Modeling of Nanoparticle Coalescence. *Advanced Theory and Simulations*, 2: 1900013, 2019.

254. Chen, Y., Zhao, X., and Xiao, P.: Effect of surface curvature on oxidation of a MCrAlY coating. *Corros. Sci.*, 163: 108256, 2020.

255. Jeurgens, L. P. H., Sloof, W. G., Tichelaar, F. D., and Mittemeijer, E. J.: Thermodynamic stability of amorphous oxide films on metals: Application to aluminum oxide films on aluminum substrates. *Phys. Rev. B*, 62: 4707-4719, 2000.

256. Fehlner, F. P.: Low temperature oxidation, the role of vitreous oxides. 1986.

257. Ahn, C. C., and Krivanek, O. L. 1983. *EELS Atlas: A Reference Guide of Electron Energy Loss Spectra Covering All Stable Elements*: Gatan.

258. Ewels, P., Sikora, T., Serin, V., Ewels, C. P., and Lajaunie, L.: A Complete Overhaul of the Electron Energy-Loss Spectroscopy and X-Ray Absorption Spectroscopy Database: eelsdb.eu. *Microsc. Microanal.*, 22: 717-724, 2016.

259. Feldhoff, A., Martynczuk, J., Arnold, M., Myndyk, M., Bergmann, I., Šepelák, V., Gruner, W., Vogt, U., Hähnel, A., and Woltersdorf, J.: Spin-state transition of iron in (Ba0.5Sr0.5)(Fe0.8Zn0.2)O3-δ perovskite. *J. Solid State Chem.*, 182: 2961-2971, 2009.

260. Zhao, Y., Feltes, T. E., Regalbuto, J. R., Meyer, R. J., and Klie, R. F.: In situ electron energy loss spectroscopy study of metallic Co and Co oxides. *J. Appl. Phys.*, 108: 063704, 2010.

261. Potapov, P. L., Kulkova, S. E., Schryvers, D., and Verbeeck, J.: Structural and chemical effects on EELS L3,2 ionization edges in Ni-based intermetallic compounds. *Phys. Rev. B*, 64: 184110, 2001.

262. Ngantcha, J. P., Gerland, M., Kihn, Y., and Rivière, A.: Correlation between microstructure and mechanical spectroscopy of a Cu-Cu2 O alloy between 290 K and 873 K. *Eur. Phys. J. Appl. Phys.*,

215

29: 83-89, 2005.

263. Wang, F., Malac, M., and Egerton, R. F.: Energy-loss near-edge fine structures of iron nanoparticles. *Micron*, 37: 316-323, 2006.

264. Wang, Z. L., Yin, J. S., Mo, W. D., and Zhang, Z. J.: In-Situ Analysis of Valence Conversion in Transition Metal Oxides Using Electron Energy-Loss Spectroscopy. *The Journal of Physical Chemistry B*, 101: 6793-6798, 1997.

265. Varela, M., Oxley, M. P., Luo, W., Tao, J., Watanabe, M., Lupini, A. R., Pantelides, S. T., and Pennycook, S. J.: Atomic-resolution imaging of oxidation states in manganites. *Phys. Rev. B*, 79: 2009.

266. Himmel, L., Mehl, R., and Birchenall, C. E.: Self-diffusion of iron in iron oxides and the Wagner theory of oxidation. *JOM*, 5: 827-843, 1953.

267. Carter, R., and Richardson, F.: An examination of the decrease of surface-activity method of measuring self-diffusion coefficients in wustite and cobaltous oxide. *JOM*, 6: 1244-1257, 1954.

268. Volpe, M. L., and Reddy, J.: Cation Self‐Diffusion and Semiconductivity in NiO. *J. Chem. Phys*, 53: 1117-1125, 1970.

269. Moore, W. J., and Selikson, B.: The diffusion of copper in cuprous oxide. *J. Chem. Phys*, 19: 1539-1543, 1951.

270. Purton, J. A., Barrera, G. D., Allan, N. L., and Blundy, J. D.: Monte Carlo and Hybrid Monte Carlo/Molecular Dynamics Approaches to Order− Disorder in Alloys, Oxides, and Silicates. *The Journal of Physical Chemistry B*, 102: 5202-5207, 1998.

271. Zhu, Q., Zou, L., Zhou, G., Saidi, W. A., and Yang, J. C.: Early and transient stages of Cu oxidation: Atomistic insights from theoretical simulations and in situ experiments. *Surf Sci.*, 652: 98-113, 2016.

272. Curnan, M. T., Andolina, C. M., Li, M., Zhu, Q., Chi, H., Saidi, W. A., and Yang, J. C.: Connecting Oxide Nucleation and Growth to Oxygen Diffusion Energetics on Stepped Cu(011) Surfaces: An

Experimental and Theoretical Study. *J. Phys. Chem. C*, 123: 452-463, 2018.

273. Saidi, W. A., Lee, M., Li, L., Zhou, G., and McGaughey, A. J. H.: Ab initio atomistic thermodynamics study of the early stages of Cu(100) oxidation. *Phys. Rev. B*, 86: 245429, 2012.

274. Zhu, Q., Saidi, W. A., and Yang, J. C.: Step-Edge Directed Metal Oxidation. *J. Phys. Chem. Lett.*, 7: 2530-2536, 2016.

275. Vitos, L., Ruban, A. V., Skriver, H. L., and Kollár, J.: The surface energy of metals. *Surf Sci.*, 411: 186-202, 1998.

276. Xie, P., Yao, Y., Huang, Z., Liu, Z., Zhang, J., Li, T., Wang, G., Shahbazian-Yassar, R., Hu, L., and Wang, C.: Highly efficient decomposition of ammonia using high-entropy alloy catalysts. *Nat Commun*, 10: 4011, 2019.

277. Pedersen, J. K., Batchelor, T. A. A., Bagger, A., and Rossmeisl, J.: High-Entropy Alloys as Catalysts for the CO2 and CO Reduction Reactions. *ACS Catalysis*, 10: 2169-2176, 2020.

278. Ahn, C. C., Krivanek, O. L., and Disko, M. M. 1983. *EELS atlas: a reference collection of electron energy loss spectra covering all stable elements*: HREM Facility, Center for Solid State Science, Arizona State University.

APPENDIX

218

Regarding Incident 3773608 Request of permission for ACS Editor's Choice article
1 message

support@services.acs.org <support@services.acs.org>   Wed, Aug 26, 2020 at 10:04 PM
To: bsong25@uic.edu

ACS
Chemistry for Life®

Dear Dr. Song,

Your permission requested is granted and there is no fee for this reuse. In your planned reuse, you must cite the ACS article as the source, add this direct link https://pubs.acs.org/doi/10.1021/acsnano.6b04234 and include a notice to readers that further permissions related to the material excerpted should be directed to the ACS.

If you need further assistance, please let me know.

Sincerely,
Simran Mehra
ACS Publications Support
Customer Services & Information
Website: https://help.acs.org/

Incident Information:

Incident #:	3773608
Date Created:	2020-08-27T06:16:59
Priority:	3
Customer:	Boao Song
Title:	Request of permission for ACS Editor's Choice article
Description:	Dear ACS office,

I would like to request permission for the following article to be used in my thesis titled

In situ TEM Investigations of Catalysis Dynamics in Service Conditions

https://doi.org/10.1021/acsnano.6b04234

219

220

Direct in Situ Determination of the Mechanisms Controlling Nanoparticle Nucleation and Growth

ACS Publications
Most Trusted. Most Cited. Most Read.

Author: Taylor J. Woehl, James E. Evans, Ilke Arslan, et al

Publication: ACS Nano

Publisher: American Chemical Society

Date: Oct 1, 2012

SPRINGER NATURE

Direct observation of noble metal nanoparticles transforming to thermally stable single atoms

Author: Shengjie Wei et al
Publication: Nature Nanotechnology
Publisher: Springer Nature
Date: Jul 16, 2018

Copyright © 2018, Springer Nature

Order Completed

Thank you for your order.

This Agreement between University of Illinois at Chicago – Boao Song ("You") and Springer Nature ("Springer Nature") consists of your license details and the terms and conditions provided by Springer Nature and Copyright Clearance Center.

Your confirmation email will contain your order number for future reference.

License Number	4896541415061	🖶 Printable Details
License date	Aug 26, 2020	

📄 Licensed Content

Licensed Content Publisher	Springer Nature
Licensed Content Publication	Nature Nanotechnology
Licensed Content Title	Direct observation of noble metal nanoparticles transforming to thermally stable single atoms
Licensed Content Author	Shengjie Wei et al
Licensed Content Date	Jul 16, 2018

📋 Order Details

Type of Use	Thesis/Dissertation
Requestor type	academic/university or research institute
Format	print and electronic
Portion	figures/tables/illustrations
Number of figures/tables/illustrations	1
High-res required	no
Will you be translating?	no
Circulation/distribution	100 - 199
Author of this Springer Nature content	no

📄 About Your Work

Title	In situ TEM Investigations of Catalysis Dynamics in Service Conditions
Institution name	University of Illinois at Chicago
Expected presentation date	Sep 2020

📁 Additional Data

Portions	Figure 3a

223

Requestor Location

Tax Details

University of Illinois at
Chicago
929 West Taylor St

Requestor Location

CHICAGO, IL 60607
United States
Attn: University of Illinois at
Chicago

$ Price

Total   0.00 USD

Total: 0.00 USD

CLOSE WINDOW   ORDER MORE

224

Copyright
Clearance
Center

RightsLink

Home

? Help

Email Support

Boao Song ∨

Dynamic Atom Clusters on AuCu Nanoparticle Surface during CO Oxidation

ACS Publications
Most Trusted. Most Cited. Most Read.

Author: Langli Luo, Shuyue Chen, Qian Xu, et al

Publication: Journal of the American Chemical Society

Publisher: American Chemical Society

Date: Feb 1, 2020

PERMISSION/LICENSE IS GRANTED FOR YOUR ORDER AT NO CHARGE

BACK

CLOSE WINDOW

225

Electron–Water Interactions and Implications for Liquid Cell Electron Microscopy

ACS Publications
Most Trusted. Most Cited. Most Read.

Author: Nicholas M. Schneider, Michael M. Norton, Brian J. Mendel, et al

Publication: The Journal of Physical Chemistry C

Publisher: American Chemical Society

Date: Sep 1, 2014

Copyright © 2014, American Chemical Society

Facet development during platinum nanocube growth

Author:
Hong-Gang Liao,Danylo Zherebetskyy,Huolin Xin,Cory Czarnik,Peter Ercius,Hans Elmlund,Ming Pan,Lin-Wang Wang,Haimei Zheng

Publication: Science

Publisher: The American Association for the Advancement of Science

Date: Aug 22, 2014

Copyright © 2014, Copyright © 2014, American Association for the Advancement of Science

Order Completed

Thank you for your order.

This Agreement between University of Illinois at Chicago -- Boao Song ("You") and The American Association for the Advancement of Science ("The American Association for the Advancement of Science") consists of your license details and the terms and conditions provided by The American Association for the Advancement of Science and Copyright Clearance Center.

Your confirmation email will contain your order number for future reference.

License Number	4896550206442	🖨 Printable Details
License date	Aug 26, 2020	

☑ Licensed Content

Licensed Content Publisher	The American Association for the Advancement of Science
Licensed Content Publication	Science
Licensed Content Title	Facet development during platinum nanocube growth
Licensed Content Author	Hong-Gang Liao,Danylo Zherebetskyy,Huolin Xin,Cory Czarnik,Peter Ercius,Hans Elmlund,Ming Pan,Lin-Wang Wang,Haimei Zheng
Licensed Content Date	Aug 22, 2014
Licensed Content Volume	345
Licensed Content Issue	6199

🗑 Order Details

Type of Use	Thesis / Dissertation
Requestor type	Scientist/individual at a research institution
Format	Print and electronic
Portion	Figure
Number of figures/tables	1

📄 About Your Work

Title	In situ TEM Investigations of Catalysis Dynamics in Service Conditions
Institution name	University of Illinois at Chicago
Expected presentation date	Sep 2020

📂 Additional Data

Portions	Figure 1

227

Requestor Location

University of Illinois at
Chicago
929 West Taylor St

Requestor Location

CHICAGO, IL 60607
United States
Attn: University of Illinois at
Chicago

$ Price

Total   0.00 USD

Tax Details

Total: 0.00 USD

CLOSE WINDOW   ORDER MORE

229

High-Resolution Electron Microscopy and Spectroscopy of Ferritin in Biocompatible Graphene Liquid Cells and Graphene Sandwiches

Author: Robert F. Klie, Tolou Shokuhfar, Qiao Qiao, et al

Publication: Advanced Materials

Publisher: John Wiley and Sons

Date: Feb 3, 2014

© 2014 WILEY-VCH Verlag GmbH & Co. KGaA, Weinheim

Order Completed

Thank you for your order.

This Agreement between University of Illinois at Chicago – Boao Song ("You") and John Wiley and Sons ("John Wiley and Sons") consists of your license details and the terms and conditions provided by John Wiley and Sons and Copyright Clearance Center.

Your confirmation email will contain your order number for future reference.

License Number	4896550390560		🖶 Printable Details
License date	Aug 26, 2020		

☑ Licensed Content

Licensed Content Publisher	John Wiley and Sons
Licensed Content Publication	Advanced Materials
Licensed Content Title	High-Resolution Electron Microscopy and Spectroscopy of Ferritin in Biocompatible Graphene Liquid Cells and Graphene Sandwiches
Licensed Content Author	Robert F. Klie, Tolou Shokuhfar, Qiao Qiao, et al
Licensed Content Date	Feb 3, 2014
Licensed Content Volume	26
Licensed Content Issue	21
Licensed Content Pages	5

📖 Order Details

Type of use	Dissertation/Thesis
Requestor type	University/Academic
Format	Print and electronic
Portion	Figure/table
Number of figures/tables	1
Will you be translating?	No

📄 About Your Work

Title	In situ TEM Investigations of Catalysis Dynamics in Service Conditions
Institution name	University of Illinois at Chicago
Expected presentation date	Sep 2020

📂 Additional Data

Portions	Figure 3

230

⊙ **Requestor Location**		▤ **Tax Details**	
	University of Illinois at Chicago 929 West Taylor St	Publisher Tax ID	EU826007151
Requestor Location			
	CHICAGO, IL 60607 United States Attn: University of Illinois at Chicago		

$ Price

Total	0.00 USD

Would you like to purchase the full text of this article? If so, please continue on to the content ordering system located here: Purchase PDF
If you click on the buttons below or close this window, you will not be able to return to the content ordering system.

Total: 0.00 USD

CLOSE WINDOW   ORDER MORE

High-Resolution EM of Colloidal Nanocrystal Growth Using Graphene Liquid Cells

Science

MAAAS

Author:
Jong Min Yuk,Jungwon Park,Peter Ercius,Kwanpyo Kim,Daniel J. Hellebusch,Michael F. Crommie,Jeong Yong Lee,A. Zettl,A. Paul Alivisatos

Publication: Science

Publisher: The American Association for the Advancement of Science

Date: Apr 6, 2012

Copyright © 2012, Copyright © 2012, American Association for the Advancement of Science

Order Completed

Thank you for your order.

This Agreement between University of Illinois at Chicago -- Boao Song ("You") and The American Association for the Advancement of Science ("The American Association for the Advancement of Science") consists of your license details and the terms and conditions provided by The American Association for the Advancement of Science and Copyright Clearance Center.

Your confirmation email will contain your order number for future reference.

License Number	4896550483524	🖶 Printable Details
License date	Aug 26, 2020	

☑ Licensed Content

Licensed Content Publisher	The American Association for the Advancement of Science
Licensed Content Publication	Science
Licensed Content Title	High-Resolution EM of Colloidal Nanocrystal Growth Using Graphene Liquid Cells
Licensed Content Author	Jong Min Yuk,Jungwon Park,Peter Ercius,Kwanpyo Kim,Daniel J. Hellebusch,Michael F. Crommie,Jeong Yong Lee,A. Zettl,A. Paul Alivisatos
Licensed Content Date	Apr 6, 2012
Licensed Content Volume	336
Licensed Content Issue	6077

▥ Order Details

Type of Use	Thesis / Dissertation
Requestor type	Scientist/individual at a research institution
Format	Print and electronic
Portion	Figure
Number of figures/tables	1

▤ About Your Work

Title	In situ TEM Investigations of Catalysis Dynamics in Service Conditions
Institution name	University of Illinois at Chicago
Expected presentation date	Sep 2020

▤ Additional Data

Portions	Figure 1b

232

○ **Requestor Location**

University of Illinois at
Chicago
929 West Taylor St

Requestor Location

CHICAGO, IL 60607
United States
Attn: University of Illinois at
Chicago

Tax Details

$ **Price**

Total   0.00 USD

Total: 0.00 USD

CLOSE WINDOW   ORDER MORE

233

SPRINGER NATURE

In situ atomic-scale imaging of the metal/oxide interfacial transformation

Author: Lianfeng Zou et al

Publication: Nature Communications

Publisher: Springer Nature

Date: Aug 21, 2017

Copyright © 2017, Springer Nature

In Situ Observation of Hydrogen-Induced Surface Faceting for Palladium–Copper Nanocrystals at Atmospheric Pressure

Author: Ying Jiang, Hengbo Li, Zhemin Wu, et al

Publication: Angewandte Chemie International Edition

Publisher: John Wiley and Sons

Date: Sep 4, 2016

Order Completed

Thank you for your order.

This Agreement between University of Illinois at Chicago – Boao Song ("You") and John Wiley and Sons ("John Wiley and Sons") consists of your license details and the terms and conditions provided by John Wiley and Sons and Copyright Clearance Center.

Your confirmation email will contain your order number for future reference.

License Number	4896550596557	🖨 Printable Details
License date	Aug 26, 2020	

📄 Licensed Content

Licensed Content Publisher	John Wiley and Sons
Licensed Content Publication	Angewandte Chemie International Edition
Licensed Content Title	In Situ Observation of Hydrogen-Induced Surface Faceting for Palladium–Copper Nanocrystals at Atmospheric Pressure
Licensed Content Author	Ying Jiang, Hengbo Li, Zhemin Wu, et al
Licensed Content Date	Sep 4, 2016
Licensed Content Volume	55
Licensed Content Issue	40
Licensed Content Pages	4

📋 Order Details

Type of use	Dissertation/Thesis
Requestor type	University/Academic
Format	Print and electronic
Portion	Figure/table
Number of figures/tables	1
Will you be translating?	No

📄 About Your Work

Title	In situ TEM Investigations of Catalysis Dynamics in Service Conditions
Institution name	University of Illinois at Chicago
Expected presentation date	Sep 2020

📁 Additional Data

Portions	Figure 2

⊙ **Requestor Location**		☰ **Tax Details**	
	University of Illinois at Chicago 929 West Taylor St	Publisher Tax ID	EU826007151
Requestor Location			
	CHICAGO, IL 60607 United States Attn: University of Illinois at Chicago		
$ **Price**			
Total	0.00 USD		

Would you like to purchase the full text of this article? If so, please continue on to the content ordering system located here: Purchase PDF
If you click on the buttons below or close this window, you will not be able to return to the content ordering system.

Total: 0.00 USD

CLOSE WINDOW   ORDER MORE

236

SPRINGER NATURE

Ion-association complexes unite classical and non-classical theories for the biomimetic nucleation of calcium phosphate

Author: Wouter J. E. M. Habraken et al

Publication: Nature Communications

Publisher: Springer Nature

Date: Feb 19, 2013

Copyright © 2013, Nature Publishing Group, a division of Macmillan Publishers Limited. All Rights Reserved.

Order Completed

Thank you for your order.

This Agreement between University of Illinois at Chicago -- Boao Song ("You") and Springer Nature ("Springer Nature") consists of your license details and the terms and conditions provided by Springer Nature and Copyright Clearance Center.

Your confirmation email will contain your order number for future reference.

License Number	4942880389556
License date	Nov 06, 2020

🖶 Printable Details

☑ Licensed Content

Licensed Content Publisher	Springer Nature
Licensed Content Publication	Nature Communications
Licensed Content Title	Ion-association complexes unite classical and non-classical theories for the biomimetic nucleation of calcium phosphate
Licensed Content Author	Wouter J. E. M. Habraken et al
Licensed Content Date	Feb 19, 2013

▤ Order Details

Type of Use	Thesis/Dissertation
Requestor type	academic/university or research institute
Format	print and electronic
Portion	figures/tables/illustrations
Number of figures/tables/illustrations	1
High-res required	no
Will you be translating?	no
Circulation/distribution	500 - 999
Author of this Springer Nature content	no

🗋 About Your Work

Title	In situ TEM Investigations of Catalysis Dynamics in Service Conditions
Institution name	University of Illinois at Chicago
Expected presentation date	Nov 2020

🗀 Additional Data

Portions	figure 1

237

⦿ **Requestor Location**		▦ **Tax Details**

Requestor Location

University of Illinois at
Chicago
929 West Taylor St

CHICAGO, IL 60607
United States
Attn: University of Illinois at
Chicago

$ Price

Total   0.00 USD

Total: 0.00 USD

CLOSE WINDOW   ORDER MORE

239

In situ TEM Investigations of Catalysis Dynamics in Service Conditions

https://doi.org/10.1021/cr400544s

The portion of the content will be Figure 1.Thank you.

Sincerely,

Boao "Bob" Song

Department of Mechanical and Industrial Engineering
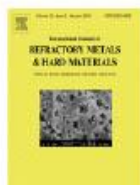
University of Illinois at Chicago

bsong25@uic.edu

{CMI: MCID1068571}

240

Mechanisms of the hydrogen reduction of molybdenum oxides

Author: Werner V. Schulmeyer, Hugo M. Ortner

Publication: International Journal of Refractory Metals and Hard Materials

Publisher: Elsevier

Date: July 2002

Order Completed

Thank you for your order.

This Agreement between University of Illinois at Chicago -- Boao Song ("You") and Elsevier ("Elsevier") consists of your license details and the terms and conditions provided by Elsevier and Copyright Clearance Center.

Your confirmation email will contain your order number for future reference.

License Number	4938451460570		🖶 Printable Details
License date	Oct 29, 2020		

☑ Licensed Content

Licensed Content Publisher	Elsevier
Licensed Content Publication	International Journal of Refractory Metals and Hard Materials
Licensed Content Title	Mechanisms of the hydrogen reduction of molybdenum oxides
Licensed Content Author	Werner V. Schulmeyer,Hugo M. Ortner
Licensed Content Date	Jul 1, 2002
Licensed Content Volume	20
Licensed Content Issue	4
Licensed Content Pages	9
Journal Type	S&T

▥ Order Details

Type of Use	reuse in a thesis/dissertation
Portion	figures/tables/illustrations
Number of figures/tables/illustrations	1
Format	both print and electronic
Are you the author of this Elsevier article?	No
Will you be translating?	No

📄 About Your Work

Title	In situ TEM Investigations of Catalysis Dynamics in Service Conditions
Institution name	University of Illinois at Chicago
Expected presentation date	Nov 2020

🗀 Additional Data

Portions	Figure 1

241

Requestor Location

	University of Illinois at Chicago 929 West Taylor St
Requestor Location	CHICAGO, IL 60607 United States Attn: University of Illinois at Chicago

Tax Details

Publisher Tax ID	98-0397604

Price

Total	0.00 USD

Total: 0.00 USD

CLOSE WINDOW

ORDER MORE

242

ELSEVIER

Operando liquid cell electron microscopy of discharge and charge kinetics in lithium-oxygen batteries

Author:
Kun He,Xuanxuan Bi,Yifei Yuan,Tara Foroozan,Boao Song,Khalil Amine,Jun Lu,Reza Shahbazian-Yassar

Publication: Nano Energy

Publisher: Elsevier

Date: July 2018

Order Completed

Thank you for your order.

This Agreement between University of Illinois at Chicago -- Boao Song ("You") and Elsevier ("Elsevier") consists of your license details and the terms and conditions provided by Elsevier and Copyright Clearance Center.

Your confirmation email will contain your order number for future reference.

License Number	4896550699532		🖨 Printable Details
License date	Aug 26, 2020		

📋 Licensed Content

Licensed Content Publisher	Elsevier
Licensed Content Publication	Nano Energy
Licensed Content Title	Operando liquid cell electron microscopy of discharge and charge kinetics in lithium-oxygen batteries
Licensed Content Author	Kun He,Xuanxuan Bi,Yifei Yuan,Tara Foroozan,Boao Song,Khalil Amine,Jun Lu,Reza Shahbazian-Yassar
Licensed Content Date	Jul 1, 2018
Licensed Content Volume	49
Licensed Content Issue	n/a
Licensed Content Pages	8
Journal Type	S&T

🗑 Order Details

Type of Use	reuse in a thesis/dissertation
Portion	figures/tables/illustrations
Number of figures/tables/illustrations	1
Format	both print and electronic
Are you the author of this Elsevier article?	No
Will you be translating?	No

📄 About Your Work

Title	In situ TEM Investigations of Catalysis Dynamics in Service Conditions
Institution name	University of Illinois at Chicago
Expected presentation date	Sep 2020

📁 Additional Data

Portions	Figure 3

⊘ Requestor Location		▤ Tax Details	
	University of Illinois at Chicago 929 West Taylor St	Publisher Tax ID	98-0397604
Requestor Location			
	CHICAGO, IL 60607 United States Attn: University of Illinois at Chicago		

$ Price

Total	0.00 USD

Total: 0.00 USD

CLOSE WINDOW   ORDER MORE

244

245

Real-Time Imaging of Nanoscale Redox Reactions over Bimetallic Nanoparticles

Author: Shu Fen Tan, See Wee Chee, Zhaslan Baraissov, et al
Publication: Advanced Functional Materials
Publisher: John Wiley and Sons
Date: Jul 16, 2019

© 2019 WILEY-VCH Verlag GmbH & Co. KGaA, Weinheim

Order Completed

Thank you for your order.

This Agreement between University of Illinois at Chicago – Boao Song ("You") and John Wiley and Sons ("John Wiley and Sons") consists of your license details and the terms and conditions provided by John Wiley and Sons and Copyright Clearance Center.

Your confirmation email will contain your order number for future reference.

License Number	4896550898593	🖨 Printable Details
License date	Aug 26, 2020	

☑ Licensed Content

Licensed Content Publisher	John Wiley and Sons
Licensed Content Publication	Advanced Functional Materials
Licensed Content Title	Real-Time Imaging of Nanoscale Redox Reactions over Bimetallic Nanoparticles
Licensed Content Author	Shu Fen Tan, See Wee Chee, Zhaslan Baraissov, et al
Licensed Content Date	Jul 16, 2019
Licensed Content Volume	29
Licensed Content Issue	37
Licensed Content Pages	10

🗎 Order Details

Type of use	Dissertation/Thesis
Requestor type	University/Academic
Format	Print and electronic
Portion	Figure/table
Number of figures/tables	2
Will you be translating?	No

🗎 About Your Work

Title	In situ TEM Investigations of Catalysis Dynamics in Service Conditions
Institution name	University of Illinois at Chicago
Expected presentation date	Sep 2020

🗀 Additional Data

Portions	Figure 1

246

⊙ Requestor Location　　　　　**▤ Tax Details**

| | University of Illinois at Chicago 929 West Taylor St | Publisher Tax ID | EU826007151 |

Requestor Location

CHICAGO, IL 60607
United States
Attn: University of Illinois at
Chicago

$ Price

Total　　　　　0.00 USD

Would you like to purchase the full text of this article? If so, please continue on to the content ordering system located here: Purchase PDF
If you click on the buttons below or close this window, you will not be able to return to the content ordering system.

Total: 0.00 USD

CLOSE WINDOW　　　　　ORDER MORE

247

248

The Role of Gas in Determining Image Quality and Resolution During In Situ Scanning Transmission Electron Microscopy Experiments

Author: Yuanyuan Zhu, Nigel D. Browning
Publication: ChemCatChem
Publisher: John Wiley and Sons
Date: Aug 2, 2017

© 2017 Wiley-VCH Verlag GmbH & Co. KGaA, Weinheim

Order Completed

Thank you for your order.

This Agreement between University of Illinois at Chicago -- Boao Song ("You") and John Wiley and Sons ("John Wiley and Sons") consists of your license details and the terms and conditions provided by John Wiley and Sons and Copyright Clearance Center.

Your confirmation email will contain your order number for future reference.

License Number	4896551031349	🖨 Printable Details
License date	Aug 26, 2020	

🗹 Licensed Content

Licensed Content Publisher	John Wiley and Sons
Licensed Content Publication	ChemCatChem
Licensed Content Title	The Role of Gas in Determining Image Quality and Resolution During In Situ Scanning Transmission Electron Microscopy Experiments
Licensed Content Author	Yuanyuan Zhu, Nigel D. Browning
Licensed Content Date	Aug 2, 2017
Licensed Content Volume	9
Licensed Content Issue	18
Licensed Content Pages	8

🗐 Order Details

Type of use	Dissertation/Thesis
Requestor type	University/Academic
Format	Print and electronic
Portion	Figure/table
Number of figures/tables	1
Will you be translating?	No

🗐 About Your Work

Title	In situ TEM Investigations of Catalysis Dynamics in Service Conditions
Institution name	University of Illinois at Chicago
Expected presentation date	Sep 2020

🗀 Additional Data

Portions	Figure 1

249

Requestor Location

	University of Illinois at Chicago
	929 West Taylor St
Requestor Location	
	CHICAGO, IL 60607
	United States
	Attn: University of Illinois at Chicago

Tax Details

Publisher Tax ID	EU826007151

$ Price

Total	0.00 USD

Would you like to purchase the full text of this article? If so, please continue on to the content ordering system located here: Purchase PDF
If you click on the buttons below or close this window, you will not be able to return to the content ordering system.

Total: 0.00 USD

CLOSE WINDOW

ORDER MORE

250

Theory of the spatial resolution of (scanning) transmission electron microscopy in liquid water or ice layers

Author: Niels de Jonge

Publication: Ultramicroscopy

Publisher: Elsevier

Date: April 2018

Order Completed

Thank you for your order.

This Agreement between University of Illinois at Chicago -- Boao Song ("You") and Elsevier ("Elsevier") consists of your license details and the terms and conditions provided by Elsevier and Copyright Clearance Center.

Your confirmation email will contain your order number for future reference.

License Number	4938440466680	🖶 Printable Details
License date	Oct 29, 2020	

☑ Licensed Content

Licensed Content Publisher	Elsevier
Licensed Content Publication	Ultramicroscopy
Licensed Content Title	Theory of the spatial resolution of (scanning) transmission electron microscopy in liquid water or ice layers
Licensed Content Author	Niels de Jonge
Licensed Content Date	Apr 1, 2018
Licensed Content Volume	187
Licensed Content Issue	n/a
Licensed Content Pages	13
Journal Type	S&T

🗋 Order Details

Type of Use	reuse in a thesis/dissertation
Portion	figures/tables/illustrations
Number of figures/tables/illustrations	2
Format	both print and electronic
Are you the author of this Elsevier article?	No
Will you be translating?	No

📄 About Your Work

Title	In situ TEM Investigations of Catalysis Dynamics in Service Conditions
Institution name	University of Illinois at Chicago
Expected presentation date	Nov 2020

🗀 Additional Data

Portions	Figure 2

251

Requestor Location

	University of Illinois at Chicago 929 West Taylor St
Requestor Location	
	CHICAGO, IL 60607 United States Attn: University of Illinois at Chicago

Tax Details

Publisher Tax ID	98-0397604

Price

Total	0.00 USD

Total: 0.00 USD

CLOSE WINDOW

ORDER MORE

Unveiling the gas-dependent sintering behavior of Au-TiO2 catalysts via environmental transmission electron microscopy

JOURNAL OF CATALYSIS

Author:
Guanxing Li,Ke Fang,Yuzhuo Chen,Yang Ou,Shanjun Mao,Wentao Yuan,Yong Wang,Hangsheng Yang,Ze Zhang,Yong Wang

Publication: Journal of Catalysis

Publisher: Elsevier

Date: August 2020

Order Completed

Thank you for your order.

This Agreement between University of Illinois at Chicago -- Boao Song ("You") and Elsevier ("Elsevier") consists of your license details and the terms and conditions provided by Elsevier and Copyright Clearance Center.

Your confirmation email will contain your order number for future reference.

License Number	4896551112518		🖶 Printable Details
License date	Aug 26, 2020		

📄 Licensed Content

Licensed Content Publisher	Elsevier
Licensed Content Publication	Journal of Catalysis
Licensed Content Title	Unveiling the gas-dependent sintering behavior of Au-TiO2 catalysts via environmental transmission electron microscopy
Licensed Content Author	Guanxing Li,Ke Fang,Yuzhuo Chen,Yang Ou,Shanjun Mao,Wentao Yuan,Yong Wang,Hangsheng Yang,Ze Zhang,Yong Wang
Licensed Content Date	Aug 1, 2020
Licensed Content Volume	388
Licensed Content Issue	n/a
Licensed Content Pages	7
Journal Type	S&T

🗑 Order Details

Type of Use	reuse in a thesis/dissertation
Portion	figures/tables/illustrations
Number of figures/tables/illustrations	1
Format	both print and electronic
Are you the author of this Elsevier article?	No
Will you be translating?	No

📄 About Your Work

Title	In situ TEM Investigations of Catalysis Dynamics in Service Conditions
Institution name	University of Illinois at Chicago
Expected presentation date	Sep 2020

📁 Additional Data

Portions	Figure 2

253

Requestor Location

| | University of Illinois at Chicago 929 West Taylor St | Publisher Tax ID | 98-0397604 |

Requestor Location

CHICAGO, IL 60607
United States
Attn: University of Illinois at Chicago

$ Price

Total 0.00 USD

Total: 0.00 USD

CLOSE WINDOW   ORDER MORE

254

Revealing Sintering Kinetics of MoS2-Supported Metal Nanocatalysts in Atmospheric Gas Environments via Operando Transmission Electron Microscopy

ACS Publications
Most Trusted. Most Cited. Most Read.

Author: Boao Song, Timothy T. Yang, Yifei Yuan, et al

Publication: ACS Nano

Publisher: American Chemical Society

Date: Apr 1, 2020

Copyright © 2020, American Chemical Society

255

ACS Publications
Most Trusted. Most Cited. Most Read.

In Situ Oxidation Studies of High-Entropy Alloy Nanoparticles

Author: Boao Song, Yong Yang, Muztoba Rabbani, et al

Publication: ACS Nano

Publisher: American Chemical Society

Date: Oct 1, 2020

Copyright © 2020, American Chemical Society

256

Boao Song

Education

University of Illinois at Chicago	Chicago, IL
Ph.D. Mechanical Engineering	Sep 2015-Sep 2020

ASU HRTEM Winter School Scholarship, Gatan EELS/EFTEM Analysis Training School

University of Rochester	Rochester, NY
Master of Science, Materials Engineering	Sep 2012-July 2014

Nanjing University of Science and Technology	Nanjing, China
Bachelor of Engineering, Materials Science and Engineering	Sep 2008-July 2012

Academic Experience

University of Illinois at Chicago

Mechanical and Materials Research Assistant   Chicago, IL

- Developed *in situ* gas and liquid TEM methods to observe heterogeneous catalysis behaviors in reaction condition.
- Innovated *in situ* gas TEM characterization of catalyst durability at elevated temperature in various gas phases.
- Designed bimetallic heterogeneous catalysts on 2D substrates to diminish high-temperature catalyst degradation.
- Initiated *in situ* liquid TEM technique to explore metallic nanoparticle nucleation and growth on solid-liquid interface.
- Integrated S/TEM and spectroscopy of EDS/EELS to analyze working catalyst's structural and chemical properties.
- Pending patent of designing novel multifunctional *in situ* TEM sample stage with fast and easy mounting mechanism.

University of Rochester

Chemical Engineering Research Assistant   Rochester, NY

- Enhanced proton conductivity by electroplated highly dense c-axis oriented apatite crystal for fuel cell membrane.
- Designed electrochemical process to synthesize doping catalyst with highly uniform size and particle distribution.
- Identified catalyst morphology, crystal structure and chemical composition by SEM, EDS, XPS, Raman techniques.
- Executed catalytic induced drug delivery project to optimize infection prevention in biomedical implant application.
- Extended 20% drug release duration of apatite supported catalyst to improve solid-liquid chemical biocompatibility.

Nanjing University of Science and Technology

Materials Research Assistant   Nanjing, China

- Evolved two new preparation processes for thin film electrolyte by solid-state and sol-gel synthesis.
- Determined best fuel cell performance by testing ceramic powder from 1350 to 1500° C in various time scales.
- Optimized ceramic phase transition performance by ion doping under characterization of SEM and TEM.
- Boosted 15% ionic conductivity of fuel cell LaSiO electrolyte membranes with aluminum ionic doping.

Publications

1. *In situ* study of nucleation and growth dynamics of Au nanoparticles on MoS_2 nanoflakes.

   Nanoscale 10 (33), 15809-15818.

   B. Song, K. He, Y. Yuan, S. Sharifi-Asl, M. Cheng, J. Lu, W. A. Saidi, and R. Shahbazian-Yassar.

2. Revealing Sintering Kinetics of MoS_2 Supported Metal Nanocatalysts in Atmospheric Gas Environments via Operando Transmission Electron Microscopy. *ACS Nano, 14 (4), 4074-4086*

   B. Song, T. T Yang, Y. Yuan, S. Sharifi-Asl, M. Cheng, W. A Saidi, Y. Liu, Reza Shahbazian-Yassar.

3. *In Situ* Oxidation Studies of High-Entropy Alloy Nanoparticles. *ACS Nano, 2020*

    B. Song, Y. Yang, M. Rabbani, T. T Yang, K. He, X. Hu, Y. Yuan, P. Ghildiyal, V.P. Dravid, M.R. Zachariah, W. A Saidi, Y. Liu, R. Shahbazian-Yassar.

4. Aerosol Synthesis of high entropy alloy nanoparticles. *Langmuir*, 36 (8), 1985-1992

    Y Yang, B Song, X Ke, F Xu, KN Bozhilov, L Hu, R Shahbazian-Yassar, M R Zachariah.

5. Identifying Catalytic Active Sites of Trimolybdenum Phosphide (Mo_3P) for Electrochemical Hydrogen Evolution. *Advanced Energy Materials* (2019): 1900516.

    A Kondori, M Esmaeilirad, A Baskin, B Song, J Wei, W Chen, C Segre, R Shahbazian-Yassar, D Prendergast, M Asadi.

6. Oxygen Functionalized Copper Nanoparticles for Solar-Driven Conversion of Carbon Dioxide to Methane. *ACS Nano*, 14 (2), 2099-2108

    M Esmaeilirad, A Kondori, B Song, A Belmonte, J Wei, K Kucuk, S Khanvilkar, E Efimoff, W Chen, C Segre, R Shahbazian-Yassar, M Asadi.

7. Atomic column heights detection in metallic nanoparticles using deep convolutional learning. *Computational Materials Science* (2020), 180

    M Ragone, V Yurkiv, B Song, A Ramsubramanian, R Shahbazian-Yassar, F Mashayek.

8. Ordering Heterogeneity of [MnO6] Octahedra in Tunnel-Structured MnO_2 and Its Influence on Ion Storage. *Joule*. 3 (2), 471-484

    Y Yuan, C Liu, BW Byles, W Yao, B Song, M Cheng, Z Huang, K Amine, E Pomerantseva, R Shahbazian-Yassar, J Lu.

9. Elevated-temperature 3D printing of hybrid solid-state electrolyte for Li-ion batteries. *Advanced Materials,* 2018, 1800615.

    M. Cheng, Y. Jiang, W. Yao, Y. Yuan, R. Deivanayagam, T. Foroozan, Z. Huang, B. Song, R. Rojaee, T. Shokuhfar, Y. Pan, J. Lu, and R. Shahbazian-Yassar.

10. Operando liquid cell electron microscopy of discharge and charge kinetics in lithium-oxygen batteries. *Nano Energy,* 2018, 49, 338-345.

    K. He, X. Bi, Y. Yuan, T. Foroozan, B. Song, K. Amine, J. Lu, and R. Shahbazian-Yassar.

11. Facet-Dependent Thermal Instability in $LiCoO_2$. *Nano Lett*er, 2017, 17, 2165–2171.

    S. Sharifi-Asl, F. A. Soto, A. Nie, Y. Yuan, H. Asayesh-Ardakani, T. Foroozan, V. Yurkiv, B. Song, F. Mashayek, R. F. Klie, K. Amine, J. Lu, P. B. Balbuena, and R. Shahbazian-Yassar.

12. The Influence of Large Cations on the Electrochemical Properties of Tunnel-Structured Metal Oxides. *Nature Commun*ications, 2016, 7, 13374.

    Y. Yuan, C. Zhan, K. He, H. Chen, W. Yao, S. Sharifi-Asl, B. Song, Z. Yang, A. Nie, X. Luo, H. Wang, S. M. Wood, K. Amine, M. S. Islam, J. Lu, and R. Shahbazian-Yassar.

13. Selective Ionic Transport Pathways in Phosphorene. *Nano Lett*er, 2016, 16, 2240–2247.

    A. Nie, Y. Cheng, S. Ning, T. Foroozan, P. Yasaei, W. Li, B. Song, Y. Yuan, L. Chen, A. Salehi-Khojin, F. Mashayek, R. Shahbazian-Yassar.

Conference Presentations

1. **(Invited)** In situ TEM as a way to reveal catalyst dynamics in application conditions. B Song, Yuzi Liu, Reza Shahbazian-Yassar. Midwest Microscopy and Microanalysis Society Spring Meeting 2020. (postponed)

2. **(Best Poster Presentation Awardee)** Revealing Sintering Kinetics of Nanocatalysts on MoS_2 in Hydrogen Environment via *Operando* TEM. B Song, Yifei Yuan, Soroosh Sharifi-Asl, Yuzi Liu, Reza Shahbazian-Yassar. IEEE Nanotechnology Council 2019.

3. *Operando* TEM Investigation of Sintering Kinetics of Nanocatalysts on MoS_2 in Hydrogen Environment. B Song, Yifei Yuan, Soroosh Sharifi-Asl, Yuzi Liu, Reza Shahbazian-Yassar. Microscopy and Microanalysis 2019.

4. *In situ* TEM Investigation on Rotation and Coalescence Behaviors of Au Nanoparticles on h-BN Substrate. Boao Song, Yifei Yuan, Ramin Rojaee, Reza Shahbazian-Yassar. Microscopy and Microanalysis 2019.

5. **(Best Student Poster Awardee)** *Operando* TEM Investigation of Sintering Kinetics of Nanocatalysts on MoS_2 in Hydrogen Environment. B Song, Yifei Yuan, Soroosh Sharifi-Asl, Yuzi Liu, Reza Shahbazian-Yassar. ANL APS/CNM Users Meeting 2019.

6. *In situ* TEM Investigation of Anti-sintering Au@Pt Core-shell Nanostructures on MoS_2 at Elevated Temperatures. B Song, Yifei Yuan, Soroosh Sharifi-Asl, Yuzi Liu, Reza Shahbazian-Yassar. Microscopy and Microanalysis 2018.

7. In Situ Observation of Au Nanoparticles Nucleation and Growth on Ultrathin MoS_2 Substrate. B Song, K He, Y Yuan, S Sharifi-Asl, M Cheng, J Lu, W Saidi, Reza Shahbazian-Yassar. Materials Research Society 2017.

259